



UNIVERSITÀ DEGLI STUDI DI TRIESTE
XXVIII CICLO DEL DOTTORATO DI RICERCA IN FISICA

**ADVANCES IN
SEEDED FREE ELECTRON LASERS:
GENERATION AND CONTROL OF STABLE
AND FULLY COHERENT X-RAY PULSES
IN CONVENTIONAL AND EXOTIC
CONFIGURATIONS**

Settore scientifico-disciplinare: FIS/03

DOTTORANDO
EUGENIO FERRARI

COORDINATORE
PROF. PAOLO CAMERINI

SUPERVISORE DI TESI
PROF. GIOVANNI DE NINNO
PROF. ALFONSO FRANCIOSI

ANNO ACCADEMICO 2014-2015



UNIVERSITÀ DEGLI STUDI DI TRIESTE
XXVIII CICLO DEL DOTTORATO DI RICERCA IN FISICA

ADVANCES IN
SEEDED FREE ELECTRON LASERS:
GENERATION AND CONTROL OF STABLE
AND FULLY COHERENT X-RAY PULSES
IN CONVENTIONAL AND EXOTIC
CONFIGURATIONS

Settore scientifico-disciplinare: FIS/03

DOTTORANDO
EUGENIO FERRARI

Eugenio Ferrari

COORDINATORE
PROF. PAOLO CAMERINI

Paolo Camerini

SUPERVISORE DI TESI
PROF. GIOVANNI DE NINNO
PROF. ALFONSO FRANCIOSI

Giovanni De Nino
Alfonso Franciosi

ANNO ACCADEMICO 2014-2015

Advances in Seeded Free Electron Lasers: Generation
and Control of Stable and Fully Coherent X-ray Pulses in
Conventional and Exotic Configurations

Eugenio Ferrari

April 11, 2016

Introduction

Light sources are amongst the most effective tools to explore the properties of matter. This includes, e.g., the possibility of studying how atoms or molecules aggregate, break up or change their characteristics under the effect of their environment. However, to be suited for this purpose, a light source must have well defined features. Specifically, light pulses must have wavelengths and temporal durations comparable to the ones involved in the process one wants to probe. In the case of atoms and molecules, the latter occurs at nanometric scale (X-ray wavelengths) and in the femtosecond temporal domain. Furthermore the pulses have to be powerful, in order to produce many events and generate an adequate statistics for the sample under study. For many advanced experiments also a well-defined polarization and a high degree of transverse and longitudinal coherence are fundamental assets. Examples of light sources are X-ray tubes and synchrotrons, which are capable of emitting pulses in the X-ray wavelength region, but with long time durations (of the order of tens of picoseconds) and reduced coherence, and conventional lasers that are instead fully coherent and may generate powerful ultra-short pulses. This allows the investigation of both non-linear and extremely fast processes. However, conventional lasers emit radiation in the visible or ultraviolet spectral regions only, due to the lack of active and transparent media capable of supporting lasing at the XUV and X-ray wavelengths.

Single-pass free electron lasers (FELs) can deliver high power femtosecond pulses in the XUV and X-ray spectral region. Moreover, they are characterized by a high degree of coherence, offering the opportunity to combine the advantages of X-ray sources and lasers.

In this Thesis I will focus on single-pass FELs seeded by an external laser, as all the measurements presented in the following were performed at FERMI, which is the first XUV user facility based on such a scheme.

After introducing the necessary concepts of Accelerator and FEL physics, I will describe the main components of the FERMI facility and illustrate its performance, which has been reached also thanks to the work presented in this manuscript.

I will then come to the specific topics of my work, starting from a systematic investigation of the polarization properties of the emitted light in both the conventional setup and in the so-called “crossed polarized undulator scheme”. The experiments we have carried out confirm the full tunability of the polarization of the light generated by FERMI. This study was possible thanks to a large collaboration with experimental groups from DESY (Germany), LOA (France) and LDM (Elettra).

Then I will focus on the analysis of the most impressive property of a seeded FEL source, namely the longitudinal coherence. I will show that the coherence properties of the FEL pulses at FERMI can be shaped by accurately manipulating the seed and electron-beam parameters.

The seeded FEL scheme is particularly sensitive to the properties of the electron beam. A relevant part of my activity was dedicated to the commissioning of a laser heater, a device that allows to control the electron-beam energy spread. The latter plays a major

role in the process leading the FEL to saturation. Together with the colleagues I was able to demonstrate that the shape of the energy spread distribution is preserved from the laser heater up to the FEL. This has a significant impact on the FEL performance, both in terms of minimum wavelength achievable and for the production of multicolour FEL light.

Finally I will focus on the new trend of pump-probe multicolour FEL experiments, which represent a paradigmatic example of synergy between accelerator physicists and experimentalists, who use light to investigate matter. This part of my activity provided me with the invaluable opportunity to work both on the optimization of the light source and on the execution of state-of-the-art experiments on matter samples.

In this Thesis I will describe my contribution to the understanding and development of the FERMI machine. I had the possibility to take part in the commissioning of almost the whole machine as a member of the FERMI Commissioning Team. I significantly contributed to all the experiments and results reported in the following by designing, implementing and fine-tuning the FEL source in collaboration with the colleagues of the FERMI team, as well as in the data acquisition, analysis, reduction and interpretation.

Table of contents

Introduction	4
<hr/>	
1 Accelerator Physics	9
1.1 Particle accelerator theory	9
1.1.1 Electron beam dynamics	9
1.1.2 Magnetic bunch length compression	13
1.2 Synchrotron Radiation	15
1.2.1 Undulator	15
1.2.2 Spontaneous Radiation	17
<hr/>	
2 Free Electron Lasers	21
2.1 FEL physics	21
2.2 Mathematical description	22
2.2.1 3D model	23
2.2.2 Pierce parameter and universal scaling	23
2.2.3 1D model	24
2.3 Wave amplification	24
2.3.1 Linear stability analysis	25
2.4 Bunching and saturation	27
2.4.1 Deep saturation	27
2.5 3D and dispersion effects	28
2.6 FEL configurations	29
2.6.1 Oscillator configuration	30
2.6.2 Single-pass configuration	30
2.6.3 SASE	31
2.6.4 Seeded FELs	31
2.7 State of art	33
<hr/>	
3 FERMI FEL	39
3.1 FERMI facility	39
3.1.1 PADReS	41
3.1.2 The experimental stations	42
3.2 FEL-1 commissioning and performance	44
3.3 FEL-2 commissioning and performance	48
3.4 SASE at FERMI	53

4 Laser Heater	63
4.1 Introduction	63
4.1.1 Microbunching instability	63
4.1.2 Landau damping and laser heating	64
4.1.3 Energy spread and laser heating	66
4.2 FERMI laser heater	67
4.2.1 Layout	67
4.2.2 Longitudinal phase space and heating	70
4.2.3 Microbunching Instability suppression	71
4.3 LH impact on FEL	74
4.4 LH Beating	81
4.5 Conclusions	87
<hr/>	
5 FEL Polarization	91
5.1 The polarization of light	92
5.2 The measurement of light polarization	93
5.2.1 The VUV-optical polarimeter	94
5.2.2 The e-TOF polarimeter	95
5.2.3 The fluorescence polarimeter	97
5.2.4 The photon transport system	98
5.3 Results	100
5.3.1 VUV-optical measurements and analysis	100
5.3.2 e-TOF polarimeter	102
5.3.3 Fluorescence polarimeter	105
5.3.4 Summary	107
5.4 Crossed polarized undulators	108
5.4.1 Gaussian propagation model	109
5.4.2 Pollution effects	114
5.4.3 Experimental results	119
5.4.4 Summary	130
<hr/>	
6 Coherence Control	135
6.1 Phase-Locked FEL pulses	135
6.1.1 Experimental setup	136
6.1.2 Interferogram creation and measurements	136
6.1.3 Interferogram analysis	137
6.1.4 Summary	140
6.2 SPIDER reconstruction of FEL pulses	140
6.2.1 The SPIDER algorithm	140
6.2.2 Generation of the interferogram	142
6.2.3 Analysis of the interferogram	144
6.2.4 Reproducibility of the spectro-temporal reconstruction	144
6.2.5 Summary	145
6.3 Spectro-temporal shaping of seeded FEL pulses	146
6.3.1 How to control the FEL pulse shape	146
6.3.2 Experimental results	147
6.3.3 Summary	148

7 Two Color FEL	153
7.1 Two seed pulses, single radiator harmonic	154
7.1.1 Generation of twin FEL pulse	154
7.1.2 Proof-of-principle pump and probe experiment	155
7.1.3 Summary	160
7.2 Two seed pulses, FEL radiator tuned at different harmonics for wide wave-length tunability	161
7.2.1 Scheme implementation	162
7.2.2 Resonant-pump/resonant-probe magnetic scattering experiment	164
7.2.3 Summary	170
7.3 One seed pulse, two harmonics locked in phase	172
7.3.1 Scheme implementation	172
7.3.2 Test experiment	174
7.3.3 Summary	176
Appendices	183
<hr/>	
A Diagnostics	185
A.1 Electron beam diagnostics	185
A.2 The transverse diagnostics	185
A.2.1 The wire-scanner	186
A.3 Timing system	187
A.4 The longitudinal diagnostics	187
A.4.1 The relative Bunch Length Monitor (BLM)	187
A.4.2 The Bunch Arrival Monitor (BAM)	188
A.4.3 Electro-optical sampling (EOS)	189
A.5 RF deflectors	191
A.6 Longitudinal phase space characterization	191
A.7 The hole	193
A.8 Conclusions and prospective	195
<hr/>	
B Data Acquisition and Analysis	197
B.1 Real time capabilities at FERMI	197
B.2 The acquisition program	197
B.2.1 Types of acquisition	198
B.2.2 Data acquired during scans	199
B.3 The analysis program	200
B.3.1 Data selection	201
B.3.2 Data filtering	201
B.3.3 Data analysis and plot	202
B.3.4 Visual correlator	204
B.3.5 Image analysis	206
B.3.6 Machine setup	206
B.4 Conclusion	206

Chapter 1

Accelerator Physics

1.1 Particle accelerator theory

Accelerator physics relates primarily to the interaction of charged particles with electromagnetic fields. Detailed knowledge of this interaction allows the design of accelerators meeting specific goals and the prediction of charged particle beam behaviour in those accelerators. The interplay between particles and fields is called beam dynamics [1].

1.1.1 Electron beam dynamics

Several techniques exist to accelerate charged particles [2]. Modern linear accelerators, also called LINACs, use radio frequency (RF) cavities in order to accelerate the particles to the desired energy [1]. Inside the RF cavities a strong longitudinal electric field is maintained, with frequencies from hundreds of MHz up to few GHz.

When a particle, in our case an electron, passes through a LINAC cavity its energy is changed by the interaction with the RF accelerating (decelerating) field. The energy gain (loss) is:

$$\frac{d(\gamma mc^2)}{dt} = eV \sin(\omega_{RF}t + \phi), \quad (1.1)$$

where V is the peak accelerating voltage of the cavity, ϕ is the phase in between the RF wave and the electron bunch, ω_{RF} is the RF (angular) frequency, m is the particle's rest mass, e the electron charge and c the speed of light. The Lorentz factor γ is defined as

$$\gamma = \frac{1}{\sqrt{1 - \beta^2}} \quad (1.2)$$

with $\beta = \frac{|\vec{v}|}{c}$, \vec{v} being the velocity of the electron.

Other than acceleration, the motion of a charged particle in electromagnetic fields is governed by the Lorentz force:

$$\frac{d(\gamma m \vec{v})}{dt} = e \left(\vec{v} \times \vec{B} \right), \quad (1.3)$$

where \vec{B} is the magnetic field generated by the magnet.

In any particle accelerator a reference trajectory is defined by design. This is the trajectory that each of the particles should follow. Using electromagnetic fields one forces the

particles to move as close as possible to the design trajectory. The typical fields used for beam guiding are provided by stationary magnetic fields. The magnetic fields are generated in magnets which are typically specialized in order to provide the required field. Dipole (bending) magnets are used to bend the trajectory of the particles along the design orbit, if the design orbit is not a straight path [3]. As the bending angle depends on the particle momentum, the design trajectory is defined for the nominal momentum of the particles p_0 . It follows that particles with a different momentum p will follow a different trajectory than the design one. It is useful to define δ , the relative deviation of the momentum of the particle from the nominal one. Variations in the particles' momentum tends to spread the beam in the transverse direction. In order to control the beam transverse dimensions transverse focusing has to be implemented. This is normally done using quadrupole magnets.

The design orbit typically lies within a plane and all magnets are oriented in such a way that the particle motion can be decoupled in the horizontal and vertical direction [1]. It is convenient to describe the motion of individual particles in terms of coordinates related to the reference particle. At any longitudinal position s along the reference trajectory, the instantaneous position of a particle can be expressed in the curvilinear coordinate system (x, y, s) , schematically represented in Fig. 1.1.

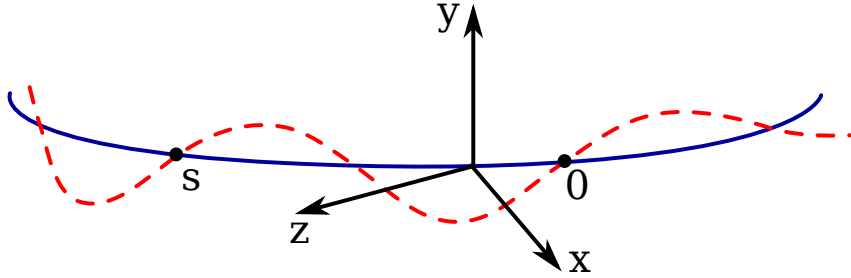


Figure 1.1: Reference system along the design orbit (blue curve) and oscillations around it (red dashed line). Image courtesy of F. Curbis.

The linear equation of motion for an electron in an accelerator for the independent variable s can be expressed as [3]:

$$\frac{d^2x}{ds^2} = -K_x(s)x + \frac{\delta}{\rho(s)} = p_0(1 + \delta), \quad (1.4)$$

where terms of second and higher order in (x, y, δ) are neglected. $\rho(s)$ is the local bending radius along the beam trajectory at the position s [3]. $K_x(s)$ is a function of the magnetic elements present along the beam trajectory and describes the focusing (defocusing). A proper arrangement of alternating quadrupolar fields is required to keep particles close to the design trajectory simultaneously in both transverse planes [3]. Eq. (1.4) is an Hill's differential equation [4]. The homogeneous equation have a general solution that can be expressed as linear combination of $u_1(s)$ and $u_2(s)$ in the interval $s_0 \leq s \leq L$:

$$\begin{aligned} x(s) &= a_1u_1(s) + a_2u_2(s) \\ x'(s) &= a_1u_1'(s) + a_2u_2'(s). \end{aligned} \quad (1.5)$$

Eqs. (1.5) can be rewritten in matrix form as:

$$X(s) = U(s) \cdot A, \quad (1.6)$$

where

$$X(s) = \begin{pmatrix} x(s) \\ x'(s) \end{pmatrix}; U(s) = \begin{pmatrix} u_1(s) & u_2(s) \\ u'_1(s) & u'_2(s) \end{pmatrix}; A = \begin{pmatrix} a_1 \\ a_2 \end{pmatrix}. \quad (1.7)$$

The matrix equation, Eq. (1.6), yields to a representation of the general solution in terms of the initial conditions $X(s_0)$. It can be expressed as:

$$X(s) = M(s, s_0) \cdot X(s_0), \quad (1.8)$$

where M is called the transfer matrix [1]. The described considerations can be naturally extended to the y plane.

The transfer matrix can be written as:

$$M(s, s_0) = \begin{pmatrix} C(s) & S(s) \\ C'(s) & S'(s) \end{pmatrix}, \quad (1.9)$$

where C and S are cosine and sine-like solutions of Hill's equation satisfying the initial conditions:

$$C(s_0) = 1; C'(s_0) = 0; S(s_0) = 0; S'(s_0) = 1. \quad (1.10)$$

The transfer matrices M can be written for the specific elements present along the beam trajectory. The transfer matrix of a beamline (a collection of elements) is obtained via matrix multiplication of the transfer matrices of the single elements. A solution of the inhomogeneous equation, Eq. (1.4), can be found by using Green's functions, resulting in the particular solution $\delta\eta(s)$ with [1, 5]:

$$\eta(s) = S(s) \int_{s_0}^s \frac{C(t)}{\rho(t)} dt - C(s) \int_{s_0}^s \frac{S(t)}{\rho(t)} dt, \quad (1.11)$$

the momentum dispersion function. Physically, $\delta\eta(s)$ is the horizontal offset of an electron with relative momentum deviation δ from the design orbit at position s , provided the electron was moving on the design orbit in a small interval around s_0 . As for the homogeneous solution, also the general solution of the inhomogeneous equation can be expressed in matrix notation:

$$\begin{pmatrix} x(s) \\ x'(s) \\ \delta \end{pmatrix} = \begin{pmatrix} C(s) & S(s) & \eta(s) \\ C'(s) & S'(s) & \eta'(s) \\ 0 & 0 & 1 \end{pmatrix} \begin{pmatrix} x(s_0) \\ x'(s_0) \\ \delta \end{pmatrix}. \quad (1.12)$$

Intuitively, it is possible to extend the matrix formulation to include both transverse planes and the longitudinal motion of the particles inside the beam. This is done by describing the particle coordinates with a 6-dimensional vector $\bar{X}(\bar{x}(s))$, where $\bar{x}(s) = (x, x', y, y', z, \delta)$. In the latter the longitudinal position of the particle z , relative to the beam centroid $z_0 = 0$ has been introduced. Summarizing the above considerations one can write the matrix equation of the particles inside the bunch in the six dimension phase space as

$$\bar{X}(\bar{x}(s)) = R \cdot \bar{X}(\bar{x}(s_0)). \quad (1.13)$$

Any element R_{ij} of matrix R for a particular lattice component indicates the influence of the value assumed by the coordinate j at the start of the element, on the coordinate i at the end of the element. Let's consider for example relativistic particles with different energy that move on different paths in an element that has $R_{56} \neq 0$. Their longitudinal separation, if the other coordinates are the same for the two particle and at the first order in the energy separation, evolves in this way:

$$\Delta z_f = \Delta z_i + R_{56} \cdot \frac{\Delta E}{E}, \quad (1.14)$$

where Δz_f is the separation after the element, Δz_i is the separation before the element and $\frac{\Delta E}{E}$ is the relative energy separation of the two particles.

It is usually possible to assume a decoupling of the two transverse planes dynamics, that allows to set to zero the R matrix elements that couple $x - x'$ to $y - y'$. A further simplification is consider a beamline without any RF cavities, leading to the R matrix:

$$R = \begin{pmatrix} R_{11} & R_{12} & 0 & 0 & 0 & R_{16} \\ R_{21} & R_{22} & 0 & 0 & 0 & R_{26} \\ 0 & 0 & R_{33} & R_{34} & 0 & 0 \\ 0 & 0 & R_{43} & R_{44} & 0 & 0 \\ R_{51} & R_{52} & R_{53} & R_{54} & 1 & R_{56} \\ 0 & 0 & 0 & 0 & 0 & 1 \end{pmatrix}. \quad (1.15)$$

The general solution of the homogeneous Hill's equation can also be expressed in the phase-amplitude form [6]

$$\begin{aligned} x(s) &= \sqrt{a_x \beta_x(s)} \cos(\phi_x(s) + \Psi_x) \\ y(s) &= \sqrt{a_y \beta_y(s)} \cos(\phi_y(s) + \Psi_y), \end{aligned} \quad (1.16)$$

where $\beta_x(s)$, $\beta_y(s)$ are the horizontal and vertical the betatron function, $\phi_x(s)$, $\phi_y(s)$ the horizontal and vertical phase advance function. Also, $a_x(s)$, $a_y(s)$ and Ψ_x , Ψ_y are real constants specifying the particular solution. The betatron function completely describes, in a given accelerator, the transverse focusing. The maximum displacement of a particle from the design orbit at position s are:

$$\begin{aligned} \Delta_x &= \sqrt{a_x \beta_x(s)} \\ \Delta_y &= \sqrt{a_y \beta_y(s)}. \end{aligned} \quad (1.17)$$

The phase-amplitude solution can be rewritten in $x(s)$ and $x'(s)$ according to [6]:

$$\begin{aligned} \gamma_x x^2 + 2\alpha_x x x' + \beta_x x'^2 &= a_x \\ \gamma_y y^2 + 2\alpha_y y y' + \beta_y y'^2 &= a_y. \end{aligned} \quad (1.18)$$

Eqs. (1.18) define two ellipses in the coordinates space, one in the (x, x') plane and one in the (y, y') plane, both centered at $(0, 0)$ and with area πa_x , πa_y . The motion of the particles can be interpreted as oscillations on an ellipse in phase space. The shape of the ellipses varies along the accelerator according to the transfer matrices M , while the area is a constant of motion, called the Courant-Snyder invariant. The relation of Courant-Snyder parameters to the ellipse is sketched in Fig. 1.2.

The evolution of the electron beam distribution can be described by means of the covariance matrix

$$\sigma_x = \begin{pmatrix} \langle x^2 \rangle & \langle x x' \rangle \\ \langle x x' \rangle & \langle x'^2 \rangle \end{pmatrix}, \quad (1.19)$$

evolving from s_0 to s_1 according to the matrix formalism:

$$\sigma_x(s_1) = M \sigma_x(s_0) M^T. \quad (1.20)$$

$\langle x \rangle$ and $\langle x^2 \rangle$ are the first and second moment of the beam distribution. It is possible to demonstrate [5] that the following relation holds:

$$\begin{aligned} \epsilon_x \beta_x(s) &= \langle x(s)^2 \rangle \\ \epsilon_y \beta_y(s) &= \langle y(s)^2 \rangle, \end{aligned} \quad (1.21)$$

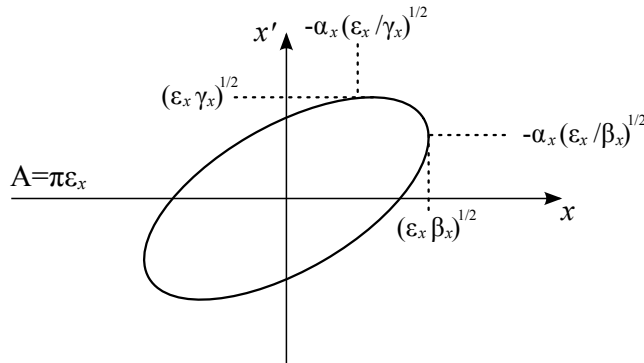


Figure 1.2: Phase space ellipse. Image courtesy of F. Curbis.

where ϵ_x (ϵ_y) is called horizontal (vertical) geometric emittance [5]. It is defined as:

$$\epsilon_x = \sqrt{\det(\sigma_x)} = \sqrt{\langle x^2 \rangle \langle x'^2 \rangle - \langle xx' \rangle^2}. \quad (1.22)$$

The emittance represents the (RMS) area occupied by the beam in the $x - x'$ space (similar definition is also possible for the vertical transverse space). The quantity $\langle x(s)^2 \rangle$, corresponding to the element $(\sigma_x)_{11}$ of the covariance matrix, can be directly measured in a LINAC by looking at the bunch transverse profile. This implies that it is possible to measure the product of emittance and the beta function at the profile monitor location. By implementing the quadrupole scan technique [5] it is further possible to recover the Twiss parameters α , β and γ of the beam at the same location and thus gain full knowledge of the transverse dynamics of the electron bunch.

1.1.2 Magnetic bunch length compression

In order to increase the beam current, thus to increment the beam brightness, bunch length compression is usually implemented. The technique decreases the bunch length by ballistic contraction of their path length through a magnetic chicane, typically composed of 4 identical bending magnets. The requirement of a chicane is due to the fact that all the particles in the electron beam are ultra-relativistic and they practically travel all at the same speed, which is approximately the speed of light. The chicane provides a path length depending on the energy of each electron, in particular higher energy electrons will travel on a shorter trajectory. If the electrons toward the tail of the bunch have a higher energy than the ones towards the head, the tail will follow a shorter, i.e. faster path while the ones in the head will follow a longer path. The net effect is that the bunch edges will approach the central part of the beam reducing the overall bunch length.

To introduce the required energy dependence along the beam (time-energy correlation) one can change the accelerating phase of structures upstream the bunch compressor from the “crest” (maximum accelerating voltage, $\phi = 90^\circ$) to an “off-crest” condition, as schematically described in Fig. 1.3. In this condition the particles towards the tail of the bunch (blue dot) are accelerated by the RF wave of the accelerating structure more than the ones towards the head (red dot).

Notice that in the mathematical description that follows, we have chosen a longitudinal coordinate system such that the head of the bunch is located at $z < 0$. We also define the relative energy variation that will be used in the following as:

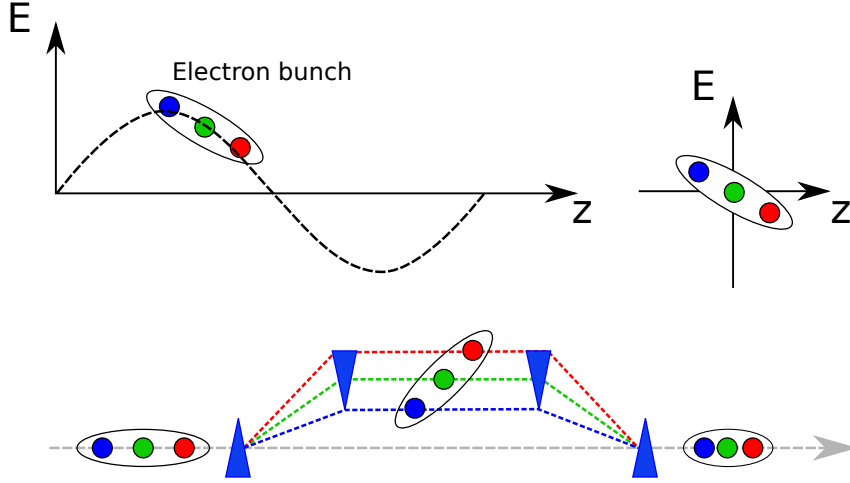


Figure 1.3: Schematic representation of off-crest acceleration in a LINAC cavity (top) and of a 4-dipole symmetric bunch compressor (bottom). The cavity is set at a phase that introduces a time-energy correlation inside the electron beam. This is due to the different amplitude of the RF field for different parts of the electron beam. The different beam paths, depending on the particle energy, are also shown. Higher energy particles (towards the tail) travel on a shorter path with respect to the lower energy particles (towards the head of the bunch). Image courtesy of S. Di Mitri.

$$\delta = \frac{\delta\gamma}{\gamma_0}. \quad (1.23)$$

As a first approximation we can expand the path length dependence on the energy to the first order in δ . Such dependence can be described, using the matrix formalism, as

$$R_{56} = \frac{\partial z}{\partial \delta}. \quad (1.24)$$

In this approximation the relative position of a particle inside the beam after the bunch compression is:

$$z_f = z_i + R_{56}\delta, \quad (1.25)$$

where z_i is the position of the same particle before the chicane.

For a 4 magnet chicane composed of rectangular and identical magnets R_{56} has an approximate expression [7] that reads

$$R_{56} \simeq -2\theta^2(d + \frac{2}{3}l_{eff}), \quad (1.26)$$

where θ is the deflection angle of the bending magnet, d is the distance between the first and the second magnet and l_{eff} is the magnetic length of one magnet.

Also δ can be expanded to the 1st order:

$$\delta = hz, \quad (1.27)$$

with h the linear energy chirp of the beam.

If we consider an electron beam of energy E_0 entering a LINAC with energy gain $E = eV \times \sin \phi$ with V the peak accelerating voltage and ϕ the phase in between the accelerating field and the electrons, the linear energy chirp of the beam can be written as:

$$h = \frac{d\delta}{dz} = \frac{2\pi}{\lambda_{RF}} \frac{eV \cos \phi}{E_0 + eV \sin \phi}. \quad (1.28)$$

The initial electron bunch (RMS) length is σ_{z_0} . By substituting Eq. (1.27) and (1.28) into Eq. (1.25), one can evaluate the (RMS) bunch length after compression which results to be:

$$\sigma_z = \langle z^2 - \langle z \rangle^2 \rangle \simeq \sigma_{z_0} (1 + hR_{56}) = \frac{\sigma_{z_0}}{C}. \quad (1.29)$$

It is customary to introduce the compression factor C , the ratio of the initial and final bunch length, defined as

$$C = \frac{1}{1 + h \cdot R_{56}}. \quad (1.30)$$

The peak current of the beam after compression is increased by a factor equal to the compression factor. The beam is compressed for $C > 1$, which implies, from Eq. (1.30), that $h \cdot R_{56} < 0$. One can also see from Eq. (1.26) that R_{56} is negative so a positive chirp is needed to compress the beam.

Up to now we described the linear approximation of the bunch compression, i.e., assuming linear dependence in z and δ . In this approximation any point of the beam undergoes the same compression factor and the bunch shape is preserved, so by starting with a flat current profile it is possible to get a flat current distribution at the LINAC end, usually preferred for FEL operations. In reality higher order terms can be present in the beam energy chirp. If one considers a second order term, the transformation of the bunch longitudinal coordinate through the magnetic chicane and the quantity δ at the 2nd order are [7]:

$$z_f = z_i + R_{56}\delta + T_{566}\delta^2 \quad (1.31)$$

$$\delta = hz + h'z^2 \quad (1.32)$$

$$h' = \frac{d^2(\delta)}{dz^2} = \frac{1}{2} \frac{dh}{dz} = -\left(\frac{2\pi}{\lambda_{RF}}\right)^2 \frac{eV \sin \phi}{E_0 + eV \sin \phi}, \quad (1.33)$$

where $T_{566} = -\frac{3}{2}R_{56}$ describes the second order dependence of the chicane transport matrix on energy. It has been shown that the second order terms lead to a non-linear compression for a $C > 3$ [8], with a non-linear dependence of the particle position z and a non-linear compression factor along the beam. This leads to the rise of unwanted current spikes at the edges of the bunch. The usage of an harmonic RF accelerating cavity [9, 10] can be adopted in order to also introduce an equal and opposite 2nd order term in the beam energy chirp that cancels out the second order energy chirp, thus reinstating a linear compression.

1.2 Synchrotron Radiation

1.2.1 Undulator

An undulator is an insertion device composed of a periodic magnetic structure with period $\lambda_u = 2\pi/k_u$ and amplitude $\vec{B}_u(z) = (B_{u,x}, B_{u,y})$. In the reference frame of Figure 1.1 the magnetic field can be described as

$$\begin{aligned} B_{u,x}(z) &= B_{0x} \cos(k_u z), \\ B_{u,y}(z) &= -B_{0y} \sin(k_u z). \end{aligned} \quad (1.34)$$

The magnetic field is generated by two arrays of permanent magnets, with alternating polarity. The structure forces the electrons to follow an oscillating trajectory. If $B_{0x} = 0$ the undulator is called planar. In this case the magnetic field is sinusoidal and lies in the (yOz) plane, see Figure 1.4(a). Instead, if $B_{0x} = B_{0y} = B_0$ the undulator is called helical, see Figure 1.4(b), as the generated magnetic field describes an helix centered on the undulator axis: its projection on the (xOy) plane is a circle. In the intermediate cases the undulator is in an elliptical configuration. Its magnetic field can be described as the superposition between a circular and a linear components: its projection on the (xOy) plane is an ellipse.

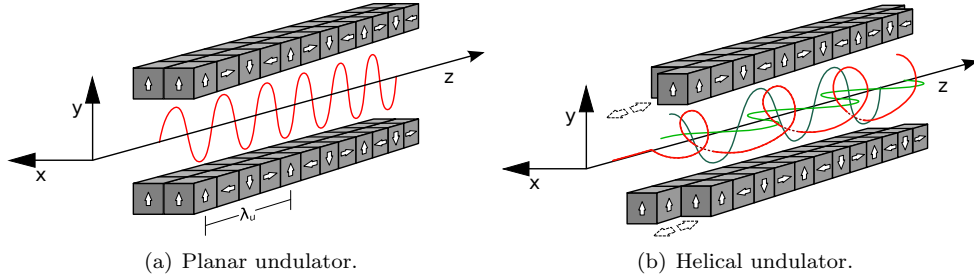


Figure 1.4: Magnetic field (red continuous line) of an undulator. For the helical case the two field components are also shown (green lines).

The interaction between the electrons and the undulator field is ruled by the Lorentz force. Using Eq. (1.3) one can observe that the electrons oscillate on a trajectory that has the same symmetry of the magnetic field.

To see that, we integrate Eq. (1.3) once to find the expression for the velocity of the electron having energy γ [11]

$$\begin{aligned}\beta_{ex} &= \frac{K_y}{\gamma} \cos(k_u z), \\ \beta_{ey} &= -\frac{K_x}{\gamma} \sin(k_u z), \\ \beta_{ez} &= \sqrt{\beta_e^2 - \beta_{ex}^2 - \beta_{ey}^2},\end{aligned}\tag{1.35}$$

where the undulator strengths in x and y directions, $K_{x,y}$, are defined as [11]

$$K_{x,y} = \frac{e\lambda_u B_{0x,y}}{2\pi mc}.\tag{1.36}$$

It's also customary to define the total strength parameter as

$$K = \sqrt{K_x^2 + K_y^2}.\tag{1.37}$$

The longitudinal (along z axis) velocity of the electrons depends on the configuration of the device. Indeed, combining together Eqs. (1.35), we obtain:

- for the planar case

$$\begin{aligned}\beta_{ez} &= \sqrt{1 - \frac{1}{\gamma^2} (1 + K_x^2 \sin^2(k_u z))} \\ &\simeq \sqrt{1 - \frac{1}{\gamma} \left(1 + \frac{K^2}{2} (1 - \cos(2k_u z))\right)},\end{aligned}\quad (1.38)$$

- and for the helical case:

$$\beta_{ez} = \sqrt{1 - \frac{1 + K^2}{\gamma^2}}. \quad (1.39)$$

With a second integration step one gets

$$\begin{aligned}x &= \frac{K_y}{k_u \gamma} \sin(k_u z), \\ y &= -\frac{K_x}{k_u \gamma} \cos(k_u z), \\ z &= \beta_{ez} ct.\end{aligned}\quad (1.40)$$

In the case of a planar undulator the electron trajectory is (almost) “sinusoidal”, on a plane that is perpendicular to the magnetic field, see Figure 1.5(a). For an helical undulator, instead, the electrons describe a helix, centered on the axis of the device, see Figure 1.5(b).

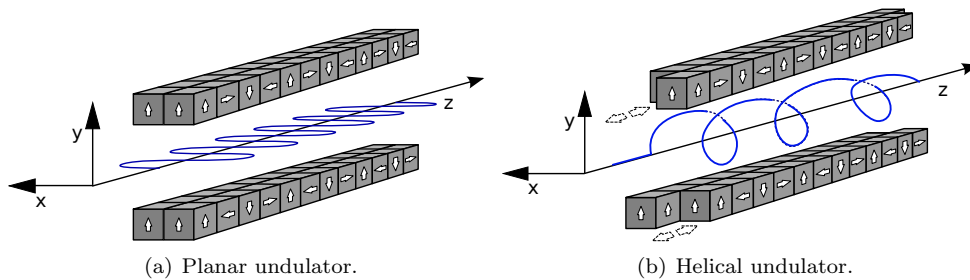


Figure 1.5: *Electron trajectory (blue continuous line) inside an undulator.*

An APPLE-II type undulator [12, 13] is a particular kind of insertion device made of two pairs of magnetic chains mounted on rails that can slip one with respect to the other. In this way, one can vary the phase between one chain and the other in a definite and continuous way, switching from planar to helical configuration and passing (continuously) through all intermediate configurations.

1.2.2 Spontaneous Radiation

As we have just seen, the electrons inside an undulator are subject to a force, so they are accelerated and emit synchrotron radiation: this light is called spontaneous emission.

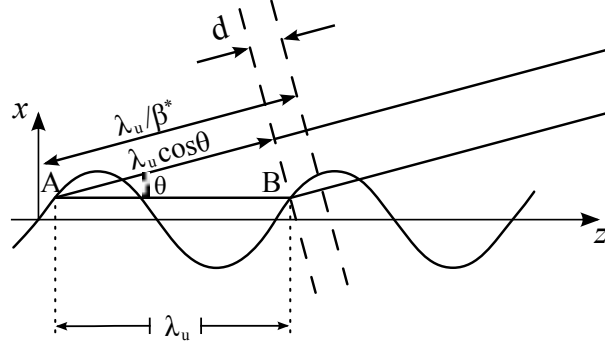


Figure 1.6: Interference in an undulator. Image reproduced from [14].

The properties of the radiation emitted by an undulator can simply be understood in terms of interference [14] of wave-fronts emitted by the same electron at different points of the magnetic lattice (see Figure 1.6).

The electrons are moving along z direction with the mean drift velocity

$$c\beta^* \simeq c\beta \left(1 - \frac{K^2}{4\gamma^2} \right) \simeq 1 - \frac{1}{2\gamma^2} - \frac{K^2}{4\gamma^2}, \quad (1.41)$$

where β^* is the mean drift velocity of the electron, normalized to c .

In the time it takes to the electron to move through one period length from point A to an equivalent point B (λ_u/β^*c) the wave-front from A has advanced by a distance λ_u/β^* and hence is ahead of the radiation emitted at point B by a distance d that can be expressed as:

$$d = \frac{\lambda_u}{\beta^*} - \lambda_u \cos \theta, \quad (1.42)$$

where θ is the angle of emission with respect to the electron beam axis. When this distance is equal to an integer number, n , of radiation wavelengths (λ_{rad}) there is constructive interference of the radiation emitted by the same electron at equivalent points (e.g., A and B in Figure 1.6). This relation can be expressed as:

$$\frac{\lambda_u}{\beta^*} - \lambda_u \cos \theta = n\lambda_{rad}. \quad (1.43)$$

Inserting in the previous equation the expression for the average electron velocity, Eq. (1.41), the interference conditions results

$$\lambda_r = \frac{\lambda_u}{2\gamma^2} \frac{1}{n} \left(1 + \frac{K^2}{2} + \gamma^2 \theta^2 \right), \quad (1.44)$$

where we substituted $\lambda_{rad} = \lambda_r$ and $n = 1, 2, 3, \dots$ is the harmonic number.

The undulator emission occurs at λ_r and at its harmonics λ_r/n . The relation is valid for any undulator configuration, using the appropriate value of K defined by Eqs. (1.36) and (1.37).

The maximum frequency is observed on-axis.

This relation allows to give evidence to one of the most precious features of synchrotron radiation, i.e. tunability, which is the possibility to adjust the emission wavelength either by varying the electron energy γ , or the strength K .

The spontaneous emission is only partially coherent (in the transverse direction), due to the well defined spatial period of the undulator, but it is not coherent longitudinally, as each electron emits radiation independently, so without a definite phase relation with respect to the emission of others particles.

The radiation intensity is therefore proportional to the number of emitting electrons.

The interference model can supply further information about the spread in wavelength as follows. If the undulator consists of N_u periods and its total length is $L_u = N_u \lambda_u$, the condition for constructive interference over the entire length becomes:

$$\frac{L_u}{\beta^*} - L_u \cos \theta = n N_u \lambda_{rad}. \quad (1.45)$$

Vice versa, the interference becomes destructive when there is one extra wavelength of wavefront separation over the length of the device:

$$\frac{L_u}{\beta^*} - L_u \cos \theta = n N_u \lambda' + \lambda'. \quad (1.46)$$

Subtracting Eq. (1.45) and (1.46) yields the range of emitted wavelengths at fixed angle θ :

$$\frac{\Delta \lambda}{\lambda} = \frac{1}{n N_u}. \quad (1.47)$$

This corresponds to the linewidth (full width at half maximum, FWHM) of the emitted radiation at the n^{th} harmonic.

It's also possible to calculate the spectral distribution of the emitted radiation using the well known formalism of the Lienard-Weichert potentials [15]. The fundamental formula is

$$\frac{d^2 I}{d\Omega d\omega} = \frac{e^2 \omega^2}{4\pi^2 c} \left| \int_{-\infty}^{+\infty} \vec{n} \times (\vec{n} - \vec{\beta}) \exp \left[i\omega \left(t - \frac{\vec{n} \cdot \vec{r}(t)}{c} \right) \right] dt \right|^2, \quad (1.48)$$

where \vec{n} is the (instantaneous) versor of the direction between the charge and the observer, Ω is the solid angle, ω is the angular frequency of the radiation and $\vec{r}(t)$ is the position of the charge, as defined in Eq. (1.40).

Focusing on the simpler case of the planar undulator, one finds that the emitted on-axis energy per unit frequency and solid angle reads

$$\frac{d^2 I}{d\Omega d\omega} = \frac{e^2}{4\pi\epsilon_0 c} \left(\frac{K N_u \lambda_u}{\gamma} \right)^2 \sum_{n(\text{odd})}^{\infty} \frac{A_n^2}{\lambda^2} \left(\frac{\sin(\delta_n)}{\delta_n} \right)^2, \quad (1.49)$$

with

$$A_n \approx J_{\frac{n+1}{2}} \left(\frac{nK^2}{4 + 2K^2} \right) - J_{\frac{n-1}{2}} \left(\frac{nK^2}{4 + 2K^2} \right), \quad (1.50)$$

and

$$\delta_n = \pi N_u \left(n - \frac{\lambda_r}{\lambda} \right). \quad (1.51)$$

where J_n are the Bessel functions and N_u is the number of magnetic periods in the undulator, n the harmonic number.

In the case of a planar undulator the odd harmonics are emitted both on- and off-axis, while the even harmonics can be found only off-axis. In the case of an helical undulator, only the fundamental is emitted on-axis, while all the other harmonics are emitted off-axis [11]. This is exact only for an electron beam with divergence equal to zero. If the

divergence is different from zero, the resulting spectrum is the convolution between the angular distribution of the radiation and the distribution of the electron bunch.

The emitted radiation has a definite polarization with the same symmetry of the motion of the electrons, so it is linear (s or p) if the undulator is in planar configuration, and it is circular (left or right hand) if the device is in helical configuration.

References

- [1] H. Wiedemann. *Particle Accelerator Physics*. New York: Springer, 2007.
- [2] P.J. Bryant. “A brief history and review of accelerators”. In: *Proc. of General accelerator physics school of CERN 1992*. CERN, Geneva. 1994.
- [3] E.D. Courant and H.S. Snyder. In: *Ann. Phys.* 3.1 (1958).
- [4] L.A. Pipes. *Applied Mathematics for Engineers and Physicists*. McGraw-Hill, 1958.
- [5] J. Rossbach and P. Schmüser. “Basic course on accelerator optics”. In: *Proc. of general accelerator physics school of CERN 1992*. Vol. 1. CERN, Geneva. 1994, p. 17.
- [6] M. Röhrs. “Investigation of the Phase Space Distribution of Electron Bunches at the FLASH LINAC Using a Transverse Deflecting Structure”. PhD thesis. Hamburg, (Germany): Hamburg University, 2008.
- [7] P. Emma. *Bunch Compressor Options for the New TESLA Parameters*. SEA-98-54. 1998.
- [8] S. Di Mitri. “Machine Design and Electron Beam Control of a Single-Pass LINAC for Free-Electron Laser: The FERMI@Elettra Case Study”. PhD thesis. 2011.
- [9] D. Dowell et. al. In: *Proc. of PAC 1995, Dallas, Texas*. 1995.
- [10] P. Emma. Tech. rep. LCLS-TN-01-1. 2011.
- [11] H. Onuki and P. Elleaume, eds. *Undulators, Wigglers and Their Applications*. CRC Press, London, 2002.
- [12] S. Sasaki K. Miyata T. Takada. “A new undulator for generating variably polarized radiation”. In: *Jpn. J. Appl. Phys.* 31 (1992), pp. L1794–L1796.
- [13] S. Sasaki. “Analyses for a planar variably-polarizing undulator”. In: *Nuclear Instruments and Methods in Physics Research Section A: Accelerators, Spectrometers, Detectors and Associated Equipment* 347.1-3 (Aug. 1994), pp. 83–86. DOI: [10.1016/0168-9002\(94\)91859-7](https://doi.org/10.1016/0168-9002(94)91859-7).
- [14] R. P. Walker. *Insertion devices: undulators and wigglers*.
- [15] J. D. Jackson. *Classical electrodynamics*. New York: J. Wiley, 1975.

Chapter 2

Free Electron Lasers

2.1 FEL physics

The working principle of a single-pass FEL relies on the interaction between an ultra-relativistic electron beam and a co-propagating electromagnetic wave, in the presence of a static and periodic magnetic field generated by an undulator. Inside the magnetic field, electrons are forced to follow an oscillating trajectory, and the transverse component of their velocity is coupled to the co-propagating wave. This interaction results in a force along the direction of propagation. Depending on their phase with respect to the electromagnetic field, electrons can gain or lose energy. Eventually, the interaction causes a density modulation in the electron bunch: particles distribute in micro-bunches on the scale of the radiation wavelength and its harmonics. Such a “bunching” is the source of coherent FEL emission. The FEL process starts when there is a net amplification of the electromagnetic wave to the detriment of the electrons’ energy. The emitted intensity is amplified along the longitudinal coordinate of the undulator, until the interaction between the electrons and the radiation becomes strongly non-linear: at this point, through mechanisms that we will describe in the following, the process reaches saturation and the emitted intensity becomes nearly stationary.

In principle, the electrons can couple with electromagnetic fields with an arbitrary frequency, but, in general, this does not imply a net energy transfer between the electrons and the wave. In fact, on average, when an electron transfers energy to the field, there is another particle that gains energy at expense of the wave. In order to have a net energy transfer, the coupling must be “resonant”. Such a condition is schematically represented in Figure 2.1.

In Figure 2.1(a), the electron position (thin arrow) is chosen so that it feels a positive component of the magnetic field of the wave: the particle feels a decelerating force and loses energy.

Along its motion inside the undulator, the electron “slips” back with respect to the wave-front. This behavior is mainly due to two reasons: the electron velocity is lower than the speed of light; the electron follows a sinusoidal trajectory while the light follows a straight path. The resonance condition implies that the “slippage” of the electron with respect to the wave must be equal to one wavelength of the radiation for every undulator period.

In Figure 2.1(b) we can observe what happens after a distance equal to half the undulator period. The electron, in this position, has a delay of $\lambda_r/2$ with respect to the wave-front, the magnetic field and the velocity have opposite sign with respect to Figure 2.1(a), which means that the particle feels again a decelerating force: it again loses energy. In Figure 2.1(c)

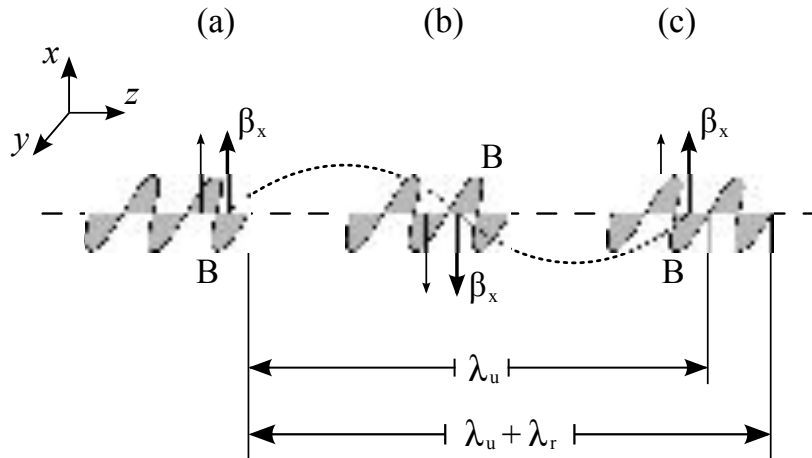


Figure 2.1: Phases relations between the electromagnetic wave and the electron beam, in resonance condition. Dashed line: electron trajectory. Shaded parts represent the magnetic component of the co-propagating wave (B), from [1]. Case of planar undulator.

the situation is again the one of Figure 2.1(a): at this point the electron has accumulated a delay with respect to the co-propagating wave equal to λ_r . This situation is the only one in which the electron loses continuously energy and transfers it to the radiation field. In fact, one can show that there is a net gain and the electromagnetic wave is amplified when the electron beam is slightly out of resonance: in the case of perfect resonance, in fact, half of electrons gain energy and half lose energy, so no net energy transfer is present. This is shown in Figure 2.1 by the presence of another electron (bold arrow) which is in the condition of continuous absorption of energy from the field.

The slippage requirement can be expressed by the condition

$$\frac{\lambda_u(1 - \beta_x)}{\beta_x} = \lambda_r, \quad (2.1)$$

where β_x is the mean longitudinal velocity of the electron, normalized to c .

One can show [2] that this relation can be written as

$$\lambda_r = \frac{\lambda_u}{2\gamma^2} \left(1 + \frac{K^2}{2} + \gamma^2\theta^2 \right). \quad (2.2)$$

This relation is equivalent to the one for the spontaneous undulator emission, see Eq. (1.44). Therefore, in order to have amplification of the electromagnetic field which co-propagates with the electrons, the radiation wavelength must be equal to the one which corresponds to the center of spontaneous emission.

2.2 Mathematical description

In this section we will describe the FEL process, starting from the Maxwell and Lorentz equations. The description will be done in a three dimensional framework, but can be reduced to the one dimensional case by means of some approximations.

2.2.1 3D model

We consider a mono-energetic electron beam moving through an undulator generating a static magnetic field $\vec{B}_u(z)$, see Figure 1.4(a) or 1.4(b). In the same region, we assume the existence of a co-propagating electromagnetic field $\vec{E} = -\frac{1}{c} \frac{\partial \vec{A}}{\partial t}$ and $\vec{B} = \nabla \times \vec{A}$, where \vec{A} is the vector potential of the radiation field. The radiation field has a wavelength λ_r and a frequency $\omega_r = \frac{c2\pi}{\lambda_r}$.

The evolution of the momentum and the energy of each electron is determined by the Newton-Lorentz equations

$$\begin{cases} \frac{d(\gamma m \vec{v})}{dt} = e \left[\vec{E} + \frac{\vec{v}}{c} \times (\vec{B}_u + \vec{B}) \right], \\ \frac{d(\gamma m c^2)}{dt} = e \vec{E} \cdot \vec{v}_y. \end{cases} \quad (2.3)$$

Although the 3D model described above is more general and accounts for the three dimensional effects, it is also possible to describe the FEL process in a 1D framework. Before presenting the equations of the 1D model, we will describe the parametrization we will use, and the so called ‘‘universal scaling’’. For the details of the derivation process, we advice [3, 4].

2.2.2 Pierce parameter and universal scaling

The so-called fundamental FEL parameter, or Pierce parameter, ρ is defined as:

$$\rho = \frac{1}{\gamma_r} \left(\frac{K \omega_p}{4 c k_u} \right)^{\frac{2}{3}}, \quad (2.4)$$

where $\omega_p = \sqrt{\frac{4\pi e^2 n_e}{m}}$ is the plasma frequency, with n_e the electron number density and γ_r is the resonant energy¹.

It is convenient to parametrize the system using the following set of variables

$$\begin{cases} \Gamma_j \equiv \frac{\gamma_j}{\rho \langle \gamma \rangle_0}, \\ \tilde{A} \equiv \frac{\omega_r}{\omega_p \sqrt{\rho \langle \gamma \rangle_0}} \exp(i\delta \tilde{z}) \frac{e \lambda_r E}{2\pi m c^2}, \\ \tilde{\theta}_j \equiv \theta_j - \delta \tilde{z}, \\ \tilde{z} \equiv 2 \left(\frac{\gamma_r}{\langle \gamma \rangle_0} \right)^2 k_u \rho z, \\ \tilde{t} \equiv 2 \left(\frac{\gamma_r}{\langle \gamma \rangle_0} \right)^2 k_u \rho t, \end{cases} \quad (2.5)$$

¹The resonant energy can be obtained by inverting Eq. (2.2), which leads ($\theta = 0$) to

$$\gamma_r = \sqrt{\frac{\lambda_u}{2\lambda_r} (1 + K^2)}.$$

where $\langle \gamma \rangle_0$ is the average electron energy at the undulator entrance and t is the time variable. The phase θ_j of the j -th electron in the “ponderomotive” (undulator + wave field), is defined as

$$\theta = (k_r + k_u)z - \omega_r t. \quad (2.6)$$

Finally, δ is the energy-detuning parameter defined as:

$$\delta = \frac{1}{\rho} \frac{\langle \gamma \rangle_0^2 - \gamma_r^2}{\gamma_r^2}. \quad (2.7)$$

2.2.3 1D model

In the regime we are interested in (the so-called Compton regime), the energy of the electron beam is high and the charge density is low, which results in $\rho \ll 1$. Assuming the relative energy variation of electrons is:

$$\left| \frac{\gamma_j - \langle \gamma \rangle_0}{\langle \gamma \rangle_0} \right| \ll 1, \quad (2.8)$$

and defining the variable “momentum” as:

$$\tilde{p}_j = \Gamma_j - \frac{1}{\rho} = \frac{1}{\rho} \frac{\gamma_j - \langle \gamma \rangle_0}{\langle \gamma \rangle_0}, \quad (2.9)$$

we can express the steady-state equations as:

$$\left\{ \begin{array}{l} \frac{d\tilde{\theta}_j}{d\tilde{z}} = \tilde{p}_j, \\ \frac{d\tilde{p}_j}{d\tilde{z}} = -\tilde{A} \exp(i\theta_j) - \tilde{A}^* \exp(-i\theta_j), \\ \frac{d\tilde{A}}{d\tilde{z}} = i\delta\tilde{A} + \langle \exp(-i\tilde{\theta}) \rangle, \end{array} \right. \quad (2.10)$$

where

$$b = \langle \exp(-i\tilde{\theta}) \rangle \quad (2.11)$$

is the electron bunching parameter.

2.3 Wave amplification

We now determine the conditions leading to wave amplification. These are the conditions under which the system, supposed initially in an equilibrium state, becomes linearly unstable.

2.3.1 Linear stability analysis

Starting from an equilibrium state characterized by no initial field ($\tilde{A}_0 = 0$), zero bunching ($\langle \exp(-i\tilde{\theta}) \rangle = 0$) and cold beam ($\langle p_j \rangle_0 = 0$), we want to follow the evolution of the system until the wave reaches saturation. Eqs. (2.10), can be linearised and twofold differentiated with respect to \bar{z} , obtaining the third order differential equation:

$$\frac{d^3}{d\bar{z}^3} \tilde{A} - i\delta \frac{d^2}{d\bar{z}^2} \tilde{A} - i\tilde{A} = 0. \quad (2.12)$$

Searching a solution in the form $\tilde{A}(z) \sim \exp(i\lambda z)$, we obtain the well-known cubic equation for λ :

$$\lambda^3 - \delta\lambda^2 + 1 = 0. \quad (2.13)$$

Two situations are possible: if the solution is made of three real roots, the system is stable; if instead the solution corresponds to one real root ($\lambda = \lambda_1$) and two complex-conjugate roots ($\lambda = \lambda_2 \pm i\lambda_3$), then the system is unstable. In the latter case the field amplitude grows exponentially along the undulator as

$$\tilde{A}(z) \propto \exp(\lambda_3 \bar{z}) \equiv \exp(gz), \quad (2.14)$$

where g is the exponential gain per unit length and can be written as:

$$g = \lambda_3 \frac{4\pi\rho}{\lambda_u} \left(\frac{\gamma_r}{\langle \gamma \rangle_0} \right)^2. \quad (2.15)$$

In Figure 2.2 is shown the gain curve as a function of \bar{z} in the resonant case ($\delta = 0$). We can observe that the amplification shows a “lethargic” behavior before the start of the gain. During this phase, the linear modes interfere between each other, until the mode with the exponential behavior prevails.

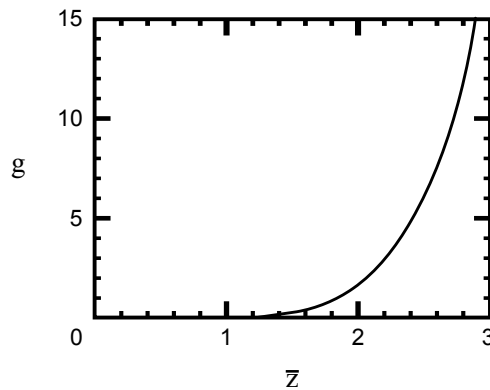


Figure 2.2: Intensity of the field as a function of \bar{z} . Image reproduced from [4].

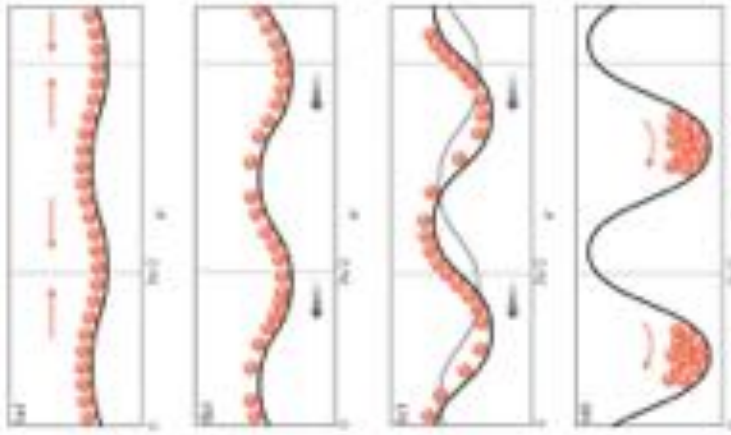


Figure 2.3: Bunching evolution. (a) electrons are randomly distributed in phase (initial condition corresponds to weak electromagnetic field. (b) and (c) electrons start bunching on the scale of the wavelength and the electromagnetic wave is amplified. (d) electrons are at the maximum bunching achievable.

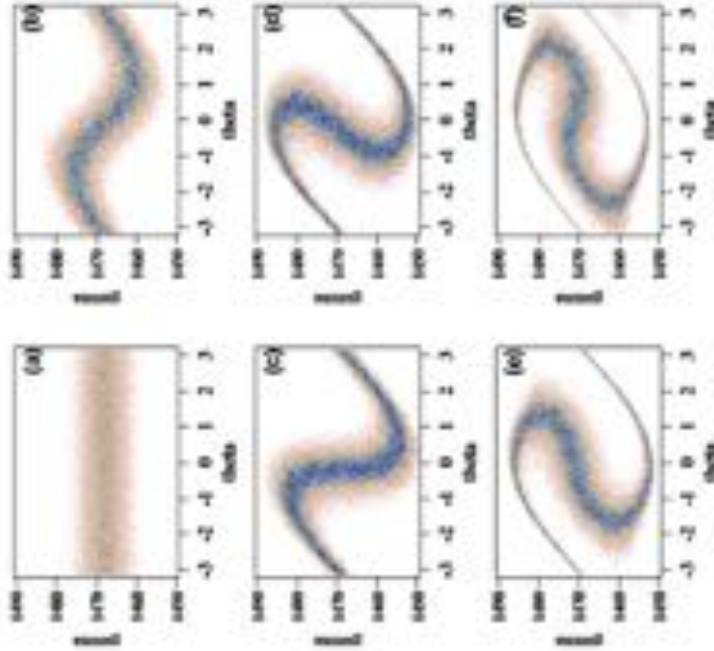


Figure 2.4: Evolution of the electron-beam phase space. (a) initial distribution, (b) energy modulation, (c) spatial modulation (bunching), (d) slight overbunching, (e) and (f) overbunching, courtesy F. Curbis.

2.4 Bunching and saturation

The bunching coefficient defined in Eq. (2.11) is one of the key parameters in the FEL description. We consider the longitudinal mean velocity of electrons ($\bar{\beta}_z$) and the phase velocity (v_p) of the ponderomotive field. When an electron beam starts to interact with an electromagnetic wave, all the particles are randomly distributed in phase with respect to the wave (see Figure 2.3(a)).

As the resonance condition ($c\bar{\beta}_z = v_p$) is satisfied half of particles absorb energy from the electromagnetic wave and the other half transfer energy to the wave (low gain): this causes the electrons to cluster where the ponderomotive phase is zero and hence the amplification is zero.

The velocity of the resonant electrons is then $c\bar{\beta}_z > v_p$, and they bunch around a phase where there is positive gain.

Figure 2.4 explains the saturation mechanism, as it occurs in the electron phase space (γ, θ) . The interaction with the ponderomotive wave induces a modulation of the electrons' energy. This energy modulation evolves in spatial modulation, which is the bunching. The maximum gain occurs when the electron phase is advanced of a phase equal to a quarter of the ponderomotive force period. As the beam proceeds further inside the undulator, the spatial modulation arises also where the ponderomotive force is positive and this causes "over-bunching". At this point the process reaches the saturation because the electrons are not any more able to transfer their energy to the wave. The saturation is not a stationary state because the system do not reach an equilibrium condition. The evolution of the spatial distribution of the electrons at the scale of the resonant wavelength is schematically shown in Figure 2.5.

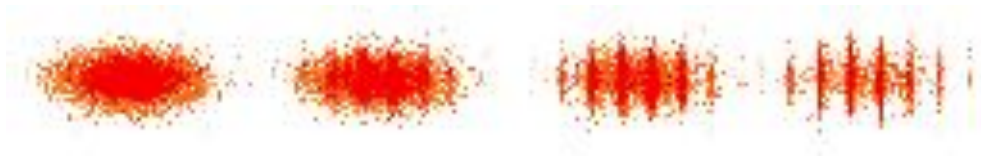


Figure 2.5: How the spatial distribution (bunching) evolves in an electron beam, courtesy F. Curbis.

Following a more mathematical approach, one can perform a Fourier analysis of the beam density distribution: the bunching on the h -th harmonic is defined as the h -th Fourier coefficient of this series expansion.

2.4.1 Deep saturation

In order to get the behavior of $|A|^2$ it is necessary to integrate numerically the Eqs. (2.10). The result one obtains is shown in Figure 2.6.

Once the saturation is reached, the intensity does not attain a stationary regime, but it oscillates around an average value, of the order of the unity. From this consideration we can conclude that

$$|A|^2 \propto \frac{|E|^2}{\rho n} \Rightarrow |E|^2 \propto n^{4/3}, \quad (2.16)$$

which means that the process is characterized by a collective behavior.

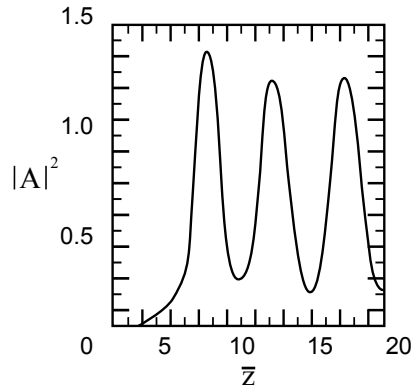


Figure 2.6: Intensity of the field as a function of \bar{z} . Image reproduced from [4].

2.5 3D and dispersion effects

The 1D model we have considered up to now does not take into account the effects due to the transverse dynamics of the system. These include the effects that come from the finite dimensions of the electron beam, the angular divergence of the particles and the angular divergence of the radiation. Moreover, one has to take into account the fact that the electron beam is not mono-energetic. Such effects may deteriorate the performance of the system.

Emittance and diffraction

As we have seen in Chapter 1, the emittance ϵ is a quantity that takes into account the finite transverse dimension of the beam, σ , and the angular dispersion of the particles inside it, σ' . There are several different factors that contribute to the emittance value, as the temperature of the cathode from which the electrons are extracted, the inhomogeneities of the acceleration fields, etc.

If we suppose that we can neglect the diffraction effects, i.e. when the undulator length L_u is matched to the Rayleigh length of the radiation, we can find a qualitative condition that must be satisfied by the emittance in order to have an optimal transverse coupling between the radiation and the electrons. The optimal coupling occurs when the transverse areas of the electron and radiation beams are almost equal. Indeed, if this condition is satisfied, all the electrons contribute to the amplification of the electromagnetic wave. The radiation spot size is given by $w_0 \simeq \sqrt{\lambda L_u}$, while the radiation angular divergence (at diffraction limit) is $\sigma' \simeq \sqrt{\lambda/L_u}$: this means that the transverse emittance of the radiation beam is $w_0 \sigma' \simeq \lambda$.

The condition for the optimal coupling can be therefore expressed as

$$\epsilon \lesssim \lambda. \quad (2.17)$$

This condition becomes more critical as the emitted wavelength becomes shorter.

In order to take into account the transverse interaction and the diffraction, while keeping the 1D formalism, requires the introduction of a “filling factor”, which modifies the expression of the ρ parameter (see [5]).

Energy dispersion

In the realistic case the electron beam is not mono-energetic, but it is instead characterized by a certain energy distribution $f(\gamma)$. By solving Eqs. (2.10), one finds the dispersion

relation

$$\lambda - \delta + \int_{-\infty}^{+\infty} d\gamma \frac{f(\gamma)}{(\lambda + \gamma)^2} = 0, \quad (2.18)$$

which determines the stability of the system. In the mono-energetic approximation this relation reduces to Eq. (2.12).

If we consider (as an example) a rectangular distribution defined as

$$f(\gamma) = \begin{cases} \frac{1}{2\mu} & \text{if } -\mu \leq \gamma \leq \mu \\ 0 & \text{elsewhere} \end{cases}, \quad (2.19)$$

where μ is the half-width of the distribution, the cubic equation becomes

$$\lambda - \delta(\lambda^2 - \mu^2) + 1 = 0. \quad (2.20)$$

As shown in Figure 2.7, the width of the distribution can significantly modify the gain curve $\lambda_3 = \lambda(\delta)$: this can eventually lead to suppression of the amplification.

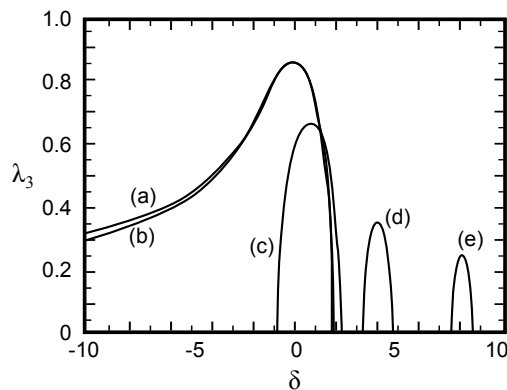


Figure 2.7: Behaviour of the imaginary part of the root of the cubic equation (2.20), as a function of the detuning δ , if the beam has a rectangular energy distribution. (a) $\mu = 0$, (b) $\mu = 0.1$, (c) $\mu = 1$, (d) $\mu = 4$, (e) $\mu = 8$. Image reproduced from [4].

In fact, the maximum gain values decreases as $(2\mu)^{-1/2}$.

2.6 FEL configurations

There are several FEL configurations. First of all, one can distinguish between the single-pass configuration, where the amplification of the electromagnetic wave occurs in one passage through the undulator, and the oscillator configuration, in which the electromagnetic wave is stored inside an optical cavity and lasing is achieved as the results of a large number of light-electron interaction inside the undulator.

Single-pass FEL can be in turn subdivided in two classes, depending on the origin of the electromagnetic wave which co-propagate with the electron beam inside the undulator: we can distinguish between SASE (Self Amplified Spontaneous Emission) and seeded configurations, if the electromagnetic field is generated by the spontaneous emission of the electrons or if it comes from an external “seed” source (respectively).

2.6.1 Oscillator configuration

The oscillator configuration is characterized by an optical cavity that encloses the undulator. In order to enhance the emission it is customary to take advantage of the interference created by an optical klystron. The presence of interference fringes enhances the gain of the amplification process. In FEL oscillators [6], the initial co-propagating field is provided by the spontaneous emission of electrons emitted when the latter pass through the undulators. The emitted radiation is stored into the optical cavity, made by two mirrors with very high reflectivity, and amplified during many successive interactions with the electron beam, until saturation is achieved.

The electron beam can be provided either by a storage ring or a linear accelerator. The oscillator configuration allows to generate FEL radiation in the visible-VUV range or in the IR. In Figure 2.8 is shown an example of an FEL in oscillator configuration, installed on a storage ring.

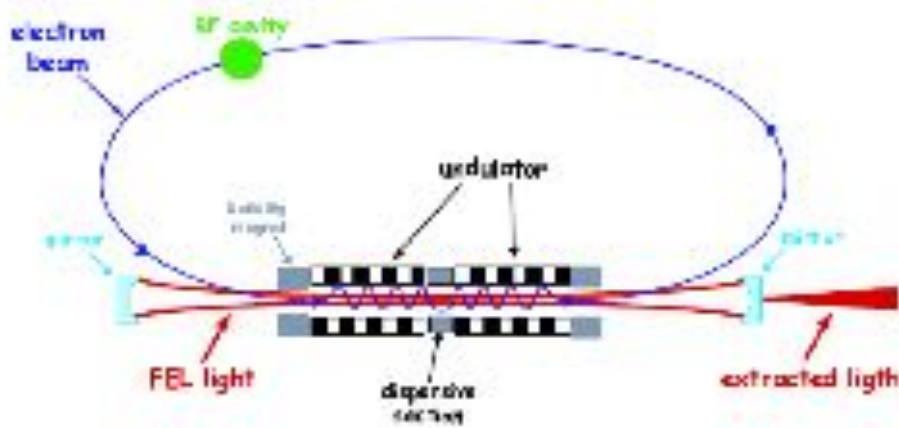


Figure 2.8: An example of storage ring FEL, operated in oscillator configuration, courtesy M.E. Couprie.

The spectral width of the emitted radiation is mainly determined by the mirrors of the optical cavity, which are normally characterized by a narrow bandwidth (few percent around the central line) and by a high (95% or more) reflectivity.

The main limitation of this setup is due to the lack of robust materials with high reflectivity in the VUV and X-rays range. This limits the possibility of reaching very short wavelength using this kind of devices.

2.6.2 Single-pass configuration

Since there is lack of materials with the required high reflectivity necessary to operate oscillator FEL's in the X-ray spectral region, there has been a great interest in developing single-pass FEL's that do not need mirrors. In this configuration, the electron beam interacts with the electromagnetic field and amplifies it in a single pass through the undulator. In Figure 2.9 we show a scheme of a single-pass FEL based on a linear accelerator source. When considering single-pass FELs two different configurations can be distinguished, depending on the origin of the electromagnetic wave which co-propagates with electrons in the undulator: the SASE [7–13] or the seeded configurations [14–21].

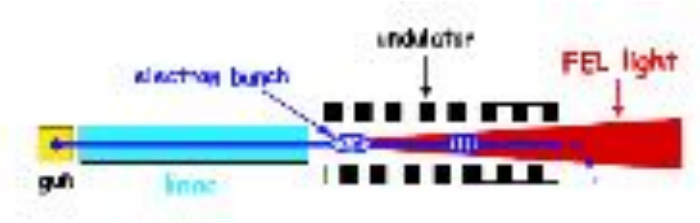


Figure 2.9: An example of an FEL operated in single-pass configuration. The gun produces an electron beam, that is accelerated by an accelerator (also called LINAC) and finally injected into the undulator. Courtesy F. Curbis.

2.6.3 SASE

The SASE takes advantage of the spontaneous emission of electrons propagating through the undulator. The FEL amplifier is seeded by the incoherent spontaneous radiation emitted by the beam in the first part of the undulator [22]. The laser power grows exponentially along the undulator with a characteristic gain length $L_g = \lambda_u / (4\pi\sqrt{3}\rho)$ [11, 22, 23], where ρ is the FEL parameter. Saturation is reached after about $20 L_g$. The electromagnetic wavelength which is amplified by the electrons is given by the resonance condition, Eq. (2.2). Quite long undulators (tens of meters) are normally needed for this process to take place. Since it originates from spontaneous emission, the SASE radiation preserves the noisy characteristics of the latter: the emitted radiation is the envelope of a series of random spikes with variable duration, intensity and position inside the envelope. The light characteristic strongly depends on the electron beam properties: for example, if different bunches have significant different currents, or significant (mean) energy fluctuations, also the radiation will display significant shot-to-shot fluctuations in the intensity and/or in the wavelength [24, 25]. The SASE output has very good spatial mode and is easily tunable, just by changing the energy of the electrons and/or the undulator parameter (like “standard” synchrotron radiation). However, radiation shows an incoherent temporal structure, resulting from the envelope of a series of micro-pulses with random intensity and duration.

2.6.4 Seeded FELs

The lack of temporal coherence can be overcome using an external source of radiation to seed the amplification process that inherits the coherence properties of the external source itself. This external source can be an external laser, the non-linear harmonics produced in gas (HHG) or another FEL [26, 27]. The direct seeding is however limited by the availability of external sources at very short wavelengths.

High Gain Harmonic Generation

A different approach to take advantage of the seed coherence properties, as well as to reach short wavelengths, uses the electron beam as an active medium to generate radiation at harmonics of the seed laser itself [15, 17–20]. One of the most efficient schemes to generate harmonic radiation relies on at least two independent undulators, see Figure 2.10, the second one being tuned to one of the harmonics of the first.

The first undulator, called “modulator”, is tuned in order to be resonant at the same wavelength of the external seed. The seed is focused inside the modulator and transversally superimposed to the electron beam, as well as synchronized in time in order to have an

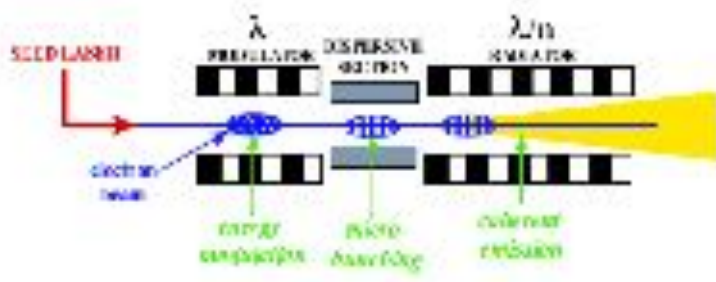


Figure 2.10: Seeded harmonic generation scheme. Image courtesy of F. Curbis.

effective interaction between the electrons and the seed itself. The laser-electron interaction produces energy modulation in the particle distribution, which can be converted into spatial modulation (bunching) via the usage of a short magnetic chicane, also called dispersive section, placed between the undulators. The dispersive section modifies the electrons path depending on their energy. Fourier analysis of the electron beam density emerging from the dispersive section evidences the presence of bunching at the seed laser wavelength and its harmonics. According to [15] the bunching fraction at the exit of the dispersive section can be expressed as:

$$b_m = \exp\left(-\frac{1}{2}m^2\sigma_\gamma^2 D^2\right) J_m(m\Delta\gamma_S D), \quad (2.21)$$

where m is the harmonic number, $D \equiv 2\pi R_{56}/\gamma_0\lambda$, R_{56} is the strength of the dispersive section, $\lambda = \lambda_S/m$ is the emitted radiation wavelength, γ_0 the electron beam Lorentz factor, $\Delta\gamma_S$ is the seed laser-induced energy modulation amplitude, and J_m is the m^{th} order Bessel function. Eq. (2.21) is only valid in the hypothesis that the seed laser intensity is constant along the modulator, its radius σ_r is much greater than that of the electron beam σ_x , and more importantly, that the (incoherent) energy spread of the electron beam follows a Gaussian distribution with (RMS) σ_γ . We will see in Chapter 4 that a different distribution of the electron beam energy can influence the bunching coefficient of the HGHG process.

The electron beam is then injected into the second undulator, called “radiator” and tuned at one of the harmonics of the seed, where it emits coherent radiation that can be amplified via the FEL process up to saturation.

According to Eq. (2.21), the bunching at harmonic m is significant only if $\Delta\gamma_S \geq m\sigma_\gamma$. However, in order to have an effective FEL gain in the radiator, $\Delta\gamma_S/\gamma_0$ must not overcome the FEL parameter $\rho \sim 10^{-3}$ [4]. These two conditions are competing so only a trade-off is possible, which can be summarized in a requirement on the normalized energy spread $\sigma_\gamma/\gamma_0 \leq \rho/m$. The result effectively limits the possible maximum harmonic number, i.e., the minimum wavelength reachable, at which significant FEL radiation can be emitted using the scheme.

In order to overcome the limit describe above, a successive HGHG stage with modulator, dispersive section and radiator can follow the first one, using the radiation coming from the first radiator as seed. This is the case of the second FEL line of FERMI (named FEL-2) that will be presented in Chapter 3.

Other seeding schemes

The above mentioned limitations could be overcome if different proposed schemes would be implemented (e.g., [21, 28, 29]). One of the most promising scheme is the echo-enabled harmonic generation [28] approach which is based on multiple stages of modulation and dispersion to modify the electron beam's longitudinal phase space (LPS) introducing in it fine structures. Those structures permit efficient emission of FEL radiation at higher harmonic numbers compared to standard HGHG even if a relatively large energy spread is present at the undulator entrance.

Recently the self-seeding scheme [26] has been successfully implemented to seed a SASE-based source. In this scheme the SASE radiation produced in the first part of the undulator is monochromatized via a dedicated soft [30] or hard [31] monochromator. Such radiation is then used to seed the electron beam in the second part of the undulator in a direct seeded amplifier scheme.

2.7 State of art

We conclude this Chapter presenting the current status of the FEL-based sources, focusing on single-pass devices. For a detailed list of existing FEL projects, see e.g. [32].

The FEL idea was first proposed in 1971 by J.M.J. Madey [33], while the first FEL operation has been obtained at Stanford [6], in 1977, with emission of coherent radiation in the IR range. The visible range was reached on the ACO storage ring [34] in 1983.

The principle of SASE was proposed in 1980 [10] and 1984 [11]. The first demonstration of saturation has been achieved at LEUTL (Low Energy Undulator Test Line, Advanced Photon Source, Argonne, USA) [35] in 2000.

The High Gain Harmonic Generation (HGHG) scheme has proposed in 1991 [15] and tested at Deep Ultra Violet FEL (National Synchrotron Light Source, BNL, USA) with the generation of the first coherent UV FEL radiation at 266 nm [17, 18, 36] in 2000.

In recent years a number of machines started user operations in the VUV, soft and hard X-rays wavelength range. Based on the SASE scheme is FLASH [37, 38] (Free-electron Laser in Hamburg) at DESY (Germany) first lasing was achieved in 2000 and it reached the shortest wavelength at 4.1 nm. Linac Coherent Light Source [39, 40] (SLAC, Stanford, USA) obtained first lasing in 2009 and is currently operating in the soft and hard X-rays up to 12.82 keV. SACLA (Spring-8 Compact SASE Source) [41] at Spring-8 (Japan) lased in 2011 and its shortest wavelength is 0.634 Å.

Both FLASH and LCLS are undergoing an upgrade phase (phase-II) to extend the capabilities of the sources and to overcome the limitations arisen during the first years of operations.

Based on the HGHG seeded scheme are FERMI (Elettra, Italy), with operation range of 4-100 nm [27, 42, 43], sFLASH [44] at Desy, SDUV-FEL at Shanghai [45, 46].

Under development or commissioning based on SASE are European XFEL [47] (DESY, Germany), SwissFEL (PSI) [48, 49], PAL XFEL [50] with target shortest wavelength 0.1 nm.

Single-pass experiments can also be based on storage rings. In particular, based on the HG scheme, are present at Elettra [51, 52] in Italy and UVSOR [53] in Japan. The DELTA project [54-56] at the Dortmund University, also based on a storage ring, can produce radiation at wavelengths ~ 20 nm.

In table 2.1 a summary of the FEL projects is reported.

Table 2.1: Single-pass VUV and X-ray FEL facilities. Status: (C) under construction, (O) in operation, (U) open to User experiments, (D) in design. The accelerator can be normal conducting (NC), superconducting (SC). If not specified, it is a LINAC. Data from [32, 57]

Name	Location	Status	Accelerator	Wavelength [nm]	Beam energy [GeV]	Q [pC]	I [kA]
EuXFEL	Hamburg, Germany	C	SC	0.05 - 4.7	14.0	250	5.0
SACLA	Riken, Japan	O/U	NC	0.063 - 0.3	8.45	300	4.0
PAL XFEL	Pohang, South Korea	C	NC	0.1	10.0	200	3.0
SwissFEL	Villigen, Switzerland	C	NC	0.1 - 0.7/0.7 - 7	5.8	200	3.0
LCLS	Menlo Park, USA	O/U	NC	0.12 - 1.5	14.0	250	3.0
LCLS-II	Menlo Park, USA	D	SC	0.6	4.5	150	3.5
FERMI	Basovizza, Italy	O/U	NC	4 - 18/16 - 100	1.5	700	0.7
FLASH	Hamburg, Germany	O/U	SC	4.1 - 45	1.2	500	2.5
FLASH-II	Hamburg, Germany	O/U	SC	4.0	1.2	1000	1.2
SXFEL	Shanghai, China	C	NC	8.8-200	0.84	500	0.6
OK-4	Duke Univ., USA	O/U	storage ring	193-400			
CLARA	Daresbury, UK	T	NC	100	0.25	250	0.4
SDUV FEL	Shanghai, China	O	NC	328	0.14	500	0.05
SPARC	Frascati, Italy	O	NC	530	0.10	300	0.12
MARIE	Los Alamos, USA	D	NC	0.03	20	100	3.4
SR-FEL	Basovizza, Italy	storage ring	85 - 390	0.7 - 1.8			

References

- [1] R. Bakker. PhD thesis. 1993.
- [2] G. Dattoli A. Renieri. “Free electron lasers”. In: <http://cas.web.cern.ch/cas/Pruhonice/PDF/Renieri.pdf>.
- [3] W. Colson. “The nonlinear wave equation for higher harmonics in free-electron lasers”. In: *IEEE J. Quantum Electron.* 17.8 (1981), pp. 1417–1427.
- [4] R. Bonifacio F. Casagrande G. Cerchioni L. De Salvo Souza P. Pierini N. Piovella. “Physics of the high-gain FEL and superradiance”. In: *Riv. Nuovo Cimento* 13.9 (1990).
- [5] M. Xie. “Exact and variational solutions of 3D eigenmodes in high gain {FELs}”. In: *Nuclear Instruments and Methods in Physics Research Section A: Accelerators, Spectrometers, Detectors and Associated Equipment* 445.1–3 (2000), pp. 59–66. ISSN: 0168-9002. DOI: [10.1016/S0168-9002\(00\)00114-5](https://doi.org/10.1016/S0168-9002(00)00114-5).
- [6] D.A.G. Deacon L.R. Elias G.J. Ramian H.A. Schwettman T.I. Smith. “First operation of a free electron laser”. In: *Phys. Rev. Lett.* 38 (1977), p. 892.
- [7] S. V. Milton E. Gluskin S. G. Biedron R. J. Dejus P. K. Den Hartog J. N. Galayda K.-J. Kim J. W. Lewellen E. R. Moog V. Sajaev N. S. Sereno G. Travish N. A. Vinokurov N. D. Arnold C. Benson W. Berg J. A. Biggs M. Borland J. A. Carwardine Y.-C. Chae G. Decker B. N. Deriy M. J. Erdmann H. Friedsam C. Gold A. E. Grelick M. W. Hahne K. C. Harkay Z. Huang E. S. Lessner R. M. Lill A. H. Lumpkin O. A. Makarov G. M. Markovich D. Meyer A. Nassiri J. R. Noonan S. J. Pasky G. Pile T. L. Smith R. Soliday B. J. Tieman E. M. Trakhtenberg G. F. Trento I. B. Vasserman D. R. Walters X. J. Wang G. Wiemerslage S. Xu B.-X. Yang. “Observation of self-amplified spontaneous emission and exponential growth at 530 nm”. In: *Phys. Rev. Lett.* 85 (2000), pp. 988–991.
- [8] M. Babzien I. Ben-Zvi P. Catravas J.-M. Fang T. C. Marshall X. J. Wang J. S. Wurtele V. Yakimenko L. H. Yu. “Observation of self-amplified spontaneous emission in the near-infrared and visible wavelengths”. In: *Phys. Rev. E* 57 (1998), pp. 6093–6100.
- [9] J. Andruszkow et al. “First observation of self-amplified spontaneous emission in a free-electron laser at 109 nm wavelength”. In: *Phys. Rev. Lett.* 85 (2000), pp. 3825–3829.
- [10] A. M. Kondratenko E. L. Saldin. “Generation of coherent radiation by a relativistic electron beam in an undulator”. In: *Part. Accel.* 10 (1980), pp. 207–216.
- [11] R. Bonifacio C. Pellegrini L. M. Narducci. “Collective instabilities and high-gain regime in a free electron laser”. In: *Opt. Comm.* 50.373 (1984).
- [12] B. Murphy C. Pellegrini. “Generation of high intensity coherent radiation in the soft x-ray and VUV region”. In: *Journ. OSA* 259.373 (1985).
- [13] R. Brinkmann. “The European XFEL project”. In: *Proceedings of the 2006 FEL Conference*. 2006.
- [14] R. Coisson F. De Martini. *Physics of quantum electronics*. Addison-Wesley Reading, 1982.
- [15] L. H. Yu. “Generation of intense UV radiation by subharmonically seeded single pass free electron lasers”. In: *Phys. Rev. A* 44.5178 (1991).

- [16] A. Doyuran M. Babzien T. Shaftan L. H. Yu L. F. DiMauro I. Ben-Zvi S. G. Biedron W. Graves E. Johnson S. Krinsky R. Malone I. Pogorelsky J. Skaritka G. Rakowsky X. J. Wang M. Woodle V. Yakimenko J. Jagger V. Sajaev I. Vasserman. “Characterization of a high-gain harmonic-generation free-electron laser at saturation”. In: *Phys. Rev. Lett.* 86.5902 (2001).
- [17] L. H. Yu L. DiMauro A. Doyuran W. S. Graves E. D. Johnson R. Heese S. Krinsky H. Loos J. B. Murphy G. Rakowsky J. Rose T. Shaftan B. Sheehy J. Skaritka X. J. Wang Z. Wu. “First ultraviolet high-gain harmonic-generation free-electron laser”. In: *Phys. Rev. Lett* 91.074801 (2003).
- [18] A. Doyuran L. DiMauro W. S. Graves R. Heese E. D. Johnson S. Krinsky H. Loos J. B. Murphy G. Rakowsky J. Rose T. Shaftan B. Sheehy Y. Shen J. Skaritka X. J. Wang Z. Wu L. H. Yu. “Experimental study of a high-gain harmonic-generation free-electron laser in the ultraviolet”. In: *Phys. Rev. ST Accel. Beams* 7.050701 (2004).
- [19] E. Allaria F. Curbis M. Coreno M.B. Danailov B. Diviacco C. Spezzani M. Trovó G. De Ninno. “Experimental characterization of nonlinear harmonic generation in planar and helical undulators”. In: *Phys. Rev. Lett.* 100.17 (2008), p. 174801.
- [20] G. De Ninno E. Allaria M. Coreno S. Chowdhury F. Curbis M. B. Danailov B. Diviacco M. Ferianis E. Karantzoulis E. C. Longhi I. V. Pinayev C. Spezzani M. Trovó V. N. Litvinenko. “Self-induced harmonic generation in a storage-ring Free-Electron Laser”. In: *Phys. Rev. Lett.* 100.10 (2008), p. 104801.
- [21] E. Allaria G. De Ninno. “Soft-X-Ray coherent radiation using a single-cascade Free-Electron Laser”. In: *Phys. Rev. Lett.* 99.1 (2007), p. 014801.
- [22] H. Haus. In: *IEEE Journal of Quantum Electronics* 17 (1981), pp. 1427–1435.
- [23] G. Dattoli et al. In: *IEEE Journal of Quantum Electronics* 17 (1981), pp. 1371–1387.
- [24] P. Pierini and W. M. Fawley. “Shot noise startup of the 6 nm SASE FEL at the TESLA test facility”. In: *Nucl. Instr. and Meth. A* 375 (1996), pp. 332–335.
- [25] K.-J. Kim. “Three-dimensional analysis of coherent amplification and self-amplified spontaneous emission in free-electron lasers”. In: *Phys. Rev. Lett.* 57 (1986), pp. 1871–1874.
- [26] G. Geloni, V. Kocharyan, and E. Saldin. “A novel self-seeding scheme for hard X-ray FELs”. In: *Journal of Modern Optics* 58.16 (2011), pp. 1391–1403. DOI: [10.1080/09500340.2011.586473](https://doi.org/10.1080/09500340.2011.586473). eprint: <http://dx.doi.org/10.1080/09500340.2011.586473>.
- [27] E. Allaria et al. “Two-stage seeded soft-X-ray free-electron laser”. In: *Nature Photonics* 7.11 (2013), pp. 913–918. DOI: [10.1038/nphoton.2013.277](https://doi.org/10.1038/nphoton.2013.277).
- [28] G. Stupakov. “Using the Beam-Echo Effect for Generation of Short-Wavelength Radiation”. In: *Phys. Rev. Lett.* 102 (7 2009), p. 074801. DOI: [10.1103/PhysRevLett.102.074801](https://doi.org/10.1103/PhysRevLett.102.074801).
- [29] H. Deng and C. Feng. “Using Off-Resonance Laser Modulation for Beam-Energy-Spread Cooling in Generation of Short-Wavelength Radiation”. In: *Phys. Rev. Lett.* 111 (8 2013), p. 084801. DOI: [10.1103/PhysRevLett.111.084801](https://doi.org/10.1103/PhysRevLett.111.084801).
- [30] D. Ratner et al. “Experimental Demonstration of a Soft X-Ray Self-Seeded Free-Electron Laser”. In: *Phys. Rev. Lett.* 114 (5 2015), p. 054801. DOI: [10.1103/PhysRevLett.114.054801](https://doi.org/10.1103/PhysRevLett.114.054801).

-
- [31] et al J. Amann. “Demonstration of self-seeding in a hard X-ray free-electron laser”. In: *Nature Photonics* 6 (2012). ISSN: 0168-9002. DOI: [10.1038/nphoton.2012.180](https://doi.org/10.1038/nphoton.2012.180).
- [32] http://sbfel3.ucsb.edu/www/vl_fel.html.
- [33] J.M.J. Madey. “Stimulated emission of Bremmstahlung in a periodic magnetic field”. In: *Jour. Appl. Phys.* 42 (1971), p. 1906.
- [34] M. Billardon P. Elleaume J. M. Ortega C. Bazin M. Bergher M. Velghe Y. Petroff. “First Operation of a Storage-Ring Free-Electron Laser”. In: *Phys. Rev. Lett.* 51 (1983), pp. 1652–1655.
- [35] S.V. Milton E. Gluskin N.D. Arnold C. Benson W. Berg S.G. Biedron M. Borland Y.-C. Chae R.J. Dejus P.K. Den Hartog B. Deriy M. Erdmann Y.I. Eidelman M.W. Hahne Z. Huang K.-J. Kim J.W. Lewellen Y. Li A.H. Lumpkin O. Makarov E.R. Moog A. Nassiri V. Sajaev R. Soliday B.J. Tieman E.M. Trakhtenberg G. Travish I.B. Vasserman N.A. Vinokurov X.J. Wang G. Wiemerslage B.X. Yang. “Exponential gain and saturation of a self-amplified spontaneous emission free-electron laser”. In: *Science* 292.5524 (2001), pp. 2037–2041.
- [36] L.-H. Yu M. Babzien I. Ben-Zvi L.F. DiMauro A. Doyuran W. Graves E. Johnson S. Krinsky R. Malone I. Pogorelsky J. Skaritka G. Rakowsky L. Solomon X.J. Wang M. Woodle V. Yakimenko S.G. Biedron J.N. Galayda E. Gluskin J. Jagger V. Sajaev I. Vasserman. “High-gain harmonic-generation free-electron laser”. In: *Science* 289.5481 (2000), pp. 932–934.
- [37] W. Ackermann et al. “Operation of a free-electron laser from the extreme ultraviolet to the water window”. In: *Nature Photonics* 1.6 (June 2007), pp. 336–342. DOI: [10.1038/nphoton.2007.76](https://doi.org/10.1038/nphoton.2007.76).
- [38] <http://flash.desy.de/accelerator/>.
- [39] P. Emma et al. “First lasing and operation of an angstrom-wavelength free-electron laser”. In: *Nature Photonics* 4.9 (Sept. 2010), pp. 641–647. DOI: [10.1038/nphoton.2010.176](https://doi.org/10.1038/nphoton.2010.176).
- [40] <http://lcls.slac.stanford.edu>.
- [41] T. Ishikawa et al. “A compact X-ray free-electron laser emitting in the sub-angstrom region”. In: *Nature Photonics* 6.8 (Aug. 2012), pp. 540–544. DOI: [10.1038/nphoton.2012.141](https://doi.org/10.1038/nphoton.2012.141).
- [42] E. Allaria et al. “Highly coherent and stable pulses from the FERMI seeded free-electron laser in the extreme ultraviolet”. In: *Nature Photonics* 6.10 (2012), pp. 699–704. DOI: [10.1038/nphoton.2012.233](https://doi.org/10.1038/nphoton.2012.233).
- [43] www.elettra.trieste.it/FERMI.
- [44] J. Bödewadt. “Recent Results From FEL Seeding At FLASH”. In: *Proceedings of the 2015 IPAC Conference*. Richmond, VA, USA, 2015.
- [45] Chen J. H. et al. “Operating the SDUV-FEL with the echo-enabled harmonic generation scheme.” In: *Chinese Phys. C* 33 (2009), pp. 706–710.
- [46] Z.T. Zhao and D. Wang. “Progress in the SDUV-FEL and development of X-ray FELs in Shanghai”. In: *Proceedings of the 2010 Free-Electron Laser Conference*. Malmö, Sweden, 2010, pp. 15–19.
- [47] http://xfel.desy.de/technical_information/photon_beam_parameter/.
- [48] R. Ganter. “SwissFEL Status Report”. In: *Proceedings of the 2015 FEL Conference*. WEA03. Daejeon, South Korea, 2015.

- [49] <https://www.psi.ch/swissfel/swissfel>.
- [50] H.-S. Lee et al. “Current Status of PAL-XFEL Facility”. In: *Proceedings of the 2015 FEL Conference*. WEA01. Daejeon, South Korea, 2015.
- [51] C. Spezzani et al. “Sub-picosecond coherent VUV source on the Elettra storage ring”. In: *Nucl. Instr. and Meth. A* 596 (2008), pp. 451–458.
- [52] G. De Ninno et al. “Generation of Ultrashort Coherent Vacuum Ultraviolet Pulses Using Electron Storage Rings: A New Bright Light Source for Experiments”. In: *Phys. Rev. Lett.* 101 (5 2008), p. 053902. DOI: [10.1103/PhysRevLett.101.053902](https://doi.org/10.1103/PhysRevLett.101.053902).
- [53] M. Labat. PhD thesis. 2008.
- [54] D. N`lle F. Brinker M. Negrazus D. Schirmer K. Wille. “DELTA, a new storage-ring-FEL facility at the University of Dortmund”. In: *Nucl. Instr. and Meth. A* 296 (1990), pp. 263–269.
- [55] B. Baasner, D. N`lle, and D. Schirmer. “DELTA, a status report of the storage ring FEL facility at the University of Dortmund”. In: *Nucl. Instr. and Meth. A* 331 (1993), pp. 163–167.
- [56] D. N`lle and DELTA Group. “Progress of the commissioning of the DELTA storage ring FEL facility”. In: *Nucl. Instr. and Meth. A* 375 (1996), ABS48–ABS50.
- [57] S. Di Mitri and M. Cornacchia. “Electron beam brightness in linac drivers for free-electron-lasers”. In: *Physics Reports* 539.1 (2014). Electron beam brightness in linac drivers for free-electron-lasers, pp. 1 –48. ISSN: 0370-1573. DOI: [10.1016/j.physrep.2014.01.005](https://doi.org/10.1016/j.physrep.2014.01.005).

Chapter 3

FERMI FEL

3.1 FERMI facility

The FERMI single-pass seeded FEL is a user facility that has been designed for producing high-quality photon pulses in the EUV and soft-X-ray spectral range [1, 2]. The first undulator line, FEL-1 [3], produces coherent radiation in the spectral range from 100 nm to 20 nm. The second undulator line, FEL-2 [4], covers the spectral range between 20 nm and 4 nm. Both FEL lines are based on the HGHG scheme, single stage for FEL-1 and double-stage for FEL-2.

FERMI is composed of three main parts: the linear accelerator, the FEL lines and the user beamlines. The infrastructure for the LINAC and the FEL lines has been built 5 m underground for radiation protection purposes. A schematic layout of the facility is shown in Fig. 3.1.

The FERMI LINAC provides the electron beam necessary for the operations of the FEL. The electron bunches are generated in a high-gradient photocathode gun and accelerated by a normal conducting linear accelerator up to the required beam energy, typically in the range 1.0 to 1.5 GeV.

The S-band, 2.998 GHz, RF photoinjector is based on the 1.6 cell electron gun [5] developed at BNL/SLAC/UCLA [6]. The beam is extracted when a UV photoinjector laser (PIL) interacts with a copper cathode. At the gun exit the beam energy is ~ 5 MeV. The gun cavity is equipped with a solenoid magnet that is used to compensate the transverse defocusing of the beam space charge and to prevent emittance degradation. Two S-band RF accelerating cavities (violet squares in Fig. 3.1, top) boost the beam energy up to ~ 100 MeV implementing the emittance compensation scheme [7]. The typical bunch charge used is of the order of 800 pC, while the initial bunch duration is ~ 10 ps.

After the initial energy boost, a laser heater system [8] (LH in Fig. 3.1) is used to fine-tune the electron beam energy spread through the interaction with an external laser in a short undulator. The FERMI laser heater will be presented in details in Chapter 4.

The main LINAC is divided into 4 logical groups, namely LINAC1 to LINAC4 (L1 - L4 in Fig. 3.1). It is composed of different types of accelerating structures, namely, seven, 4.5-m-long SLAC-type, constant gradient structures (L1 and L2), with maximum energy gain per cavity of 47 MeV and seven, 6.1-m-long Backward-Traveling Wave (BTW) structures (L3 and L4), with maximum energy gain per cavity of 140 MeV.

The first LINAC sections (L1) accelerate the beam and produce the energy chirp needed for bunch compression in the first bunch compressor (BC1). Also in L1 is located a harmonic

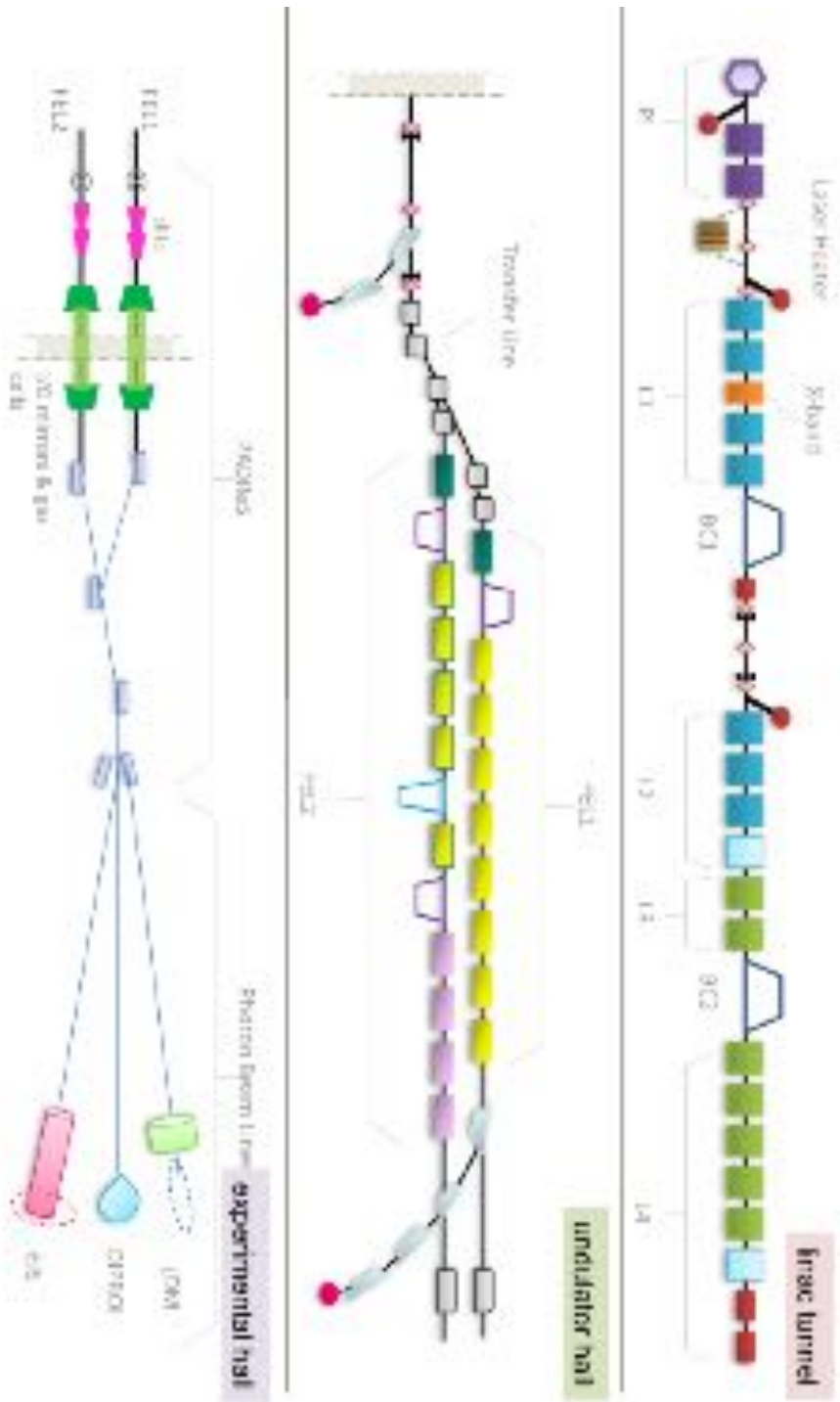


Figure 3.1: Layout of the FERMI facility. It is composed of the linac tunnel (top), where the LINAC is installed and the electron beam is produced and accelerated, the undulator hall (center), where the FEL radiation is emitted and the experimental hall (bottom) where the experiments take place.

x-band cavity (11.4GHz) which is used to linearize the compression. A second bunch compressor (BC2) is placed downstream L2 and L3. It is usually kept straight and the overall bunch compression is performed in one stage only, with nominal compression factor of 10. Note that there is still some space (bright lightblue boxes) for possible future installation of LINAC cavities for further increase the final beam energy. Along the LINAC there are 4 electron-beam spectrometer stations, where a bending magnet spectrometer is used to diagnose the beam energy (red dots in Fig. 3.1). The final bunch duration (after compression) is ~ 300 fs (RMS), with peak current 500-700 A depending on the bunch charge.

Many diagnostics are present along the machine to monitor the electron beam properties. The electron beam trajectory is monitored by 31 stripline Beam Position Monitors (BPMs', [9]) with $20\mu\text{m}$ (RMS) resolution, and can be modified by changing 24 couples of steering magnets (correctors) both in horizontal and vertical plane. The transverse properties of the beam can be monitored by means of 16 fluorescent multi-screens that can be inserted into the path of the electrons. The multi-screen stations are equipped with Optical Transition Radiation (OTR) [10] and Yttrium Aluminium Garnet (YAG) targets [11]. The multi-screens are used in particular for emittance and Twiss functions' reconstruction using the quadrupole scan technique [12]. The measurement is critical for matching the beam optics with the designed one [1]. There are also three RF-deflecting cavities (one after BC1, two at the end of L4, red boxes in Fig. 3.1) that can be used mainly as diagnostics of the longitudinal properties of the electron beam [13, 14]. A comprehensive discussion about the diagnostics present along the machine will be the subject of Appendix A.

The electron beam can be sent into either one of the two FERMI undulator lines, through a transfer line (see Fig. 3.1), constituted by 2 quadruplets of bending magnets with bending angle of 3 deg. They shift the beam horizontally from the LINAC axis by 1 or 2 m for FEL-2 and FEL-1 line, respectively. Details concerning FEL-1 and FEL-2 are discussed below.

After being used for FEL production, the electron beam is deflected via a series of bending magnets to the main beam dump area, while the FEL radiation is transported to the experimental area.

3.1.1 PADReS

The FEL beamline is completed by the photon diagnostics that are used to characterize the FERMI FEL pulses and that are placed just before the experimental end-stations.

PADReS (Photon Analysis Delivery and Reduction System, see Fig. 3.1 bottom) is the section of FERMI devoted to characterize, manipulate and deliver the FEL photons to the experimental end-stations located in the experimental hall. It is located after the undulators of both FEL lines, and before the final three end-stations in the FERMI experimental hall. The diagnostics here located provide information about several parameters of the photon beam, like intensity, spectral distribution, position, shape and coherence. Many of the diagnostics are available in a non-invasive way (intensity, spectral distribution, position) and therefore are available on a shot-to-shot basis, while others (coherence, beam profile, etc.) can be measured only in a destructive way. A gas absorber is also present and it is used to reduce the intensity of the incoming beam in case this option is needed for particular experiments.

The FEL intensity is measured by means of two gas ionization cells [15] placed in the undulator hall, just before the experimental hall. The FEL spot reconstruction can be done using one of the different YAG screens that intercept the FEL beam in different locations along the beam transport. PADReS also hosts the energy spectrometer, the split-delay line and the focusing systems of the end-stations.

PRESTO, the energy spectrometer

The Pulse-Resolved Energy Spectrometer is an online spectrometer used to record the FEL spectral distribution in a non-invasive way. It does so by extracting the first (or higher) diffraction order of the radiation, generated by a planar variable spacing grating, while carrying the zeroth order, with 97% efficiency, to the experimental stations. It is equipped with three gratings to cover the whole spectral range of both FEL-1 and FEL-2, namely 100-4 nm range. The variable spacing grating focuses the diffracted beam on a YAG screen where the FEL-induced fluorescence intensity is detected by a CCD device. The energy resolution of the system depends on the grating used and is 0.2-3.7 meV for the low energy grating, 0.3-9.5 meV for the intermediate energy grating and 0.4-8.1 meV for the high energy grating.

AC/DC, the split and delay line

The AutoCorrelator/Delay-Creator is an EUV/SXR autocorrelator that splits the incoming beam in order to create a double pulse with controllable time separation. As the wavelengths of FERMI do not allow for optical elements in transmission (due to material absorption) the split and delay line is designed to perform a wavefront-split of the incoming beam via knife-edge and successive recombination. The two semi-beams created by knife-edge travel different optical paths, ones of which can be varied by moving two mirrors along mechanical guides, creating the required time delay in between the pulses. This is in the range from -2 to ~ 30 ps [16]. The instrument is located in the experimental hall on the common optical path from the FEL to the experimental end-stations.

KAOS, the active optics system

The Kirkpatrick-Baez (KB) Active Optics System is installed before DiProI and LDM end-stations. It is a KB refocusing sections that uses thin plane adaptive mirrors that are mechanically bent to achieve the desired shape to focus in the same position in the experimental chamber the different wavelengths produced by the machine. Spots sizes as small as $5 \times 6 \mu\text{m}^2$ have been obtained [17].

3.1.2 The experimental stations

EIS

The Elastic and Inelastic Scattering (EIS) beamline is presently under final construction. It consists of two separate end-stations (EIS-TIMEX and EIS-TIMER), dedicated to two different research projects, with common goal of performing time-resolved pump-probe experiments. Each end-station takes advantage of different key properties of the FERMI source.

EIS-TIMEX end-station [18] is designed for ultrafast time-resolved studies of condensed matter under nonequilibrium conditions occurring on the sub-picosecond time scale in FEL- or laser-heated materials. Experiments are also aimed at exploring the warm dense matter (WDM) regime resulting from thermalization of the electron and ion subsystems on the picosecond time scale.

The experimental chamber and the sample environment are quite flexible in order to accommodate various possible configurations for single-shot experiments, including simple

EUV and soft x-ray absorption/reflection and pump-probe experiments where the probe can be either an external laser or the FEL itself.

EIS-TIMER end-station is a FEL-based Four-Wave-Mixing instrument [19] that will exploit the time structure, harmonic content and coherence properties of the source. Two non-collinear FEL pulses (pump) are overlapped, in time and space, at the sample. Their interference originates a transient standing electromagnetic wave, called the transient grating (TG), with a spatial periodicity in the 1-100 nm range. The TG imposes a nanoscale modulation of sample parameters, whose time evolution can be monitored by measuring the diffraction of a third time-delayed coherent pulse (probe), which impinges into the sample at the Bragg angle. The time-dependent diffracted signal encodes relevant information on several kinds of dynamics, ranging from slow (>ns scale) diffusion processes to fast (sub-fs scale) electron dynamics. The implementation of this experimental scheme, nowadays used only with optical lasers, to the VUV range would be extremely useful for shedding light into the physics of disordered systems, since it will make accessible the mesoscopic kinematic region that are not in the reach of available instruments. Nanoscale TG experiments could also allow sensitive probing of thin films/interfaces, transport properties and correlations in nanostructured materials.

DiProI

For the DiProI end-station [20] the main scientific case is ultra-fast coherent imaging and nano-spectroscopies. It implements the Coherent Diffraction Imaging (CDI) technique in order to obtain the structural information on a non-periodic sample before the radiation damage has occurred. Although the object is destroyed by the intense FEL pulse, the information contained in the diffraction pattern is preserved since the different time scale between the scattered photons and the atoms motion. The collected information on a bi-dimensional CCD detector is sufficient for the reconstruction of the object image by recovering the missing phase using computational algorithm [21]. The shot-to-shot temporal and energy stability of the seeded FEL pulses at FERMI has opened extraordinary opportunities for CDI and in particular for Resonant Coherent Diffraction Imaging (R-CDI), overcoming some of the limitations imposed by the partial longitudinal coherence of the SASE-FELs. The end-station exploits the FERMI tunability to perform CDI experiments with strong resonant enhancement of the magnetic scattering signal, e.g. on Co and Fe edges. Another unique characteristic of the source exploited by the end-station is the polarization control, which allows for single-shot resonant magnetic scattering in holography approach for accessing the dynamics of magnetic processes [22].

LDM

The Low Density Matter (LDM) end-station [23] has been built for studying atomic, molecular and cluster physics. It is a modular end-station that can accommodate a broad range of detectors and systems for target preparation and investigation. The combined capabilities of the photon source such as high brilliance, short pulse length, variable polarization, coherence, photon transport and end-station allow the investigation of very dilute systems, matter under extreme irradiation conditions causing, e.g. multiple electronic excitation, multiple ionization, Coulomb explosion, non-linear optics and dichroism.

3.2 FEL-1 commissioning and performance

After being accelerated to the desired electron beam energy, the electron beam is injected into the undulator line where FEL action takes place. FEL-1 undulator system is composed of a modulator and a radiator, see Figure 3.2. The modulator has a total length of 3 m and its magnetic period is 100 mm, for a total of 30 magnetic periods. The modulator resonance can be tuned by varying the gap in between the magnetic arrays, in order to maintain the resonance condition for different electron beam energies and seed laser wavelengths. The radiator is composed of six APPLE-II type undulator sections specifically designed for meeting the stringent FEL requirements [24]. The APPLE-II scheme allows for the first time the implementation of a high-gain FEL with polarization control. Further details about the polarization at FERMI will be presented in Chapter 5. Each radiator section has a length of 2.4 m and magnetic period of 55 mm and their resonance can be arbitrarily tuned, again by varying the gap. This requires the presence of phase shifter devices which are installed in each section break. They are required to maintain the correct phase relation between the electron beam and the FEL radiation in between one radiator section and the next. In the break sections also a quadrupole magnet, to manipulate the beam size, and a BPM for beam trajectory control, are installed.

An external UV laser provides the seed signal, which needs to be accurately synchronized with the electron beam. The stringent synchronization requirements are achieved at FERMI with an all-optical timing system [25] that provides a stable reference to all machine systems, including the radio-frequency plants, the photo-injector and the seed laser. In order for the seeding process to be effective both transverse and longitudinal electron beam-seed laser superposition must be ensured. The transverse alignment is done superimposing the electron bunch with the seed laser onto two YAG screens placed at the two ends of the modulator. For the longitudinal alignment a fast photodiode can be used for a cursory superposition (within 200 ps), while the final longitudinal alignment is done adjusting a remotely controlled optical delay line along the seed laser path, looking at the FEL signal.

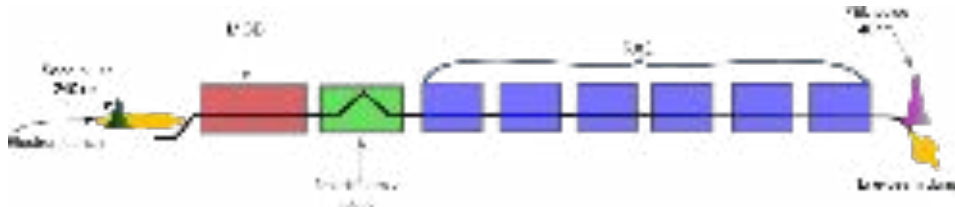


Figure 3.2: Schematic representation of the FEL-1 beamline. Courtesy E. Allaria.

For the FEL-1 data here reported, the third harmonic of a Ti:sapphire laser was used as the seed laser with $\lambda_{seed} = 260$ nm. Alternatively an Optical Parametric Amplifier (OPA) setup can also be used as seeding source [27] with tunable $\lambda_{seed} = 230 - 260$ nm or 280-340 nm. In the case of the third harmonic, the seed laser pulses has a typical duration of 150 fs FWHM, peak power of ~ 100 MW and bandwidth of ~ 0.8 nm, which is a factor of ~ 1.2 larger than the Fourier limit, assuming a Gaussian pulses. The HGHG FEL emission in this conditions easily exceeds several tens of μJ from the 4th harmonic of the seed (65 nm) down to the 13th harmonic (20 nm). Clear evidence of coherent emission was also observed at the 15th harmonic (17 nm) and below.

The measured harmonic conversion efficiency exceeds the theoretical predictions made during the design of the machine [1]. The unexpected and welcomed results are understood to be determined by the energy spread of the beam, which as we will see in Chapter 4

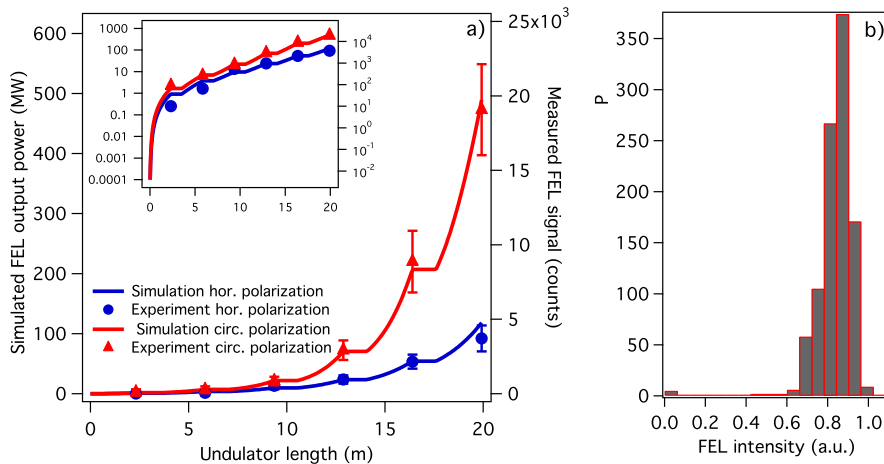


Figure 3.3: Measured FEL intensity at 32.5 nm. (a) Measured FEL pulse energy as a function of the number of undulator sections used in the radiator, together with the predicted FEL power obtained from GINGER numerical simulations [26]. Red marks refer to circular polarization, while blue marks are relative to horizontal polarization of the radiator sections. The error bars are obtained from the statistical distribution from several consecutive pulses. Inset: the same data reported on a logarithmic scale. (b) Shot-to-shot distribution of the pulse energy for 1000 consecutive FEL pulses. The distribution is characterized by a standard deviation of $\sim 10\%$ which reflects the shot-to-shot fluctuations of the electron-beam parameters. Image reproduced from [3].

strongly affects the HGHG performance [28, 29]. For each one of the different harmonic of the seed laser the FEL is optimized by tuning the amount of energy modulation produced in the modulator, which is controlled by changing the seed laser power and the strength of the dispersive section. Typical values of the R_{56} for the dispersive section are in the range 40-70 μm . In the following the results obtained for the FEL radiation at the 8th harmonic (32.5 nm) are reported. Similar results were obtained in the whole spectral range of FEL-1.

After optimization of the FEL process to maximize the output power at 32.5 nm in either circular or linear polarization, we measured the gain curve, i.e. the FEL power as a function of the number of radiator sections. In Figure 3.3a the gain curve results are shown for both polarizations, also in logarithmic scale in the inset. The data clearly show the different gain lengths L_g associated with the two polarization states of the undulator. Fitting the data using an exponential curve allows us to compute the gain length for the two cases, which results in ~ 2.5 m for planar polarization and ~ 2.0 m for circular polarization. This results agree with the gain length computed via the ρ parameter and Xie [30] formulas, evaluated using the electron beam parameters reported in Table 3.1. As known from theory the circular polarization is characterized by a shorter gain length and higher output power due to the better coupling of the electromagnetic field and the electrons (J_m coefficient in Eq. (2.21)). A good agreement has been also obtained with the results of numerical simulations performed using GINGER numerical code [26], also reported in Figure 3.3a.

It is worth noting that FEL-1 achieves power levels close to SASE saturation using a radiator of $\sim 6-8$ gain lengths, instead of the typical ~ 20 gain lengths generally required for SASE [31]. The power fluctuations are of the order of 10%, as shown in Fig. 3.3b where the distribution of the intensity of 1000 shots is reported. The results show another advantage of using an externally seeded FEL, which is the ability of keeping the power

fluctuations under control without the need to enter into deep saturation as required in the case of SASE [32]. Other than requiring an even longer undulator the deep saturation SASE regime as been predicted to be characterized by a degraded longitudinal and transverse coherence [33], so in general SASE FELs may require operation where a compromise between maximum output power, reduced fluctuations and high coherence is present. This condition has been demonstrated to be less critical for FERMI where these properties can be controlled simultaneously.

It is important to point out the different nature of the power fluctuations between SASE and HGHG FELs. The deterministic origin of the HGHG implies that the power fluctuations derive from shot-to-shot fluctuations of the properties of the electron and seed laser beams, so they are mainly limited by technological factors. The SASE process is instead inherently stochastic [32].

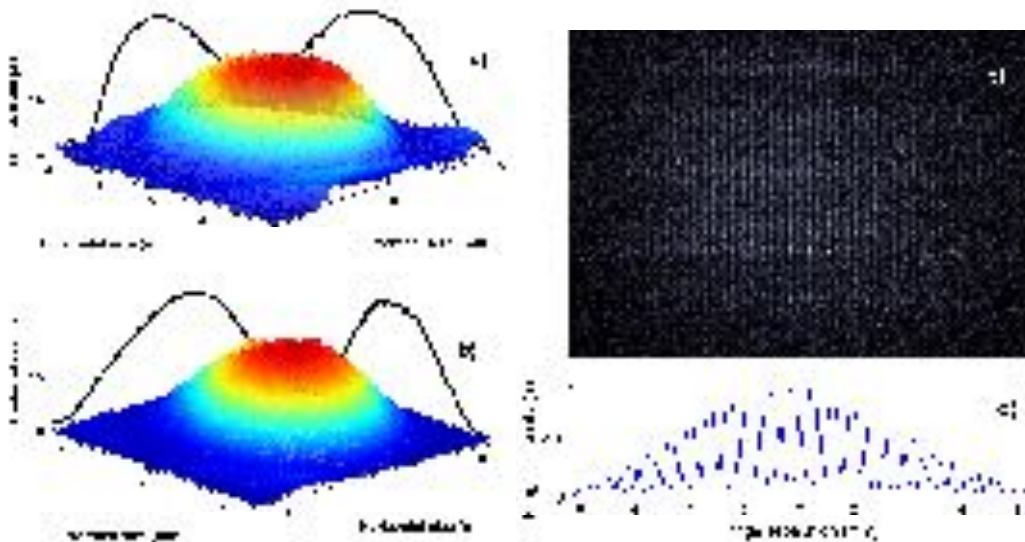


Figure 3.4: Measured beam profiles and double slit diffraction pattern. (a) FEL spot measured on a YAG screen at ~ 52.5 m from the radiator exit. The spot has a Gaussian profile with (RMS) sizes of ~ 2 mm in vertical and horizontal directions. (b) FEL spot on a second YAG screen positioned ~ 72.5 m downstream from the radiator. The measured beam dimensions are 2.6 mm and 2.4 mm, respectively. (c, d) Interference pattern on the second YAG screen for the Young experiment. The slits, placed ~ 8.5 m before the screen, had an aperture of $20 \mu\text{m}$ and separation of 0.8 mm. Image reproduced from [3].

In a seeded FEL the coherence properties of the seed are imprinted on the electron beam that is generating the FEL radiation. A good transverse and longitudinal coherence is hence expected. For the transverse one, in Figure 3.4a,b the measured transverse profile is reported for FEL radiation at 32.5 nm. From the analysis of the data it is possible to show that the FEL pulses are very close to a diffraction-limited Gaussian beam, with beam waist size of $\sim 200 \mu\text{m}$, located at the center of the last undulator. The size is consistent with the electron beam size at that point. Moreover, a high degree of transverse coherence is also confirmed by the results of Young's double-slit experiment [34], shown in Fig. 3.4c. Analysis of the reported data indicates that more than 90% of the diffraction pattern intensity is maintained at a slit separation of 0.8 mm.

One of the most attractive features of seeded FELs is the possibility of obtaining highly

Table 3.1: Measured electron-beam parameters used to operate FEL-1 in the reported experiments.

Parameter	Value	Units
Energy	1.24	GeV
Slice energy spread (RMS)	<150	keV
Emittance (projected)	~ 4	mm mrad
Charge	450	pC
Peak current	200-300	A
Beam size (RMS)	~ 150	μm
Pierce parameter ρ	$\sim 1.3 \times 10^{-3}$	

stable output spectra [35–37]. The spectral properties of the FEL critically depend on the properties of the seed laser [38]. The results obtained at FERMI are shown in Fig. 3.5, where both a single-shot spectrum (Fig. 3.5a) and a sequence of 500 consecutive single-shot spectra (Fig. 3.5b) are reported. Figure 3.5a also shows the measured spectrum of the seed laser pulse. The spectra are reported in meV around their central photon energy (4.8 eV (260 nm) for the seed and 38.5 eV (32.5 nm) for the FEL). The measured FEL bandwidth is 20 meV (RMS), yielding a relative bandwidth of $\sim 5 \times 10^{-4}$. This number should be compared with ρ (Table 3.1), which approximately corresponds to the expected bandwidth of SASE emission under the same experimental conditions. The relative spectral bandwidth measured at FERMI is an order of magnitude smaller than the one observed at SASE FELs operating in the EUV and soft X-ray spectral regions [32, 39].

Figure 3.5a shows that the FEL bandwidth is larger than that of the seed laser. However, we believe that this increase is not associated with a degradation of the longitudinal coherence of the FEL pulse, but rather with a natural shortening of the FEL pulse duration relative to the seed pulse. This effect has been theoretically predicted [40] and it is also well reproduced in numerical simulations that mimic the presented setup. It is, however, important to point out that even without considering such a shortening of the FEL pulse, the time-bandwidth product is already smaller than a factor of 4 with respect to SASE. Another attractive property for energy-resolved experiments is the wavelength stability, or equivalently the photon energy stability (shot-to-shot) of the light sources. In Fig. 3.5b a series of successive spectra are reported as a function of the photon energy and shot number. The normalized photon-energy stability is of the order of 7×10^{-5} (RMS) which represents a noticeable improvement when compared to the results obtained for the SASE scheme in the same photon energy range [32, 39, 41], further proving the advantages of the seeded scheme in terms of stability of the output radiation.

The presented results show that FEL-1 is a seeded source capable of producing high-intensity pulses in the EUV range with close to transform-limited bandwidth and unprecedented stability in intensity, photon energy and spectral bandwidth, as well as full control of polarization as we will see in Chapter 5.

Our experiments lend further support to the idea of using seeded FELs to generate better laser-like properties in the X-ray range [3]. Because the control of pulse parameters that seeded FELs can afford is an important asset for many experimental FEL applications, the performance of FERMI is the reference for other proposed seeding techniques that are currently under study, like the seeding using high harmonic generation (HHG) in gases [37], the echo-enabled harmonic generation [42] and others.

The deterministic nature of the HHG process allowed us to achieve substantial improvements relative to SASE FELs. The main limitation is the capability of going to very short wavelengths, hence the presence of a second FEL line in the facility.

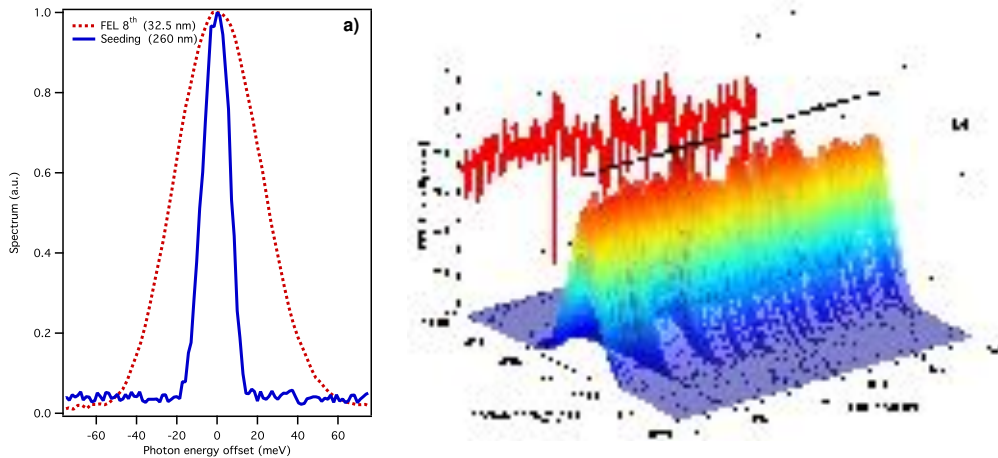


Figure 3.5: *FEL spectra at 32.5 nm. (a) Measured FEL and seed laser spectrum (dashed red and continuous blue lines respectively). (b) Acquisition of 500 consecutive FEL spectra. Image reproduced from [3].*

The above-described results refer to the “normal” operation of FEL-1. As we will see in Chapter 7, it has been also demonstrated that the machine can operate in different exotic modes to produce, e.g., two pulses for pump-probe experiments.

3.3 FEL-2 commissioning and performance

To overcome the limitations due to the small wavelength range of FEL-1, another beamline is installed in parallel with the latter. FEL-2 is specifically designed [1] to operate as a two-stage HGHC cascade in the wavelength range of 20 to 4 nm. The fresh-bunch configuration enhances the FEL emission at high harmonic orders by avoiding a gain depression due to the energy spread induced by the first-stage FEL interaction [4].

The layout of the FERMI FEL-2 beam line is shown in Fig. 3.6. The first stage is a small replica of FEL-1, with a linearly polarized modulator (M1), dispersive section and a radiator (R1) constituted of two, 55-mm-period APPLE-II type undulators. The coherent radiation they emit constitutes the seed of the second stage. It is usually operated in the low-gain regime due to the limited length of the radiator. After that the magnetic delay line chicane (DL) is installed which is used for the required time delay for the fresh-bunch mode. The delay line introduces a controllable time delay on the electron bunch with respect to the first stage radiation up to ~ 1 ps. Typical values of the delay are ~ 200 fs. Other than creating the required delay for the fresh bunch, the associated chromatic dispersion ($R_{56} < 120$ mm) removes nearly all the coherent bunching in the electron beam created in the first stage. This prevents emission from the bunched part of the beam in the second stage, creating an unwanted spurious emission. The second stage is based on the HGHC scheme so it is constituted by the second-stage modulator (M2), physically identical to the first-stage radiators and the second-stage radiator (R2) composed of six, 35-mm-period, Apple II type [44] undulators with magnetic length of 2.4 m. The second stage usually works in high-gain regime, where both the FEL radiation intensity and coherent bunching exponentially increase along the second part of the radiator. All undulators have variable

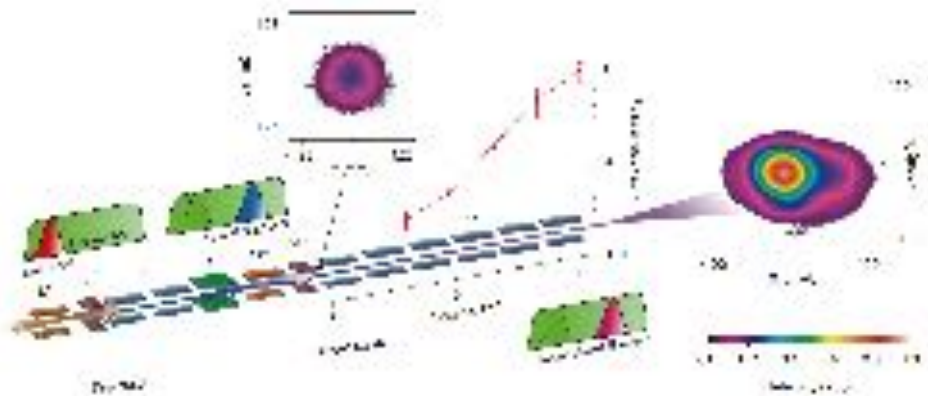


Figure 3.6: Layout of FEL-2 undulator line. The first stage consists of an external seed modulating in energy the electron beam in the first-stage modulator ($M1$), followed by a dispersive section ($DS1$) that produces strong coherent bunching and subsequent coherent emission at a higher harmonic in the two first-stage radiators ($R1$). In the fresh-bunch scheme [43], the first stage is followed by the delay line (DL), which ensures that the radiation emitted by the first undulator is superimposed temporally over a fresh portion of the electron beam in the second-stage modulator ($M2$). The second-stage radiators ($R2$) are resonantly tuned to a harmonic of the first-stage radiation. The exponential growth of the second-stage FEL output as a function of the number of resonant radiators is shown, together with the downstream transverse mode shapes of the radiation emitted by each stage (32 nm in the first stage and 10.8 nm in the second stage). Image reproduced from [4].

gap to control their resonant wavelength as the LINAC is kept at fixed electron beam energy.

In Table 3.2 the electron beam parameters used for the experiments here reported are summarized.

Table 3.2: Measured electron-beam parameters used to operate FEL-2 in the reported experiments.

Parameter	Value	Units
Energy	1.0 - 1.2	GeV
Slice energy spread (RMS)	~ 100	keV
Emittance (projected)	~ 1.5	mm mrad
Charge	500	pC
Peak current	300-500	A
Beam size (RMS)	~ 150	μm

The input seed laser has a wavelength $\lambda_{seed} = 260$ nm, the third harmonic of a Ti:sapphire laser, time duration FWHM of 180 fs and peak power up to 100 MW. As for FEL-1 an OPA setup can be used to ensure the full wavelength tunability in the operation range. The FEL output consists of two discrete wavelength components, one from each stage, approximately superimposed in time and with a harmonic relation between each other and with the original seed laser. The pulse energies of these two components can be measured by two independent systems on a shot-by-shot basis. The same holds for their spectra, which can be detected using the PRESTO spectrometer.

The resonant wavelength of the emission from the second stage is $\lambda_2 = \lambda_{seed} / (h_1 \times h_2)$ with h_1, h_2 the harmonic up-conversion in the first and second stage, respectively. The operating wavelength range of FEL-2 second stage is 12 - 4.1 nm. The initial studies have

been performed at the longer wavelengths, in particular $\lambda_2 = 10.8$ nm ($h_1 \times h_2 = 24$) and $\lambda_2 = 8.2$ nm ($h_1 \times h_2 = 32$).

In Fig. 3.6, upper panel, the gain curve of the second stage is reported. One can see that the second stage output increases by more than one order of magnitude as the number of radiator sections increases from 3 to 6. The measured increase in the output power is a clear evidence of the exponential gain process typical of FELs operating in the high gain regime. The transverse intensity distribution from the second stage follows a Gaussian profile in the far field, as it is also reported in Fig. 3.6, in the whole spectral range of operation.

In Figure 3.7 the spectral properties of the second stage radiation are reported for the two above mentioned wavelengths. In Figure 3.7(a) a typical single-shot spectrum at $\lambda_2 = 10.8$ nm is shown with the statistics relative to 1400 individual pulses exploited in Fig. 3.7(c).

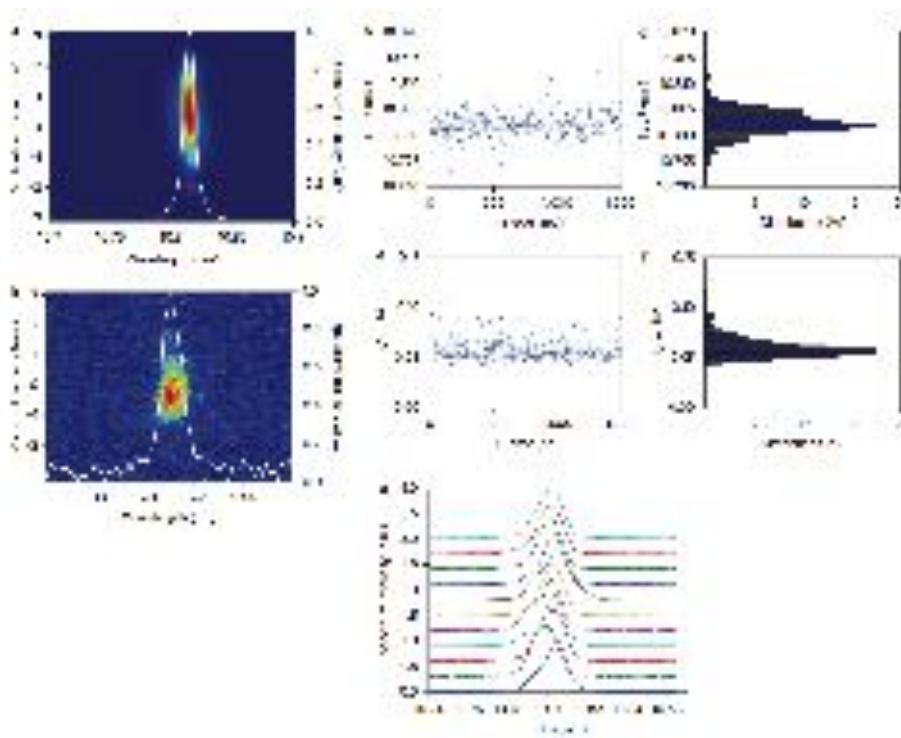


Figure 3.7: *Second-stage spectral results. (a,b) Single-shot FEL spectra from the second stage at 10.8 nm (a) and 5.4 nm (b). (c,f) Results of Gaussian fits (c,e) to the wavelength centroid and spectral FWHM bandwidth for a sequence of 1400 pulses at 10.8 nm, together with the corresponding histogram distributions (d,f). The average wavelength in the data set is 10.802 nm, and the (RMS) wavelength stability is 0.003 nm (3 pm). The average (RMS) bandwidth is 0.006 nm (6 pm), relative bandwidth of 0.06%. (g) Sequence of stacked spectra at 10.8 nm. Image reproduced from [4].*

An example of a typical spectrum at 5.4 nm ($h_1 \times h_2 = 48$) is shown in Fig. 3.7(b). The shown spectra further prove that the emitted radiation has a good spectral stability in contrast to that of a SASE FEL. As previously found in seeded FEL studies [45–47], the purity of the second stage spectra is sensitive to the initial seed laser power, in particular when a too high seed power is used the resulting spectral output is characterized by multi-peaked spectral distribution. The typical pulse energy for the first-stage radiator is in the range 1–5 μ J, which corresponds to a peak intensity of \sim 10–50 MW if the pulse shortening [48]

is taken into account. The second-stage output could be as large as $100 \mu\text{J}$ at 10.8 nm wavelength, equivalent to a peak power exceeding 1 GW . Unfortunately, the second stage emission is characterized by a substantial level of intensity fluctuations. Even in cases where the machine stability in the first stage is smaller than 20% (FWHM), the second stage can show pulse energy fluctuations of the order of 50-60% (FWHM). This demonstrates that the process is very sensitive to the intensity fluctuations of the first stage, which are mainly due to timing jitter between the electrons and the seed, as well as to variations of the electron beam properties along the pulse such as energy and current. In Figure 3.8 we report the output energy measurement done simultaneously for both stages. By removing 20% of shots with the lowest second stage pulse energy one can see that there is a clear correlation in pulse energy between the first and second stage output, or equivalently that nearly all shots with high second stage pulse energy originate from a first stage pulse with high energy. In the reported electron beam configuration (1.2 GeV) the average energy per pulse is $\sim 25 \mu\text{J}$ at 8.2 nm , $\sim 8 \mu\text{J}$ at 6.5 nm and $\sim 1 \mu\text{J}$ at 5.4 nm . The shortest wavelength where the spectrum was detectable was 4.3 nm ($h_1 \times h_2 = 60$).

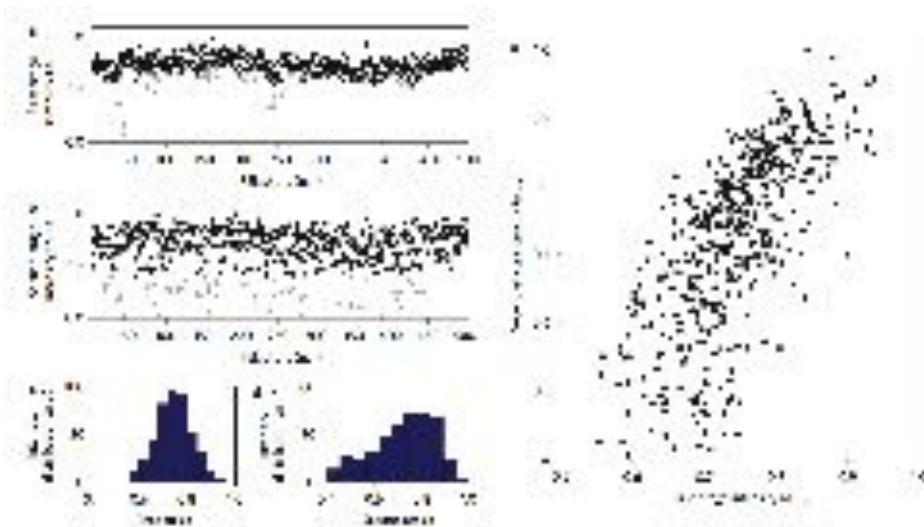


Figure 3.8: Shot-to-shot FEL pulse energy fluctuations. *a,b*, Simultaneous data collected over approximately 1 min for both the first stage with $\lambda_1 = 32 \text{ nm}$ (*a*) and the second stage with $\lambda_2 = 10.8 \text{ nm}$ (*b*). Resultant histograms for each stage (*c,d*) and the correlation between the energy of each stage (*e*) after eliminating 20% of the shots (shown in grey) with the lowest second-stage energy. Image reproduced from [4].

More recently, it has been possible to use the full electron beam energy (1.5 GeV) to explore the lower wavelength range of the FEL-2 beamline. In Figure 3.9 example of single shot spectra at 5.4 nm ($h_1 \times h_2 = 48$) and 4.04 nm ($h_1 \times h_2 = 64$) are reported [49]. Evidence of fourth harmonic signal at 1.3 nm has also been observed [50]. An example is reported in Fig. 3.10, where the spectrogram of the second and fourth harmonics of the second stage radiator is shown. The radiator was tuned at a fundamental wavelength of 5.4 nm . In the insert the spectrum of the third harmonic is shown, in arbitrary units, as a function of the wavelength.

The results obtained on FEL-2 represent the first successful generation of high power FEL radiation with excellent transverse properties and narrow spectral bandwidth in the soft X-ray regime, using a seeded, two-stage harmonic upshift procedure in the fresh bunch

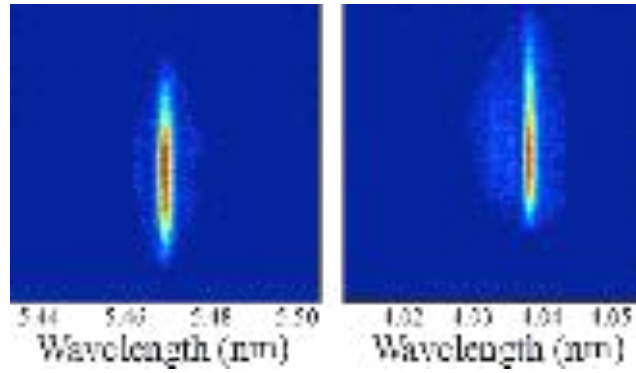


Figure 3.9: Shot-to-shot FEL spectra at high photon energy.

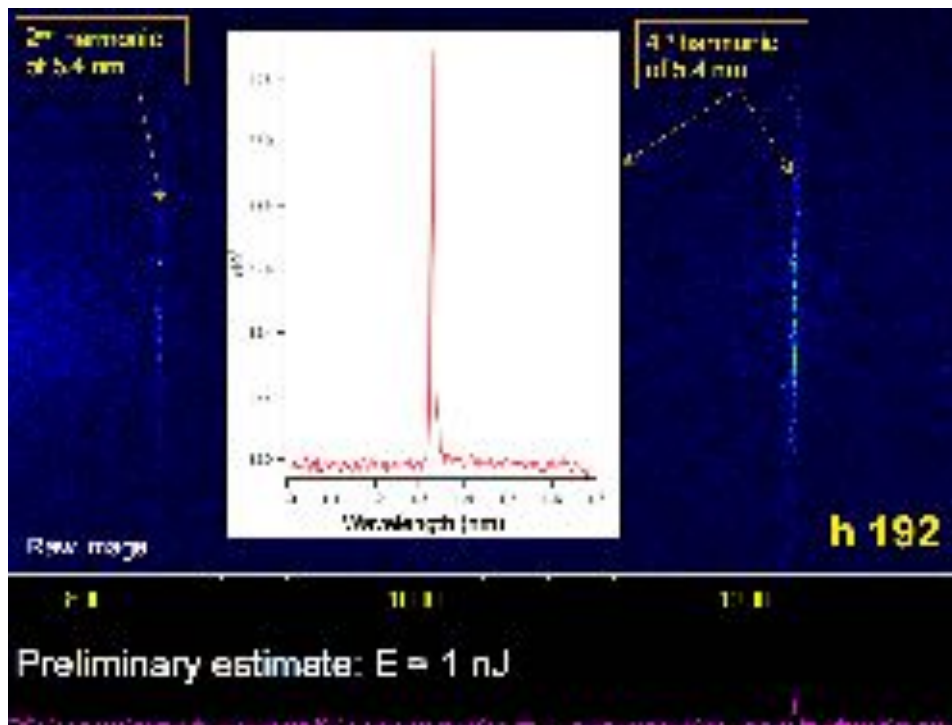


Figure 3.10: Example of 1.3 nm spectrum. The insert shows the spectrum of the FEL at the 192nd harmonic of the seed laser, as a function of wavelength. It corresponds to the fourth harmonic of the second stage radiator. The spectrum has been obtained using the image in the back where the signal of the second harmonic is also visible.

scheme [4]. The installation of an additional radiator section in the first stage radiator, foreseen by the end of 2015, will improve the intensity stability of the FEL. Nevertheless user experiments have already been performed using the FEL-2 radiation and external users runs will begin in the first quarter of 2016.

3.4 SASE at FERMI

Although the FERMI facility is based, designed and optimized for the seeding HGHG scheme, nevertheless SASE operations have been demonstrated [51]. In particular, the first experimental demonstration of enhancement of self-amplified spontaneous emission has been obtained via usage of an optical klystron scheme. Powerful radiation has been produced in the extreme ultraviolet range, with an intensity few order of magnitude larger than in pure SASE mode, and the data have been used to benchmark an existing theoretical model [52].

SASE optical klystron

A possibility to reduce the overall saturation length in a SASE amplifier consists in implementing the optical klystron concept also on these kinds of light-sources. Theoretical studies [52–56] have shown that the increase in density modulation induced by the optical klystron dispersive section brings to a significant reduction of the total length of undulator needed to reach saturation. The optical klystron performance in a high-gain FEL is strongly influenced by the electron beam relative uncorrelated energy spread δ , that has to be much smaller than the FEL parameter ρ . The 1-D approximate expression of the optical klystron power gain G relative to the value in pure SASE mode can be expressed as [52]:

$$G \approx \frac{1}{9} \left[5 + D^2 e^{-\frac{D^2 \delta^2}{\rho^2}} + 2\sqrt{3} D e^{-\frac{D^2 \delta^2}{2\rho^2}} \right] \quad (3.1)$$

where $\lambda_r = 2\pi/k_r$ is the resonant wavelength, $D = k_r R_{56} \rho$ and R_{56} is the strength of the dispersive section. From Eq. (3.1) the maximum theoretical power gain factor G_{max} occurs when $R_{56} k_r \delta = 1$ and results to be:

$$G_{max} \approx \frac{1}{9} \left[5 + \left(\frac{\rho}{\delta} \right)^2 e^{-1} + 2\sqrt{3} \left(\frac{\rho}{\delta} \right) e^{-1/2} \right] \quad (3.2)$$

Notice that the prediction of Eq. (3.2) confirms that smaller uncorrelated energy spread in the beam, the higher G_{max} is expected to be.

Measurements of enhanced SASE

At FERMI the optical klystron setup can be obtained by properly tuning the modulator to the same resonance of the radiators. The electron beam parameters used for the experiment are summarized in Table 3.3.

FERMI has been designed to operate in HGHG seeded mode [28], as such the electron bunch it uses has to satisfy stringent requirements concerning the slice energy spread, that has to be several times smaller than the ρ parameter [2].

In our experiment we tuned both modulator and radiator at 43 nm and, if the dispersive section is turned off, we observed SASE emission of the order of few μJ . The radiator was tuned in circular polarization to increase the FEL output energy per pulse taking advantage of the better electron-photon coupling. By turning on the dispersive section and scanning the R_{56} in the range 0 to 300 μm we measured the progressive increment of the FEL pulse

Table 3.3: Summary of the electron beam parameters used during the experiment.

Parameter	Value	Unit
Beam energy	1.05	GeV
Peak Current	500	A
Slice energy spread	100	keV
Slice normalized emittance	1.0	mm mrad
Bunch length (RMS)	300	fs
Beam spot size at the radiator (RMS)	100	μm

energy associated to the optical klystron enhancement. As the optical klystron efficiency is influenced by the electron beam slice energy spread (see Eq. (3.2)), we also varied the laser heater pulse energy, which changes the slice energy spread of the beam, see Chapter 4. Figure 3.11 shows some relevant cases.

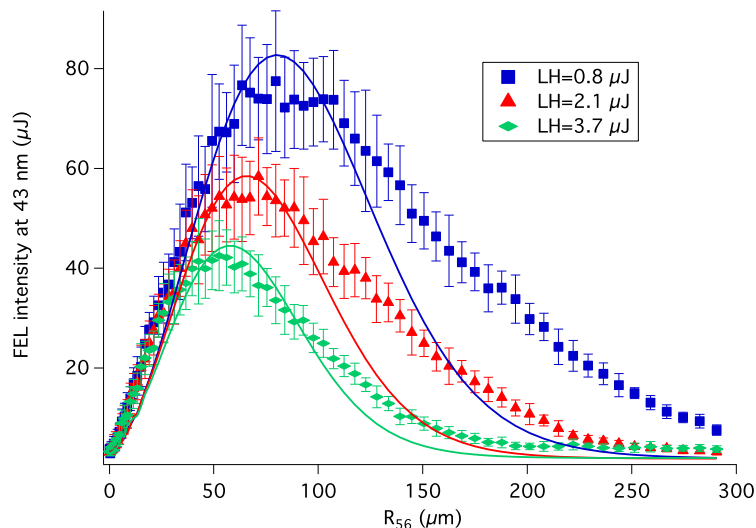


Figure 3.11: FEL output energy in optical klystron SASE regime at 43 nm versus the chicane R_{56} for different laser heater intensities. Solid lines correspond to the theoretical gain factor G calculated using Eq. (3.1). Image reproduced from [51].

The R_{56} value that maximizes the optical klystron efficiency is called R_{56}^{opt} . One can observe that, for increasing values of the laser heater intensity, i.e. larger δ of the beam, the optical klystron gain decreases in efficiency and R_{56}^{opt} shifts towards lower values. Eventually when the slice energy spread becomes too large the optical klystron has no contribution anymore and $R_{56}^{opt} = 0$.

Table 3.4 reports the values of R_{56}^{opt} measured in the three cases plotted in Fig. 3.11 and the relative slice energy spread (δ) of the electron beam at the undulator as inferred by the condition $R_{56}^{opt} k_r \delta = 1$. In all cases the condition $\delta \ll \rho$ is still verified ($\rho = 1.7 \cdot 10^{-3}$ in the experiment).

The expected optical klystron gain G vs R_{56} of Eq. (3.1) has been calculated for the three cases and the results are compared in Fig. 3.11 (solid lines) with the measured optical klystron enhancement.

Table 3.4: Relative slice energy spread δ calculated from the condition $R_{56}^{opt} k_r \delta = 1$ for different laser heater configurations.

LH energy (μJ)	δ	R_{56}^{opt} (μm)
0.8	$8.6 \cdot 10^{-5}$	86
2.1	$1.0 \cdot 10^{-4}$	69
3.7	$1.1 \cdot 10^{-4}$	55

Actually, the 1-D theory makes the strong assumption that the energy spread has a Gaussian distribution in a temporal slice and is constant along the electron bunch. However, as we will see in Chapter 4, this is not the case for a real electron beam in which collective effects, e.g. microbunching instability, lead to a non uniform distribution of the time-sliced energy spread. In our measurements, when the laser heater intensity is very low (blue square data in Fig. 3.11), and the microbunching instability is not completely suppressed, experimental data and 1-D theory expectations agree only qualitatively. Instead, when the laser heater is strong enough (green diamond data), the microbunching instability is almost suppressed and the experiment results are in good agreement with the 1-D theory.

In order to maximize the optical klystron FEL intensity it is necessary to find the best compromise between microbunching instability suppression and small-induced slice energy spread, thus a fine-tuning of the laser heater energy is required. In Fig. 3.12 a laser heater intensity scan, while keeping constant R_{56} at $80 \mu\text{m}$, is reported. Notice also that the cases previously considered for LH energy are reported on the same curve with the same markers used in Fig. 3.11.

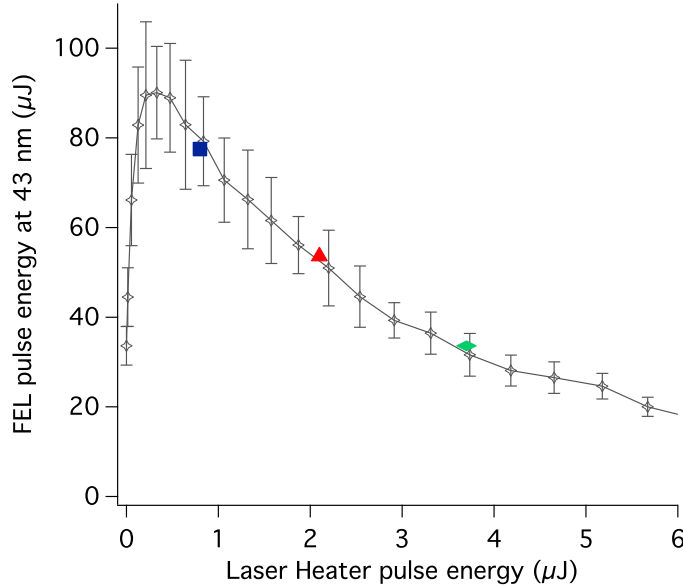


Figure 3.12: FEL intensity at 43 nm in optical klystron configuration with $R_{56} = 80 \mu\text{m}$ versus laser heater intensity. The three laser heater intensity cases are shown on the curve as blue (0.8 μJ), red (2.1 μJ) and green (3.7 μJ) markers respectively. Image reproduced from [51].

The optical klystron enhancement to SASE has been measured at other two wavelengths

(32.4 nm and 20 nm). In Figure 3.13 the three cases are reported as a function of the chicane R_{56} . The intensities have been normalized to the pure SASE case ($R_{56} = 0$). The low efficiency of the optical klystron at 20 nm is mainly due to the weak magnetic strength of the FERMI modulator at this wavelength [1]. In fact despite the large tuning range of the modulator, it has been designed to be resonant in the range from 200-300 nm, which leads to a poor coupling in between the radiation and the electron beam at 20 nm.

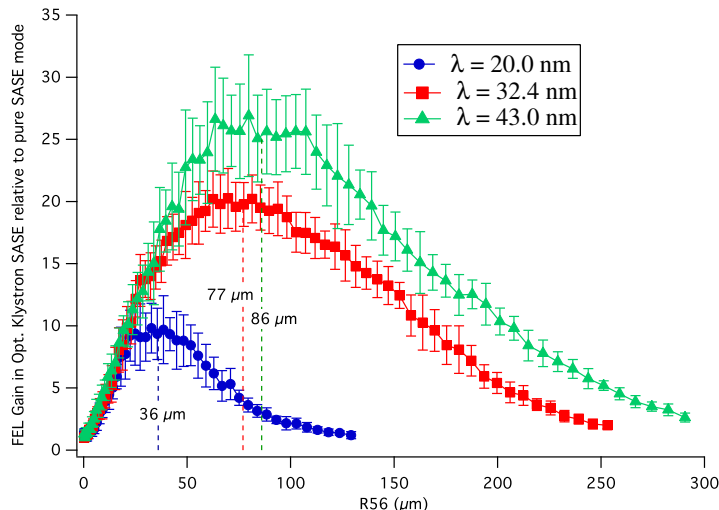


Figure 3.13: Optical SASE FEL relative enhancement through optical klystron at 43 nm, 32.4 nm and 20 nm. The optimum R_{56}^{opt} corresponding to the measured maximum gain is highlighted in the plot for each wavelength case. Each data point is the statistical average over 20 consecutive shot-to-shot FEL pulses with an error bar corresponding to their standard deviation. Image reproduced from [51].

It is possible to compare the theoretical G_{max}^{th} and the experimental one from the data of Figure 3.13, as the ratio between the pure SASE power and the maximum optical klystron intensity. The obtained G_{max}^{th} is in agreement (within 10%) with the peak of the gain factor measured in the experiment.

From the optimal condition $R_{56}^{opt} k_r \delta = 1$ one can see that it is further possible to compute the value of the beam slice energy spread δ . A summary of the obtained values for the quantities of interest is reported in Tab. 3.5.

Table 3.5: The ρ parameter, the theoretical G_{max}^{th} as foreseen by Eq. (3.2) and the optimum R_{56}^{opt} for the FERMI optical klystron operating at 43 nm, 32.4 nm and 20 nm.

λ_r (nm)	ρ	δ	G_{max}^{th}	R_{56}^{opt}
43	$1.7 \cdot 10^{-3}$	$8.0 \cdot 10^{-5}$	23	86
32.4	$1.3 \cdot 10^{-3}$	$6.7 \cdot 10^{-5}$	21	77
20	$1.1 \cdot 10^{-3}$	$8.9 \cdot 10^{-5}$	9.1	36

The optical klystron scheme has been also furthermore tested on FEL-2 line [4]. A fine tuning of the different dispersive sections present allowed to strongly enhance the pure SASE emission, obtaining intense photon pulses of about 100 μ J at 12 nm.

The optical klystron enhancement to the SASE process translates in a reduced number

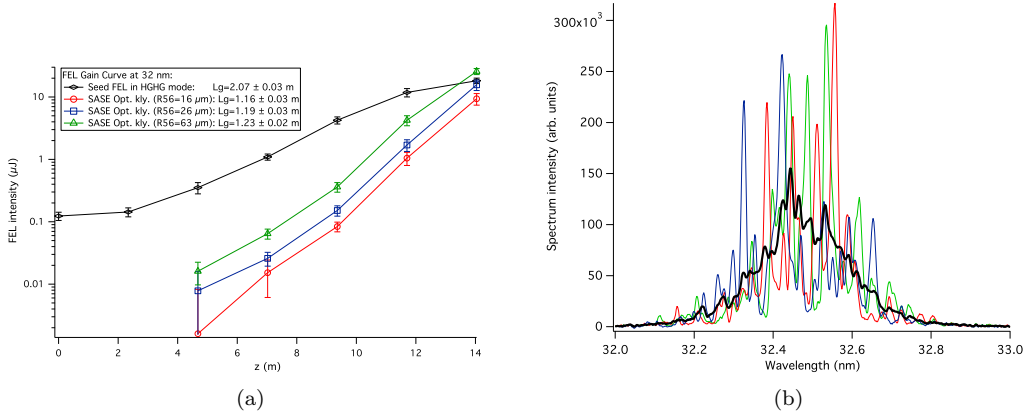


Figure 3.14: (a) Comparison between the FEL gain curve measured in optical klystron SASE mode for different dispersive section settings and in HGHG seeded mode. Each data point corresponds to a undulator length (2.32 m). In the HGHG seeded FEL, we measured the output intensity also after the modulator and the first radiator. (b) Singe-shot (thin lines) optical klystron FEL spectra when all radiators are tuned (thin color lines). Black bold line shows the averaged spectrum over 20 shots ((RMS) bandwidth: $3.3 \cdot 10^{-3}$). Image reproduced from [51].

of undulators needed to reach the FEL saturation. In order to evaluate the actual advantage of this configuration, the FEL gain length has been calculated by measuring the exponential growth of the FEL output versus the number of resonant radiators.

The exponential gain of the optical klystron SASE at 32.4 nm for three values of R_{56} is reported in Fig. 3.14(a), also with a comparison with a measured gain curve obtained in seeded mode. One can notice a relevant difference in between the SASE and seeded processes. In the latter case, as the bunching is induced by an external seed, a significant emission of radiation is occurring in the first radiator (data at $z=2.34$ m). Instead, due to SASE lethargy [31], the optical klystron emission reaches a detectable level only after the second radiator. Also notice that, due to the enhanced energy spread due to the seeding process, the SASE exponential gain is higher due to the smaller slice energy spread in the beam.

The measured gain length L_g in SASE optical klystron is about 1.2 m, in very good agreement with the numerical simulations results by GENESIS1.3 [57], and in addition it is very similar to the expected L_g in pure SASE mode. Also from theory [52] it is expected that the optical klystron does not change the SASE gain length. From the measurements one can observe that increasing the R_{56} up to the optimum value leads to an increase in the FEL emission after the second radiator but it does not affect the slope of the optical klystron SASE gain curve, confirming that the gain length is independent from the R_{56} setting. At 32.4 nm, assuming a pure SASE saturation length of $\approx 20 L_g$, the presence of the optical klystron ($R_{56} = 77 \mu\text{m}$ (see Fig. 3.13)) would allow to reach SASE saturation saving about 15% of the total undulators length, with respect to standard SASE operation.

Figure 3.14 shows three consecutive FEL spectra acquired in the optical klystron SASE configuration when all radiators are tuned at 32.4 nm. By averaging over a series of spectra it results that the spectral bandwidth is $\sigma_\lambda/\lambda = 3.3 \cdot 10^{-3} \sim 2\rho$.

In conclusion the optical klystron enhancement to SASE FEL has been experimentally demonstrated at FERMI, providing XUV photons with intensity in the order of 100 μJ . The

experiments have confirmed that the optical klystron FEL performance is strongly influenced by the electron beam relative uncorrelated energy spread, that must be significantly smaller than the FEL ρ parameter. The experimental results are in good agreement with the prediction of 1-D theory when microbunching structures in the longitudinal phase space are fully suppressed and the slice energy spread along the bunch could be considered uniform. We have also demonstrated that a seeded HGHG FEL can be also operated efficiently in SASE mode by implementing the optical klystron scheme.

The experiments conducted at FERMI constitutes a proof-of-principle of the optical klystron efficiency in the X-UV regime and pave the way for its application in X-ray SASE FELs.

References

- [1] C. J. et al. Bocchetta. *FERMI@Elettra FEL Conceptual Design Report*. Sincrotrone Trieste, 2007.
- [2] E. Allaria et al. “The FERMI@Elettra free-electron-laser source for coherent x-ray physics: photon properties, beam transport system and applications”. In: *New Journal of Physics* 12.7 (2010), p. 075002.
- [3] E. Allaria et al. “Highly coherent and stable pulses from the FERMI seeded free-electron laser in the extreme ultraviolet”. In: *Nature Photonics* 6.10 (2012), pp. 699–704. DOI: [10.1038/nphoton.2012.233](https://doi.org/10.1038/nphoton.2012.233).
- [4] E. Allaria et al. “Two-stage seeded soft-X-ray free-electron laser”. In: *Nature Photonics* 7.11 (2013), pp. 913–918. DOI: [10.1038/nphoton.2013.277](https://doi.org/10.1038/nphoton.2013.277).
- [5] G. Penco et al. “Optimization of a high brightness photoinjector for a seeded FEL facility”. In: *Journal of Instrumentation* 8.05 (2013), P05015.
- [6] D. Palmer. “The next generation photoinjector”. PhD thesis. Menlo Park, CA, USA: Stanford University, 1998.
- [7] B.E. Carsten. “Space-charge-induced emittance compensation in high brightness photoinjectors”. In: *Particle Accelerators*. Vol. 49. 1995, pp. 27–65.
- [8] S. Spampinati et al. “Laser heater commissioning at an externally seeded free-electron laser”. In: *Phys. Rev. ST Accel. Beams* 17 (12 2014), p. 120705. DOI: [10.1103/PhysRevSTAB.17.120705](https://doi.org/10.1103/PhysRevSTAB.17.120705).
- [9] *Libera Single-Pass detector*. Instrumentation Technologies.
- [10] V.L. Ginzburg and V.N. Tsytovich. *Transition radiation and Transition Scattering*. Adam Hilger, Bristol, UK, 1990.
- [11] W. Graves, P.G. O’Shea, and E.D. Johnson. In: *Proc. of PAC 1997*. Vancouver, Canada, 1997, p. 1993.
- [12] J. Rossbach and P. Schmüser. “Basic course on accelerator optics”. In: *Proc. of general accelerator physics school of CERN 1992*. Vol. 1. CERN, Geneva. 1994, p. 17.
- [13] M. Petronio. “Research and Applications of Radio-Frequency Deflecting Cavities”. PhD thesis. University of Trieste, 2009.
- [14] M. Röhrs. “Investigation of the Phase Space Distribution of Electron Bunches at the FLASH LINAC Using a Transverse Deflecting Structure”. PhD thesis. Hamburg, (Germany): Hamburg University, 2008.

-
- [15] M. Zangrando et al. In: *Proc. of SPIE 8078, Advances in X-ray Free-Electron Lasers: Radiation Schemes, X-ray Optics, and Instrumentation*. 80780I. Prague, Czech Republic, 2011.
- [16] et. al. M. Zangrando. “The Soft X-ray Free-Electron Laser FERMI@Elettra”. In: *Optical Technologies for Extreme-Ultraviolet and Soft X-ray Coherent Sources*. Springer, 2015.
- [17] M. Zangrando et al. “Recent results of PADReS, the Photon Analysis Delivery and REduction System, from the FERMI FEL commissioning and user operations”. In: *J. Synchrotron Rad., or in press* (2015).
- [18] C. Masciovecchio et al. “EIS: the scattering beamline at FERMI”. In: *J. Synchrotron Rad.* 22.553 (2015).
- [19] F. Bencivenga et al. “Four-wave mixing experiments with extreme ultraviolet transient gratings”. In: *Nature* 520.7546 (Apr. 2015), pp. 205–208. DOI: [10.1038/nature14341](https://doi.org/10.1038/nature14341).
- [20] F. Capotondi et al. “Invited Article: Coherent imaging using seeded free-electron laser pulses with variable polarization: First results and research opportunities”. In: *Review of Scientific Instruments* 84.5 (2013). DOI: [10.1063/1.4807157](https://doi.org/10.1063/1.4807157).
- [21] H. N. Chapman A. Barty M. J. Bogan S. Boutet M. Frank S. P. Hau-Riege S. Marchesini B. W. Woods S. Bajt W. H. Benner R. A. London E. Plonjes M. Kuhlmann R. Treusch S. Dusterer T. Tschentscher J. R. Schneider E. Spiller T. Moller C. Bostedt M. Hoener D. A. Shapiro K. O. Hodgson D. van der Spoel F. Burmeister M. Bergh C. Caleman G. Hultdt M. M. Seibert F. R.N.C. Maia R. W. Lee A. Szoke N. Timneanu J. Hajdu. “Flash diffraction imaging with a soft X-ray free-electron laser”. In: *Nature Phys.* 2 (2006), pp. 839–843.
- [22] C. von Korff Schmising et al. “Imaging Ultrafast Demagnetization Dynamics after a Spatially Localized Optical Excitation”. In: *Phys. Rev. Lett.* 112 (21 2014), p. 217203. DOI: [10.1103/PhysRevLett.112.217203](https://doi.org/10.1103/PhysRevLett.112.217203).
- [23] C. Svetina et al. “The Low Density Matter (LDM) beamline at FERMI: optical layout and first commissioning”. In: *Journal of Synchrotron Radiation* 22.3 (2015), pp. 538–543. DOI: [10.1107/S1600577515005743](https://doi.org/10.1107/S1600577515005743).
- [24] M. Kokole et al. “Magnetic characterization of the FEL-1 undulators for the FERMI@ELETTRA free-electron laser”. In: *Proceedings of the 2010 Free-Electron Laser Conference*. 2010, pp. 664–666.
- [25] M. Ferianis et al. “The Copper Free FERMI Timing System: Implementation and Results”. In: *Proc. Beam Instrumentation Workshop*. 2010, pp. 398–402.
- [26] W. M. Fawley. Tech. rep. LBNL-49625-Rev.1, Report No. LCLS-TN-04-3. LBNL, SLAC, 2004.
- [27] E. Allaria et al. “Tunability experiments at the FERMI@Elettra free-electron laser”. In: *New Journal of Physics* 14.11 (2012), p. 113009.
- [28] L. H. Yu. “Generation of intense UV radiation by subharmonically seeded single pass free electron lasers”. In: *Phys. Rev. A* 44.5178 (1991).
- [29] E. Allaria G. De Ninno. “Soft-X-Ray coherent radiation using a single-cascade Free-Electron Laser”. In: *Phys. Rev. Lett.* 99.1 (2007), p. 014801.
- [30] M. Xie. “Exact and variational solutions of 3D eigenmodes in high gain {FELs}”. In: *Nuclear Instruments and Methods in Physics Research Section A: Accelerators, Spectrometers, Detectors and Associated Equipment* 445.1–3 (2000), pp. 59–66. ISSN: 0168-9002. DOI: [10.1016/S0168-9002\(00\)00114-5](https://doi.org/10.1016/S0168-9002(00)00114-5).

- [31] E. Saldin, E. Schneidmiller, and M.V. Yurkov. *The Physics of Free Electron Lasers*. Springer Science, 2000.
- [32] W. Ackermann et al. “Operation of a free-electron laser from the extreme ultraviolet to the water window”. In: *Nature Photonics* 1.6 (June 2007), pp. 336–342. DOI: [10.1038/nphoton.2007.76](https://doi.org/10.1038/nphoton.2007.76).
- [33] E.L. Saldin, E.A. Schneidmiller, and M.V. Yurkov. “Coherence properties of the radiation from X-ray free electron laser”. In: *Opt. Commun.* 281 (2008), pp. 1179–1188.
- [34] A. Singer et al. “Transverse-coherence properties of the free-electron-laser FLASH at DESY”. In: *Phys. Rev. Lett.* 101.254801 (2008).
- [35] G. De Ninno et al. “Generation of Ultrashort Coherent Vacuum Ultraviolet Pulses Using Electron Storage Rings: A New Bright Light Source for Experiments”. In: *Phys. Rev. Lett.* 101 (5 2008), p. 053902. DOI: [10.1103/PhysRevLett.101.053902](https://doi.org/10.1103/PhysRevLett.101.053902).
- [36] L.-H. Yu M. Babzien I. Ben-Zvi L.F. DiMauro A. Doyuran W. Graves E. Johnson S. Krinsky R. Malone I. Pogorelsky J. Skaritka G. Rakowsky L. Solomon X.J. Wang M. Woodle V. Yakimenko S.G. Biedron J.N. Galayda E. Gluskin J. Jagger V. Sajaev I. Vasserman. “High-gain harmonic-generation free-electron laser”. In: *Science* 289.5481 (2000), pp. 932–934.
- [37] G. Lambert et al. “Injection of harmonics generated in gas in a free-electron laser providing intense and coherent extreme-ultraviolet light”. In: *Nat Phys* 4.4 (Apr. 2008), pp. 296–300. DOI: [10.1038/nphys889](https://doi.org/10.1038/nphys889).
- [38] E. Allaria, M. D. Danailov, and G. De Ninno. “Tunability of a seeded free-electron laser through frequency pulling”. In: *Eur. Phys. Lett.* 89.064005 (2010).
- [39] P. Emma et al. “First lasing and operation of an angstrom-wavelength free-electron laser”. In: *Nature Photonics* 4.9 (Sept. 2010), pp. 641–647. DOI: [10.1038/nphoton.2010.176](https://doi.org/10.1038/nphoton.2010.176).
- [40] D. Ratner et al. “Laser phase errors in seeded free electron lasers”. In: *Phys. Rev. ST Accel. Beams* 15 (3 2012), p. 030702. DOI: [10.1103/PhysRevSTAB.15.030702](https://doi.org/10.1103/PhysRevSTAB.15.030702).
- [41] J. Welch et al. “FEL spectral measurements at LCLS”. In: *Proceedings of the 2011 Free-Electron Laser Conference*. 2011, pp. 461–464.
- [42] G. Stupakov. “Using the Beam-Echo Effect for Generation of Short-Wavelength Radiation”. In: *Phys. Rev. Lett.* 102 (7 2009), p. 074801. DOI: [10.1103/PhysRevLett.102.074801](https://doi.org/10.1103/PhysRevLett.102.074801).
- [43] I. Ben-Zvi, K. M. Yang, and L. H. Yu. In: *Nucl. Instrum. Methods Phys. Res. A* 318 (1992), p. 726.
- [44] S. Sasaki. “Analyses for a planar variably-polarizing undulator”. In: *Nuclear Instruments and Methods in Physics Research Section A: Accelerators, Spectrometers, Detectors and Associated Equipment* 347.1-3 (Aug. 1994), pp. 83–86. DOI: [10.1016/0168-9002\(94\)91859-7](https://doi.org/10.1016/0168-9002(94)91859-7).
- [45] X. J. Wang et al. “Efficiency and Spectrum Enhancement in a Tapered Free-Electron Laser Amplifier”. In: *Phys. Rev. Lett.* 103 (15 2009), p. 154801. DOI: [10.1103/PhysRevLett.103.154801](https://doi.org/10.1103/PhysRevLett.103.154801).
- [46] E. Allaria et al. “FEL commissioning at FERMI@Elettra”. In: *Proceedings of the 2011 Free-Electron Laser Conference*. 2011.

-
- [47] L. Giannessi et al. “High-Order-Harmonic Generation and Superradiance in a Seeded Free-Electron Laser”. In: *Phys. Rev. Lett.* 108 (16 2012), p. 164801. DOI: [10.1103/PhysRevLett.108.164801](https://doi.org/10.1103/PhysRevLett.108.164801).
- [48] E.L. Saldin, E.A. Schneidmiller, and M.V. Yurkov. “Study of a noise degradation of amplification process in a multistage HGHG FEL”. In: *Opt. Commun.* 202 (2002), pp. 169–187.
- [49] L. Giannessi et al. “The FERMI Seeded FEL Facility: Operational Experience and Future Prospectives”. In: *Proceedings of the 2015 FEL Conference*. Daejeon, South Korea, 2015.
- [50] L. Giannessi. Private Communication.
- [51] G. Penco et al. “Experimental Demonstration of Enhanced Self-Amplified Spontaneous Emission by an Optical Klystron”. In: *Phys. Rev. Lett.* 114 (1 2015), p. 013901. DOI: [10.1103/PhysRevLett.114.013901](https://doi.org/10.1103/PhysRevLett.114.013901).
- [52] Y. Ding et al. “Optical klystron enhancement to self-amplified spontaneous emission free electron lasers”. In: *Phys. Rev. ST Accel. Beams* 9 (7 2006), p. 070702. DOI: [10.1103/PhysRevSTAB.9.070702](https://doi.org/10.1103/PhysRevSTAB.9.070702).
- [53] N.A. Vinokurov et al. In: *Nucl. Instrum. and Meth. A* 375 (1996), p. 264.
- [54] S.J. Hahn and K.H. Pae. In: *Journal of the Korean Phys. Soc.* 31 (1997), p. 856.
- [55] K.J. Kim. In: *Nucl. Instrum. and Meth. A* 407 (1998), p. 126.
- [56] E.L. Saldin, E.A. Schneidmiller, and M.V. Yurkov. In: *arXiv [physics.acc-ph]* (2003).
- [57] S. Reiche. “GENESIS 1.3: a fully 3D time-dependent FEL simulation code”. In: *Nucl. Instr. and Meth. A* 429 (1999). <http://pbpl.physics.ucla.edu/~reiche/>, pp. 243–248.

Chapter 4

Laser Heater

4.1 Introduction

LINAC-driven VUV and X-ray FELs require beams with high peak current, low transverse emittances and small energy spread [1]. Unfortunately, these beams are susceptible to the development of collective effects that can spoil their brightness, degrading or even completely suppressing the FEL emission process. One of the mentioned effects is microbunching instability (μ BI), which leads to a broadband modulation of the electron beam energy and (longitudinal) charge distribution [2–6].

4.1.1 Microbunching instability

The μ BI is the result of an instability in the LINAC that amplify small modulations naturally present in the electron beam at its generation, due to, e.g., non-uniformities in the cathode where the electrons are generated. The initial electron-beam modulation can be amplified in the downstream accelerator via impedance-mediated interaction with the surrounding of the beam (LINAC elements) or via self-interaction processes, like the longitudinal space charge (LSC) field [7]. The electrons in the bunch generate, due to Coulomb repulsion, a self field which they interact. Usually electrons are ultra-relativistic, so the interaction of their self field only changes the energy of the particles, rather than their relative position along the bunch.

The LSC further energy modulates the particles of the beam, usually on the micron scale (micro-bunching). Energy modulation can be transformed in density modulation, when the beam travels through a dispersive region, like a magnetic compressor chicane. This can further increase the LSC field acting on the particles with positive (and large) gain of the modulation amplitude. A further contribution to the amplitude of energy modulation may come from coherent synchrotron radiation emission (CSR) in bending magnets. Beams with high brightness are particularly susceptible to modulation effects due to the dependence of CSR and μ BI on bunch length and peak current.

The μ BI can be characterized by the gain factor G , defined as the ratio between the final and initial modulation amplitude, or, equivalently, as the ratio between the initial and final bunching fraction. Typical values of the μ BI gain for FEL sources based on LINAC accelerators can be as high as 10^5 [4, 8], so even an almost immeasurable initial modulation can develop in an extremely strong micro bunched beam. An example of μ BI gain curve for the FERMI LINAC is reported in Figure 4.1.

The final longitudinal phase space (LPS) of a microbunched beam can therefore exhibit both density and energy modulations on the multi to sub-micron scale. Non-uniformities present in the electron beam can significantly impact the degree of coherence and output power of an FEL in general and of a seeded FEL in particular as they influence the pulse properties which would be changing on the same scale. The modulation scale depends on the Fourier transform of the charge distribution of the beam and it is usually in the μm wavelength scale [2, 7]. Short-wavelength modulations cause an increase in the “slice” energy spread of the beam effectively decreasing the overall FEL power. Long-wavelength modulations can instead locally change the electron beam energy and thus they can modify the resonant FEL wavelength.

4.1.2 Landau damping and laser heating

Beams with small emittances and small energy spread are susceptible to instability development because they lack the uncorrelated dispersion of particles trajectories inside a magnetic compressor which is responsible of the smearing of any modulation present in the longitudinal phase space up to that point. A large enough uncorrelated energy spread and transverse geometric emittance can therefore induce, respectively, longitudinal [7, 9] and transverse Landau damping [4].

To illustrate the principle, consider the electron path length difference in a dipole magnet of length s and bending radius r , to the first order in the initial particle coordinates (position and divergence) u_0 , u'_0 and the relative energy deviation δ_0 [10]:

$$\begin{aligned} \Delta l(s) &= \int_0^s \frac{u(s')}{r(s')} ds' + \frac{1}{2} \int_0^s u'^2(s') ds' \\ &= u_0 \int_0^s \frac{C(s')}{r(s')} ds' + u'_0 \int_0^s \frac{S(s')}{r(s')} ds' + \delta_0 \int_0^s \frac{\eta(s')}{r(s')} ds' + o(u_0^2, u_0'^2, \delta_0^2) \\ &\simeq u_0 \theta(s) + u'_0 r (1 - \cos \theta(s)) + \delta_0 R_{5,6}(s) \simeq u_0 \eta'(s) + u'_0 \eta(s) + \delta_0 R_{5,6}(s). \end{aligned} \quad (4.1)$$

Here θ is the bending angle, $C(s)$ and $S(s)$ are the principal trajectories [11], η is the energy dispersion function, η' its first derivative with respect to the curvilinear longitudinal coordinate s [12]. Eq. (4.1) is valid in the small angle approximation ($\theta \ll 1$).

Eq. (4.1) is composed of three terms: the first two provide transverse Landau damping [13] as they depend on the position and divergence, while the last term is energy-dependent and provides longitudinal Landau damping of the microbunching-induced modulations. If one considers a monochromatic beam ($\delta_0 = 0$) with finite emittance ϵ_0 , the (RMS) value of the path length difference in Eq. (4.1) results in:

$$\begin{aligned} \sqrt{\langle \Delta l^2(s) \rangle} &= [\langle u_0^2 \rangle \eta'^2(s) + \langle u_0'^2 \rangle \eta^2(s) + 2 \langle u_0 u_0' \rangle \eta(s) \eta'(s)]^{1/2} \\ &= \sqrt{\epsilon_0 (\beta \eta'^2 + 2\alpha \eta \eta' + \gamma \eta^2)}, \end{aligned} \quad (4.2)$$

where α , β and γ are the Twiss functions of the electron beam [12].

When the longitudinal Landau damping is considered, one can write the gain G (bunching ratio) of the μBI in the presence of a single compression chicane [2, 4] as a function of the wavenumber k :

$$G(k) = \left| \frac{b_f}{b_0} \right| \sim Ck |R_{56} \frac{\Delta\gamma(k)}{\gamma}| \frac{I}{I_A} \exp\left(-\frac{1}{2} \left(Ck R_{56} \frac{\sigma_{\delta,0}}{\gamma} \right)\right), \quad (4.3)$$

with C the compression factor, I the peak current of the beam, I_A the Alfvén current, $\sigma_{\delta,0}$ the uncorrelated energy spread *before* compression, $\Delta\gamma(k)$ being the energy modulation at the wavenumber k . An example of the μ BI gain curve, computed in the linear approximation with Eq. (4.3) is reported in Figure 4.1.

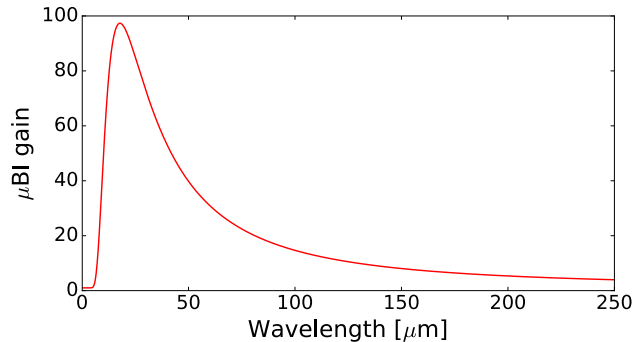


Figure 4.1: Gain function for the μ BI at the end of the FERMI LINAC, as a function of the modulation wavelength. Image courtesy of E. Roussel.

In order to control the μ BI gain via longitudinal Landau damping in a LINAC-based light source, the use of a “laser heater” (LH) device has been proposed [2] and successfully implemented [5, 14]. The working principle relies on a controlled increase of the *uncorrelated* energy spread of the beam in the low-energy section of the machine, before the instability has a chance to significantly build up. The increase of the energy spread of the beam, from the typical ~ 1 keV (RMS) level at the injector level to ~ 10 keV (RMS) suppresses the μ BI [4], as one can see from the dumping exponential in Eq. (4.3).

The (controlled) increase of the energy spread is obtained through the interaction of the electron beam with an external laser, usually in the infrared wavelength range. The light-electron interaction is assisted by the magnetic field generated by a short undulator. As a result of the interaction the electron beam becomes energy modulated on the laser wavelength scale. The amount of “heating”, i.e. the amplitude of the modulation, can be tuned by changing the laser power. The modulation should intuitively develop microbunching instead of curing it, but the LH undulator is cleverly located at the center of a small magnetic chicane. As the beam travels through the second half of such a chicane the modulation is washed out due to the electrons’ path length difference [1].

The smearing condition of the chicane [4] can be expressed as:

$$|R_{51}\sigma_x|, |R_{52}\sigma_{x'}| \gg \lambda_c = \frac{\lambda_L}{2\pi}, \quad (4.4)$$

where R_{51} , R_{52} are the elements of the R matrix [12] which correlate the transverse variables x , x' and longitudinal position, σ_x , $\sigma_{x'}$ are respectively the (RMS) electron beam size and divergence, λ_c is the critical wavelength below which the smearing is effective and λ_L is the wavelength of the laser interacting with the electrons.

While the LH has been proven to suppress the μ BI, it nevertheless increases the overall energy spread of the e-beam, decreasing the beam brightness. An alternative proposed approach to cope with the μ BI uses RF deflecting cavities up and downstream of a magnetic compressor [15]. The approach in this case is to induce a *reversible* local energy spread increase in between the two RF deflectors in order to suppress the conversion of the energy modulation into density modulation, which could happen in the magnetic compressor. The

tight tolerances in the RF stability and higher cost of the device if compared to the LH, represent the main drawbacks of the scheme. To date, most of existing and future FELs foresee the use of a laser heater [1].

4.1.3 Energy spread and laser heating

The LH interaction can be described as follows. Suppose a fundamental Gaussian mode laser which co-propagates together with a (transversally) round electron beam inside an undulator characterized by a length L_u , strength parameter K and periodicity λ_u . The undulator is supposed to be shorter compared to both the Rayleigh length Z_R of the laser and the beta functions $\beta_{x,y}$ of the electrons which have an energy $\gamma_0 mc^2$. The laser wavelength λ_L satisfies the resonant condition given by $\lambda_L = \lambda_u(1 + K^2/2)/(2\gamma_0^2)$. The amplitude of the energy modulation induced by the laser-electron interaction, neglecting small changes in laser and electron beam sizes, can be expressed as follows [4]:

$$\Delta\gamma_L(r) = \sqrt{\frac{P_L}{P_0}} \frac{KL_u}{\gamma_0\sigma_L} (J_0(\chi) - J_1(\chi)) \exp\left(-\frac{r^2}{4\sigma_L^2}\right). \quad (4.5)$$

Here $\chi = \frac{K^2}{4 + 2K^2}$, P_L is the peak laser power, $P_0 = I_A mc^2/e \simeq 8.9$ GW, $J_{0,1}$ are the Bessel functions, r is the radial coordinate and σ_L the (RMS) laser spot size in the undulator.

The electron distribution, assumed initially Gaussian both in energy and transverse coordinates, is modified by the laser-electron interaction as

$$f_0(z, \Delta\gamma_0, r) = \frac{I_0}{ec\sqrt{2\pi}\sigma_{\gamma_0}} \exp\left\{-\frac{[\Delta\gamma_0 - \Delta\gamma_L(r) \sin(k_L z)]^2}{2\sigma_{\gamma_0}^2}\right\} \frac{1}{2\pi\sigma_x^2} \exp\left(-\frac{r^2}{2\sigma_x^2}\right), \quad (4.6)$$

where z is the longitudinal coordinate along the bunch, $z > 0$ being the bunch head. By integration of Eq. (4.6) in z and r one can obtain the modified energy distribution of the electron beam.

$$\begin{aligned} V(\Delta\gamma_0) &= 2\pi \int r dr \int dz f_0(z, \Delta\gamma_0, r) = \\ &= \frac{1}{\pi\sigma_x^2\sqrt{2\pi}\sigma_{\gamma_0}} \int r dr \exp\left(-\frac{r^2}{2\sigma_x^2}\right) \int \frac{d\xi}{\sqrt{\Delta\gamma_L(r)^2 - (\Delta\gamma_0 - \xi)^2}} \exp\left(-\frac{\xi^2}{2\sigma_{\gamma_0}^2}\right). \end{aligned} \quad (4.7)$$

Finally, it is also possible (and useful) to explicitly compute the energy spread dependence of the electron beam upon the laser power P_L as [5]:

$$\Delta\gamma = \frac{K(J_0(\chi) - J_1(\chi))}{\gamma_0} \sqrt{\frac{P_L}{P_0}} \int_0^{L_u} \sqrt{\frac{\sigma_L^2(z)}{\sigma_x^2 + \sigma_L^2(z)}} \frac{1}{\sigma_L(z)} dz, \quad (4.8)$$

where the explicit dependence of the laser spot size along the undulator is considered.

In Figure 4.2 the energy distribution after the laser heater is reported for two different conditions of the electron and laser spot sizes. The blue line corresponds to the case $\sigma_L \gg \sigma_x$, i.e. when the laser spot size is much larger than the electron beam size, while the red curve corresponds to the case $\sigma_L \approx \sigma_x$, i.e. when the laser spot size is matched to the e-beam size.

Using a larger laser spot size may be useful to establish the initial laser-electron interaction, but the resulting energy profile shows a double-horn distribution which does not

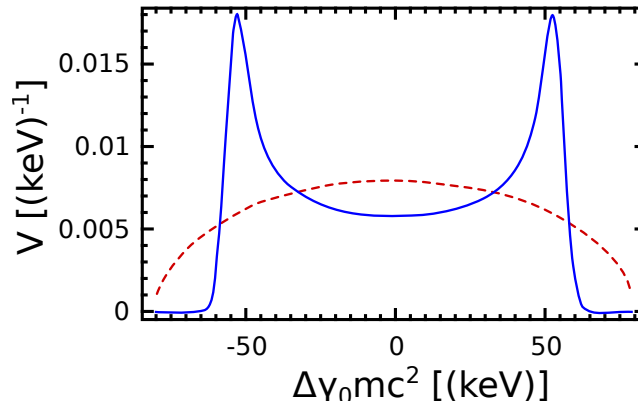


Figure 4.2: *Electron energy distribution after the laser heater for a large laser spot (blue solid curve) and for a matched laser spot (red dashed curve). Image reproduced from [4].*

contribute much to suppress the μ BI. The two sharp spikes at $\Delta\gamma_0 \approx \pm\Delta\gamma_L(0)$ act like two separate cold beams (they have a small energy spread) and are therefore subject to develop the instability as the original beam. If instead the laser and electron spot sizes are comparable the modulation amplitude experienced by the electrons has a strong radial dependence. The off-axis electrons experience smaller modulation as the laser field is smaller than the on-axis ones. The resulting heating is more uniform in terms of the energy spread, leading to a distribution which resembles a Gaussian one, that induces a more effective Landau damping [4]. Notice that, while the energy distribution for the matched case *resembles* a Gaussian curve, it is not *exactly* one. In the following we will see that this discrepancy has an impact on the performance of the FEL. Recently [16] it has been proposed to use different laser transverse modes in order to achieve an exact Gaussian energy distribution.

Although only a perfect transverse alignment between the laser and the electron beams has been considered in the above derivation, the resulting energy profile does not deviate significantly for a relative offset that is on the order of the (RMS) beam size.

4.2 FERMI laser heater

Due to the above mentioned concerns regarding uncontrolled μ BI growth, a LH system was installed at the end of the FERMI injector, where the e-beam energy is approximately 100 MeV [17, 18]. It is located in an acceleration-free beamline upstream the first magnetic compressor chicane (BC1 in Figure 3.1).

4.2.1 Layout

The FERMI LH consists of a short, planar undulator located in a magnetic chicane where an external infrared laser pulse is superimposed temporally and spatially on the electron beam. The laser-electrons interaction within the undulator produces an energy modulation on a longitudinal scale length corresponding to the laser wavelength, which in the case of FERMI is 783 nm. As mentioned above, the second half of the chicane smears the energy modulation in time, leaving the beam with a larger incoherent energy spread than at the LH entrance. Figure 4.3 shows the trajectory of the electron and laser beams in the LH chicane, as well as the magnets (dipole) and the available diagnostics, namely screens and beam

position monitors (BPM). In Table 4.1 the main FERMI LH parameters are summarized. A review of the commissioning phase of the device is reported in [14].

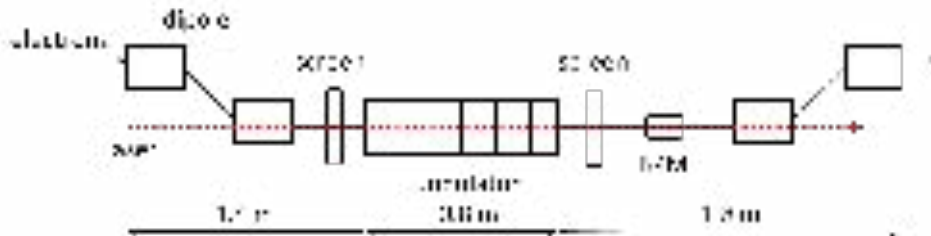


Figure 4.3: Schematic representation of the LH setup implemented at FERMI. Image reproduced from [14].

Table 4.1: FERMI LH parameters.

Parameter	Symbol	Value	Units
Undulator period	λ_u	40	mm
Number of periods	N_u	12	
Undulator strength	K	0.8 - 1.17	
Laser wavelength	λ_L	783	nm
Laser pulse duration	Δt_L	8-15	ps
Laser energy per pulse	E_L	< 80	μJ
Laser spot size	130-220	σ_L	μm
e-beam spot size	σ_x	100	μm
Horizontal offset in the chicane		30	mm
Bending angle	θ	3.5	deg

The laser pulse inducing the heating effect is a small fraction of the Ti:Sa laser [19] used in the photo injector system [20]. The LH pulse is transported to an optical table in the LINAC tunnel where it can be manipulated via remotely controlled optics. The pulse temporal duration can be adjusted within the range 8-15 ps via a grating stretcher. The latter is important because the FERMI injector can be optimized with different electron bunch lengths (temporal duration), so similarly different LH laser pulse lengths are needed in order to accommodate all the possible e-beam longitudinal durations. The available energy per pulse can be as high as 50 μJ at the center of the LH undulator, corresponding to a laser peak power of 20-50 MW (for the different pulse durations). According to theory [4], the available power level can induce up to ~ 70 keV of energy spread (RMS) on the electron beam. The nominal value of beam heating required by FEL operation with optimal μBI suppression is in the range of 10 keV (RMS) [6]. In Figure 4.4 the energy spread added to the electron beam by the LH interaction is reported as a function of the LH laser pulse energy. It has been computed via Eq. (4.8) and the parameters of Table 4.1.

The LH laser pulse energy is finely controlled via a remotely controlled polarimeter, with minimum energy of ~ 0.25 μJ . While the initial phase of the LH commissioning was carried out at full laser power in order to account for possible misalignment and to obtain a stronger signal of the induced heating, to date the maximum energy has been reduced to ~ 50 μJ per pulse. A separate shutter can completely inhibit the laser pulse propagation to the undulator, which will be referred as “LH off” operation.

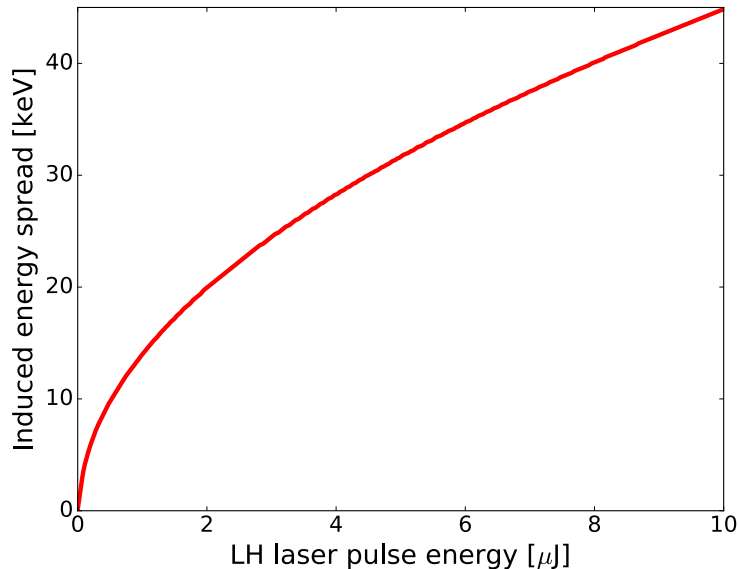


Figure 4.4: LH induced energy spread as a function of the LH laser pulse energy.

The undulator is a 40 mm period, variable gap device with 12 periods. The gap can be remotely varied in order to change the resonant condition to match the external laser wavelength for different e-beam energies, which are typically in the range 95-120 MeV. The relative energy bandwidth has been estimated to be $\sim 4\%$, with an error in the gap-K strength calibration of the order of 0.3%. The nearby horizontal electron spectrometer (LH spectrometer) allows measurement of the electron beam energy with a relative accuracy better than 1%.

The diagnostics available at the LH chicane (see Fig. 4.3) include two scintillating multi-screen stations equipped with Chromox ($\text{Al}_2\text{O}_3 : \text{Cr}$) targets located at each side of the undulator, as well as a beam position monitor (BPM) for the electron-beam positioning. The Chromox screens are capable of imaging both the laser and the electron beam and are used to diagnose the spatial overlap the two beams. The laser-electron superposition is routinely performed using three remotely controllable steering mirrors. Typical positioning accuracy of the laser beam is in the sub 10 μm range thanks to piezo tip-tilt stage. The laser pointing is kept stable using a feedback loop, which fixes the position of the virtual undulator focus, imaged via a CCD changing the piezo motors. This ensures that the system is kept aligned despite the possible presence of slow thermal drifts.

Figure 4.5 shows the laser and electron beam transverse profiles measured at the two screens located at both ends of the undulator. The laser beam is focused to a symmetric $\sim 220 \mu\text{m}$ (RMS) waist at the center of the undulator, while typical e-beam sizes at the same position are $\sim 130 \mu\text{m}$ (RMS). Since both the electron beam and the LH laser originate from the same drive laser they have an intrinsic timing relation. A cursory temporal alignment (within ~ 200 ps) is performed by looking at the signals coming from a photodiode for the laser beam and from the BPM for the e-beam. The final temporal overlap (with fs-level accuracy) is then adjusted empirically by scanning a remotely controlled (laser) delay line while looking at the heating effects on the e-beam. The typical signals used to verify the LH operativity are either the FEL output power itself or the increase in the beam energy spread at a diagnostic station. Another signature of the suppression of the μBI is the reduction of

coherent optical transition radiation (COTR) [21, 22], see Appendix A, arising at diagnostic screens, which was reported to be a direct consequence of microbunching suppression at optical frequencies [5, 14, 23].

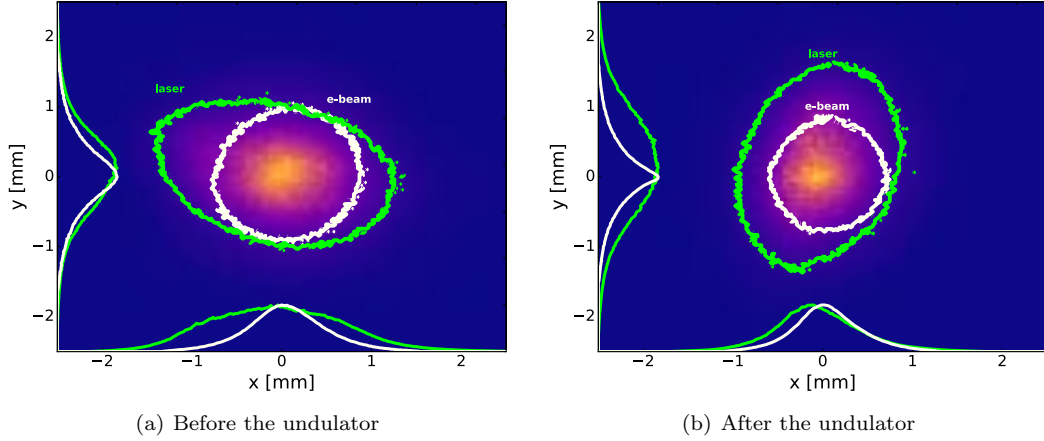


Figure 4.5: Superimposed laser (green) and electron (white) beams on the two Chromox screens before 4.5(a) and after 4.5(b) the LH undulator. The two contours encircle 90% of the area for the two beams. The horizontal and vertical profiles are also shown. The beam sizes are almost matched in transverse size and exhibit a satisfactory superposition.

4.2.2 Longitudinal phase space and heating

The LPS of beam after laser-electron interaction can be imaged via a vertical RF deflector coupled with to a horizontal bending magnet spectrometer (see Appendix A for further details).

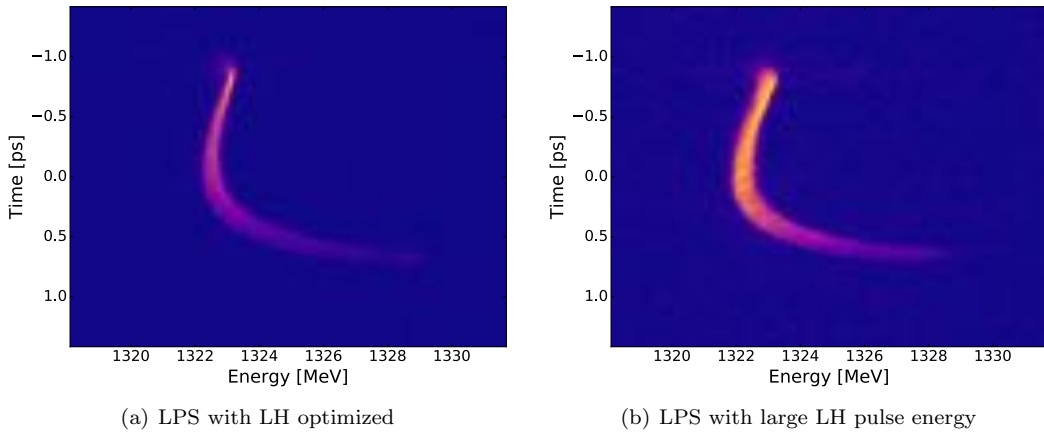


Figure 4.6: LPS reconstruction of the e-beam using a RF deflector coupled to an electron spectrometer for the case LH pulse energy $0.25 \mu\text{J}$ (left) and $18.3 \mu\text{J}$ (right).

An example of the LPS of the electron beam is reported in Figure 4.6 for reduced LH

pulse energy ($0.25 \mu\text{J}$, Fig. 4.6(a)) and for larger laser pulse energy ($18 \mu\text{J}$, Fig. 4.6(b)). The beam head is located on the top of the figures (smaller times).

Slice energy spread

Measuring the LPS enable us to evaluate the energy spread on a small slice along the electron beam, which corresponds to the portion of beam which is responsible of the FEL process. The evolution of the slice energy spread as a function of the laser pulse energy is reported in Figure 4.7. A red cross, corresponding to the measured slice energy spread when the LH is off, is also reported.

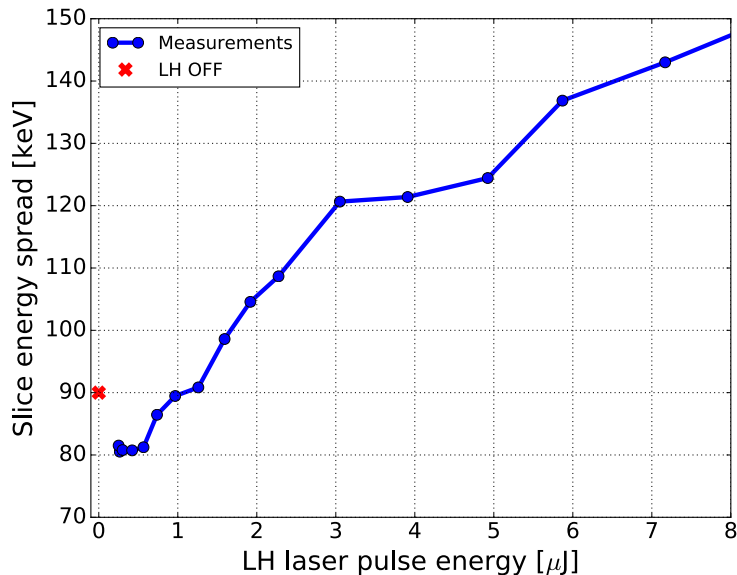


Figure 4.7: Measured (RMS) slice energy spread at the LINAC end as a function of the LH laser pulse energy. The slice energy spread when the LH is off is also reported (red cross). Notice that, by increasing the energy spread via the LH interaction, the final beam energy spread has a minimum, corresponding to the suppression of the μBI , at $\sim 0.5 \mu\text{J}$ laser pulse energy.

While the (RMS) energy spread introduced by the LH in the electron beam is always increasing with the LH laser pulse energy (see Fig. 4.4), the final (RMS) slice energy spread of the beam shows a minimum at $\sim 0.5 \mu\text{J}$ laser pulse energy. A slight increase in the initial energy spread of the electron beam, $< 5 \text{ keV}$ induced by the LH, lead to an efficient Landau damping of the μBI gain and a reduced energy spread at the LINAC end. After the minimum the slice energy spread becomes larger and larger as the laser pulse energy is increased.

4.2.3 Microbunching Instability suppression

In this section the focus will be on the effects of LH on the electron beam dynamics downstream the first bunch compressor (BC1) when only one bunch compressor is active, which corresponds to the usual machine setup for FERMI. Data presented here are relative to a 2.8 ps (RMS) long (at the gun exit), 700 pC charge electron beam that experiences a compression $C \sim 10$. Clear evidence of μBI arises when the LH is off and when the compression factor C exceed 3. The peak current after compression is $\sim 550 \text{ A}$.

A clear indication of the presence of a strong μ BI modulation in the FERMI electron beam is the evidence of COTR radiation. The COTR is a coherent radiation emitted when the beam passed through OTR screens [23].

Figure 4.8 shows the transverse beam spot imaged on the OTR station located just downstream of the first bunch compressor in the LH on and off cases. This screen is routinely used for diagnostic purposes and is of paramount importance for keeping the e-beam optics during compression under control. When the LH is switched off (Fig. 4.8(a)) the beam spot is contaminated by COTR, its sizes are larger than the “real” beam, showing also significant intensity and shape fluctuations together with phantom beams. Any measure made in this configuration is then highly unreliable and without the LH a beam size reconstruction would be impossible.

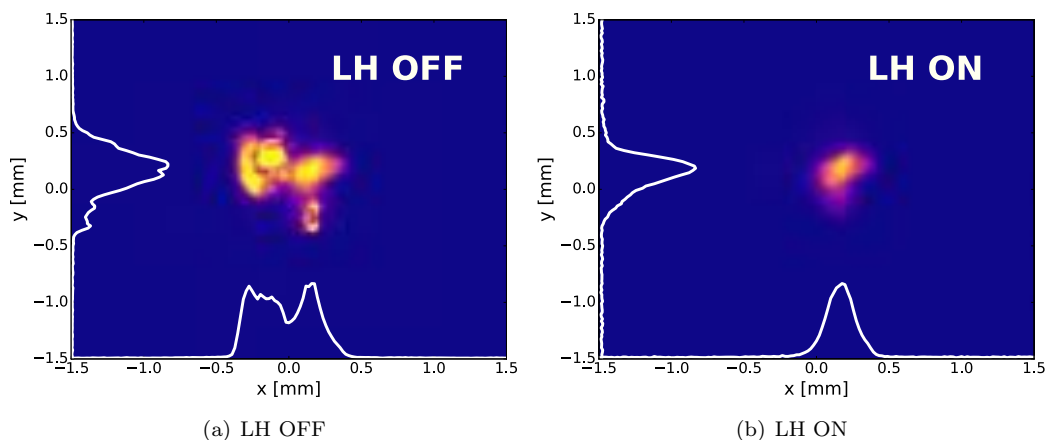


Figure 4.8: Transverse electron beam profile imaged on the OTR station located just downstream of the first bunch compressor, in the case LH off (left) and on (right). The evidence of COTR contamination is represented by the different apparent beam sizes measured in the two cases.

Figure 4.9 shows the amplitude of the integrated OTR signal as a function of the LH laser pulse energy measured on a screen located at just after the bunch compressor (see Fig. 4.9(a)) and at the LINAC end (see Fig. 4.9(b)).

The OTR integrated intensity decays as the LH heating is increased, approaching an asymptotic level when the LH laser energy per pulse exceeds the $\sim 2.5 \mu\text{J}$ level, corresponding to an increase of the beam energy spread of $\sim 20 \text{ keV}$ induced by the LH interaction. The (asymptotic) value of the intensity corresponds to the incoherent OTR level measured upstream the bunch compressor. Note that in the above data the suppression of the COTR emission happens for modulation wavelengths in the range between $0.2 \mu\text{m}$ and $0.9 \mu\text{m}$, corresponding to the operation range of the CCD camera used for the measurements.

The successful suppression of the COTR along the LINAC allows the use of the OTR screens for diagnostic purposes also after beam compression. Characterized by an improved spatial resolution ($\sim 35 \mu\text{m}$) if compared to YAG screens ($\sim 80 \mu\text{m}$), they allow for a better reconstruction of the electron beam transverse dimensions, e.g., during the measurement of the Twiss parameters for matching [24].

This is further demonstrated by looking at the (RMS) transverse beam sizes at the OTR screen, e.g. just downstream of the bunch compressor as in the case reported in Fig. 4.10, where the beam (RMS) horizontal and vertical sizes are shown as a function of the LH laser pulse energy. When instead the LH is turned on (Fig. 4.8(b)) with significant heating

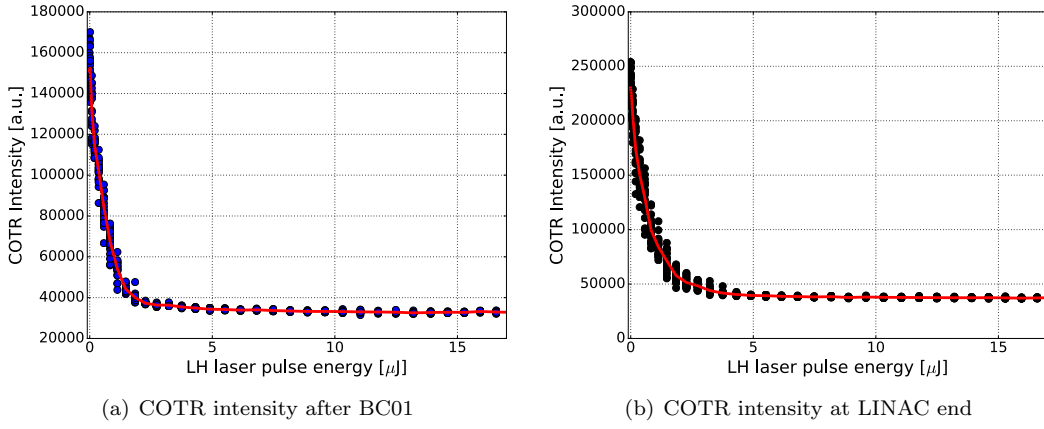


Figure 4.9: COTR analysis at an OTR screens downstream the bunch compressor. The intensities of the radiation are reported as a function of the LH laser pulse energy, and correspond to a screen just downstream the bunch compressor and at the LINAC end. Notice the decay of the intensity at the screen as the LH laser energy increase, a clear indication of the suppression of the μ BI instability-induced modulations present in the beam.

the measured transverse sizes are smaller and also essentially constant on a shot-to-shot basis. For low heating values the beam size is contaminated by COTR, while the measured dimensions decrease as the heating increases, reaching an asymptotic value if the LH added energy spread overcomes the 8 keV level.

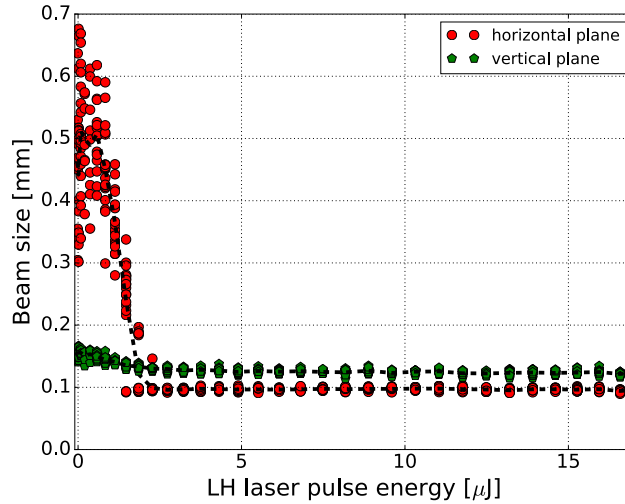


Figure 4.10: Transverse electron beam dimensions downstream BC01 as a function of the LH laser pulse energy. For the particular machine configuration the effect was larger in the horizontal direction, see Fig. 4.8, with appearance of COTR-related structures mainly in the horizontal plane.

4.3 LH impact on FEL

As already pointed out above, the LH-induced energy spread distribution does not have a Gaussian-like shape and its shape will depend upon the transverse dimensions and overlap of the laser and electron beams inside the LH undulator [5]. If the laser field is transversally uniform (i.e., very large laser size), the slice energy spread of the beam will exhibit a “double horned” profile (cfr. Figure 4.2) with separation depending on specific undulator parameters [25] and laser intensity, while the most desirable profile for μ BI suppression is obtained for matched spot sizes [4].

The control of the total energy spread and its distribution at the entrance to an FEL undulator are critical factors for the successful operation of seeded high gain FELs which rely on harmonic upshift schemes to access wavelengths much shorter than the seed wavelength λ_S [26]. In the case of high gain harmonic generation (HG) FELs [27], nearly all analyses to date presumed a Gaussian distribution for the e-beam energy spread. This hypothesis lead to an exponential suppression of FEL gain if the harmonic number corresponding to the FEL emission increases, de-factor limiting the shortest wavelengths possible for an FEL based on the HG setup.

As a reminder, the HG FEL scheme relies on the interaction of an external seed laser with a relativistic electron beam in a short undulator (the “modulator”). The interaction produces an energy modulation on the e-beam at the seed laser wavelength and that becomes a density modulation (bunching) when the electron bunch passes through a short dispersive section. The bunching contains strong components at higher harmonics of the seed wavelength initiates the FEL process when the beam enters a long undulator (the “radiator”). The resulting coherent emission is further amplified through the normal FEL process, producing short wavelength output pulses characterized by excellent transverse and longitudinal coherence [28–30].

According to [27] the bunching fraction at the exit of the dispersive section can be expressed as:

$$b_m = \exp\left(-\frac{1}{2}m^2\sigma_\gamma^2 D^2\right) J_m(m\Delta\gamma_S D), \quad (4.9)$$

where m is the harmonic number, $D \equiv 2\pi R_{56}/\gamma_0\lambda$, R_{56} is the strength of the dispersive section, $\lambda = \lambda_S/m$ is the emitted radiation wavelength, γ_0 the electron beam Lorentz factor, $\Delta\gamma_S$ is the seed laser-induced energy modulation amplitude, and J_m is the m^{th} order Bessel function. Eq. (4.9) is only valid in the hypothesis that the seed laser intensity is constant along the modulator, its radius σ_r is much greater than that of the electron beam σ_x , and more importantly, that the (incoherent) energy spread of the electron beam follows a Gaussian distribution with (RMS) σ_γ .

The limits of the HG scheme mentioned above can be well understood by analyzing Eq. (4.9). According to it, the bunching at harmonic m is significant only if $\Delta\gamma_S \geq m\sigma_\gamma$. However, in order to have an effective FEL gain in the radiator, $\Delta\gamma_S/\gamma_0$ must not overcome the FEL parameter $\rho \sim 10^{-3}$ [31]. These two conditions are competing so only a tradeoff is possible, which can be summarized in a requirement on the normalized energy spread $\sigma_\gamma/\gamma_0 \leq \rho/m$. The result effectively limits the possible maximum harmonic number, i.e., the minimum wavelength reachable, at which significant FEL radiation can be emitted using the scheme. In the case of FERMI $m \leq 8$ if a (typical) 1.2-GeV beam energy with (RMS) energy spread of 150 keV is considered.

If instead a non-Gaussian energy spread, like the one generated at LH, is considered, according to [4], Eq. (4.9) should be modified as:

$$b_m = \exp\left(-\frac{1}{2} m^2 C^2 \sigma_H^2 D^2\right) J_m(m\Delta\gamma_S D) \times S_H(mC\Delta\gamma_H D, \sigma_L/\sigma_x), \quad (4.10)$$

where $C \sim 10$ is compression factor of the beam, σ_H is the beam's slice energy spread entering the LH (presumed Gaussian), $\Delta\gamma_H \gg \sigma_H$ is the energy modulation induced by the LH, and S_H is a hypergeometric function (for the complete derivation and the details, see [4]).

Equation (4.10) makes two important predictions. First, the energy spread measure relevant to the exponential suppression term is the (compressed) slice energy spread at the LH, whose typical value is $C\sigma_H \approx 30$ to 50 keV, rather than the much larger, overall measured energy spread at LINAC exit reported above (100 to 300 keV). Second, for usual operations case ($\sigma_L \approx 2\sigma_x$) as at FERMI, the amplitude of the harmonic bunching at radiator entrance will oscillate as the LH laser power is increased, decaying more slowly than an exponential. However, between the LH and the modulator that initiates the FEL process, the electron beam undergoes acceleration and longitudinal manipulation (compression), so a smearing of the energy distribution present at the LH is expected and the final energy spread has been thought to be Gaussian. In the following we will demonstrate that this presumption is in fact far too pessimistic and much of the local, non-Gaussian structure induced at LH is transported along the accelerator up to the FEL. Importantly, we are going to show that the predictions of Eq. (4.10) are supported by the experimental data.

Table 4.2: Measured electron beam, laser and undulator parameters used in the experiment. For the FEL undulators, the first number refers to the modulator, the second to the radiator.

	Parameter	at LH	at FEL
e ⁻ beam	Charge	500 pC	500 pC
	Energy	95 MeV	1.2 GeV
	Slice energy spread (RMS)	5 keV	100-300 keV
	Bunch length (RMS)	3 ps	300 fs
	Size (at undulator, (RMS))	100 μm	100 μm
Laser	Wavelength	783 nm	260 nm
	Pulse duration (RMS)	8 ps	80 fs
	Energy	< 70 μJ	$\sim 50 \mu\text{J}$
	Size (at undulator; (RMS))	150 μm	300 μm
Und.	Period	40 mm	100 mm / 55 mm
	Number of periods	12	30 / 6 x 42
	Strength parameter (K)	0.8-1.17	3.8-4.1 / 0.6-2.8
	Dispersion (D)	—	3.5-7

Using the same setup presented before (see Appendix A) the electron energy distribution at the LINAC end was measured, with parameters reported in Table 4.2.

Figure 4.11(a) shows the measured LPS for a narrow time slice near the temporal center of the electron beam as a function of the LH pulse energy. Note that, although at zero LH heating the energy distribution strongly resembles a Gaussian curve in shape, as the heating is increased the energy distribution widens and flattens out in the center. Figure 4.11(b) shows details of the energy distribution for the case where the LH energy was 42 μJ . As shown by the curves of Fig. 4.11(c), it is apparent that the measured energy distributions with LH on does not follow a Gaussian curve, but instead exhibit a much flatter central region and

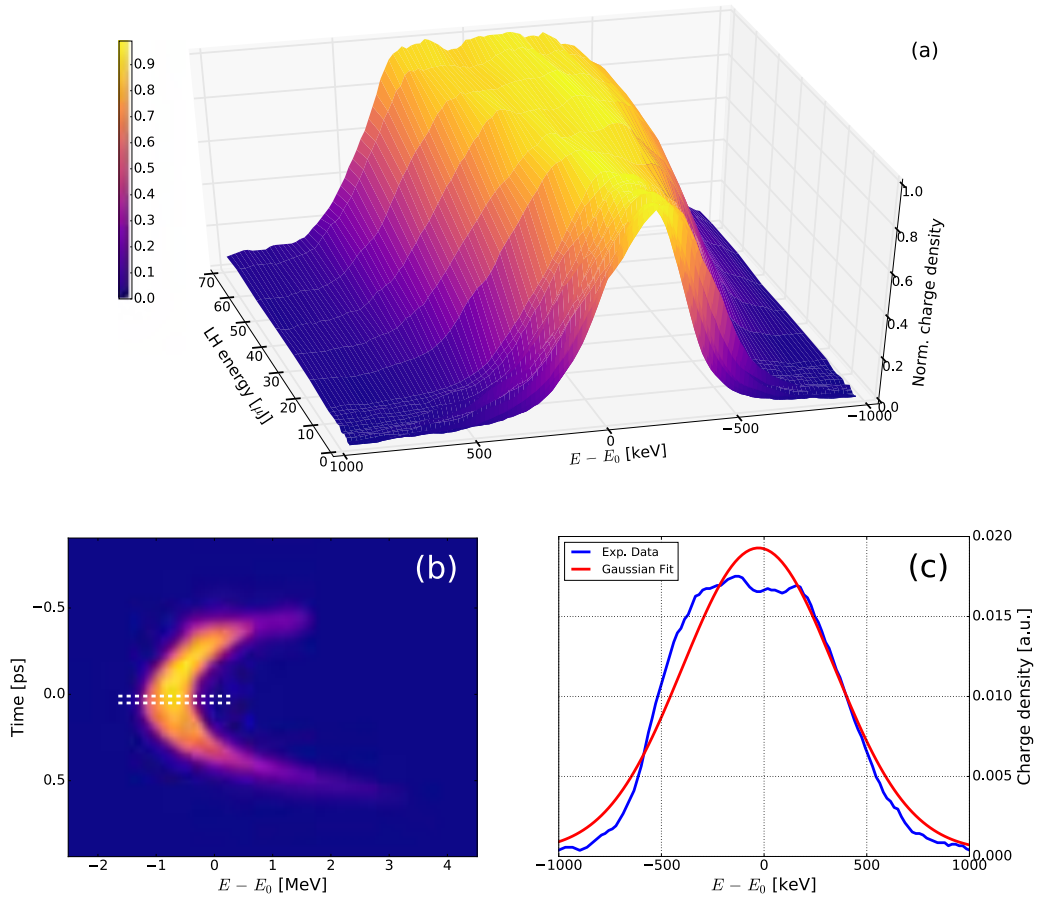


Figure 4.11: (a) Measured slice energy spectrum of the e -beam in the diagnostic station at the LINAC end as a function of the LH laser pulse energy. (b) Electron beam LPS reconstruction for an LH laser pulse energy of $42 \mu\text{J}$. (c) Projected energy distribution of a central slice (dashed region in (b)) together with a Gaussian fit with the same second moment and integral area. Image reproduced from [26].

a fasted drop in the tails. The different shape of the energy distribution in between small and large heating is only due to the limited resolution of the measurement setup, estimated to be ~ 70 keV: if the (RMS) energy spread is lower than the resolution, the measured energy distribution is the convolution with a Gaussian curve. In fact, both theory [4] and numerical simulations (see Figure 4.12) predict that the shape of the energy distribution is independent on the LH laser power and only dependent on the ratio in between the laser and the electron beam transverse sizes.

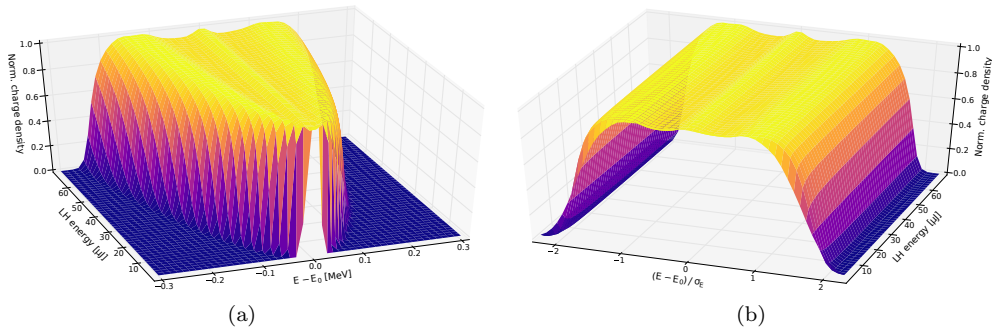


Figure 4.12: (a) Simulated slice energy spectrum just after LH, as a function of the LH laser power. (b) Same, but all the slices are normalized to have the same (RMS) width. The shape of the energy distribution at LH output is independent of the laser power. Simulations performed using GENESIS1.3 numerical code [32].

In the following, we will focus on the dependence of FEL output on the laser heating. As previously demonstrated at LCLS [5], a very small heating is enough to suppress microbunching instability growth resulting in a significant improvement in FEL performance at FERMI [33].

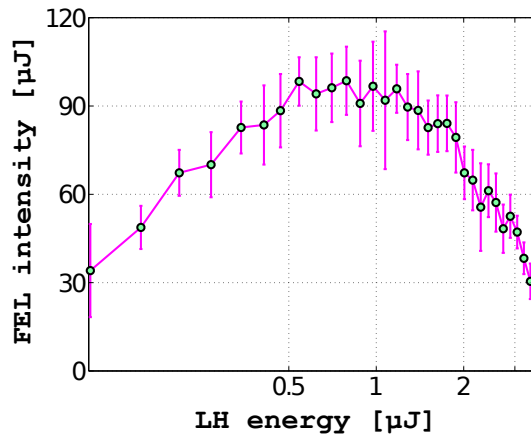


Figure 4.13: FEL output energy per pulse at $\lambda = 32.5$ nm ($m = 8$). The results show that optimized laser heating nearly triples the FEL output relative to no heating. Image reproduced from [26].

Figure 4.13 shows the FEL output pulse energy at 32.5 nm wavelength as a function of the LH laser energy per pulse. It is readily observable a threefold enhancement between optimal LH power (0.6 μ J) and LH off case. The small amount of LH heating is suppressing μ BI growth and minimizes the effective energy spread of the beam entering the undulator.

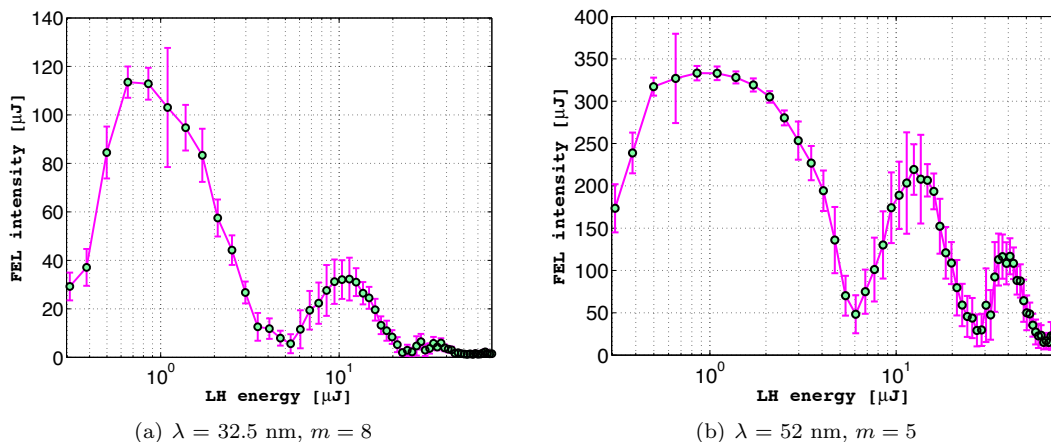


Figure 4.14: FEL output energy per pulse at (a) $\lambda = 32.5 \text{ nm}$ ($m = 8$) and (b) $\lambda = 52 \text{ nm}$ ($m = 5$) as a function of LH laser energy over a larger energy range than Figure 4.13. The results show that the FEL pulse energy oscillates for larger values of LH energy.

If instead the LH energy is increased beyond the optimum, up to $3 \mu\text{J}$, the FEL output drops back to the LH-off level. This is understood to be due to the increased energy spread of the beam which is suppressing μBI , as well as dumping the FEL gain.

Surprisingly if one only considers predictions from Eq. (4.9), when the LH heating is further increased an interesting FEL behaviour begins to occur as the output pulse energy increases again, showing a series of slowly damped oscillations (see Fig. 4.14). The heating levels at which the oscillations are happening are expected to be correlated to a strongly suppressed FEL output due to the increased energy spread which should inhibit the FEL gain if Eq. (4.9) is applied directly.

In order to compare the experimental results with theoretical predictions, the FEL was operated with only three radiators in resonance to the desired harmonic (of the six available undulators). In the 3-radiator configuration, cfr. Fig. 4.15, the FEL gain is small (note the reduced output pulse energy with respect to Figure 4.14) and the output pulse energy is (almost) proportional to the square of the bunching factor. This should allow a meaningful comparison between the data and Eqs. (4.9) and (4.10). The results are reported in Fig. 4.15. The measured FEL output energy at $\lambda = 32.5 \text{ nm}$ ($m = 8$) as a function of the LH laser pulse energy is shown, together with the theoretical predictions of Eqs. (4.9) and (4.10). The evaluation was performed based on the laser and electron beam parameters of Table 4.2. One can observe that the location of the maxima and minima, as well as the amplitude of the measured oscillations are in excellent agreement with the predictions of Eq. (4.10) (filled line in Fig. 4.15), which corresponds to a non-Gaussian energy spread distribution as the one observed at the LINAC end. Note that the drop in FEL power happening at low LH pulse energy is due to the unsuppressed μBI , which is not considered in either Eqs. (4.9) or (4.10).

The dependence of the secondary maxima has been investigated as a function of some of the parameters of Eq. (4.10), namely the harmonic number (see Figure 4.16(a)), the seed power and the dispersion (see Figure 4.16(b)).

The control of the energy spread shape, in our case via the manipulation of the LH properties, offers an exciting possibility to extend the tuning range of a single stage HGHG FEL down to wavelengths associated with very high harmonics, e.g., for a 260-nm seed laser,

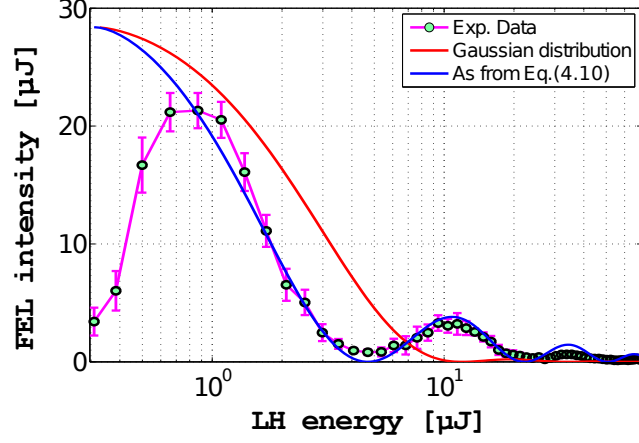


Figure 4.15: Comparison between experimental data (dots) ($\lambda = 32.5$ nm, $m = 8$) and theoretical predictions of the FEL intensity as a function of the LH pulse energy. In order to reduce the FEL gain and being able to directly apply Eq. (4.9) and (4.10), only three radiators were used. This condition corresponds to an FEL pulse energy which is almost proportional to the square of the bunching b_m^2 . The dashed curve shows the standard prediction of Eq. (4.9) for b_m^2 that assumes a Gaussian energy spread at undulator entrance. The filled curve represents the prediction of Eq. (4.10) for b_m^2 and includes non-Gaussian LH heating effects. Image reproduced from [26].

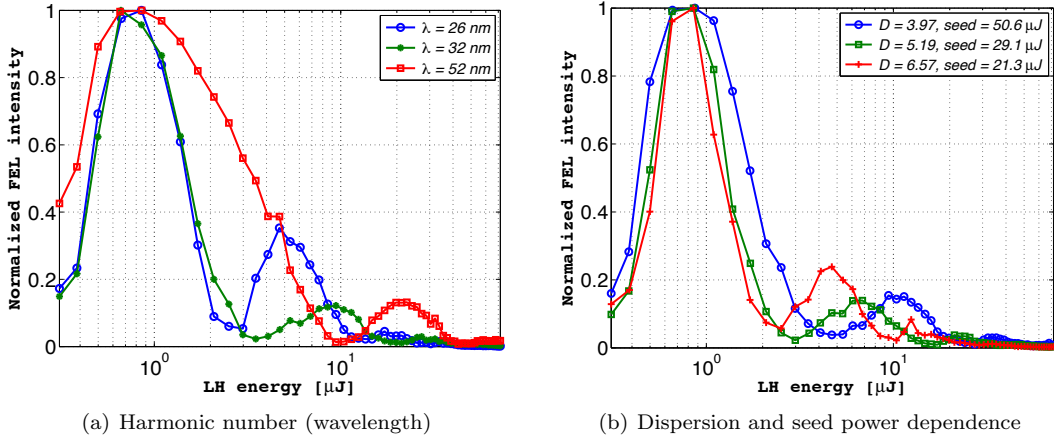


Figure 4.16: Dependence of the modulation effect on the harmonic number (a) and seed power/dispersion (b). The data have been normalized to maxima for easier comparison.

harmonics $m \geq 25$ and wavelengths smaller than 10 nm [26]. The mentioned wavelengths had been thought to be out of reach for a single stage HGHG based device like FERMI FEL-1 if the electron beam energy had a Gaussian distribution with $\sigma_\gamma \sim 150$ keV. To further demonstrate this possibility a series of numerical FEL simulations have been performed, using the GINGER code [34]. The simulations were performed considering FEL-1 parameters and e-beams with both Gaussian and LH induced energy distributions. In each case for fair comparison the (RMS) of the distribution was the same, corresponding to an energy spread $\sigma_\gamma = 150$ keV. This value corresponds to the measured one for the LH settings that maximizes the FEL power (LH $\simeq 1 \mu\text{J}$).

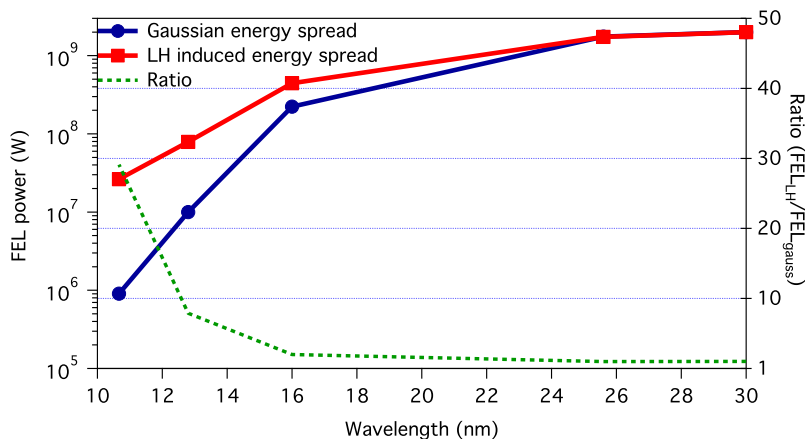


Figure 4.17: Simulation of HGHG emitted power as a function of the harmonic number, in the case of a Gaussian slice energy spread distribution (dots) and the measured distribution induced by LH (squares). Both distribution have the same (RMS) σ_γ and for each point, the FEL was optimized in terms of the seed laser power and dispersion. The intensity ratio is also reported (dashed line). Simulations performed using GINGER numerical code. Image reproduced from [26].

The results of the simulations are reported in Fig. 4.17. Up to $\lambda = 26$ nm ($m = 10$) there seems not to be a significant difference for the emitted FEL power on the two electron energy distributions. Instead, as expected from Eq. (4.10) at shorter wavelengths the non-Gaussian distribution is capable of much higher output powers. At $\lambda = 10$ nm ($m = 26$) the ratio between the two cases is more than a factor 30. The predicted FEL power for the Gaussian energy distribution is less than 1 MW, while it raises to about 30 MW if the LH-induced energy spread distribution is considered. In our understanding, similar bunching level can be achieved in both cases, but if one considers the non-Gaussian energy spread the required seed laser power is lower. The lower seed laser induces a reduced energy spread to the electron beam with respect to the Gaussian case, thus enhancing the FEL gain [35] and increasing the final FEL power emitted in the radiator.

This is a tantalizing result as it suggests that it would be possible to cover a much larger tuning range with a single stage HGHG configuration than what was initially predicted by controlling (or even manipulating) details of the energy spread distribution induced by the laser heater. This would allow to reach much shorter wavelengths without the need of more complicated seeding schemes such as echo-enabled harmonic generation or a two-stage HGHG [36, 37]. The mentioned situation might be already the case at FERMI FEL-1 where, despite a lower wavelength limit of 20 nm experiments has been successfully carried out at 10 nm and shorter wavelengths [38]. The experiment inspired also a simulation study by

the SD-UV FEL group on the impact of the energy distribution shape for different seeding schemes [39].

4.4 LH Beating

In the previous section the possibility of transporting the energy distribution generated at LH down to the LINAC end was demonstrated. A natural extension is to look at the conjugate variable of the energy that is the time. An additional modulation induced by the LH may be sustained and amplified by the μ BI along the LINAC up to the entrance of the undulators and could be controlled. Such a modulation was in fact observed for the first time at FERMI FEL-1. The process strongly resembles two-frequency mixing schemes [36, 40], with the key difference that it is introduced at a very low energy along the LINAC. The strategy requires a pulse shaping of the LH laser and can be easily turned on and off for transparent FEL operations.

The experiment was done using a 1.3 GeV, 700 pC beam, in single compression ($C \sim 10$) and final peak current of ~ 650 A. The electron beam was modulated at the LH via the interaction with a modulated laser pulse at a wavelength λ_B , longer than the LH laser wavelength λ_{LH} . Note that the mentioned modulation is happening *before* the electron bunch is compressed in the bunch compressor. The LH laser envelope induces an energy spread modulation in the electron beam [41].

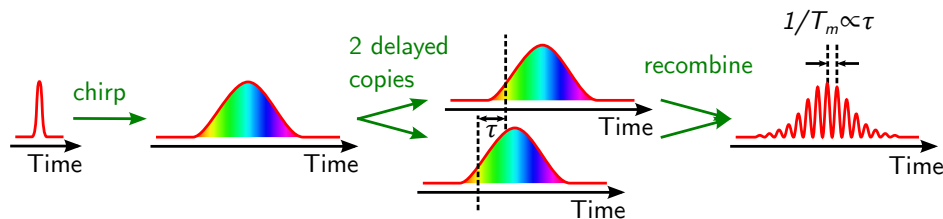


Figure 4.18: Schematic description of the chirped pulse beating technique used to produce a modulated LH laser pulse. Image courtesy of E. Roussel.

The modulated laser pulse is obtained via the chirped pulse beating technique [42], schematically represented in Figure 4.18. The technique is based on the interference between two copies of the same chirped laser pulses which are delayed in time between each other. The resulting pulse envelope is characterized by a quasi-sinusoidal modulation with a frequency proportional to the delay τ in between the two pulses.

The electric field for a laser pulse carrying a linear frequency chirp is:

$$E(t) = A(t) \exp[i(\omega_0 t + \pi a t^2)] \quad (4.11)$$

and therefore, the intensity of the modulated pulse can be expressed as:

$$\begin{aligned} I(t, \tau) &= |E(t) + E(t + \tau)|^2 \\ &= A(t)^2 + A(t + \tau)^2 + 2A(t)A(t + \tau) \cos(\omega_0 \tau + 2\pi a \tau t + \pi a \tau^2), \end{aligned} \quad (4.12)$$

where $A(t)$ is the Gaussian envelope of the pulse, ω_0 is the optical carrier frequency and $a = -c\Delta\lambda/(\lambda_0^2\Delta\sigma)$ is the linear chirp coefficient with $\Delta\lambda$ the spectrum bandwidth, λ_0 the central wavelength of the spectrum and $\Delta\sigma$ the difference between the stretched and the Fourier limited pulse duration. The induced beating frequency is $a\tau$.

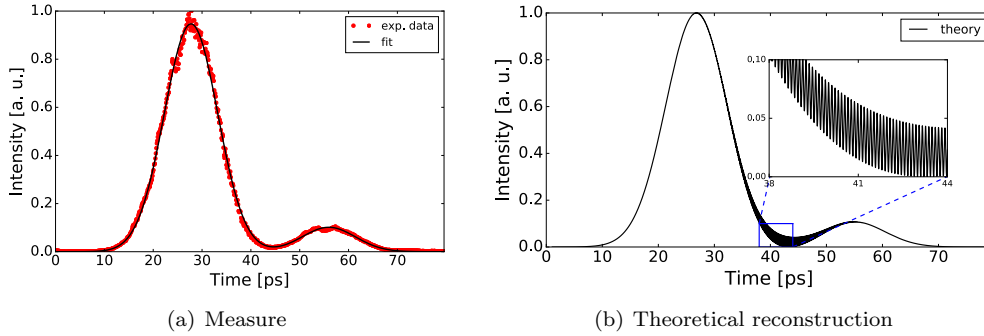


Figure 4.19: Measured (top) and theoretical reconstruction (bottom) of the LH laser pulse according to the chirped pulse beating. According to the intensity ratio of the two interacting pulses, a significant modulation is only present in between the two pulses (delay of 30 to 45 ps).

In the experiment the intensity ratio of the two laser pulses used for the chirped pulse beating generation was 1 to 10 and time delay (fixed) was 28.2 ps (Fig. 4.19). The linear chirp coefficient has been measured to be $a = -3.26 \times 10^{23} \text{ s}^{-2}$, which leads to a resulting envelope LH pulse with a beating frequency of 9.2 THz, or conversely a modulation wavelength of $\lambda_B = 32.6 \text{ }\mu\text{m}$, see Figure 4.19.

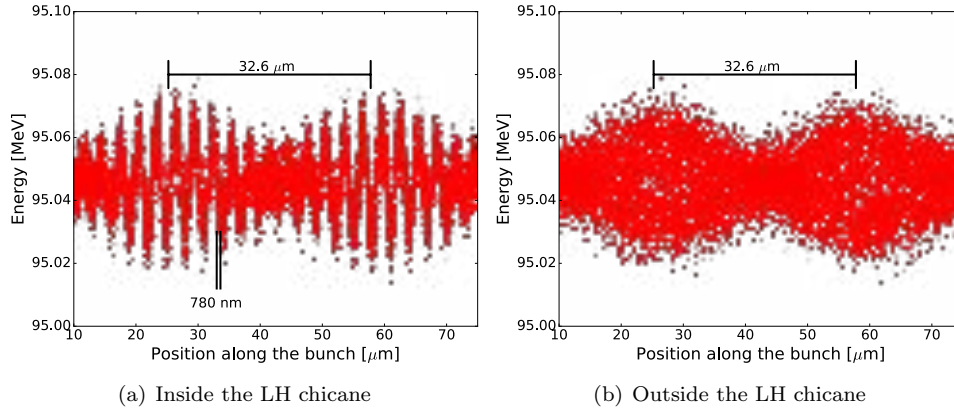


Figure 4.20: A simulated small slice in the LPS (longitudinal coordinate vs. energy) of the electron beam inside the LH chicane (a) and just after the LH chicane (b). While inside the chicane both the optical carrier wavelength (780 nm) and the beating wavelength (32.6 μm) are clearly visible, after the chicane only the beating wavelength is still present. The optical wavelength is instead smeared out by the chicane itself as expected by LH theory.

In Figure 4.20 a simulation of a small portion of the LPS of the electron beam is reported, just after the LH interaction (4.20(a)) and at the exit of the LH chicane (4.20(b)). While inside the chicane modulations at the optical carrier wavelength (780 nm) and the beating wavelength (32.6 μm) are clearly visible, after the chicane only the beating wavelength is still present, as an energy spread modulation. This is due to the smearing condition of the chicane, which is described by Eq. (4.4). For the FERMI LH parameters, $\lambda_c = 4 \text{ }\mu\text{m}$, and therefore the “conventional” LH laser modulation (780 nm) is smeared out, while the

modulation at the beating wavelength ($32.6 \mu\text{m}$) is unaffected and can still be present in the beam after the chicane.

Furthermore, due to the above mentioned intensity ratio, a significant modulation in the laser intensity is only present in between the two laser pulses. By changing a remotely controlled delay line along the laser path, one can switch between conventional LH operations (LH delay line in the 50 to 60 ps range, see also Fig. 4.21(d)) and beating experiment (LH delay line in the 30 to 45 ps range, see also Fig. 4.21(a)).

The electron energy distribution was measured in the diagnostic electron spectrometer just after the compression chicane. The electron energy measurements highlight the presence of a coherent modulation in the electron beam (Fig. 4.21(b,c)) when the electron beam overlaps the laser beating region. When instead the electron beam is in the normal LH operation mode, no energy modulation is present in the electron beam spectrum (Fig. 4.21(e,f)).

The linear energy chirp of the electron beam h , used for achieve magnetic bunch compression, is a known and controllable parameter which can be expressed, in the linear approximation, as:

$$h = \frac{1}{E} \frac{dE}{dz} = \frac{E_{L1} k_{RF} \cos \phi}{E_i + eV \sin \phi}, \quad (4.13)$$

where ϕ the RF phase of the LINAC that induces the chirp, k_{RF} the RF wavenumber, E_i the beam energy at the entrance of the accelerating structures that induce the chirp and E_{L1} the energy gain in such structures. In this experiment, the LINAC is adjusted for a linear chirp $h = -20.2 \text{ m}^{-1}$ (see caption in Fig. 4.21 for parameters).

As already mentioned before (see Appendix A), when an electron beam passes through a spectrometer the energy is mapped in the horizontal coordinate of the spectrometer screen. If the beam has a significant linear energy chirp, i.e., there is a linear correlation between energy and time, it is possible to access to the longitudinal properties of the beam itself. In fact, when such a beam passes through an energy spectrometer its longitudinal coordinate, due to the correlation, is mapped to the horizontal coordinate on the spectrometer screen.

By measuring the energy modulation period ΔE and the linear energy chirp h it is then possible to reconstruct the longitudinal modulation wavelength Δz according to $\Delta z = |\Delta E / (E * h)|$. Using the experimental measured energy modulation period of 0.18 MeV and the parameters reported in the caption of Fig. 4.21, it was possible to compute the corresponding spatial modulation which resulted to be $32.4 \mu\text{m}$. The value is in good agreement with the calculated LH beating wavelength λ_B .

As seen in the previous sections, the LH interaction changes the value of the (RMS) energy spread of the beam so, when a modulated laser is used the electron beam will exhibit a modulation in the beam energy spread at the same scale of the laser beating (see Figure 4.20). This means that, at the exit of the LH, the modulation on the electron beam is mainly in energy spread one at the beating wavelength. Such a modulation can be amplified and converted into a density one via the μBI gain process described before in the downstream LINAC.

It is possible to verify if this gain mechanism is taking place. To do so the compression factor has been increased keeping a constant energy chirp in the electron beam, while measuring the growth of the modulation amplitude in the beam energy spectrum (see Fig. 4.22(a)). Associate with μBI is the COTR that the electron beam produces on intercepting surfaces. This can be used to show the presence of density modulation at a downstream diagnostic screen. Figure 4.22(b) shows the COTR signal in the infrared spectral region as a function of the LH laser energy. The measurement has been performed in a diagnostic station located after the FEL undulators. In the normal use of the LH, i.e. without any frequency beating, as already seen in the previous section the COTR emission is suppressed as the heating level

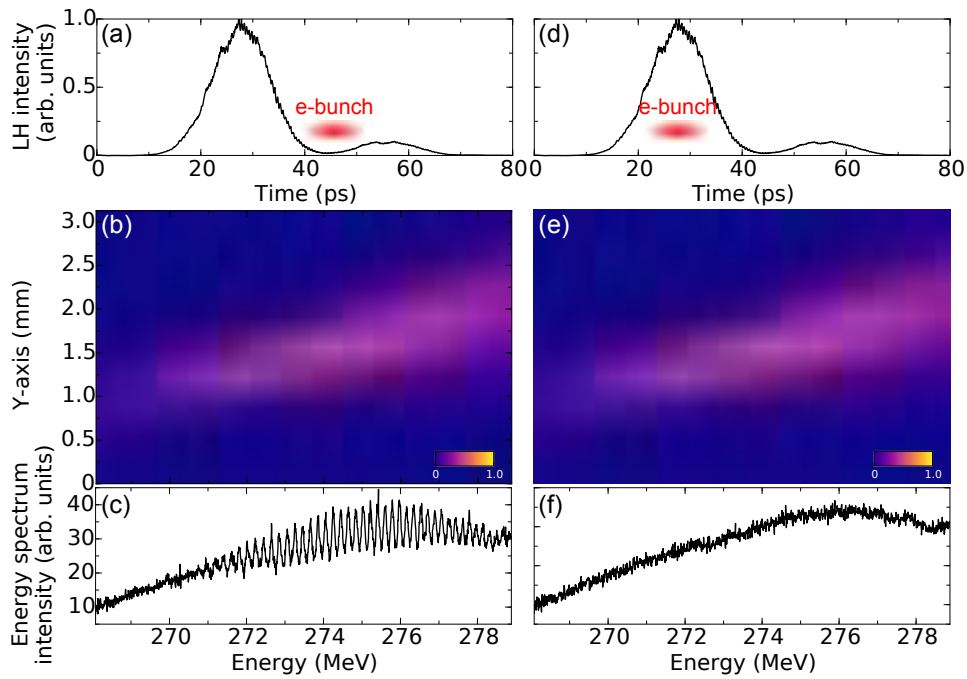


Figure 4.21: Electron beam energy spectra in the spectrometer after the bunch compressor chicane in case of energy spread modulation (a, b, c) and uniform heating (d, e, f). (a, d) Measured laser heater pulse shape and sketched overlap position with the electron bunch. (b, e) Spectrometer images (energy on the horizontal axis) (c, f) Electron beam energy spectra. When the electron bunch is overlapped to the beating region of the laser heater, a strong modulation in the energy spectrum is visible in (c). The parameters of the LINAC are: $\phi = 117\text{deg}$, $k_{RF} = 2\pi/0.1$, $E_i = 98\text{ MeV}$ and $E_{L1} = 188\text{ MeV}$. Image reproduced from [43].

increases (black line in Fig. 4.22(b)). Conversely, in the case of an induced energy spread modulation, a strong increase of the COTR signal is observed as the amount of heating energy increases (red line in Fig. 4.22(b)). This is a clear evidence of the presence of a density modulation in the beam. The COTR signal has been measured in the infrared domain and not in the visible range, according to the expected modulation wavelength induced by the LH beating. This also demonstrated that the modulation can be transported up to the FEL and can be further be used to control the FEL emission process.

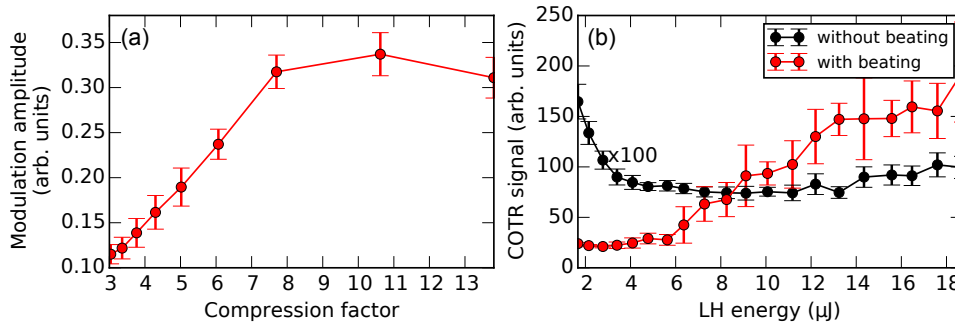


Figure 4.22: Amplitude of the modulation as a function of the compression factor applied in the magnetic chicane. (b) COTR signal at the end of the FEL-1 undulators versus the laser heater intensity in case of an energy spread modulation (red) and a uniform heating (black). The COTR signal in case of uniform heating is multiplied by a factor 100. The COTR signal is acquired using a Germanium photodiode only sensitive in the 800 - 1800 nm wavelength range. Image reproduced from [43].

As already demonstrated above, the LH is capable of suppressing the μ BI gain and to significantly increase the FEL performance with $\sim 1 \mu$ J pulse energy with a uniform longitudinal heating. In this condition the “usual” seeded FEL emission exhibits a significant shot-to-shot stability ($\sim 20\%$) with typical pulse energy of $\sim 50 \mu$ J at 27.35 nm (9th harmonic of the seed laser). The spectrum is characterized by the presence of the expected seeded single line with a (RMS) relative bandwidth of 0.69×10^{-3} and (RMS) central wavelength stability of 0.71×10^{-3} (Fig. 4.23(a), black line). Instead, in the presence of the frequency beating in the LH pulse, the FEL emission is not monochromatic anymore because when a pre-modulated beam interacts with the seed laser it leads to the emission of multi-color FEL pulses (Fig. 4.23(a), red line). Indeed, after the dispersive section the electron beam will exhibit significant bunching at wavenumber

$$k = nCk_B + mk_S, \quad (4.14)$$

where n and m are positive or negative integers, k_S is the seed laser wavenumber, k_B is the LH beating wavenumber and C the compression factor. Notice that Ck_B corresponds to the final wavenumber of the modulation at the entrance of the modulator. In Fig. 4.23(a, red line) indeed the FEL emission is composed of three colors: $k_{n=0,m=9} = 9k_S$ (i.e. 27.35 nm), $k_{n=1,m=9} = 9k_S + Ck_B$ (i.e. 27.22 nm) and $k_{n=-1,m=9} = 9k_S - Ck_B$ (i.e. 27.5 nm) with a total intensity ($\sim 25 \mu$ J) almost equally distributed among the three spectral lines. While a significant amount of bunching can be present at all wavenumbers of Eq. (4.14), only the ones that are inside the FEL amplification bandwidth can effectively undergo the FEL process and lase. In the case reported in Fig. 4.23(a) only the three visible lines satisfy the bandwidth requirements, hence the FEL emission is a three color one. By properly choosing the radiator resonance, i.e. the undulator parameter K , one can adapt the FEL

amplification properties and select the frequency components to be amplified, i.e., change m and n of Eq. (4.14) (Fig. 4.23(b)).

More interestingly, the spectral properties of each color in terms of bandwidth and the central wavelength stability are preserved with respect to the single line case of Fig. 4.23(a, black line).

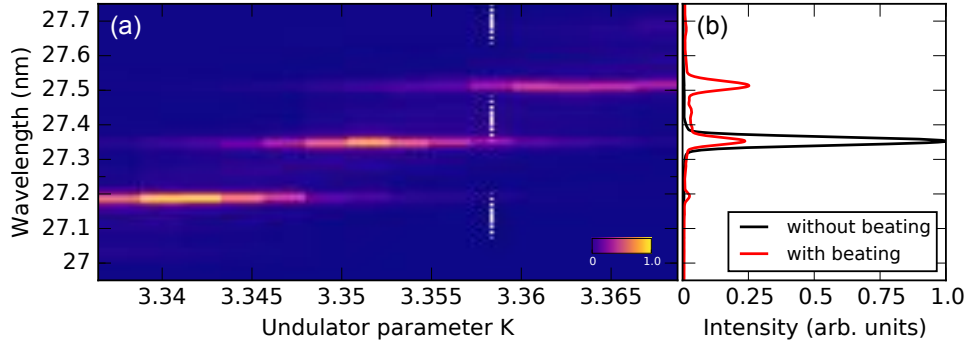


Figure 4.23: False color (a) FEL spectra in case of a uniform heating (black line) and in case of the beating (red line). Shown spectra are average over 20 shots. (b) FEL emission spectra versus radiator resonance in case of an energy spread modulation. Image reproduced from [43].

Eq. (4.14) also states that it is also possible to tune the final wavelength of the FEL lines with $m \neq 0$ by acting either on the compression factor C or on the LH beating wavenumber k_B . In Figure 4.24 the shift of the modulation-induced peaks is reported as the compression factor is increased. It is worth noticing that, since the LH modulation is induced prior of compression, the final FEL output wavelength can be tuned changing the compression factor. Such a possibility can be very useful for future FEL operations since it can provide a tunable seeded FEL without the need of a complex tunable seed laser [44].

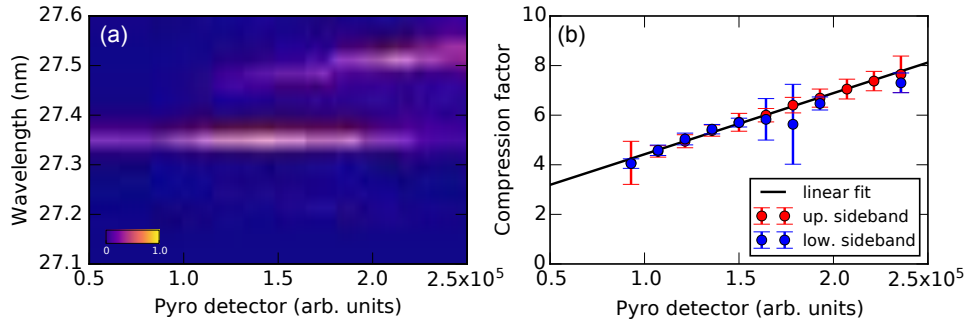


Figure 4.24: FEL spectrum versus compression factor. The false color scale (a) corresponds to the spectral intensity of the two spectral components. (b) Central wavelengths of the two spectral components. As the compression factor is changed the wavelength of the sideband is shifted. The pyro detector signal (horizontal axis) is proportional to the compression factor. Image reproduced from [43].

Differently with other methods used to produce multi-color FEL pulses [45–53], with the presented scheme the two wavelengths are temporally superposed as they are the result of a coherent modulation of the FEL field phase. This opens the possibility of new kind of experiments where the FEL radiation phase is controlled over a temporal scale of tens of

femtosecond. From the accelerator physics point of view, the technique allows the possibility of study the μ BI gain by selectively excite a particular modulation wavelength without the need of inducing a modulation at the injector. It can be also used to generate narrow band tunable THz radiation at the TeraFERMI beamline [54], similarly as proposed in [55] or mode-locked SASE radiation, similarly as proposed in [56].

4.5 Conclusions

The LH is a device capable of suppressing the μ BI gain by inducing a controllable increase in the energy spread of the electron beam. However the increase in the energy spread still represents a decrease in the e-beam brightness, so the possibility of reversely induce it is a very attractive one. The LH has been shown to be beneficial for the FEL performance in both LCLS and FERMI and almost all future FEL projects foresee the presence of such a device.

The measurements performed at FERMI are in excellent agreement with analytic predictions, as well as with numerical simulations. Optimal heating level are in the range 7-10 keV, depending on details of the e-beam as well as the compression scheme applied.

While the LH was thought to be device that “simply” increases the electron beam energy spread, it was shown to be a source of extremely interesting, rich and surprising physics. The Non-Gaussian energy spread distribution and the LH beating represent two examples of the usage of the device beyond its initial scope, in particular for a seeded FEL.

References

- [1] S. Di Mitri and M. Cornacchia. “Electron beam brightness in linac drivers for free-electron-lasers”. In: *Physics Reports* 539.1 (2014). Electron beam brightness in linac drivers for free-electron-lasers, pp. 1–48. ISSN: 0370-1573. DOI: [10.1016/j.physrep.2014.01.005](https://doi.org/10.1016/j.physrep.2014.01.005).
- [2] E.L. Saldin, E.A. Schneidmiller, and M.V. Yurkov. In: *Nucl. Instrum. Methods Phys. Res., Sect. A* 490 (2002), p. 1.
- [3] T. Shaftan and Z. Huang. “Experimental characterization of a space charge induced modulation in high-brightness electron beam”. In: *Phys. Rev. ST Accel. Beams* 7 (8 2004), p. 080702. DOI: [10.1103/PhysRevSTAB.7.080702](https://doi.org/10.1103/PhysRevSTAB.7.080702).
- [4] Z. Huang et al. “Suppression of microbunching instability in the linac coherent light source”. In: *Phys. Rev. ST Accel. Beams* 7 (7 2004), p. 074401. DOI: [10.1103/PhysRevSTAB.7.074401](https://doi.org/10.1103/PhysRevSTAB.7.074401).
- [5] Z. Huang et al. “Measurements of the linac coherent light source laser heater and its impact on the x-ray free-electron laser performance”. In: *Phys. Rev. ST Accel. Beams* 13 (2 2010), p. 020703. DOI: [10.1103/PhysRevSTAB.13.020703](https://doi.org/10.1103/PhysRevSTAB.13.020703).
- [6] M. Venturini. “Microbunching instability in single-pass systems using a direct two-dimensional Vlasov solver”. In: *Phys. Rev. ST Accel. Beams* 10 (10 2007), p. 104401. DOI: [10.1103/PhysRevSTAB.10.104401](https://doi.org/10.1103/PhysRevSTAB.10.104401).
- [7] E.L. Saldin, E.A. Schneidmiller, and M.V. Yurkov. In: *Nucl. Instrum. Methods Phys. Res., Sect. A* 528 (2004), p. 355.
- [8] M. Cornacchia et al. *FERMI@Elettra Accelerator Technical Optimization Final Report*. Tech. rep. ST/F-TN-06/15 and LBNL-60958. Elettra - Sincrotrone Trieste, 2006.

- [9] S. Heifets, G. Stupakov, and S. Krinsky. “Coherent synchrotron radiation instability in a bunch compressor”. In: *Phys. Rev. ST Accel. Beams* 5 (6 2002), p. 064401. DOI: [10.1103/PhysRevSTAB.5.064401](https://doi.org/10.1103/PhysRevSTAB.5.064401).
- [10] S. Di Mitri and M. Cornacchia. In: *Nucl. Instrum. Methods Phys. Res., Sect. A* 735 (2014), pp. 60–65.
- [11] L. Brown. Tech. rep. SLAC Report 75. SLAC, 1982.
- [12] H. Wiedemann. *Particle Accelerator Physics*. New York: Springer, 2007.
- [13] S. Di Mitri et al. “Suppression of microbunching instability with magnetic bunch length compression in a linac-based free electron laser”. In: *Phys. Rev. ST Accel. Beams* 13 (1 2010), p. 010702. DOI: [10.1103/PhysRevSTAB.13.010702](https://doi.org/10.1103/PhysRevSTAB.13.010702).
- [14] S. Spampinati et al. “Laser heater commissioning at an externally seeded free-electron laser”. In: *Phys. Rev. ST Accel. Beams* 17 (12 2014), p. 120705. DOI: [10.1103/PhysRevSTAB.17.120705](https://doi.org/10.1103/PhysRevSTAB.17.120705).
- [15] C. Behrens, Z. Huang, and D. Xiang. “Reversible electron beam heating for suppression of microbunching instabilities at free-electron lasers”. In: *Phys. Rev. ST Accel. Beams* 15 (2 2012), p. 022802. DOI: [10.1103/PhysRevSTAB.15.022802](https://doi.org/10.1103/PhysRevSTAB.15.022802).
- [16] S. Li et al. “Laser Heater Transverse Shaping to Improve Microbunching Suppression for X-ray FELs”. In: *Proceedings of the 2015 FEL Conference*. WEP005. Daejeon, South Korea, 2015.
- [17] C. J. et al. Bocchetta. *FERMI@Elettra FEL Conceptual Design Report*. Sincrotrone Trieste, 2007.
- [18] S. Spampinati, S. Di Mitri, and B. Diviacco. In: *Proceedings of the 29th Free Electron Laser Conference*. WEPPH015. Novosibirsk, Russia, 2007.
- [19] M.B. Danailov. “FEL seeding at FERMI: a root to table-top laser-like FEL performance”. In: *Proc. of SPIE 2015, Optics+Optoelectronics*. 9589-14. 2015.
- [20] G. Penco et al. “Optimization of a high brightness photoinjector for a seeded FEL facility”. In: *Journal of Instrumentation* 8.05 (2013), P05015.
- [21] V.L. Ginzburg and V.N. Tsytovich. *Transition radiation and Transition Scattering*. Adam Hilger, Bristol, UK, 1990.
- [22] D. W. Rule and R. B. Fiorito. In: *AIP Conf. Proc.* Vol. 229. 1991, p. 315.
- [23] H. Loos et al. In: *Proceedings of the 30th International Free Electron Laser Conference*. THBAUP01. Geongju, South Korea, 2008.
- [24] J. Rossbach and P. Schmüser. “Basic course on accelerator optics”. In: *Proc. of general accelerator physics school of CERN 1992*. Vol. 1. CERN, Geneva. 1994, p. 17.
- [25] A. Bambini, A. Renieri, and S. Stenholm. “Classical theory of the free-electron laser in a moving frame”. In: *Phys. Rev. A* 19 (5 1979), pp. 2013–2025. DOI: [10.1103/PhysRevA.19.2013](https://doi.org/10.1103/PhysRevA.19.2013).
- [26] E. Ferrari et al. “Impact of Non-Gaussian Electron Energy Heating upon the Performance of a Seeded Free-Electron Laser”. In: *Phys. Rev. Lett.* 112 (11 2014), p. 114802. DOI: [10.1103/PhysRevLett.112.114802](https://doi.org/10.1103/PhysRevLett.112.114802).
- [27] L. H. Yu. “Generation of intense UV radiation by subharmonically seeded single pass free electron lasers”. In: *Phys. Rev. A* 44.5178 (1991).

-
- [28] E. Allaria et al. “Highly coherent and stable pulses from the FERMI seeded free-electron laser in the extreme ultraviolet”. In: *Nature Photonics* 6.10 (2012), pp. 699–704. DOI: [10.1038/nphoton.2012.233](https://doi.org/10.1038/nphoton.2012.233).
- [29] L.-H. Yu M. Babzien I. Ben-Zvi L.F. DiMauro A. Doyuran W. Graves E. Johnson S. Krinsky R. Malone I. Pogorelsky J. Skaritka G. Rakowsky L. Solomon X.J. Wang M. Woodle V. Yakimenko S.G. Biedron J.N. Galayda E. Gluskin J. Jagger V. Sajaev I. Vasserman. “High-gain harmonic-generation free-electron laser”. In: *Science* 289.5481 (2000), pp. 932–934.
- [30] B. Liu et al. “Demonstration of a widely-tunable and fully-coherent high-gain harmonic-generation free-electron laser”. In: *Phys. Rev. ST Accel. Beams* 16 (2 2013), p. 020704. DOI: [10.1103/PhysRevSTAB.16.020704](https://doi.org/10.1103/PhysRevSTAB.16.020704).
- [31] R. Bonifacio F. Casagrande G. Cerchioni L. De Salvo Souza P. Pierini N. Piovella. “Physics of the high-gain FEL and superradiance”. In: *Riv. Nuovo Cimento* 13.9 (1990).
- [32] S. Reiche. “GENESIS 1.3: a fully 3D time-dependent FEL simulation code”. In: *Nucl. Instr. and Meth. A* 429 (1999). <http://pbpl.physics.ucla.edu/~reiche/>, pp. 243–248.
- [33] S. Spampinati et al. In: *Proceedings of the 34th International Free-Electron Laser Conference*. MOPD58. Nara, Japan, 2012.
- [34] W. M. Fawley. Tech. rep. LBNL-49625-Rev.1, Report No. LCLS-TN-04-3. LBNL, SLAC, 2004.
- [35] M. Xie. “Exact and variational solutions of 3D eigenmodes in high gain {FELs}”. In: *Nuclear Instruments and Methods in Physics Research Section A: Accelerators, Spectrometers, Detectors and Associated Equipment* 445.1–3 (2000), pp. 59–66. ISSN: 0168-9002. DOI: [10.1016/S0168-9002\(00\)00114-5](https://doi.org/10.1016/S0168-9002(00)00114-5).
- [36] G. Stupakov. “Using the Beam-Echo Effect for Generation of Short-Wavelength Radiation”. In: *Phys. Rev. Lett.* 102 (7 2009), p. 074801. DOI: [10.1103/PhysRevLett.102.074801](https://doi.org/10.1103/PhysRevLett.102.074801).
- [37] I. Ben-Zvi, K. M. Yang, and L. H. Yu. In: *Nucl. Instrum. Methods Phys. Res. A* 318 (1992), p. 726.
- [38] L. Giannessi et al. In: *Proceedings of the 34th International Free-Electron Laser Conference*. MOOB06. Nara, Japan, 2012.
- [39] G. Wang et al. “Beam energy distribution influences on density modulation efficiency in seeded free-electron lasers”. In: *Phys. Rev. ST Accel. Beams* 18 (6 2015), p. 060701. DOI: [10.1103/PhysRevSTAB.18.060701](https://doi.org/10.1103/PhysRevSTAB.18.060701).
- [40] C. Evain et al. “Frequency mixing in accelerator based sources and application to tunable seeded free-electron lasers”. In: *Phys. Rev. ST Accel. Beams* 17 (12 2014), p. 120706. DOI: [10.1103/PhysRevSTAB.17.120706](https://doi.org/10.1103/PhysRevSTAB.17.120706).
- [41] S. Bielawski et al. “Tunable narrowband terahertz emission from mastered laser-electron beam interaction”. In: *Nat Phys* 4.5 (May 2008), pp. 390–393. DOI: [10.1038/nphys916](https://doi.org/10.1038/nphys916).
- [42] A. S. Weling and D. H. Auston. “Novel sources and detectors for coherent tunable narrow-band terahertz radiation in free space”. In: *J. Opt. Soc. Am. B* 13.12 (1996), pp. 2783–2792. DOI: [10.1364/JOSAB.13.002783](https://doi.org/10.1364/JOSAB.13.002783).

- [43] E. Roussel et al. “Multicolor High-Gain Free-Electron Laser Driven by Seeded Microbunching Instability”. In: *Phys. Rev. Lett.* 115 (21 2015), p. 214801. DOI: [10.1103/PhysRevLett.115.214801](https://doi.org/10.1103/PhysRevLett.115.214801).
- [44] E. Allaria et al. “Tunability experiments at the FERMI@Elettra free-electron laser”. In: *New Journal of Physics* 14.11 (2012), p. 113009.
- [45] T. E. Glover et al. “X-ray and optical wave mixing”. In: *Nature* 488.7413 (Aug. 2012), pp. 603–608. DOI: [10.1038/nature11340](https://doi.org/10.1038/nature11340).
- [46] E. Shwartz and S. Shwartz. “Difference-frequency generation of optical radiation from two-color x-ray pulses”. In: *Opt. Express* 23.6 (2015), pp. 7471–7480. DOI: [10.1364/OE.23.007471](https://doi.org/10.1364/OE.23.007471).
- [47] F. Bencivenga et al. “Four-wave mixing experiments with extreme ultraviolet transient gratings”. In: *Nature* 520.7546 (Apr. 2015), pp. 205–208. DOI: [10.1038/nature14341](https://doi.org/10.1038/nature14341).
- [48] A. A. Lutman et al. “Experimental Demonstration of Femtosecond Two-Color X-Ray Free-Electron Lasers”. In: *Phys. Rev. Lett.* 110 (13 2013), p. 134801. DOI: [10.1103/PhysRevLett.110.134801](https://doi.org/10.1103/PhysRevLett.110.134801).
- [49] A. Marinelli et al. “Multicolor Operation and Spectral Control in a Gain-Modulated X-Ray Free-Electron Laser”. In: *Phys. Rev. Lett.* 111 (13 2013), p. 134801. DOI: [10.1103/PhysRevLett.111.134801](https://doi.org/10.1103/PhysRevLett.111.134801).
- [50] E. Allaria et al. “Two-colour pump–probe experiments with a twin-pulse-seed extreme ultraviolet free-electron laser”. In: *Nat Commun* 4 (Sept. 2013). DOI: [10.1038/ncomms3476](https://doi.org/10.1038/ncomms3476).
- [51] T. Hara et al. “Two-colour hard X-ray free-electron laser with wide tunability”. In: *Nat Commun* 4 (Dec. 2013). DOI: [10.1038/ncomms3919](https://doi.org/10.1038/ncomms3919).
- [52] C. Ronsivalle et al. “Large-bandwidth two-color free-electron laser driven by a comb-like electron beam”. In: *New Journal of Physics* 16.3 (2014), p. 033018.
- [53] A. A. Lutman et al. “Demonstration of Single-Crystal Self-Seeded Two-Color X-Ray Free-Electron Lasers”. In: *Phys. Rev. Lett.* 113 (25 2014), p. 254801. DOI: [10.1103/PhysRevLett.113.254801](https://doi.org/10.1103/PhysRevLett.113.254801).
- [54] A. Perucchi et al. “The TeraFERMI terahertz source at the seeded FERMI free-electron-laser facility”. In: *Review of Scientific Instruments* 84.2 (2013). DOI: [10.1063/1.4790428](https://doi.org/10.1063/1.4790428).
- [55] Z. Wang et al. “Echo-enabled tunable terahertz radiation generation with a laser-modulated relativistic electron beam”. In: *Phys. Rev. ST Accel. Beams* 17 (9 2014), p. 090701. DOI: [10.1103/PhysRevSTAB.17.090701](https://doi.org/10.1103/PhysRevSTAB.17.090701).
- [56] D. Xiang et al. “Mode-locked multichromatic x rays in a seeded free-electron laser for single-shot x-ray spectroscopy”. In: *Phys. Rev. ST Accel. Beams* 15 (5 2012), p. 050707. DOI: [10.1103/PhysRevSTAB.15.050707](https://doi.org/10.1103/PhysRevSTAB.15.050707).

Chapter 5

FEL Polarization

As we have seen in Chapter 3 the two FEL lines of FERMI, FEL-1 [1] and FEL-2 [2], are based on APPLE-II-type undulators [3, 4] that allow production of light with arbitrary polarization. In the following we report the first study of the polarization properties of FERMI FEL obtained using three different and independent measurement setups. The results are consistent with a degree of polarization $>90\%$ and are in agreement with numerical calculations. Moreover, we found that the optics along the photon transport from the radiators exit to the experimental beamlines does not significantly affect the FEL polarization properties. The measurements allowed a cross check of the results obtained with the different instruments used and represent a key indication for users who require a known and controllable degree of polarization. In the following, we will also present results obtained using a scheme [5] in which the light generated by undulators with orthogonal polarization states is combined in order to generate FEL radiation with arbitrary polarization.

The possibility to select the light polarization is particularly attractive for those experiments that explore the local symmetry of the sample under scrutiny, e.g., the lattice geometry of a crystal, the chirality of a molecule, or the system's magnetic moment.

Circularly polarized light in particular represents a critical tool to investigate the aforementioned properties of matter. It is associated with angular-momentum selection rules, resulting in different final states being accessible and different angular distribution, e.g., of photoelectrons [6–8]. The chirality of a system, usually derived from the geometry arrangement of its constituents and typically present in biomolecules [9], can be probed using circular dichroism which is also widely used to probe magnetic properties. In the latter the polarization of light can be used to manipulate the magnetic state on fs timescale via spin-orbit interactions [10]. X-rays holography of magnetic domains [11] requires circularly polarized light to obtain high-resolution images and to study the time evolution of the magnetic system of interest. As a final example, polarization of the incoming or outgoing radiation can be directly related to the three-dimensional electron wave function through electron tomography [12] and angular streaking [13, 14].

In synchrotron-based light sources, polarization control is achieved by using properly designed undulators that force the relativistic beam into a wiggling trajectory [4, 15–17]. However these sources are limited to longer time-scales (of the order of 10s of ps or longer) and low peak brightness.

While full polarization control is nowadays widespread in modern synchrotron radiation facilities, this is not true for most operational and planned X-ray FELs [18–20], that are usually operated with (fixed) linearly polarized undulators for reasons of reduced costs, higher magnetic fields requirements and tight specifications of the magnetic field quality.

The application of variable polarization undulators is therefore limited, at the time, to FEL facilities based on shorter length undulators. Among those currently operational, FERMI is the only one equipped with variable polarization undulators, see Chapter 3. LCLS has recently commissioned a variable polarization undulator to be used at the end of the main undulator line [21, 22] to obtain some polarization control of the output radiation. Also very recently at SACLA, by means of specially designed diamond-crystal optics that can be used in the hard x ray as a phase retarder, a high degree of circularly and vertically polarized radiation has been measured at about 1 angstrom [23].

Over the past year, users at FERMI have already taken advantage of these unique capabilities, e.g., to study dichroic effects via atomic photoionization [24] and to carry out coherent imaging in ferromagnetic materials [25, 26].

5.1 The polarization of light

Let's step back and recall what the polarization is. Polarization is a property of the waves that describes the direction in which the oscillation takes place [27]. For an electromagnetic wave, it is described by specifying the orientation of the electric field at a point of the space, over one period of the oscillation. Consider the electric vector of a plane wave. This can be written as

$$\vec{E} = \hat{\epsilon}E \exp[i(\vec{k} \cdot \vec{r} - \omega t)], \quad (5.1)$$

where \vec{k} is the wave-vector, ω is the angular frequency of the wave, E is the amplitude of the wave, \vec{r} is the position vector and $\hat{\epsilon}$ is a fixed direction. In this case, the electric field is oriented along a specific direction and such a wave is said to be linearly polarized with polarization vector $\hat{\epsilon}$.

Consider now a reference system (xyz) , like the one of Fig. 5.1. By combining two plane waves, one can express the most general plane wave propagating in the direction $\vec{k} = k\vec{z}$:

$$\vec{E}(\vec{r}, t) = (\hat{x}E_x + \hat{y}E_y) \exp[i(\vec{k} \cdot \vec{r} - \omega t)], \quad (5.2)$$

In this case the amplitudes E_x and E_y are complex numbers, allowing the possibility to have a phase difference between waves of different linear polarization.

Figure 5.1 shows some examples of the electric field vector evolution (continuous line) of a wave propagating along the z direction. The dotted and dashed lines are the components of the vector on the x and y directions. The bottom plane shows the shape traced out by the electric vector, also called Lissajous figure, which is a description of the polarization state.

In Figure 5.1(a) the two components have the same phase, so the direction of the electric vector is constant.

In Figure 5.1(c), the two components have exactly the same amplitude, but they are ninety degrees out of phase. In this case one component is zero when the other component is at maximum or minimum amplitude. In this special case the electric vector traces out a circle in the (x, y) plane, so the polarization is called circular.

In Figure 5.1(b), the two components are not in phase, but the offset between them is constant. This kind of polarization is called elliptical, because the electric vector traces out an ellipse in the (x, y) plane. This can happen either if the amplitudes are different and the phase mismatch is ninety degrees, or if they have equal amplitude, but the phase difference is not ninety degrees.

It is also customary, when the reflection optics is considered, to define a different coordinate system based on the propagation direction and the incidence plane. A p-polarized wave has the electric field parallel to this plane, while an s-polarized wave is normale to the incidence plane.

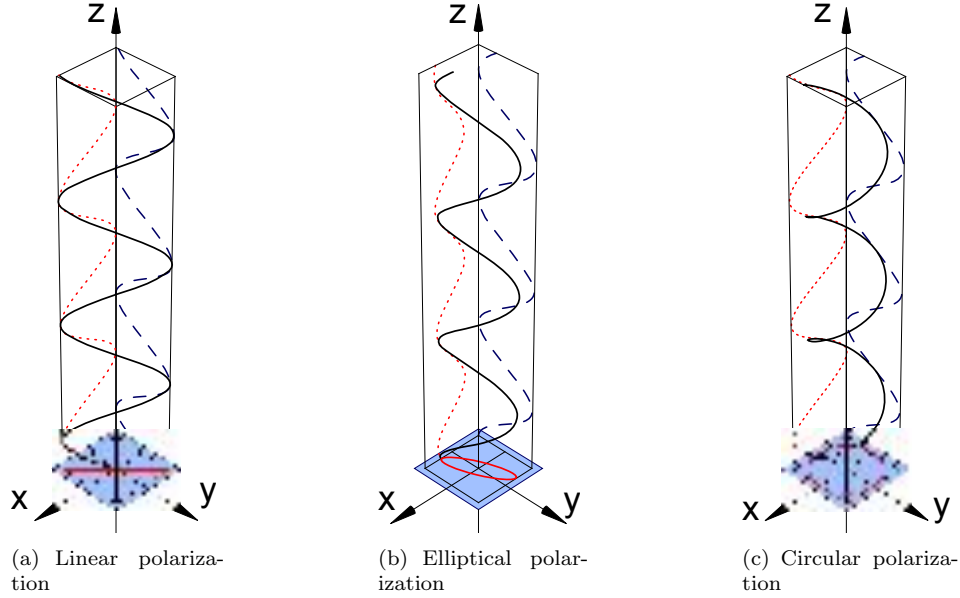


Figure 5.1: Description of the different polarizations and electric field vector evolution (continuous line) of a wave propagating along the z direction. The dotted and dashed lines are the components of the vector on the x and y directions. On the bottom plane, it is shown the shape traced out by the electric vector, which is a description of the polarization state. Images reproduced from [28].

5.2 The measurement of light polarization

Light polarization can be fully determined by measuring the so-called Stokes parameters [29]. Stokes parameters are defined as:

$$\begin{aligned}
 S_0 &= \langle |E_x|^2 \rangle + \langle |E_y|^2 \rangle = I(0^\circ) + I(90^\circ), \\
 S_1 &= \langle |E_x|^2 \rangle - \langle |E_y|^2 \rangle = I(0^\circ) - I(90^\circ), \\
 S_2 &= \Re \langle E_x E_y \rangle = I(45^\circ) - I(135^\circ), \\
 S_3 &= \Im \langle E_x E_y \rangle = I_{RHC} - I_{LHC},
 \end{aligned} \tag{5.3}$$

where $\langle \dots \rangle$ indicates a mean on a long time interval, $I(\dots)$ is the measured intensity on a particular direction, I_{RHC} and I_{LHC} are the intensities of the circular components (right and left) of the field. The total polarization fraction of the light, P , defined as

$$P = \frac{\sqrt{S_1^2 + S_2^2 + S_3^2}}{S_0} \tag{5.4}$$

represents the fractional intensity of the light that is polarized.

While in the visible wavelength range polarization measurement is straightforward [30], in the VUV spectral range the absorption of the materials represent a limiting factor and no transmission optics can be used. This means that the polarization measurement is an experiment in itself, as we will see in the following.

5.2.1 The VUV-optical polarimeter

The VUV-optical polarimeter is an all-optical device based on a well-known polarimetry scheme [31, 32]. It is composed of a polarizer and an analyzer, which can be rotated independently around the optical axis, to retrieve the complete state of polarization of an electromagnetic wave. While at infrared or visible wavelengths this type of polarimetry can be done by using transmission optics, the extension to the VUV or soft x-rays requires the usage of reflective optics due to the material absorption at such wavelengths. At each reflection onto an optical element of the polarimeter, the s and p components of the electric field experience different reflectivities, namely R_s and R_p , and different phase shifts, ϕ_s and ϕ_p . This difference enables the realisation of an XUV linear (low R_p/R_s ratio) or circular (90° phase-shift difference) polarizer and analyzer.

In Fig. 5.2 a sketch of the whole system is represented. The polarizer consists of four identical fused-silica mirrors, coated with a 35 nm layer of molybdenum and capped with 5 nm of B₄C. The choice of the particular coating is optimized for circularly polarized radiation in the 20 – 35 nm wavelength range [33]. The polarizer has been previously fully characterized at the synchrotron light source BESSY II in Berlin. For the experiment carried out at FERMI the four mirrors were set at a grazing angle of 20° in a trade-off between the R_p/R_s ratio, phase-shift difference and overall transmission.

The analyzer is made of an uncoated fused-silica mirror set at an incidence angle of 45°. At this angle, the R_p/R_s ratio for this mirror is very low in the wavelength range considered making it a very efficient analyzer. The reflected signal is measured by a $1 \times 1 \text{ cm}^2$ XUV photodiode. The angle formed by the polarizer and the horizontal plane, α , and by the analyzer with the same plane, β , are shown in Fig. 5.2. The intensity of the light at the photodiode can be theoretically described by the following expression [31, 32]:

$$\begin{aligned}
I_{out} \propto & S_0 - S_1 \cos 2\psi_1 \cos 2\alpha S_2 \cos 2\psi_1 \sin 2\alpha + \\
& + S_0 \cos 2\psi_1 \cos 2\psi_2 \cos 2\alpha \cos 2\beta + \\
& + S_0 \cos 2\psi_1 \cos 2\psi_2 \sin 2\alpha \sin 2\beta + \\
& + S_3 \sin 2\psi_1 \cos 2\psi_2 \sin \phi_1 \sin 2\alpha \cos 2\beta + \\
& - S_3 \sin 2\psi_1 \cos 2\psi_2 \sin \phi_1 \cos 2\alpha \sin 2\beta + \\
& - \frac{S_1}{2} \cos 2\psi_2 \cos 2\beta (1 + \sin 2\psi_1 \cos \phi_1) + \\
& - \frac{S_2}{2} \cos 2\psi_2 \sin 2\beta (1 + \sin 2\psi_1 \cos \phi_1) + \\
& - \frac{S_1}{2} \cos 2\psi_2 \cos 4\alpha \cos 2\beta (1 - \sin 2\psi_1 \cos \phi_1) + \\
& - \frac{S_2}{2} \cos 2\psi_2 \sin 4\alpha \cos 2\beta (1 - \sin 2\psi_1 \cos \phi_1) + \\
& - \frac{S_2}{2} \cos 2\psi_2 \cos 4\alpha \sin 2\beta (1 - \sin 2\psi_1 \cos \phi_1) + \\
& - \frac{S_1}{2} \cos 2\psi_2 \sin 4\alpha \sin 2\beta (1 - \sin 2\psi_1 \cos \phi_1),
\end{aligned} \tag{5.5}$$

where S_0 , S_1 , S_2 and S_3 are the Stokes' parameters of the FEL light at the entrance of the polarimeter, $\psi = \tan(R_p/R_s)$ and $\phi = \phi_s - \phi_p$. Subscript 1 refers to the polarizer (group of the four mirrors) and subscript 2 to the analyzer. Note that there is no ϕ_2 component to be accounted for, i.e. the phase delay into the analyzer plays no role in the measurement. The analysis of the polarization properties of the incoming radiation was performed by measuring the intensity transmitted by the polarization setup as a function of the rotation angle of

both the polarizer and analyzer optics. The Stokes parameters of the FEL radiation can be then recovered by a least square fitting of Eq. (5.5).

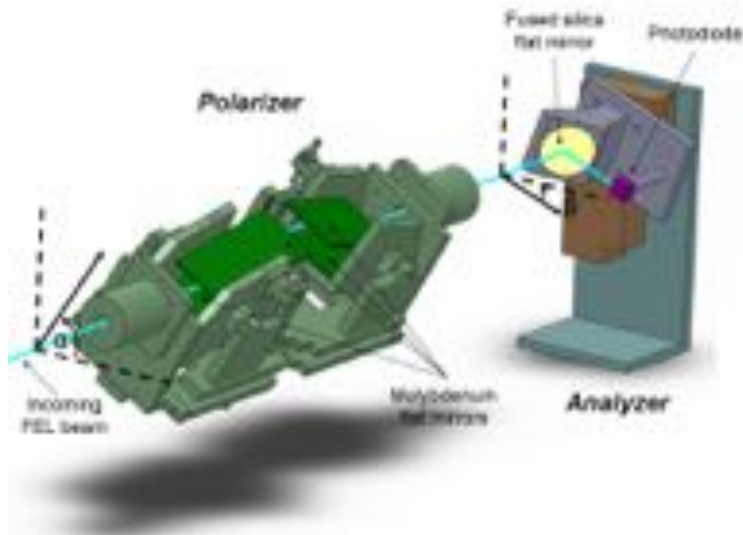


Figure 5.2: VUV-optical polarimeter setup. The polarizer and the analyzer are placed into two successive vacuum chambers. The whole setup, approximately 1.5 m long, is positioned downstream of the DiProI end station. The alignment of the setup is done using two 5 mm irises placed at the entrance and exit. The α angle can be varied from -30° to 40° , the β angle from -170° to 170° . Image reproduced from [34].

5.2.2 The e-TOF polarimeter

The e-TOF polarimeter [35] uses angle-resolved electron spectroscopy to determine the degree and direction of linear polarization of the incident radiation. This is done by measuring the angular distribution of photoelectrons produced by the FEL pulse passing through an atomic gas target. It does so by measuring, on a shot-to-shot basis, the signal coming from its 16 independent electron time-of-flight (e-TOF) spectrometers, mounted in a plane perpendicular to the FEL beam. A schematic representation of the device is reported in Fig. 5.3, together with two angular distributions corresponding to the Ne 2p (blue) and He 1s (green). The angular distribution in this plane depends on the degree and state of linear polarization of the incoming radiation, on the particular atomic gas target and on the initial state of the target that is ionized [36]. The efficiency and transmission of the different e-TOF channels can be unambiguously normalized by measuring the signal coming either from different subshells or, if the incoming photon energy is large enough, by measuring the signal of the Auger electrons [35] which is radially homogeneous.

Initially designed for and tested at the Variable Polarization XUV Beamline P04 of PETRA III [37] it has been successfully used at LCLS [22, 35] and will be installed at XFEL [38]. As it uses a gas target it is a non-invasive device capable of measuring the polarization, as well as other properties of the incoming radiation, on-line and on a shot-to-shot basis and simultaneously with other experiments.

The data acquisition system (DAQ) of the e-TOF system was integrated into the FERMI control system [39] and its data were tagged with the FERMI bunch number [40]. This

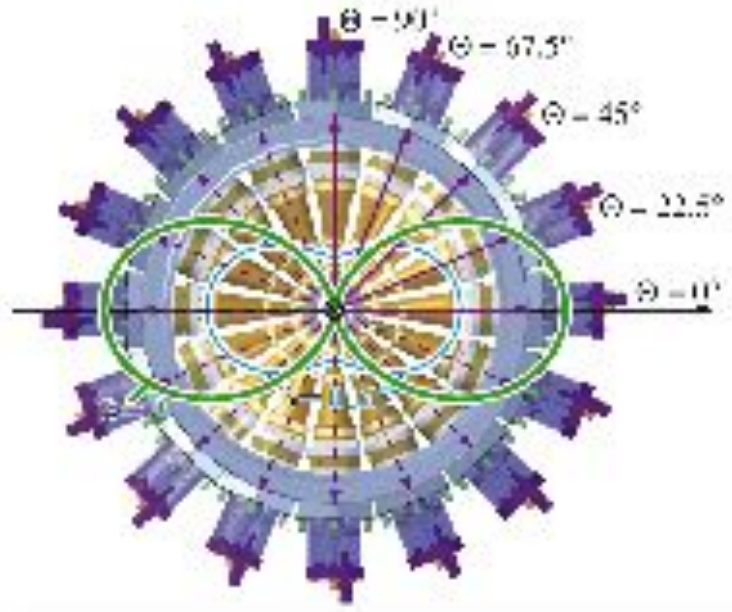


Figure 5.3: Geometry of the 16-fold electron TOF spectrometer setup. The FEL beam enters perpendicular into the plane of the figure. The angular distribution for Ne 2p (blue) and He 1s (green) photoelectrons is depicted for a wavelength of 26 nm and horizontally polarized light. Image reproduced from [34].

enabled us to do off-line cross-comparison of the polarimeter data with a set of corresponding FERMI beam parameters on a shot-by-shot basis.

For each individual FEL shot, the 16 signals corresponding to the 16 e-TOF channels give the probability distribution function of the emitted electrons. This can be fitted by a theoretical prediction taking into account the physics of the ionization process. In the dipole approximation, the angular distribution probability for the photoelectrons, or, equivalently, the angular intensity recorded by the setup, can be described as:

$$I(\theta) = 1 + \frac{\beta^{TOF}}{4} \{1 + 3P_{lin} \cos [2(\theta - \psi)]\}. \quad (5.6)$$

Here $P_{lin} = \sqrt{S_1^2 + S_2^2}$ is the degree of linear polarization, $\psi = 0.5 * \tan^{-1}(S_2/S_1)$ is the direction of the linear polarization, β^{TOF} is a parameter which describes the angular anisotropy parameter, θ is the detection angle for the photoelectron. For the case of He atoms used in the experiment, $\beta^{TOF} = 2$. Please note that β^{TOF} parameter is not an angle, nor it is related to the parameter β appearing in Eqs. (5.5) and (5.7).

Unfortunately, the circular polarization component of the radiation generates an angular distribution of the photoelectrons that is indistinguishable from an unpolarized one. The absolute degree of circular polarization can be nevertheless deduced if one assumes constant total polarization and determines the unpolarized background beforehand in the linear polarized mode of the light source [34]. If one assume that the unpolarized component is negligible [34] ($S_0 = 1$), the circular polarization component, S_3 , can be inferred from P_{lin} via quadrature difference as $S_3 = \sqrt{S_0^2 - P_{lin}^2}$.

The total transmitted intensity I_d by the polarimetry setup, in the approximation of high-extinction ratio of the polarizer and $\lambda/4$ phase retarder, can be written as

$$I_d \propto \left\{ 1 + \frac{1}{2} S_1 [\cos 2\beta + \cos(4\alpha - 2\beta)] + \frac{1}{2} S_2 [\sin 2\beta + \sin(4\alpha - 2\beta)] + S_3 \sin(2\alpha - 2\beta) \right\}. \quad (5.7)$$

Consistently with Eq. (5.5), α and β are measured relative to the horizontal axis. The horizontal direction was determined by means of a mechanical level that defined the alignment with accuracy of about 1° .

5.2.4 The photon transport system

As we have seen in Chapter 3, at the exit of the final radiator the FEL pulses enter the photon-beam-transport system (PADReS) that conveys them to the experimental stations and allows their characterisation. As one can see in Fig. 5.5, the three polarimeters were installed both at the LDM and DiProI endstations. Along the optical path of PADReS several optical elements are present and they can influence the polarization properties of the photon beam. On both beamlines there are some optical elements, namely an angle-defining aperture, a set of plane mirrors, and a diffraction grating (used at zeroth order), together with a vertical-deflecting mirror and a set of KB refocusing mirrors (KAOS in Chapter 3). Due to the operating wavelength range, all the optics work in grazing-incidence geometry.

During the measurements the photon beam followed two different paths. After the common part, comprising three horizontal reflections (PM1a, PM1b, and the grating). In both cases, the photon beam undergoes three further reflections (VDM, V-KB, and H-KB), with the first two being in the vertical plane. In total, the FEL beam experiences six reflections for DiProI (four horizontally deflecting and two vertically deflecting) and seven for LDM (five horizontally and two vertically). All mirrors are planar except the two KB types.

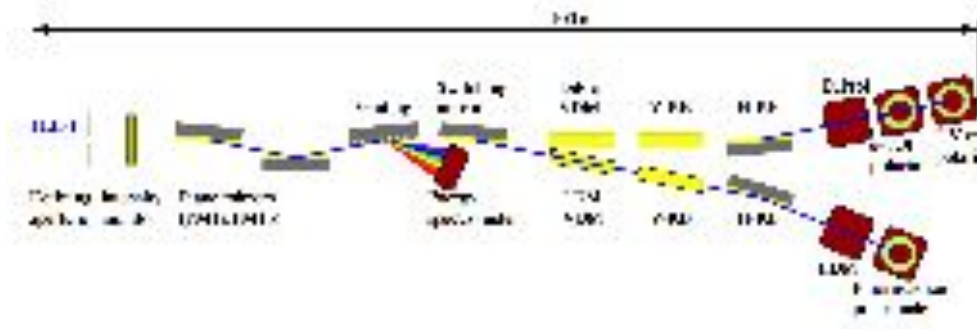


Figure 5.5: Schematic layout of the PADReS system with the three installed polarimeters: a VUV optical polarimeter and an electron time-of-flight (e-TOF) polarimeter have been installed in the DiProI beam line. A fluorescence polarimeter has been instead installed in the LDM beam line. Image reproduced from [34].

The e-TOF and the VUV-optical polarimeters were mounted in series at the exit flange of the DiProI end station. The focal position of the radiation was optimized by changing the KB parameters in order to have a spot size of $\sim 100 \times 100 \mu\text{m}^2$ in the interaction region of the e-TOF polarimeter. This configuration satisfied at the same time the optical requirements of the VUV-optical polarimeter in terms of both beam size ($2.4 \times 2.8 \text{mm}^2$ at the entrance) and angular divergence. In a similar way the focus at the LDM station was optimized to a

$\sim 1 \times 1 \text{ mm}^2$ spot. As the optical system entails reflections in both horizontal and vertical planes, the beam transport can modify the final polarization of the incoming FEL pulses. This is due to the fact that, when an optical element is used at grazing incidence, it can exhibit different reflection coefficients for the s and p polarization components, resulting in a different transmission efficiency of the beam line for the horizontal and vertical polarization.

The total transmission was estimated by the PADReS team using the optical transport code IMD [47] for both DiProI and LDM beam paths, the results are reported in Fig. 5.6. Since there are more reflections in the horizontal than in the vertical plane, the transmission for horizontally polarized radiation is less efficient than for vertically polarized radiation [34]. The difference is wavelength-dependent and more important at longer wavelengths. Again as expected by the additional reflection towards LDM, its transmission is slightly smaller than the one for DiProI. Besides affecting the transmission, the transport optics may also modify the phase delay between the horizontal and vertical polarization components. While the effect can be completely neglected for (perfectly) horizontal or vertical polarization, it must be taken into account for different polarization states.

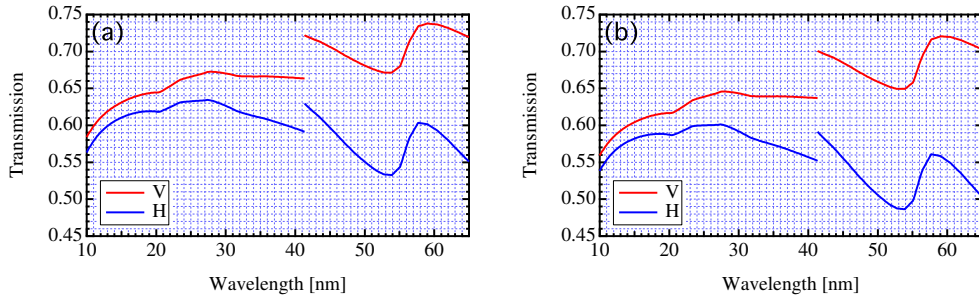


Figure 5.6: Simulated transmission for horizontal and vertical polarization as a function of wavelength for the optical transport system to the DiProI (a) and LDM (b) end stations. The step at $\sim 41.3 \text{ nm}$ (30 eV) is an artifact due to the use of two different data bases [48–50] for the computation above and below 41.3 nm . Image reproduced from [34].

The phase delay for horizontal and vertical polarization, estimated using Fresnel equations for the parameters of the PADReS mirrors [48–50], is reported as a function of the wavelength in Fig. 5.7 for the both beamlines.

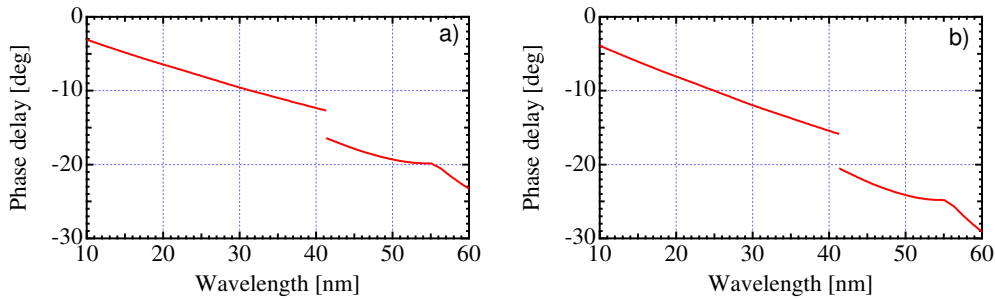


Figure 5.7: Simulated phase delay between horizontal and vertical polarization versus wavelength for the optical transport system to DiProI (a) and LDM (b). Image reproduced from [34].

The simulations reported in Figs. 5.6 and 5.7 show that, even with an ideal polarization

state at the source, the transport modifies the polarization properties of the FEL radiation in a wavelength-dependent.

5.3 Results

The polarization properties of the FEL radiation were measured with the three setups described in the previous sections. While the VUV-optical and e-TOF systems could operate in parallel, thus simultaneously characterize the same FEL pulses, the LDM apparatus was operated as an independent experiment. The latter was the only setup that required a particular wavelength of the FEL photons in order to match the desired atomic resonance.

5.3.1 VUV-optical measurements and analysis

For each FEL configuration of interest the β angle was scanned for different values of α , see Fig. 5.8. A typical measurement of the intensity collected by the photodiode at a fixed α value is shown in Fig. 5.8. For each FEL shot, the photodiode signal is normalized to the measured FEL intensity in order to account for the FEL shot-to-shot intensity fluctuations. For each value of β a significant number of shots have been acquired in order to obtain significant statistics. A least-squares fitting to Eq. (5.5) is then performed, allowing the retrieval of the Stokes parameters.

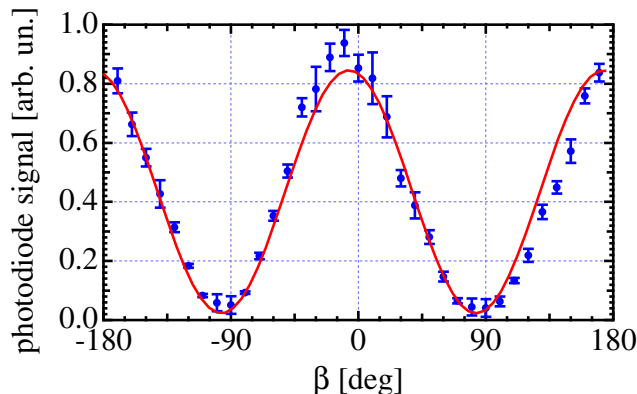


Figure 5.8: Typical data set of a β scan acquired with the optical polarimeter. The normalized detector signal averaged over 50 FEL shots (blue points) and the (RMS) errors for each β value are plotted versus the polarizer angle β . In red, the best fit is also shown. Reported data refer to FEL radiation at 26 nm in vertical polarization ($\alpha = 7^\circ$). Image reproduced from [34].

For each FEL configuration, the β scans were repeated for various α values in order to have a robust fitting procedure and to reduce the errors. The accuracy in the absolute values for the determined Stokes parameters has been estimated to be better than 0.05 according to the fitting procedure.

Figure 5.9 reports a collection of the measured average signals for various α and β , together with the fitted curves. Data reported in Figs. 5.8 and 5.9 refer to the FEL optimized at 26 nm for vertical polarization and clean spectrum. The fitting algorithm applied to the presented data set retrieves the Stokes vector $S = [1, -0.97, 0.03, 0.07]$ that characterizes the measured FEL radiation. The fitting routine is robust and returns consistent results for the different values of α , see Figure 5.9(a). Figure 5.9(b) shows the reconstructed polariza-

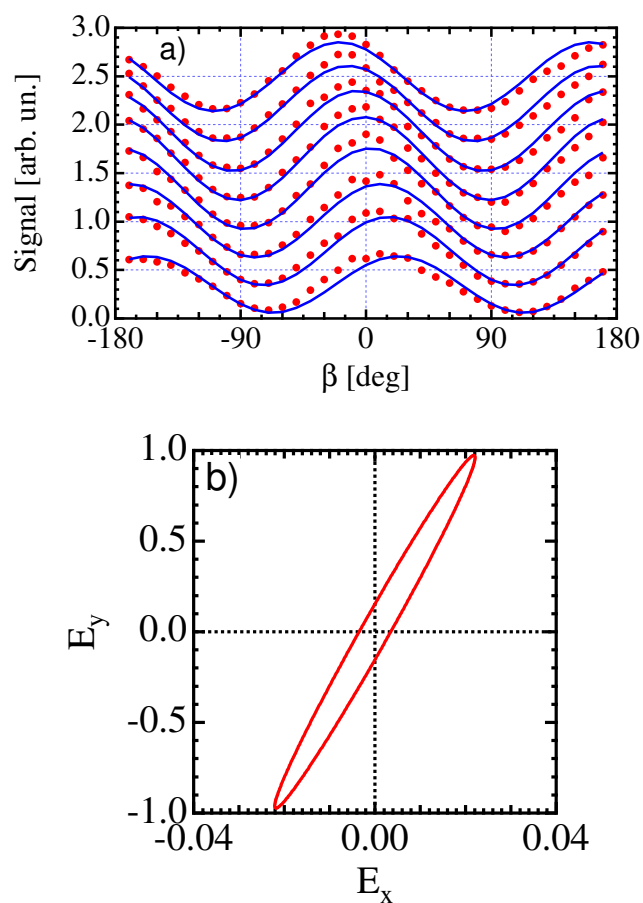


Figure 5.9: (a) Complete data set of the scans for 26 nm radiation in vertical polarization. Red points report the average signal for each value of α and β . Blue lines show the fitted curves obtained from the various β scans, allowing the retrieval of the FEL Stokes parameters. (b) Polarization ellipse reconstructed with the Stokes parameters obtained from the fit. Note the expanded horizontal scale. Image reproduced from [34].

tion ellipse obtained from the measured Stokes parameters, corresponding to a total degree of polarization of $P = 0.97$.

Similar analysis procedures have been carried out for all the data sets acquired for different polarization states and wavelengths, as summarized in Table 5.1. Unfortunately the data corresponding to horizontal polarization could not be acquired due to the reduced photon flux on the photodiode, caused by the low reflectivity of the polarizer setup for this polarization. In every other case the total degree of polarization has been found to be above 0.9 and the retrieved Stokes parameters match, as expected, the nominal polarization settings of the undulator. One should note that for the circular cases, non-negligible values of S_1 and S_2 were obtained. These values are consistent with the expected effect of the beamline optics upon the polarization of the FEL light, see Figs. 5.6 and 5.7.

Table 5.1: Results of the analysis of the VUV-optical polarimeter data. The total degree of polarization and the normalized Stokes parameters are reported for different undulator settings and wavelengths.

Wavelength [nm]	FEL polarization	Measured Polarization	S_1/S_0	S_2/S_0	S_3/S_0
26	Linear Vertical	0.97	-0.97	0.03	0.07
26	Circular Right	0.96	-0.02	0.05	0.96
32	Linear Vertical	0.96	-0.96	0.02	0.06
32	Circular Left	0.93	-0.06	-0.19	-0.91

In addition to the Stokes parameters, the data fitting procedure allows the retrieval of ψ_1 , ψ_2 , and ϕ_1 parameters, see Eq. (5.5), i.e. the R_p/R_s ratio in the polarizer and in the analyzer and the phase delay in the polarizer. The phase delay and the R_p/R_s ratio in the polarizer are in agreement with previous calibration measurements, which is a further check of the quality of the data analysis.

5.3.2 e-TOF polarimeter

After proper calibration of the setup, the analysis of the TOF signals acquired by the polarimeter allowed reconstruction of the angular distribution of the photoelectrons ionized by the polarized FEL pulses, see e.g. Fig. 5.10 via a fitting procedure based on Eq. (5.6).

As already anticipated, the e-TOF polarimeter in the configuration used during the experiments can only directly measure the degree of linear polarization, P_{lin} , while the degree of circular polarization, P_{circ} , without distinction of chirality, can only be estimated by the formula $P_{circ} = \sqrt{1 - P_{lin}^2}$ under the assumption that the radiation is fully polarized. This assumption is reasonable for the case of the FERMI FEL since it has been demonstrated, both by measurement of the linear polarization and by measurements done with the other two polarimeters that the fraction of the unpolarized light is negligible (<3%). Table 5.2 summarizes the results of the measurements done for the four “pure” polarization states at 26 nm and 32 nm.

The unique capability provided by the e-TOF polarimeter of performing single-shot polarization measurements has been exploited to study the sensitivity of the FEL polarization to the various parameters typically used to optimize the FEL output. The parameter studies were mostly made with the FEL at a 32 nm in horizontal polarization. Several series of polarization measurements were conducted as the seeding (e.g., power, relative timing with respect to the electron beam) and FEL parameters (e.g., dispersion-section strength, laser-heater power, number of radiators on resonance) were changed.

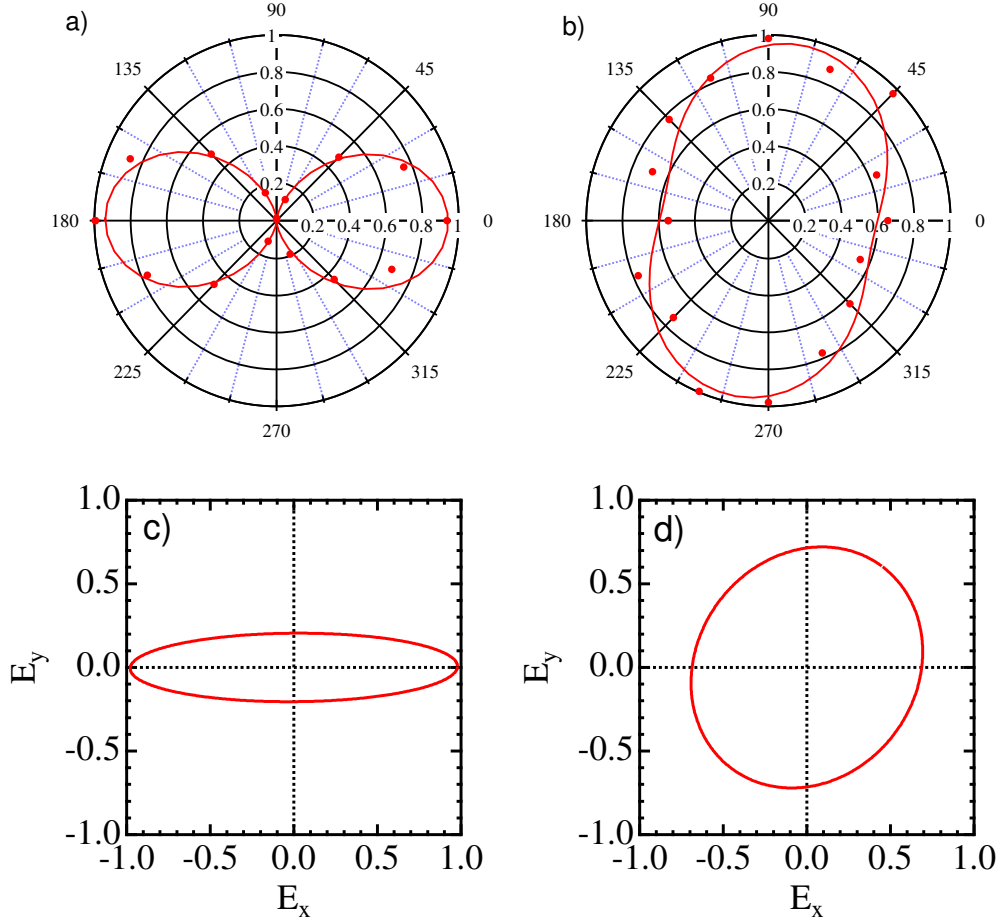


Figure 5.10: Example of the processed signal of the e-TOF showing single shot data for the photoelectron distribution on He for the FEL at 32-nm horizontally polarized (a) and circularly right polarized (b). Panels (c) and (d) report the corresponding reconstructed ellipses. Image reproduced from [34].

Table 5.2: Summary of the measured average degree of polarization for various FEL configurations. S_1 and S_2 are extracted from P_{lin} through trigonometry, S_3 is calculated assuming perfectly polarized light.

Wavelength [nm]	FEL polarization	P_{lin}	ψ [$^\circ$]	S_1/S_0	S_2/S_0	S_3/S_0
26	Linear Vertical	0.97 ± 0.02	90 ± 1	-0.97	0.01	0.25
26	Linear Horizontal	0.94 ± 0.02	0 ± 1	0.94	0.01	0.34
26	Circular Left	0.11 ± 0.02	50 ± 6	-0.02	0.11	-0.99
26	Circular Right	0.11 ± 0.02	127 ± 6	-0.03	-0.10	0.99
32	Linear Vertical	0.90 ± 0.02	91 ± 1	-0.90	-0.04	0.43
32	Linear Horizontal	0.97 ± 0.02	-1 ± 1	0.97	-0.04	0.23
32	Circular Left	0.10 ± 0.02	124 ± 5	-0.04	-0.09	-0.99
32	Circular Right	0.14 ± 0.02	53 ± 6	-0.04	0.13	0.99

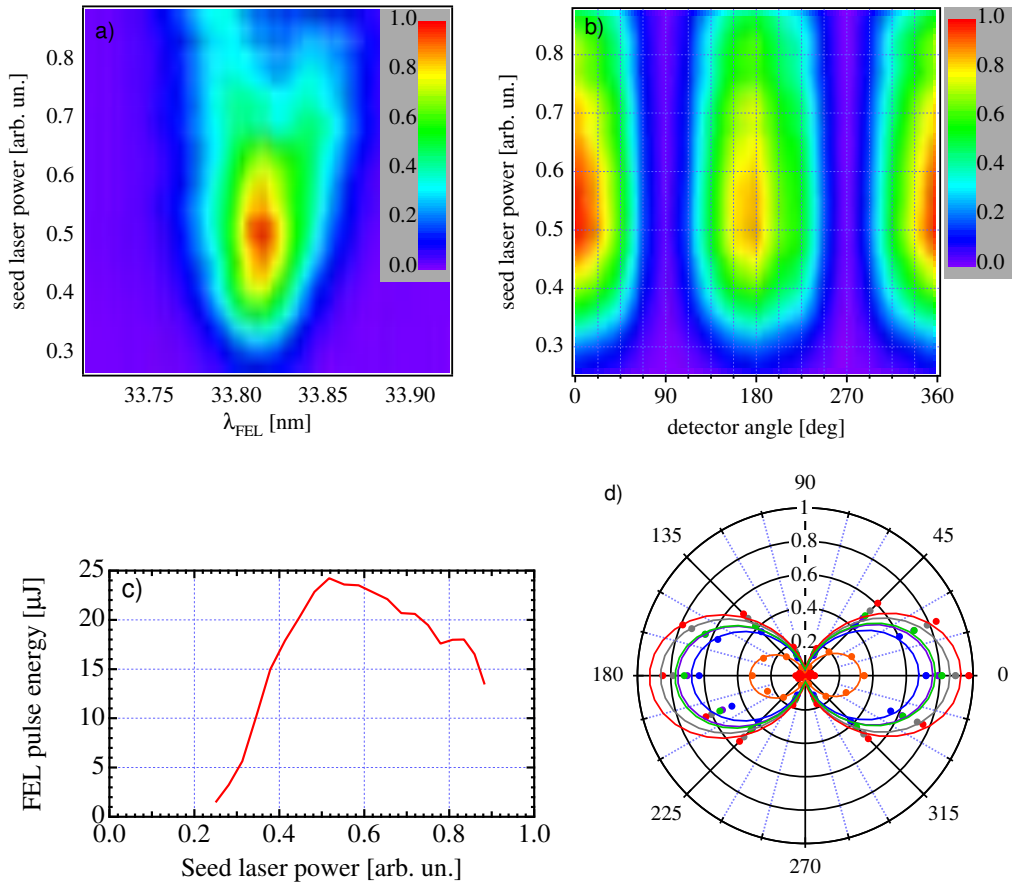


Figure 5.11: Evolution of FEL and polarization as a function of the seed-laser power: (a) FEL spectrum, (b) average signal measured by the 16 e-TOF, and (c) FEL energy per pulse as a function of the seed-laser power. Panel (d) reports the polar plot of 16 e-TOF average signals for a few seed-laser intensities and shows that the angular distribution of the signal over the 16 detectors is essentially maintained at all seeding intensities. Image reproduced from [34].

A representative data set is shown in Fig. 5.11, where the seed-laser power has been changed from the minimum value that is necessary for producing a coherent signal up to very high values that far exceed the optimum and generate strong overbunching, as is evident from structures appearing in the FEL output spectrum [51]. During this scan, we simultaneously acquired the FEL spectrum, reported in Fig. 5.11(a), the FEL intensity as measured by the PADReS intensity monitor, see Fig. 5.11(c), and the 16 e-TOF signals, Fig. 5.11(b). These signals could be directly correlated since all acquisitions were tagged with the bunch number, i.e. they can be unequivocally associated to a given FEL pulse. The results summarized in Fig. 5.11 provide strong evidence that the degree of polarization, as measured by the e-TOF, is insensitive to the seed power and to its effect on the FEL output power and spectrum [34]. Changes of critical parameters, such as the seed-laser timing, undulator resonance and strength of the dispersive section to the extent that the FEL intensity is suppressed by more than a factor 2 and the spectrum is significantly affected, have not shown any effect on the degree of the measured polarization [34]. It is important to underline that usual shot-to-shot fluctuations of the machine parameters induce variations of FEL intensity and spectral properties that are much smaller [1, 2] than those intentionally induced in the mentioned parameter scans and no correlations between polarization and other machine parameters have been observed to date.

As a reference, we report in Fig. 5.12 a measurement done with all the six radiators tuned in LH polarization mode. The degree of linearly polarized light (P_{lin}) and the direction of the polarization vector (ψ) for each FEL shot are reported in Fig. 5.12(a) and 5.12(b) respectively, along with their histograms. The lines represent the moving average of P_{lin} and ψ over 30 shots. The averages show that the light is characterized by a very high degree of horizontal polarization. Single shot fluctuations both on the degree and the direction of polarization are dominated by the statistical measurement uncertainties that, as suggested by previous experiments [34], greatly dominate the real fluctuations of the output light polarization.

The reported fluctuations of 0.1 in the degree of polarization and 3° in the direction of polarization are determined by the accuracy of the measurement and not by real fluctuations of polarization properties. The accuracy is determined by fluctuations in single e-TOF signals and may depend on the polarimeter settings. Data with a degree of linear polarization that exceeds one is physically not possible but algebraically correct for the used model.

5.3.3 Fluorescence polarimeter

Polarization measurements at LDM were carried out for linear horizontal (Fig. 5.13), circular right (data not shown), and circular left (Fig. 5.14) states for the FEL operated at a wavelength of 53.7 nm. As for the case of the VUV polarimeter, also in this case the signal for each data point was normalized to the FEL single-shot intensity. After subtraction of the background fluorescence, emitted in our understanding by the fused silica window, the Stokes parameters were determined by a least-square fitting to the function of Eq. (5.7). A summary of the obtained results is shown in Table 5.3.

In the case of linear horizontal polarization the measurement was done both with and without a phase retarder, both cases providing the same degree of polarization of the light $P = 0.92$. The maxima and minima appear at the same angular position for the two curves, which is an indication of the satisfactory alignment of the polarimeter. However, the maxima do not appear exactly at 0° but exhibit a shift of $\approx 3^\circ$ which induces a nonzero S_2 . In principle, one cannot rule out a systematic error introduced by a rotation of the polarimeter in the laboratory reference frame, even though 3° appears to be larger compared to the estimated accuracy of the initial positioning. The discrepancy could be due to the optics or

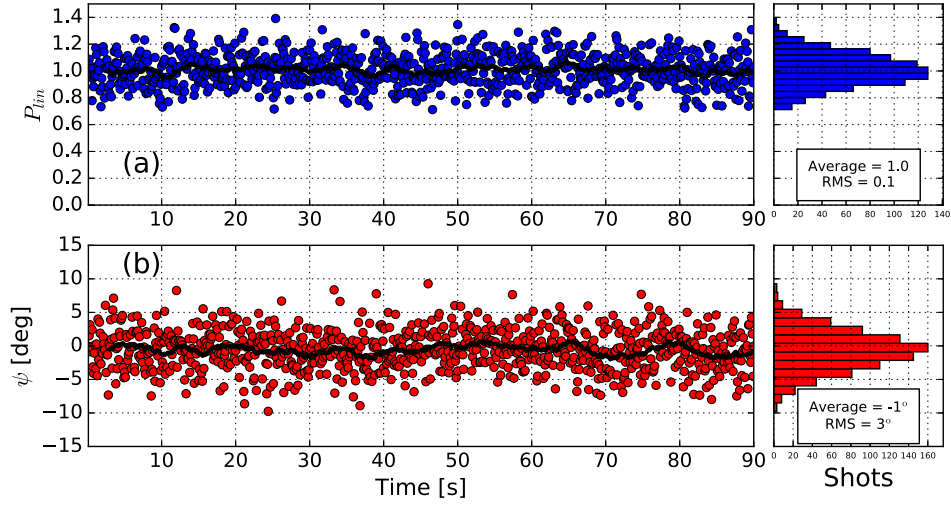


Figure 5.12: Stability of the polarization on multiple shots. (a) Degree of linear polarization (P_{lin}) and (b) direction of the polarization vector (ψ) for the FEL produced when all the undulators are tuned to “pure” linear horizontally polarized light. The lines represent the moving average over 30 shots of the reported quantities. The histograms show the distribution of the data. Image reproduced from [52].

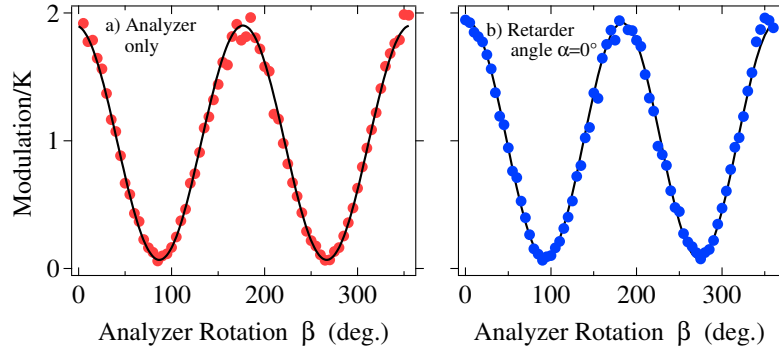


Figure 5.13: Analyzer scan (markers) and fitting curves (solid line) for the linear horizontal polarized state. (a) Linear horizontal state measured with the analyzer only, in order to determine with higher accuracy the position of the maxima. (b) Same polarization state, but measured with the complete polarimeter setup. Image reproduced from [34].

unaccounted misalignments in the experimental chamber.

A remarkable result pertaining to the circular polarization is the substantial amounts of S_1 and S_2 measured. These parameters, expected to be strictly zero for a perfectly circularly polarized light, are instead compatible with an elliptical polarization state. However, the measured values are in agreement with the predictions presented in Fig. 5.7, where a phase delay of more than 10° may occur between the horizontal and vertical polarization components for the LDM beamline. The effect is in this case large due to the relatively long wavelength used in the experiment and should be taken into account for the experiments on

Table 5.3: Summary of the results obtained with the LDM fluorescent polarimeter for different FEL nominal polarization states.

FEL polarization	Measured Polarization	S_1/S_0	S_2/S_0	S_3/S_0
Linear Horizontal	0.92	0.92	0.11	0.00
Circular Right	0.92	-0.07	0.21	0.89
Circular Left	0.93	-0.20	-0.31	-0.85

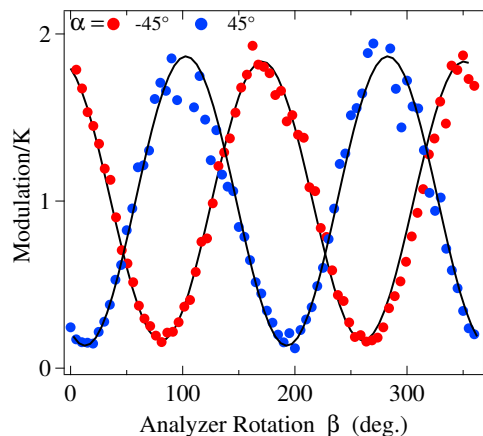


Figure 5.14: Analyzer scans for circular left polarization at $\alpha = -45^\circ$ (red) and $\alpha = 45^\circ$ (blue). Image reproduced from [34].

LDM that require a particularly high polarization purity of the radiation.

5.3.4 Summary

The results of polarization measurements obtained with the three polarimeters summarized in Tables 5.1, 5.2 and 5.3 indicate a high degree of polarization for all the cases studied [34]. The tilted elliptical polarization measured for the circularly polarized undulators case is explained and well understood as an effect of the beamline transport optics. It has been confirmed that the effect is indeed more prominent for longer wavelength. The small amount of nonpolarized light measured can be attributed to the beamline optics with residual roughness and diffraction effects.

In Fig. 5.15 the measured Stokes parameters for “pure” circularly polarized FEL light are reported, together with the predicted beamline-induced polarizing effect. The calculation takes into account the roughness of the optics as well as the carbon contamination. The measured behaviour is in very good agreement with the optical calculations accounting for the different response of the mirror to s and p polarization components.

The measurements here reported were conducted at various wavelengths and machine conditions in order to study the FEL polarization generated by FEL-1. The radiator is composed of APPLE-II type undulators which are capable of producing linearly, elliptically and circularly polarized light in the VUV soft x-ray spectral range. As in the wavelength range considered (26–55 nm) no transmission optics can be used for the polarization measurement, we took advantage of three different approaches to perform the measurement, which has been found to be mutually consistent.

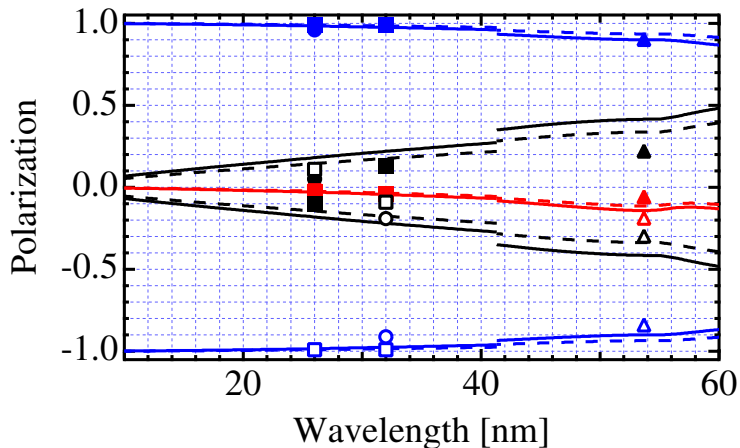


Figure 5.15: Predicted impact of the LDM (dashed lines) and DiProI (continuous line) beamline optics on the Stokes parameters (red = S_1/S_0 , black = S_2/S_0 , blue = S_3) for a circular polarized light produced at the undulator. Predictions are shown together with measured Stokes parameters at the experimental stations (circular-right filled symbols and circular-left empty symbols) obtained with the LDM setup (triangles), VUV optical polarimeter (circles), and e-TOF polarimeter (squares). See Fig. 5.6 for the step at ~ 41.3 nm. Computation courtesy of the PADReS team. Image reproduced from [34].

The measured polarization has been found to be larger than 0.9 for all the polarization states investigated. We did not find any indication that the output polarization is correlated to machine parameters. It is, however, influenced by the beam transport optics as predicted by the simulations presented. We were in fact able to measure a wavelength-dependent ellipticity when the undulators were tuned to produce circularly polarized radiation. This indicates that, in case of particularly tight requirements on the purity of the final polarization state by an experiment, a pre-compensation at the undulators should be used in order to reduce the spurious S_1 component.

5.4 Crossed polarized undulators

As we have seen in the previous paragraphs, while polarization control is widespread for synchrotron-based light sources, it is still limited for FELs. This is mainly due to technological and cost reasons. Alternative solutions for achieving polarization control, in particular for SASE FELs in the X-ray wavelength range, have been proposed and studied in the last decades [5, 53–55]. One of the most attractive possibility relies on the coherent superposition of the radiation generated by orthogonally polarized undulators [5] in a setup called the “crossed polarized undulator scheme”.

The crossed polarized undulator scheme has been already successfully implemented on a synchrotron source [56] where the light from two linearly polarized undulators has been used to produce circularly polarized light. The latter has been then used to perform magnetic dichroism experiments [57]. However the obtained degree of polarization was limited to ~ 0.4 [56] due to the partial coherence of the source, as well as the wider bandwidth of the emission. In general, in fact, the ideal source to be used for this kind of setup must have a high degree of coherence and narrow bandwidth spectrum in order to enable significant constructive interference of the two electromagnetic waves emitted by the undulators. In

the case of synchrotrons the scheme needs a monochromator to be effective. FEL sources thus represent the ideal candidate for applying the crossed polarized undulator scheme as they are capable of emitting light with much smaller bandwidth than do synchrotrons.

In fact, the control of the polarization by means of a combination of undulators with different polarization has been reported in an FEL oscillator operating in the optical klystron configuration [58]. Of interest is also the experiment performed at the SINAP FEL test facility [59], where the effectiveness of the crossed polarized undulator in single pass FELs has been demonstrated, although only in the visible spectral range and with a low-gain FEL configuration, with only limited statistics. In the following we present a model that can be used to better understand the obtained experimental results. The experiment itself is the first study of the crossed polarized undulators scheme on a high-gain seeded FEL operating in the XUV spectral range.

For facilities based on linearly polarized undulators, the crossed polarized undulator scheme is particularly useful as it allows to produce circularly polarized light. This capability is already available for the insertion devices installed at FERMI, as we have seen above. Nevertheless the crossed polarized undulator scheme is also useful at FERMI because, as we will see, it allows for emission of linearly polarized light at an arbitrary direction, which is outside the present capabilities of the APPLE-II devices. The scheme can be also used to implement fast polarization switching by simply changing the tuning of the phase shifters installed in between the undulators. The mentioned capability is interesting from the machine prospective as it does not require a change in the undulator polarization properties, which can be time consuming and can require additional optimization in terms of machine optics. Finally, the crossed polarized undulator scheme allows for the emission of linearly polarized FEL radiation without on-axis harmonic content.

5.4.1 Gaussian propagation model

Preliminary studies conducted on FERMI in October 2013 showed an unexpected decrease in the output polarization when the crossed polarized scheme was implemented [52].

The FEL beam is well-described by a diversion Gaussian mode and not a plane wave and therefore particular care is required when one considers interference. As explained in Chapter 3, between each undulator, in the break sections, exists a magnetic phase shifter. In “normal” FEL configuration the phase shifters modify the electron beam path length to ensure that slippage over the break length is exactly an integer of the radiation wavelength, so the electron beam and the radiation keep interacting with the same phase. Also, the FERMI parameters are such that the distance between the different undulators centers is larger than the Rayleigh range of the radiation, and hence the interference between the radiation emitted by each undulator must be taken into account. By looking at the FEL spot on a photon screen, see Fig. 5.16, it is readily evident that, by changing the phase shifter settings, one can change the phasing and obtain FEL mode shapes different from the single Gaussian TEM_{00} . The FEL process guides the radiation (wave-guiding effect [60]), mitigating the propagation effects of the radiation, and the maximum of FEL intensity in the lower order mode is obtained when the phase shifters are tuned in order to ensure the correct phasing between the electron and the photons.

In the case of the crossed polarized undulator scheme the interference effects can be even larger due to the reduced FEL gain and cannot be ignored. In the following we show that the loss of polarization in this configuration is related to the fact that the wavefront of the photon beam is not a plane wave and its phase varies as a function of the distance from the propagation direction. To better understand the problem we developed a simple model, based on Gaussian propagation that is capable of explaining the obtained results.

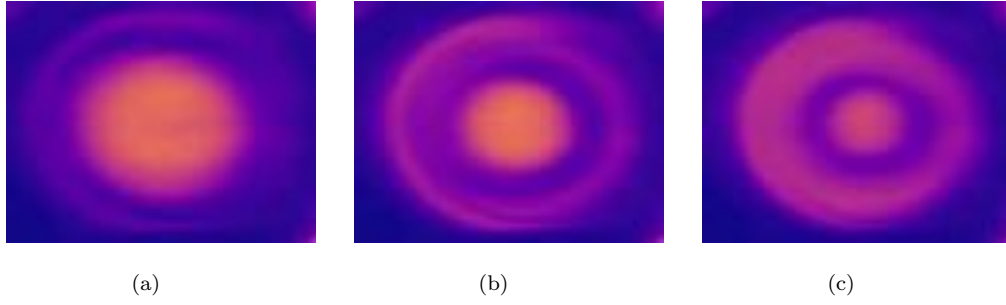


Figure 5.16: FEL transverse spot profile for two different settings of the last phase shifter. (a) the phasing enhances the emission of on-axis Gaussian mode, (b) intermediate and (c) the net emission is mainly off-axis. This demonstrates that the Gaussian propagation effects are relevant also for normal FEL operations.

Model description

The model is based on fully coherent monochromatic beams propagating in free space. The source of each field, corresponding to the FEL emission by each undulator, is presumed to be fully characterized by its waist size and divergence. The waist size is approximated to be equal to the electron beam dimension at the center of each undulator. We decompose the electric field E along Cartesian coordinates, on a plane transverse to the beam propagation direction. For simplicity we ignored misalignment effects, that could nevertheless be introduced in a more general model. In this conditions the field components corresponding to the emission of the i^{th} source can be written as

$$E_{i,x,y}(x, y, z) = E_{0i,x,y} \frac{w_{0,i}}{w_i(z)} \times \exp \left(- \left(\frac{r}{w_i(z)} \right)^2 - ikz - ik \frac{r^2}{2R} + i\chi + i\varphi_i \right), \quad (5.8)$$

where $z_{R,i} = \frac{\pi w_{0,i}^2}{\lambda}$ is the Rayleigh range of the radiation, $w_i(z) = w_{0,i} \sqrt{1 + (z/z_{R,i})^2}$ is the beam size dimension at distance z from the waist position of the source to the measurement location, $w_{0,i}$ being the waist size. k is the wavenumber, $R = z \times (1 + (z_{R,i}/z)^2)$ is the radius of curvature, $r = \sqrt{x^2 + y^2}$ the distance from the beam axis, $\chi = \tan^{-1} \left(\frac{z}{z_{R,i}} \right)$ is the Gouy's phase and φ_i is the phase between the x and y field components of the same source.

The total electric field can be then written, according to the superposition principle, as

$$E_{x,y}^{tot}(x, y, z) = \sum_i E_{i,x,y}(x, y, z_i) \times \exp(i\Delta\phi), \quad (5.9)$$

where z_i is the distance of each source from the measurement location and $\Delta\phi$ is the phase between the different superimposing fields. Notice that $\Delta\phi \neq \varphi_i$, the latter being the phase between the x and y components of the *same* field.

From the model we can compute the components of the resulting electric field on a grid and we can compute the corresponding Stokes parameters using Eq. (5.3). In the same way we can also compute the intensity I , the degree of linear polarization P_{lin} and the

direction of the linear polarization vector ψ that can be measured directly with the e-TOF polarimeter.

We started with the simplest possible configuration for the model that is only two separated sources interfering between each other, with orthogonal polarization. In Fig. 5.17 an example of the computed field parameters when a LH and LV sources, separated by a distance ~ 3 larger than the Rayleigh range of the radiation. The intensity of the two fields and their waist sizes were the same. We made this choice as we were interested in investigating the FERMI case, but the model is completely general.

Fig. 5.17(a,b,c) shows the intensity, degree of linear polarization and direction of the linear polarization vector as a function of the transverse coordinate at the measurement location, which is supposed to be in the far field. It is readily evident that the polarization properties of the radiation are changing radially along the beam. In Fig. 5.17(e,f,g) we report the same quantities as a function of the horizontal coordinate, for two fixed vertical positions, to stress the fact that both the degree and direction of the linear polarization vector are not constant due to the interference in between the two sources. If one computes the average P_{lin} by considering the whole beam, the polarization is lower than one even if the two sources have the same intensity.

We then used the model to investigate the maximum degree of polarization obtainable in a crossed polarization scheme, as a function of the distance between the two sources d . The results are reported in Fig. 5.18, where the distance has been normalized by Rayleigh range of the radiation. One can clearly see that an high degree of polarization is obtained when d/z_R is less than one, so when the distance between the two sources is less than the Rayleigh range of the radiation. In this case the sources are interfering as two plane waves and the propagation effects can be neglected. When instead $d/z_R > 1$ the linear degree of polarization is reduced. We explain this result as the variation of the phase and amplitude ratio between the two fields at the measurement location have a radial dependence along the wavefront. Different phases and amplitudes between the two sources determine different polarization properties of the resulting radiation as a function of the beam radius. By considering the average polarization of the overrrall beam spot a decrease of P_{lin} is observed.

We also used the model to explore the dependence of the polarization parameters on the phase between the two fields. In the following we focus on the case where $d/z_R > 1$, as in the experimental case. The phase is reported in λ , i.e. a shift of $\lambda/2$ corresponds to a phase shift of 180° .

LV and LH fields

When two linearly polarized fields are superimposed, the resulting radiation has a polarization state that depends on the phase between the two fields. Intuitively, two fields with the same intensity and relative phase $n\lambda/2$ (n integer) lead to a linearly polarized output field with direction at $\pm 45^\circ$ with respect to the horizontal plane. This is the case when the two fields can be described as plane waves (no propagation effects). Similarly, if the phase is $(n + 1/2)\lambda/2$, the output polarization state will be fully circular with appropriate chirality, see Fig. 5.19.

If propagation effects cannot be ignored, e.g. when the distance of the two sources is larger than the Rayleigh range, things are not so intuitive anymore. The degree of linear polarization, as shown in Fig. 5.20(a) blue line, changes from 0 to a maximum that depends on the d/z_R ratio, as shown in Fig. 5.18, and could not reach one.

The total degree of polarization, dashed line, and the intensity of the radiation, green line, are instead independent of the phase between the fields.

The direction of the linear polarization ψ , see Fig. 5.20(b) red line, shows instead a

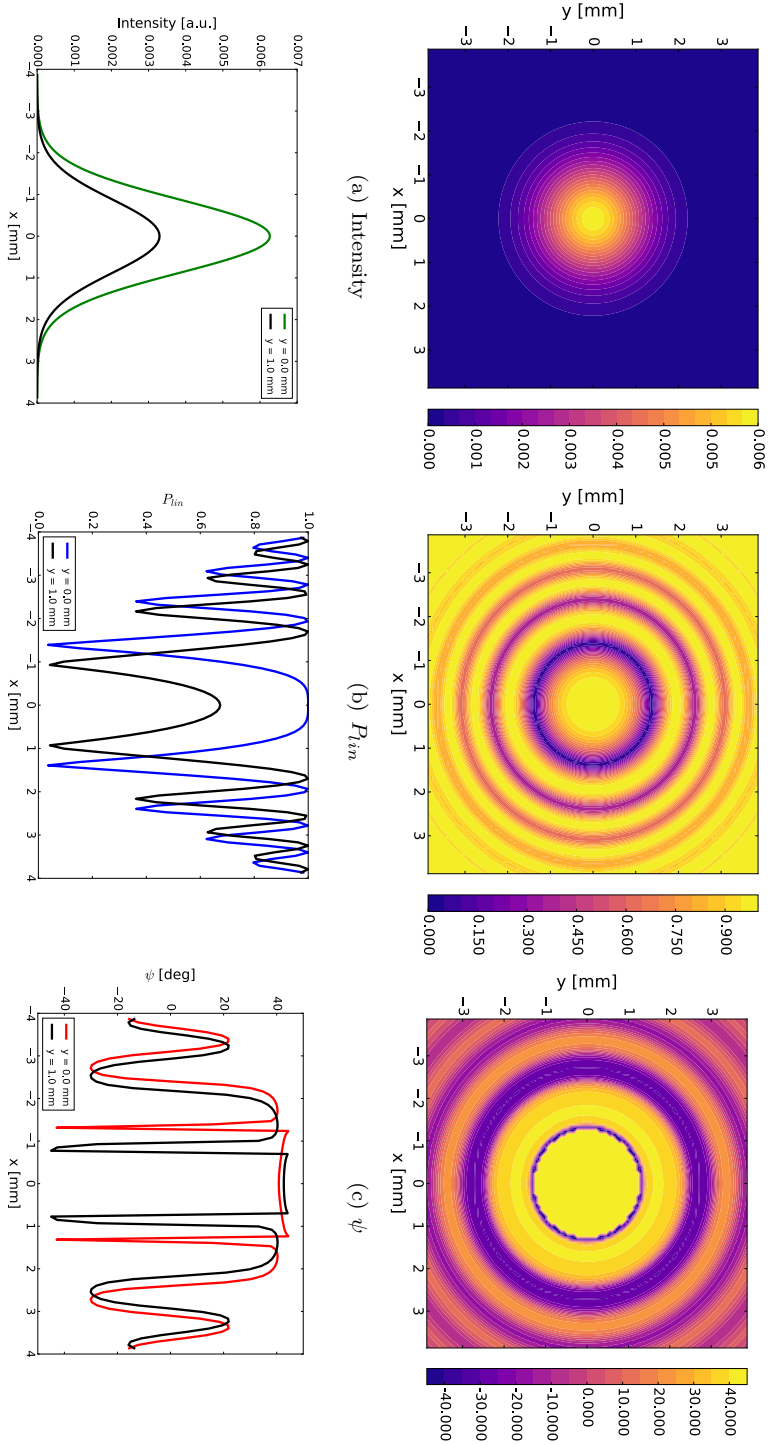


Figure 5.17: Transverse intensity, degree and direction of linear polarization, represented in false colors, of two orthogonally polarized Gaussian beams. The two sources are separated by ~ 3 zr and have the same field amplitude and waist size. The quantities are evaluated in the far field. On the lower plots, the same quantities are shown at fixed vertical position, moving along the horizontal coordinate. The black curve is the same quantity, but shifted in vertical coordinate. One can see that the polarization properties are changing along the wavefront of the total field, resulting by the superposition of the two sources.

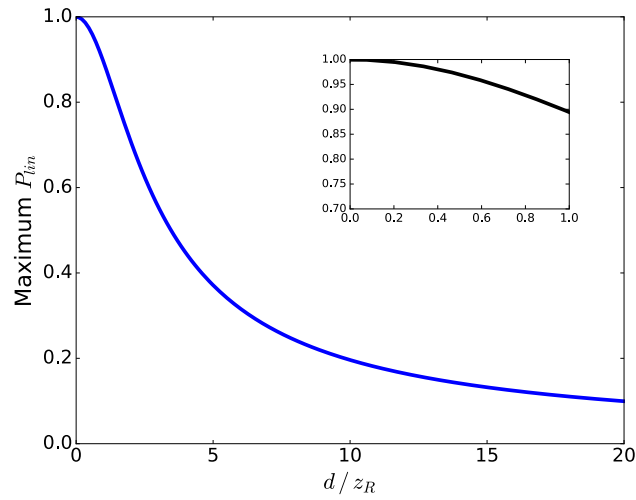


Figure 5.18: Degree of linear polarization as a function of the distance between the sources, normalized by the Rayleigh range of the radiation. The two sources have the same amplitude and linear orthogonal polarization. Insert: zoom for ratios less than one. One can see that the maximum P_{lin} obtainable depends critically on the distance between the sources, as the phase difference along the wavefront becomes more critical if the distance becomes larger than the Rayleigh range.

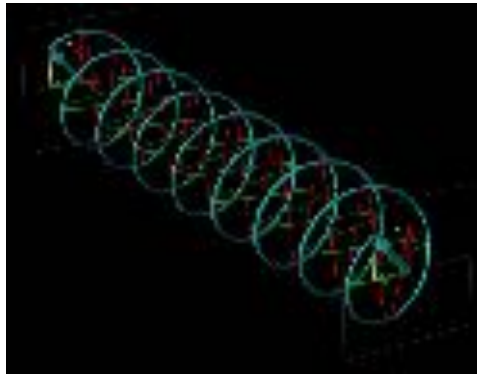


Figure 5.19: Schematic representation of the principle of the crossed polarized undulator scheme, in the case when one source in LV (green curve) and one in LH (red curve) are superimposed to produce circularly polarized light (light blue curve). Image obtained using [61].

discontinuity at the phase corresponding to the minimum of linear polarization, while it is fixed to $\pm 45^\circ$ otherwise. The discontinuity corresponds to the same phase that leads to $P_{lin} = 0$, where the radiation has its maximum obtainable degree of circular polarization. Notice that, as the degree of polarization (dashed line) is not one, only part of the radiation is effectively converted to circularly polarized light and the remainder is unpolarized radiation, so the hypothesis reported in Paragr. 5.2.2 for the computation of the degree of circular polarization P_{circ} does not hold, hence $P_{lin} = 0$ does not correspond to perfectly circular polarization, but rather to an elliptically polarized state. The unpolarized background is due to the different phases and amplitudes of the two interfering fields along the wavefront.

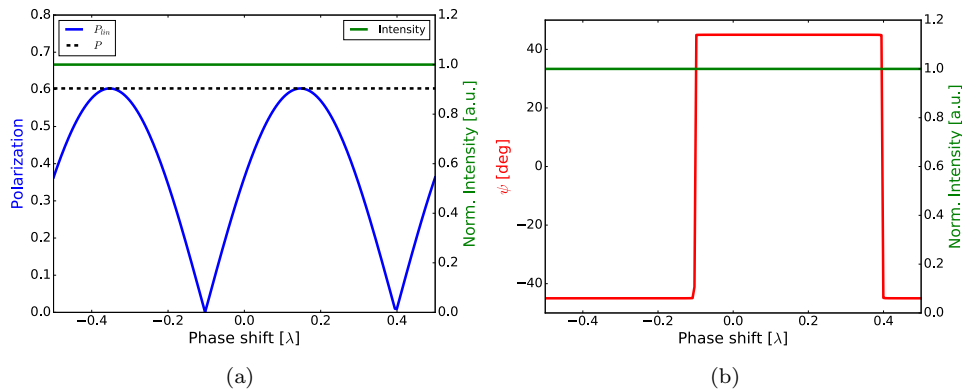


Figure 5.20: Degree of linear polarization (a) and direction (b) as a function of the phase between the two sources. The two fields have the same amplitude and linear orthogonal polarization (LV and LH), while the distance between the two sources is $\sim 3z_R$ and the collection aperture is 4σ both in horizontal and vertical direction.

CL and CR fields

The superposition of two circularly polarized fields, with opposite chirality, see Fig. 5.21, is another example of crossed polarization. If the effects due to the curvature of the wavefront can be neglected and the two sources have the same intensity, one would expect a linearly polarized resulting field with direction of polarization determined by the relative phase in between the two circularly polarized fields. By changing the phase one could adjust the direction of the linear polarization vector at will.

If instead the plane wave approximation does not hold, the propagation effects can play a crucial role as shown in Fig. 5.22. One can see that in this case the degree of linear polarization is fixed at a value lower than unity which is a function of the ratio d/z_R as before, cfr. Fig. 5.18. The same argument for the loss of the polarization used before also applies here. The direction of the linear polarization vector is changing linearly as the phase is modified.

5.4.2 Pollution effects

Up to now we only considered two superimposing fields with identical amplitude. In the following we will describe how the polarization properties of the resulting field are modified when the amplitudes are different or the two polarization vectors are not exactly orthogonal. This can induce further loss of polarization. We refer to these effects as “pollution”. The

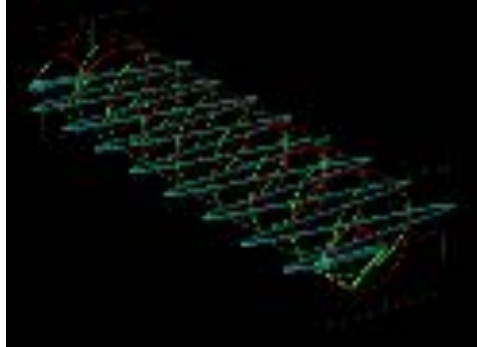


Figure 5.21: Schematic representation of the principle of the crossed polarized undulator scheme, in the case when one source in CR (green curve) and one in CL (red curve) can be superimposed to produce linearly polarized light (light blue curve). Image obtained using [61].

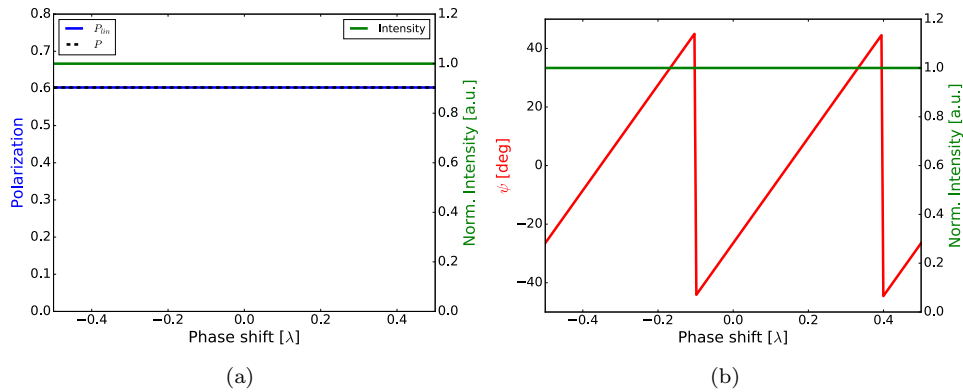


Figure 5.22: Degree of linear polarization (a) and direction (b) as a function of the phase between two circularly polarized sources (CR and CL). The two fields have the same amplitude, the distance between the two sources is $\sim 3z_R$ and the collection aperture is 4σ both in horizontal and vertical direction.

results reported in the following are relative to the LV and LH case ($d/z_R \sim 3$), but similar considerations apply to the CR and CL case. We analysed the polarization properties as a function of the phase between the two fields.

Unbalanced fields

The first and most common case is relative to a possible unbalance in intensity of the two sources. For the FEL process in particular, the intensity is increasing along the undulator due to FEL gain and therefore balancing the amplitude of the two fields is not trivial. The polarization properties of the resulting field are reported in Fig. 5.23 as a function of the phase in between the two fields, when the amplitude of the LV field is 10% larger than the LH one. The behaviour of P_{lin} , Fig. 5.23(a) is different from the unpolluted case, cfr. Fig. 5.20, as it is not possible to recover zero degree of linear polarization anymore. The distance between the maxima in P_{lin} is instead constant (same as the unpolluted case) and equal to $\lambda/2$. The direction of linear polarization, Fig. 5.23(b) does not show the sharp transition observed before and the oscillation is less than 90° . The dashed lines in Fig. 5.23 correspond instead to an amplitude unbalance of 50%: this is associated with an increase in magnitude of the effects described above. Notice that the maximum degree of linear polarization obtained is larger than in the unpolluted case and increases as the asymmetry in the amplitude of the two fields becomes larger. The resulting field is less and less elliptical as the larger field (still linear) ultimately determines the polarization state.

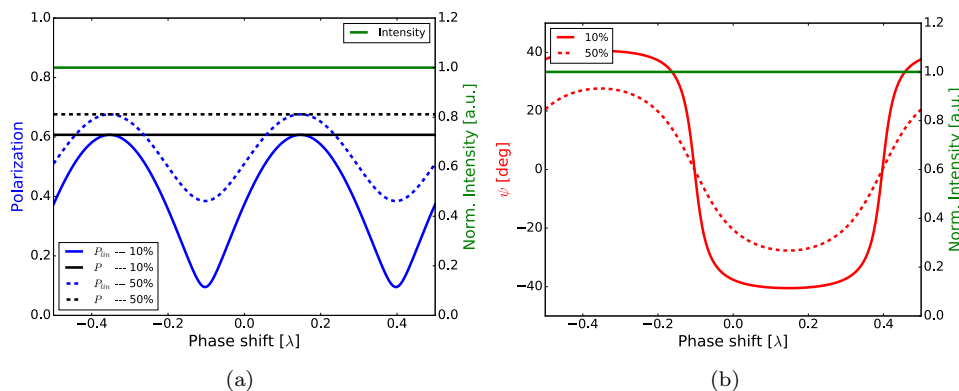


Figure 5.23: Degree of linear polarization (a) and direction (b) as a function of the phase between the two sources. Also reported is the (normalized) intensity (green). The LV field has 10% larger amplitude than LH. One can notice that the minimum and maximum P_{lin} are different from the unpolluted case, cfr. Fig. 5.20, in particular the minimum value is not zero anymore. The direction of linear polarization does not show the sharp transition observed before. The dashed lines refer to the case when the LV field has a 50% larger amplitude with respect to the LH one.

On-phase non-orthogonality

The crossed polarized scheme is also polluted if the two fields have the same amplitude (in module) but are no longer orthogonal. This can happen if one field has a tilt of the linear polarization vector with respect to the orthogonal direction of the other. The pollution in this case is due to the presence of a residual component of the first field that is parallel to the other field. The plots of Fig. 5.24 report the case of two balanced fields, but LV has a

tilt of $\sim 6^\circ$ with respect to the vertical plane, i.e. it has a component parallel to the LH field.

In this case we can notice again different behaviours for the polarization properties of the resulting field. The behaviour of P_{lin} shows asymmetric maxima as a function of the phase, while the minima are again zero. The phase corresponding to the maxima is the same as in the unpolluted case. The locations of the minima of P_{lin} are instead shifted with respect to the unpolluted case. One can also notice that the intensity is oscillating due to the interference of the residual component of one field parallel to the other. The interference is destructive or constructive depending on the phase, hence the presence of the minima and maxima in the intensity. Notice that the local maxima and minima of the intensity are in correspondence with local maxima of P_{lin} . The direction of linear polarization is almost flat with respect to the phase, except for values of the phase corresponding to $P_{lin} = 0$ where it shows a spike-like behaviour.

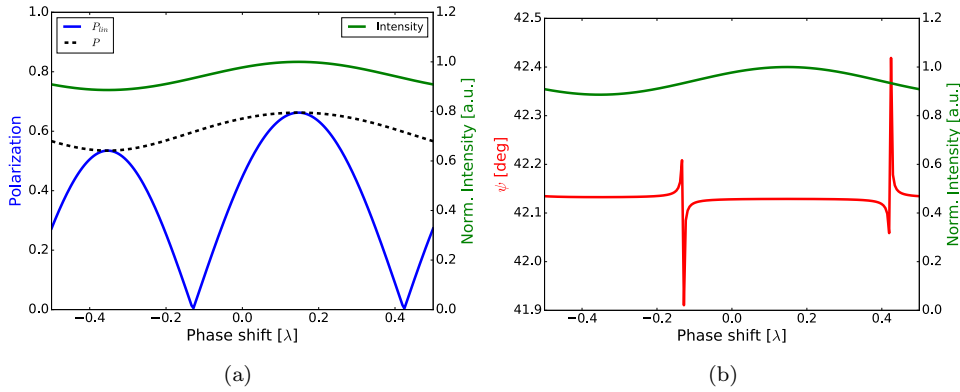


Figure 5.24: Degree of linear polarization (a, blue) and direction (b, red) as a function of the phase between the two sources. The two fields have the same amplitude, but the LV field has a tilt of $\sim 6^\circ$ with respect to the vertical plane, so the overall configuration is not orthogonal anymore. Also reported is the (normalized) intensity (green). The behaviour of P_{lin} in this case shows asymmetric maxima, while the minima are again zero as the two fields amplitudes are equal. One can notice that the intensity is oscillating as a function of the phase, as the component of the LV field, due to the tilt, interferes with the LH field. The direction of linear polarization is almost flat, except for values of the phase corresponding to $P_{lin} = 0$.

Off-phase non-orthogonality

Finally we report what happens when one of the two fields has a component parallel to the other field with a phase shift of 90° , while keeping the amplitude (in module) equal. This corresponds to an elliptical field instead of a linear one. In this case, as shown in Fig. 5.25, we observe a behaviour in between the previously two situations. The intensity shows again an oscillating trend, as the two fields have a parallel component. P_{lin} does not reach zero anymore and the direction of the polarization vector shows both sharp and smooth transition in between its maximum and minimum values. Notice also that in this case the maxima and minima of the intensity are in correspondence to the minima of P_{lin} .

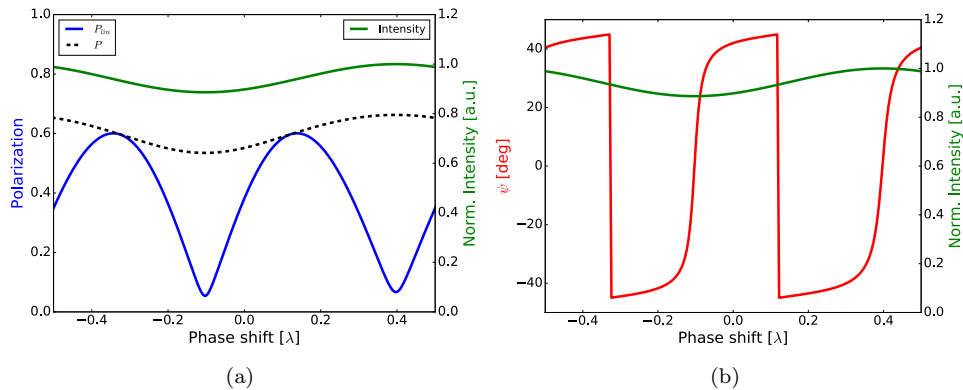


Figure 5.25: Degree of linear polarization (a, blue) and direction (b, red) as a function of the phase between the two sources. The two fields have the same amplitude, but the LV field is not perfectly linear, but has a residual ellipticity. The behaviour of P_{lin} in this case shows a shift from zero. One can notice that the intensity is oscillating as a function of the phase, as the LV field, due to the residual ellipticity, has a component parallel to the LH field that interferes, constructively or destructively depending on the phase. The direction of linear polarization shows both sharp and smooth transitions in between its maximum and minimum values.

Scan of the phase for different apertures

Our hypothesis concerning the modification of the polarization properties due to the different phase and field amplitudes between the crossed polarized fields can be further explored using the model. We investigated the dependence upon the phase between the LV and LH fields limiting the computation of the polarization parameters to small regions at different locations of the wavefront, i.e. selecting a beam aperture with size $\sim \sigma/10$, σ being the beam size at the measurement location. The results are reported in Fig. 5.26 for P_{lin} (blue) and ψ (red).

The curves show, for both quantities, significant shifts in both the location of the maxima and minima, as well as different values of extrema, for different locations along the wavefront. Combined with the results concerning the effects of a pollution in the scheme that we investigated before, the results of Fig. 5.26 confirm our hypothesis that different regions of the wavefront have different polarization states. The change in the phase corresponding to the values of extrema is a clear indication of a phase variation between the two orthogonal fields, while the change in the values of maxima and minima is a clear indication of the variation in the amplitude ratio of the interfering fields.

Summary

We developed a simple model, based on Gaussian beams, that can be used to study the interference between different monochromatic sources, e.g. in the crossed polarized undulator scheme. We showed that the maximum obtainable degree of polarization critically depends on the ratio between the distance of the sources over the Rayleigh range of the radiation.

We also investigated the dependence of the scheme on the phase in between the two sources with both linear and circular orthogonal sources. The impact of polluting effects on the scheme has been studied.

We showed that the predicted polarization properties change along the beam wavefront due to changes in the phasing and/or in the amplitude ratio of the interfering fields, leading, on average, to a loss of polarization.

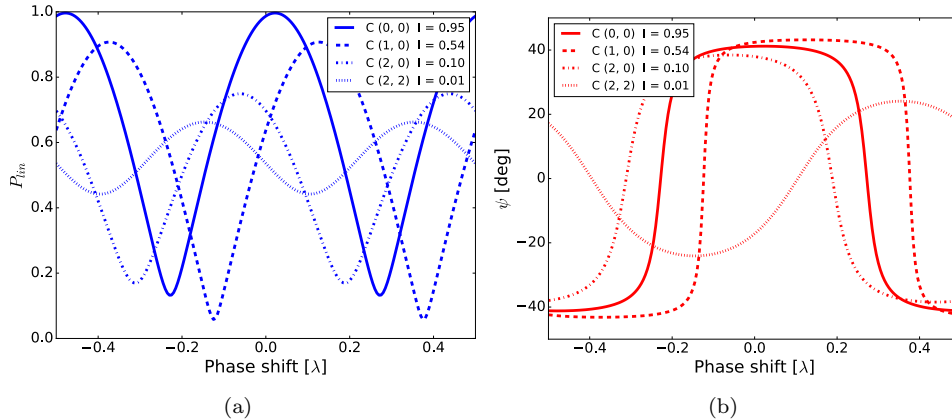


Figure 5.26: Degree of linear polarization (right, blue) and direction (left, red) as a function of the phase between the two sources, for different beam defining aperture position. The two fields have the same amplitude and have LV and LH polarization.

In its simplicity the model is extremely flexible and can be easily adapted to any setup one wants to investigate.

5.4.3 Experimental results

The experiment was carried out at FERMI FEL-1 [1]. The FEL wavelength was 23.8 nm, corresponding to the 11th harmonic of the 261.1-nm seed laser. The electron beam energy was ~ 1.45 GeV, 700 pC charge with 650 A current. The polarization data has been acquired using the e-TOF polarimeter, see Paragr. 5.2.2, capable of characterizing the polarization of the radiation on a shot-to-shot basis. Both the stability and reproducibility of the scheme constitute, in fact, one of the main concerns for the applicability of the scheme to experiments [62], hence we performed a careful characterisation of the statistical fluctuations of the FEL polarization properties.

A summary of the parameters of the experiment is reported in Tab. 5.4. As already mentioned, FEL-1 undulator chain is characterized by a distance between the sources (the centers of each undulator) that is larger than the Rayleigh range of the radiation. This leads to a decrease of the maximum degree of linear polarization obtainable with the crossed polarized scheme due to phase and/or amplitude variations along the wavefront of the beam, as investigated using the Gaussian propagation model.

Undulator length	6 x 2.4 m
Break length	1.3 m
FEL wavelength	23.8 nm
FEL source size (RMS)	120 μm
FEL Rayleigh range	1.9 m

Table 5.4: Relevant parameters for the FEL configuration used in the experiment.

FERMI setup

Each of the six undulators that constitute the FEL-1 radiator can be independently tuned in wavelength and polarization allowing various possibilities to implement the crossed polarized undulator scheme. Two different approaches are possible to implement the crossed polarized undulator scheme by either superposition of two orthogonal linearly polarized undulators to produce circular polarization or two orthogonal circularly polarized undulators to generate linear polarization.

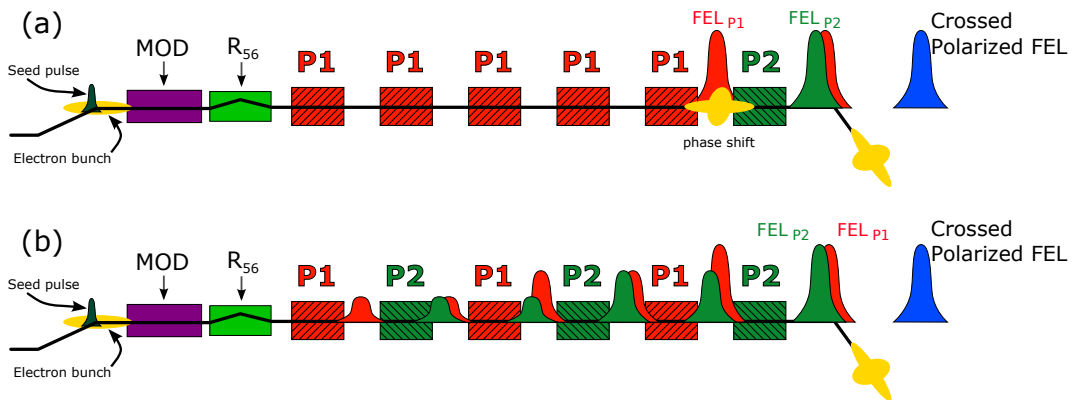


Figure 5.27: Schematic representation of the FEL-1 setup. The crossed polarized undulator scheme can be implemented as a superposition of two consecutive sources (a) or in a distributed scheme (b). Red and green represent undulators with two orthogonal polarizations (P1 and P2) that can be either CR – CL, or LH – LV that produce FEL pulses with corresponding polarization properties (FEL_{P1} and FEL_{P2}). MOD is the modulator undulator, R56 is the dispersive section. Image reproduced from [52].

Moreover, the flexibility of the undulator setup allows one to use two undulator configurations as illustrated in Fig. 5.27(a,b). Similarly to the original proposal [5], one can implement the crossed polarized undulator scheme by setting a first group of undulators to a given polarization state (CR or LH), and a second set of undulators to the corresponding orthogonal polarization (CL or LV). A critical aspect to be considered in order to obtain an efficient generation of polarized light with the crossed polarized scheme is that the intensity of the two sources should be as similar as possible. In the case of an FEL characterized by an exponential growth of the power along the radiator, one requires an unbalanced number of undulators for the two sets to satisfy this requirement. For FERMI the required conditions can be achieved by properly tuning the seeding parameters (i.e., the seed laser power, the dispersive section strength, etc.) and/or by having a different the number of undulators tuned in the two polarization states.

Another possibility, see Fig. 5.27(b), is to implement the distributed crossed polarized undulator scheme already discussed in [63, 64], in which the undulators are tuned with alternating polarization. In this case both orthogonal fields will exponentially grow in the two undulator groups that can, therefore, have the same number of undulators.

When the undulator chain is configured in crossed-polarized mode the setting of the phase shifters is extremely critical. The phase shifters can be used to control the light-electron phase in different undulators and therefore modify the phase relation in between the two orthogonal fields.

LV and LH fields

In Fig. 5.28 we report the measured degree (blue), direction (red) of linear polarization and intensity (green) as a function of the phase between the two fields, for both the consecutive (Fig. 5.28(a,b)) and distributed (Fig. 5.28(c,d)) configuration. The two undulator groups had LV and LH polarization states, with 4 undulators in LV and 2 in LH for the consecutive scheme, while all 6 were used for the distributed scheme. The data points and relative error bars are obtained as the average and standard deviation of 40 shots, acquired at each value of the phase between the two fields. The beam defining apertures were fully opened during the acquisition. The solid lines correspond to the prediction of the Gaussian propagation model for the same quantities. For the amplitudes of the fields used in the model we measured the FEL intensity as a function of the number of undulators (gain curve), obtained in the different configurations (data not shown).

By changing the phase in this linear plus linear crossed polarized undulator scheme one would be able to obtain light with full linear polarization at 45° angle from the horizontal (maxima of P_{lin}) or circularly polarized light (minima of P_{lin}). By considering the prediction of the Gaussian propagation model, we expect that the output polarization state will not have a perfect polarization state due to off-axis distortions of the wavefront.

One can see in Fig. 5.28(a,c) that in both cases P_{lin} is oscillating as a function of the phase, with maxima that correspond to the maximum polarization obtainable, which results to be 0.8 and 0.6 for the distributed and consecutive schemes, respectively. While for the distributed configuration the maxima of the curve have the same value and shape, for the consecutive configuration the maxima show the previously identified signatures of both on and off-phase pollution, most probably due to an elliptical residual with tilted angle. Notice that this agrees with the results found for the “pure” polarization case reported in Fig. 5.9(b). The pollution is further confirmed by looking at the intensity of the FEL as a function of the phase, which shows oscillations in the consecutive case. The direction of linear polarization ψ is oscillating from $\sim -40^\circ$ to $\sim 40^\circ$ for both configurations, see Fig. 5.28(b,d).

The results are well fit by the model that indicates a clear advantage in the quality of the output polarization state when the distributed scheme is implemented, as it is characterized by an increased degree of linear polarization and is less sensitive to pollution. Variations in the intensity of one of the sources in the distributed scheme is less important as the light is not further amplified in the next undulator as in the consecutive scheme.

In Fig. 5.29 we show the scan of the phase between the two fields when the measurement aperture is closed to $1 \times 1 \text{ mm}^2$ and the position of the aperture is modified in order to sample different parts of the beam wavefront. The black trace refers to the aperture fully open, as in Fig. 5.28. Both the degree (blue) and direction (red) of the linear polarization vector show significant difference for the consecutive (Fig. 5.29(a,b)) and distributed (Fig. 5.29(c,d)) schemes. The consecutive scheme shows a significant variation of the trends for both P_{lin} and ψ at different aperture centers, with different values of the maxima and minima as well as different phases corresponding to the extrema value. The distributed scheme results are instead characterized by a less spread in the behaviour as a function of the aperture position as the final wavefront is more “flat”. The phases corresponding to the extreme values are similar to the fully open aperture.

The change in the phase corresponding to the extreme values is a clear indication of the phase variation between the two orthogonal fields along the beam wavefront, while a change in the extreme values themselves is an indication of the variation in the amplitude ratio. The effect is important when the consecutive configuration is implemented, while it is mitigated for the distributed configuration.

In both cases the measured results are in satisfactory agreement with the model, see

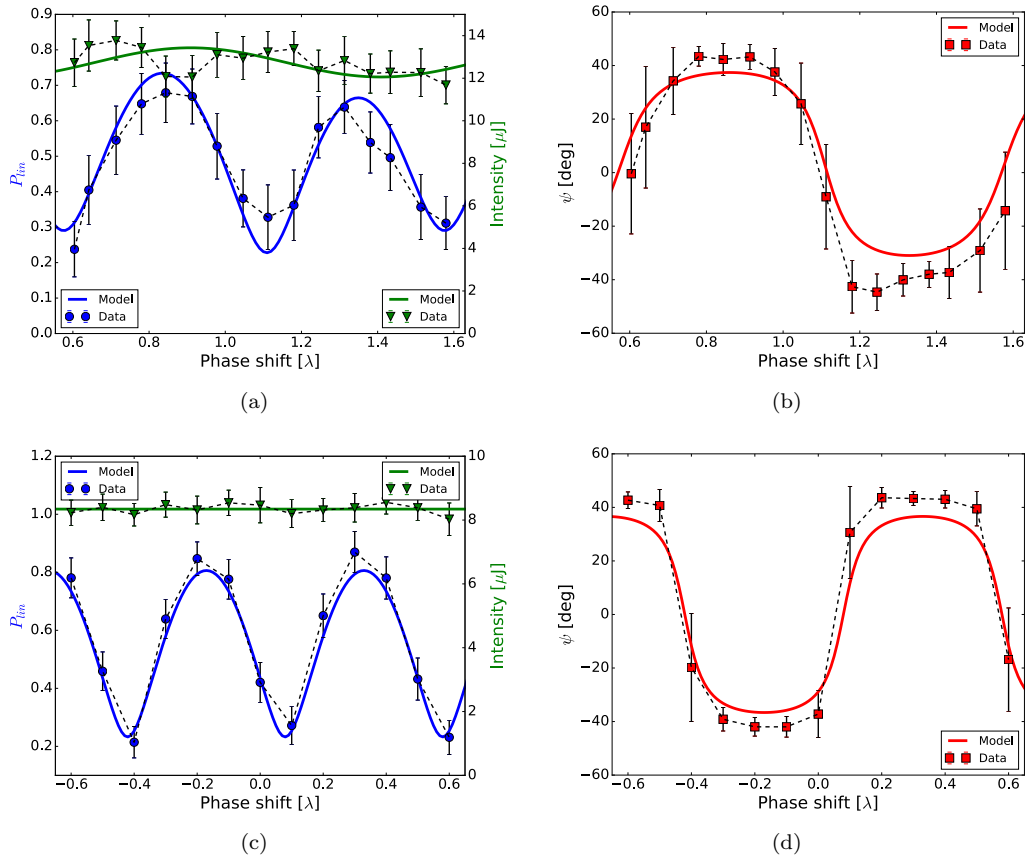


Figure 5.28: Scan of the phase between LV and LH crossed polarized fields. The degree (blue) and direction (red) of the linear polarization vector are reported as a function of the phase in between the two fields, together with the intensity of the FEL radiation (green). Data (markers) and Gaussian propagation model predictions (solid lines) are reported for the consecutive (a, b) and the distributed (c, d) schemes. The model was obtained using a reasonable set of parameters, compatible with the experimental ones. Notice that the intensity is almost constant for the distributed case, while it is oscillating in the consecutive scheme, clearly indicating the presence of pollution effects. The consecutive scheme has been obtained using 4 undulators in LV polarization and 2 in LH, while the distributed scheme was implemented using 6 undulators.

Fig. 5.26.

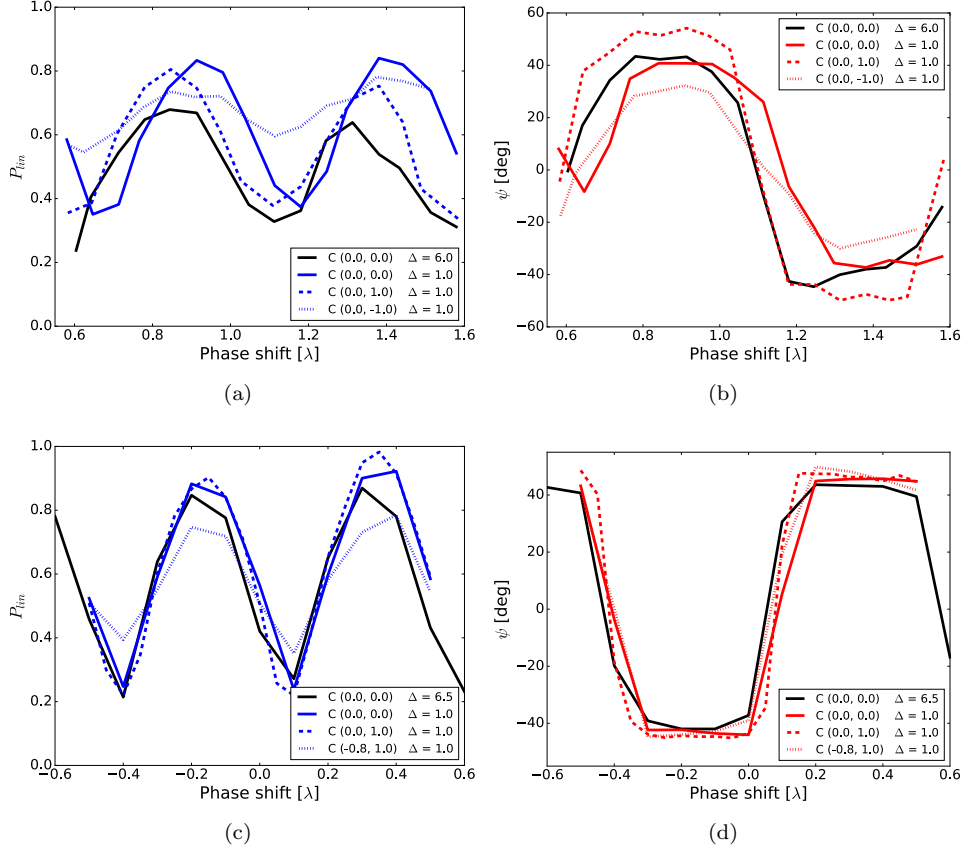


Figure 5.29: Scan of the phase between the horizontal and vertical polarized fields. The degree (blue) and direction (red) of the linear polarization vector are reported as a function of the phase in between the two fields. The data were obtained as the average of 40 consecutive shots at the same phase shift, the uncertainties are similar to Fig. 5.28 and not shown only for better clarity in the plots. The results for the consecutive (a, b) and the distributed (c, d) crossed polarized undulator scheme are shown.

Circularly polarized fields with opposite chirality

As anticipated, the crossed polarized undulator scheme can be also implemented by superimposing two circularly polarized fields with opposite chirality to obtain linearly polarized light at an arbitrary polarization direction.

In Fig. 5.30, results for the crossed polarized undulator setup are shown for the case of CL and CR radiation superimposed to generate linearly polarized light. The degree of polarization (blue) and the direction of the linear polarization vector (red) are reported as a function of time. The two top panels refer to the consecutive scheme, while the bottom two panels are relative to the distributed scheme. The consecutive scheme was implemented using 4 undulators with one chirality and 1 with the orthogonal polarization, while the distributed scheme used all 6 available devices. As predicted by the Gaussian propagation

model, limiting the collection aperture of the radiation can be used to select a region of the wavefront with similar polarization properties. The data in Fig. 5.30 was obtained by reducing the beam defining aperture to a $1 \times 1 \text{ mm}^2$ size, centered on the beam axis. The choice was made in order to increase the experimental sensitivity to small fluctuations in the polarization properties of the emitted radiation produced by the crossed polarized undulator scheme.

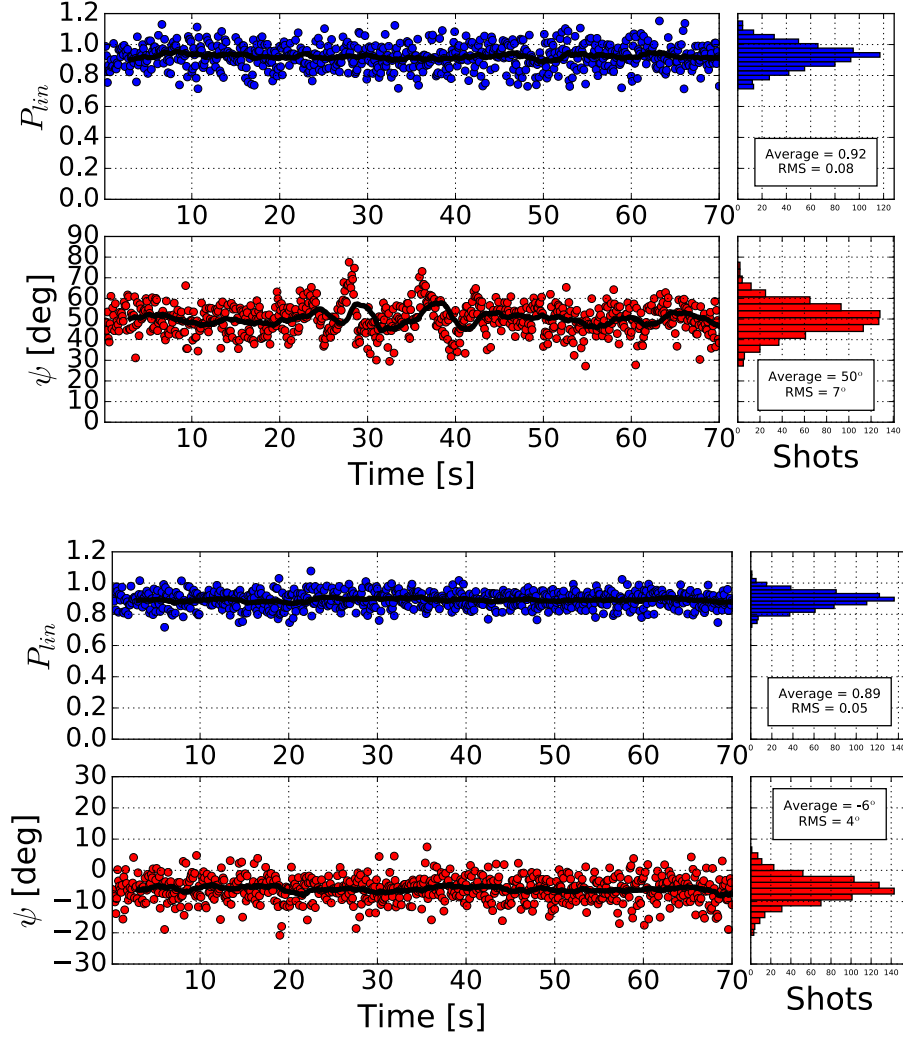


Figure 5.30: Degree and direction of the linear polarization component for the crossed circularly polarized undulators. (a) and (b) are relative to the consecutive scheme (Fig. 5.27(a)), while (c) and (d) refer to the distributed scheme (Fig. 5.27(b)). The lines represent the moving average over 30 shots of the reported quantities. The data were acquired selecting a $1 \times 1 \text{ mm}^2$ aperture, centered on the beam axis.

The average degree of linear polarization is ~ 0.9 for both cases. As remarked in [52], a significant difference for the two schemes is instead the stability of direction of the polarization vector. The (RMS) fluctuations are $\sim 4^\circ$ for the distributed scheme and $\sim 7^\circ$

for the consecutive scheme. One can notice that the difference between the two schemes is important, as the fluctuations in the distributed scheme have ‘similar amplitude of the ‘pure’ polarization state, cfr. Fig. 5.12 and are inside the estimated instrumental error. The consecutive scheme shows instead almost a factor 2 larger in the amplitude of the fluctuations. This indicates that the direction of the polarization is changing on a shot-to-shot basis as a consequence of the fluctuation on e-beam and FEL parameters.

Such a result is originated by the different sensitivity to FEL power in the two orthogonal undulator groups using the consecutive and distributed undulator schemes. A small variation in the consecutive scheme is amplified by the presence of a series of undulators with the same polarization, while it is suppressed in the distributed scheme as the FEL gain is reduced when the subsequent undulator has an orthogonal polarization with respect to the one where the variation occurred. Effects on the degree of polarization P_{lin} are smaller than the instrumental accuracy as they could not be measured.

We also measured the dependence of the polarization properties along the wavefront of the beam, again by changing the beam defining aperture center and dimensions. The results are reported in Fig. 5.31 for the intensity (green), P_{lin} (blue) and ψ (red). Fig. 5.31(a,b,c) refer to the consecutive scheme, while Fig. 5.31(d,e,f) refer to the distributed scheme. The value for each quantity (shown inside the squares) was obtained as an average over 500 shots. In both configurations one can clearly observe a variation of the degree and direction of the linear polarization vector at different locations of the beam wavefront. The maximum P_{lin} corresponds to the on-axis emission. The degree of polarization is then decaying while moving off-axis, similarly to the model prediction, see Fig. 5.17. Also the direction of the polarization vector is changing along the wavefront. This confirms that the decrease in the overall polarization observed for the crossed polarized undulator scheme is due to variations of the polarization properties along the wavefront of the beam as a consequence of the phase and relative amplitudes of the two interfering waves. This variation is important when the distance in between the orthogonal sources is larger than the Rayleigh range of the radiation, as in the present case.

The difference between the consecutive and distributed scheme, as predicted also by the model, can be observed in the central region of the beam. The distributed scheme is characterized by a larger region with similar polarization properties, while the consecutive scheme shows a faster change. Furthermore, wavefront regions that show variation in the polarization properties with respect to on-axis have a reduced intensity in the distributed case, while the intensity of such regions is still significant for the consecutive case. The contribution of such regions causes the decrease in the average degree of polarization when the full beam is considered.

Finally, in Fig. 5.32 we report the results of an experiment confirming the possibility of controlling the direction of the linear polarization by varying the phase between the two consecutive sets of undulators. The direction of linear polarization is reported, as a function of the phase in between the two circularly polarized fields, in distributed configuration. As one can see, the direction of the linear polarization vector can be arbitrarily adjusted by changing the phase in between the two fields and has a linear dependence with the phase shifter itself. If one than swaps the chirality of the two undulator groups, the same linear dependence can be obtained with opposite sign. In both cases the degree of linear polarization, i.e., ~ 0.8 , was independent of the phase, within the measurement uncertainty. This indicates the absence of pollution effects.

This result demonstrates the ability to engineer the polarization state using the crossed polarized undulator scheme. It also represent an improvement for the source, as the APPLE-II undulators installed at FERMI are only capable in the present configuration to produce linearly polarized light only along the horizontal or vertical planes.

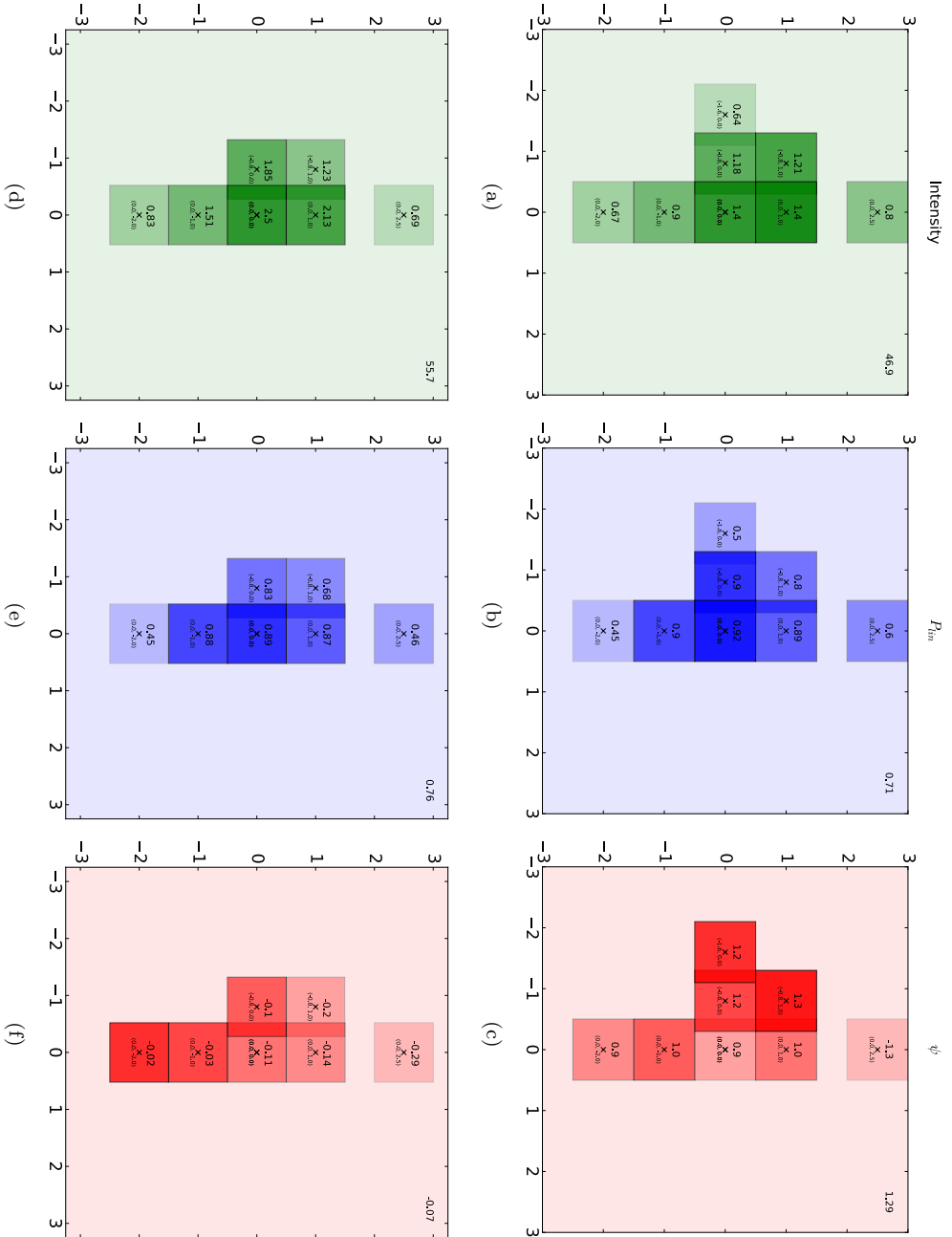


Figure 5.31: Intensity (in μJ), degree and direction (in rads) of the linear polarization for the crossed circularly polarized undulators for different beam defining aperture positions (in mm). (a, b, c) are relative to the consecutive scheme, while (d, e, f) refer to the distributed scheme. The value of each quantity is reported in the boxes that represent each different aperture position (on the top right corner for the larger aperture). One can clearly see that in both configurations the polarization properties change along the waveform, due to phase and amplitude variations in between the interfering fields. The reported values represent the average over 500 shots.

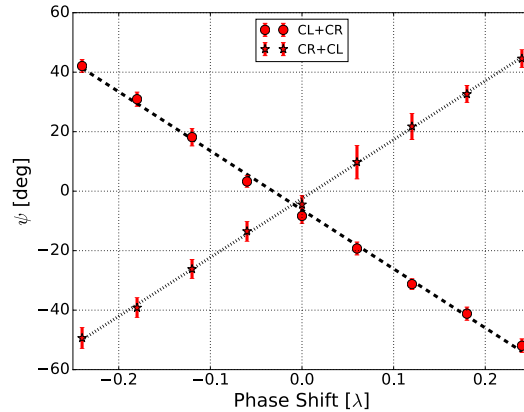


Figure 5.32: Direction of the linear polarization vector as a function of the phase between the circularly polarized fields with opposite chirality. The distributed scheme was used. ψ shows the expected linear dependence on the phase in between the two fields. By swapping the chiralities of each undulator the same linear dependence can be observed, but with opposite sign. The data were obtained by the statistical analysis (average and standard deviation) of 40 consecutive shots at the same phase shift value.

Harmonic suppression

An attractive possibility enabled by the crossed polarized undulator scheme, in the CR and CL configuration, is the ability to produce linearly polarized radiation without on-axis harmonic emission. When a linearly polarized undulator is used, the output light is also characterized by emission of on-axis odd harmonics of the fundamental undulator radiation [65]. Typical intensities associated with the third harmonic are a factor $\sim 10^{-3}$ of the fundamental, but they could significantly limit experiments, e.g. if one is interested in non-linear processes induced by the absorption of three photons at the fundamental wavelength: the linear signal induced by the absorption of the harmonic emission can be orders of magnitude larger than the nonlinear one. Using circularly polarized undulators can limit the harmonic content, as the harmonic radiation is emitted off-axis [66]. However in this case the fundamental is in a circular polarization state. The crossed polarized undulator scheme, circular plus circular, can be a viable option for both having an adequate degree of linearly polarized light without the unwanted on-axis harmonic emission.

In order to confirm this prediction we implemented the crossed polarized undulator scheme and looked at the third harmonic radiation using the photon spectrometer. The images shown in Fig. 5.33 compare the emission at 7.95 nm, the third harmonic of the fundamental wavelength used during the experiments, when all the undulators are tuned to emit linearly polarized radiation (left) and in the crossed polarized CR and CL undulator scheme (right).

One can clearly see that the harmonic radiation is not present in the case of the crossed polarized scheme. This demonstrates that we are able to suppress the signal associated to the third harmonic of the fundamental and emit linearly polarized radiation. Off-axis harmonics can be spatially filtered out using the beam defining aperture that, as we have seen above, also increases the degree of linear polarization of the radiation.

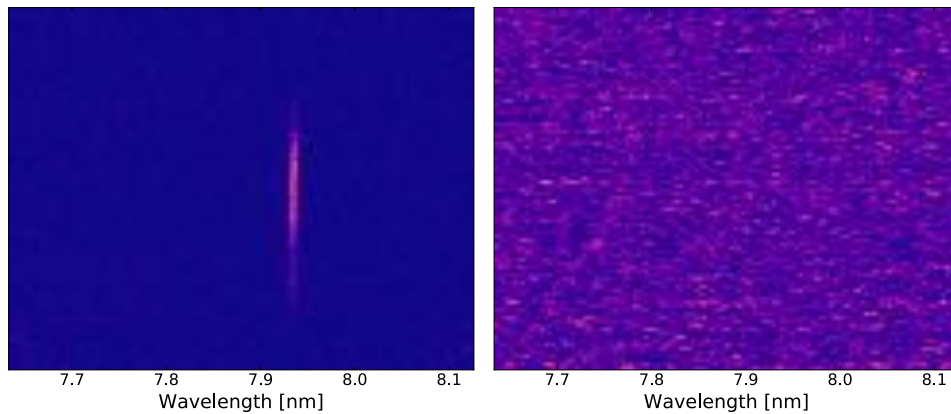


Figure 5.33: *Third harmonic spectrum of the radiation produced with a pure linear polarization tune of the undulators (left) and in the crossed polarized undulator scheme when two circularly polarized fields are superimposed in order to produce linearly polarized radiation. A harmonic signal is present for the pure polarization state and suppressed in the crossed polarized undulator scheme. This demonstrates the ability to emit linearly polarized FEL radiation without any on-axis harmonic content. The crossed polarized undulator scheme was obtained in the distributed configuration, but similar results were also confirmed with the consecutive configuration.*

Crossed polarized undulators and SASE

Finally we tested both the consecutive and the distributed configuration with SASE radiation. The results reported in the following are referred to the CR and CL polarization crossed polarized undulators to produce linearly polarized radiation. In Fig. 5.34 the consecutive (top two panels) and the distributed configuration (bottom two panels) results are shown for the degree of linear polarization (blue) and direction of linear polarization (red). The wavelength of the radiation was the same of the experiments reported for the seeding and the results shown are relative to full aperture collection.

For SASE the obtained degree of linear polarization when superimposing two circularly polarized fields is lower than the one obtained with the seeding for the same collection aperture due to the reduced longitudinal coherence of SASE with respect to seeding. One can also notice that the consecutive configuration leads to an average P_{lin} of 0.5, while the distributed configuration is characterized by an average P_{lin} of 0.27. This result is opposite to the one observed for the seeded case, where the distributed scheme can lead to a higher degree of linear polarization. In our understanding, the SASE results can be explained by considering the reduced longitudinal coherence of the SASE pulses.

Furthermore we did not observe a change in the polarization properties by limiting the collection aperture of the FEL light. In our understanding this results indicate that the limiting factor for the crossed undulator scheme in SASE is the longitudinal coherence of the radiation, rather than the change of phase and amplitude of the two superimposing fields along the wavefront. SASE is in fact characterized by a limited longitudinal coherence which limits the crossed polarized undulator scheme applicability. Similar results have been reported for the LCLS facility in SASE [22].

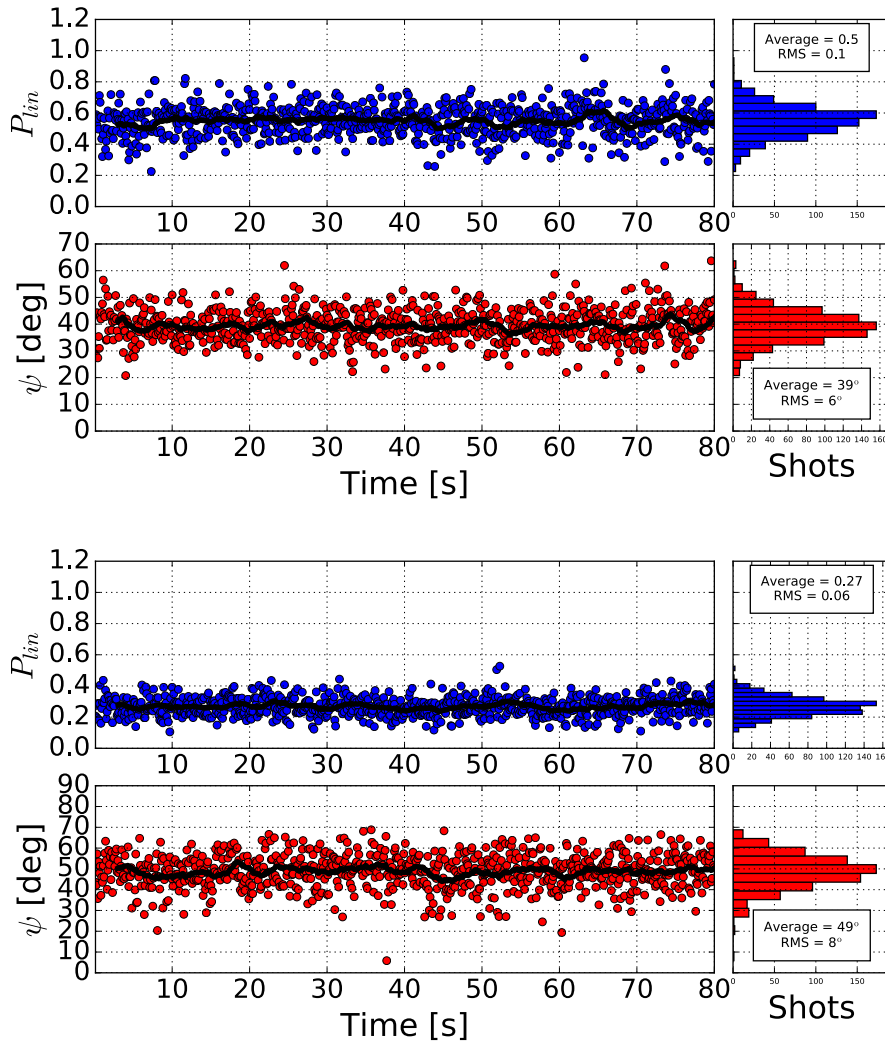


Figure 5.34: Degree and direction of the linear polarization component for the crossed circularly polarized undulators in SASE. The two top panels refer to the consecutive configuration, obtained using 4 undulators with CR and 1 undulator with CL polarization. The bottom panels refer to the distributed configuration with 6 undulators. The lines represent the moving average over 30 shots of the reported quantities. Notice that, in the case of SASE, the distributed configuration leads to a reduced degree of linear polarization with respect to the consecutive one.

5.4.4 Summary

The obtained results demonstrate the successful implementation of the crossed polarized undulator scheme at FERMI in the XUV wavelength range, in both consecutive and distributed scheme, superimposing either two linearly polarized fields or two circularly polarized ones.

The stability of both schemes has been investigated, in terms of direction of the polarization vector and degree of linear polarization. The distributed scheme has been found to be characterized by a higher shot-to-shot stability, mainly in terms of the polarization vector direction ψ . The degree of linear polarization has been found to be characterized by the same fluctuations that have been obtained with the pure LH undulator, below the instrumental noise [52]. An increase of a factor ~ 2 in the amplitude of the fluctuations of ψ has been observed for the consecutive scheme.

Both configurations are able to produce a high degree of horizontally polarized light, although lower than the one obtained in pure linear mode. The distributed scheme is characterized by a higher stability of the polarization parameters of the output radiation.

The achieved performance in terms of polarization control at FERMI can be used to extend the present capability of the two FERMI FELs to generate linearly polarized radiation with arbitrary direction, as indicated in Fig. 5.32.

The experimental results are well explained using a simple Gaussian propagation model. The key parameter is the ratio between the distance of the two sources and the Rayleigh range of the emitted radiation. If this ratio is significantly smaller than one the light emitted from the first source will not diverge significantly when superimposed to the second source point, so the total output radiation could in principle be nearly 100% polarized. If instead the ratio is larger than one, the off-axis radiation emitted from the first source will interfere at different phases with the orthogonal light emitted by the second source. Because the two orthogonal fields have different source points, only the on-axis phase can be adjusted to the desired value to define the final polarization: the relative phase and intensity of off-axis fields change with the distance from the axis. As a result, different polarization states will be produced off-axis, with a lower average degree of polarization if a large beam aperture is considered.

The good agreement with theoretical predictions of this simple model is an indication of the high degree of longitudinal coherence of the FEL pulses that are interfering to generate the polarized light. In fact, if SASE radiation is considered, the crossed polarized undulator scheme performance are poor and, in our understanding, limited by the reduced longitudinal coherence of the SASE pulses.

We also demonstrated the capability of producing linearly polarized radiation without on-axis harmonic components.

The measured levels of polarization would be sufficient for a wide range of experiments requiring polarization control. Eventually, by limiting the beam collection aperture, a high degree of polarization can be produced.

References

- [1] E. Allaria et al. “Highly coherent and stable pulses from the FERMI seeded free-electron laser in the extreme ultraviolet”. In: *Nature Photonics* 6.10 (2012), pp. 699–704. DOI: [10.1038/nphoton.2012.233](https://doi.org/10.1038/nphoton.2012.233).
- [2] E. Allaria et al. “Two-stage seeded soft-X-ray free-electron laser”. In: *Nature Photonics* 7.11 (2013), pp. 913–918. DOI: [10.1038/nphoton.2013.277](https://doi.org/10.1038/nphoton.2013.277).

-
- [3] S. Sasaki K. Miyata T. Takada. “A new undulator for generating variably polarized radiation”. In: *Jpn. J. Appl. Phys.* 31 (1992), pp. L1794–L1796.
- [4] S. Sasaki. “Analyses for a planar variably-polarizing undulator”. In: *Nuclear Instruments and Methods in Physics Research Section A: Accelerators, Spectrometers, Detectors and Associated Equipment* 347.1-3 (Aug. 1994), pp. 83–86. DOI: [10.1016/0168-9002\(94\)91859-7](https://doi.org/10.1016/0168-9002(94)91859-7).
- [5] K.-J. Kim. “Circular polarization with crossed-planar undulators in high-gain FELs”. In: *Nuclear Instruments and Methods in Physics Research, Section A: Accelerators, Spectrometers, Detectors and Associated Equipment* 445.1-3 (2000), pp. 329–332. DOI: [10.1016/S0168-9002\(00\)00137-6](https://doi.org/10.1016/S0168-9002(00)00137-6).
- [6] J. Cooper and R. N. Zare. “Angular Distribution of Photoelectrons”. In: *The Journal of Chemical Physics* 48.2 (1968), pp. 942–943. DOI: [10.1063/1.1668742](https://doi.org/10.1063/1.1668742).
- [7] N.M. Kabachnik et al. “Coherence and correlations in photoinduced Auger and fluorescence cascades in atoms”. In: *Physics Reports* 451.5-6 (2007), pp. 155–233. ISSN: 0370-1573. DOI: [10.1016/j.physrep.2007.07.005](https://doi.org/10.1016/j.physrep.2007.07.005).
- [8] K. L. Reid. “Photoelectron Angular Distributions”. In: *Annual Review of Physical Chemistry* 54.1 (2003). PMID: 12574491, pp. 397–424. DOI: [10.1146/annurev.physchem.54.011002.103814](https://doi.org/10.1146/annurev.physchem.54.011002.103814). eprint: <http://dx.doi.org/10.1146/annurev.physchem.54.011002.103814>.
- [9] M. H. M. Janssen and I. Powis. “Detecting chirality in molecules by imaging photoelectron circular dichroism”. In: *Phys. Chem. Chem. Phys.* 16 (3 2014), pp. 856–871. DOI: [10.1039/C3CP53741B](https://doi.org/10.1039/C3CP53741B).
- [10] J.-Y. Bigot, M. Vomir, and E. Beaupaire. “Coherent ultrafast magnetism induced by femtosecond laser pulses”. In: *Nat Phys* 5.7 (July 2009), pp. 515–520. DOI: [10.1038/nphys1285](https://doi.org/10.1038/nphys1285).
- [11] S. Eisebitt et al. “Lensless imaging of magnetic nanostructures by X-ray spectroholography”. In: *Nature* 432.7019 (Dec. 2004), pp. 885–888. DOI: [10.1038/nature03139](https://doi.org/10.1038/nature03139).
- [12] M. Weger et al. “Transferring the attoclock technique to velocity map imaging”. In: *Opt. Express* 21.19 (2013), pp. 21981–21990. DOI: [10.1364/OE.21.021981](https://doi.org/10.1364/OE.21.021981).
- [13] P. Eckle et al. “Attosecond Ionization and Tunneling Delay Time Measurements in Helium”. In: *Science* 322.5907 (2008), pp. 1525–1529. DOI: [10.1126/science.1163439](https://doi.org/10.1126/science.1163439). eprint: <http://www.sciencemag.org/content/322/5907/1525.full.pdf>.
- [14] P. Eckle et al. “Attosecond angular streaking”. In: *Nat Phys* 4.7 (July 2008), pp. 565–570. DOI: [10.1038/nphys982](https://doi.org/10.1038/nphys982).
- [15] J. Bahrtdt et al. “Elliptically polarizing insertion devices at BESSY II”. In: *Nuclear Instruments and Methods in Physics Research Section A: Accelerators, Spectrometers, Detectors and Associated Equipment* 467–468, Part 1.0 (July 2001), pp. 21–29. DOI: [10.1016/S0168-9002\(01\)00554-X](https://doi.org/10.1016/S0168-9002(01)00554-X).
- [16] L. Nahon and C. Alcaraz. “SU5: a calibrated variable-polarization synchrotron radiation beam line in the vacuum-ultraviolet range”. In: *Applied Optics* 43.5 (2004), pp. 1024–1037. DOI: [10.1364/AO.43.001024](https://doi.org/10.1364/AO.43.001024).
- [17] B. M. Kincaid. “A short-period helical wiggler as an improved source of synchrotron radiation”. In: *Journal of Applied Physics* 48.7 (1977), pp. 2684–2691. DOI: [10.1063/1.324138](https://doi.org/10.1063/1.324138).

- [18] W. Ackermann et al. “Operation of a free-electron laser from the extreme ultraviolet to the water window”. In: *Nature Photonics* 1.6 (June 2007), pp. 336–342. DOI: [10.1038/nphoton.2007.76](https://doi.org/10.1038/nphoton.2007.76).
- [19] P. Emma et al. “First lasing and operation of an angstrom-wavelength free-electron laser”. In: *Nature Photonics* 4.9 (Sept. 2010), pp. 641–647. DOI: [10.1038/nphoton.2010.176](https://doi.org/10.1038/nphoton.2010.176).
- [20] T. Ishikawa et al. “A compact X-ray free-electron laser emitting in the sub-angstrom region”. In: *Nature Photonics* 6.8 (Aug. 2012), pp. 540–544. DOI: [10.1038/nphoton.2012.141](https://doi.org/10.1038/nphoton.2012.141).
- [21] H.-D. Nuhn et al. “RandD towards a delta-type undulator for the LCLS”. In: *FEL 2013: Proceedings of the 35th International Free-Electron Laser Conference*. 2013, pp. 348–350.
- [22] H.-D. Nuhn et al. “Commissioning of the DELTA Undulator at LCLS”. In: *FEL 2015: Proceedings of the 37th International Free-Electron Laser Conference*. 2015, pp. 348–350.
- [23] M. Suzuki et al. “Polarization control of an X-ray free-electron laser with a diamond phase retarder”. In: *Journal of Synchrotron Radiation* 21.3 (2014), pp. 466–472. DOI: [10.1107/S1600577514004780](https://doi.org/10.1107/S1600577514004780).
- [24] T. Mazza et al. “Determining the polarization state of an extreme ultraviolet free-electron laser beam using atomic circular dichroism”. In: *Nat Commun* 5 (Apr. 2014). DOI: [10.1038/ncomms4648](https://doi.org/10.1038/ncomms4648).
- [25] F. Capotondi et al. “Invited Article: Coherent imaging using seeded free-electron laser pulses with variable polarization: First results and research opportunities”. In: *Review of Scientific Instruments* 84.5 (2013). DOI: [10.1063/1.4807157](https://doi.org/10.1063/1.4807157).
- [26] C. von Korff Schmising et al. “Imaging Ultrafast Demagnetization Dynamics after a Spatially Localized Optical Excitation”. In: *Phys. Rev. Lett.* 112 (21 2014), p. 217203. DOI: [10.1103/PhysRevLett.112.217203](https://doi.org/10.1103/PhysRevLett.112.217203).
- [27] J. D. Jackson. *Classical electrodynamics*. New York: J. Wiley, 1975.
- [28] [http://en.wikipedia.org/wiki/Polarization_\(waves\)](http://en.wikipedia.org/wiki/Polarization_(waves)).
- [29] H.G. Berry G. Gabrielse A.E. Livingston. “Measurement of the Stokes parameters of light”. In: *Appl. Opt.* 16.12 (1977), pp. 3200–3205.
- [30] E. Ferrari. “VUV and X-Ray Coherent Light With Variable Polarization From a Single-Pass Free-Electron Laser”. MA thesis. University of Trieste, 2010.
- [31] F. Schäfers et al. “Soft-x-ray polarimeter with multilayer optics: complete analysis of the polarization state of light”. In: *Appl. Opt.* 38.19 (1999), pp. 4074–4088. DOI: [10.1364/AO.38.004074](https://doi.org/10.1364/AO.38.004074).
- [32] B. Vodungbo et al. “Polarization control of high order harmonics in the EUV photon energy range”. In: *Opt. Express* 19.5 (2011), pp. 4346–4356. DOI: [10.1364/OE.19.004346](https://doi.org/10.1364/OE.19.004346).
- [33] D. H. Goldstein. *Polarized Light, 2nd ed.* New York: CRC Press, 2003.
- [34] E. Allaria et al. “Control of the Polarization of a Vacuum-Ultraviolet, High-Gain, Free-Electron Laser”. In: *Phys. Rev. X* 4 (4 2014), p. 041040. DOI: [10.1103/PhysRevX.4.041040](https://doi.org/10.1103/PhysRevX.4.041040).
- [35] J. Viefhaus. “An Online Diagnostic Unit for FEL Photon Parameter Determination and Optimization”. In: *Proceedings of the 2015 FEL Conference*. 2015.

-
- [36] S. T. Manson and A. F. Starace. “Photoelectron angular distributions: energy dependence for s subshells”. In: *Rev. Mod. Phys.* 54 (2 1982), pp. 389–405. DOI: [10.1103/RevModPhys.54.389](https://doi.org/10.1103/RevModPhys.54.389).
- [37] J. Viefhaus et al. “The Variable Polarization XUV Beamline P04 at PETRA III: Optics, mechanics and their performance”. In: *Nuclear Instruments and Methods in Physics Research, Section A: Accelerators, Spectrometers, Detectors and Associated Equipment* 710 (2013), pp. 151–154. DOI: [10.1016/j.nima.2012.10.110](https://doi.org/10.1016/j.nima.2012.10.110).
- [38] http://xfel.desy.de/technical_information/photon_beam_parameter/.
- [39] M. Lonza et al. “Status Report of the FERMI@Elettra Control System”. In: *Proceedings of ICALEPCS2011*. 2011.
- [40] L. Pivetta et al. “The FERMI@Elettra Distributed Real-time Framework”. In: *Proceedings of ICALEPCS2011*. 2011.
- [41] V.Yu Backman, S.V. Bobashev, and O.S. Vasyutinskii. “Determination of polarization of vacuum-ultraviolet radiation by fluorescence and probe-beam techniques”. English. In: *Solar Physics* 164.1-2 (1996), pp. 397–401. ISSN: 0038-0938. DOI: [10.1007/BF00146651](https://doi.org/10.1007/BF00146651).
- [42] C.J Latimer, M.A. MacDonald, and P. Finetti. “A new method for polarization analysis in the {VUV}”. In: *Journal of Electron Spectroscopy and Related Phenomena* 101–103 (1999), pp. 875–878. ISSN: 0368-2048. DOI: [10.1016/S0368-2048\(98\)00407-1](https://doi.org/10.1016/S0368-2048(98)00407-1).
- [43] H. Elliott White. *Introduction to Atomic Spectra*. New York: McGraw-Hill, 1934.
- [44] W. L. Wiese, M. W. Smith, and B. M. Glennon. *NSRDS 4 Vol. 1 Atomic Transition Probabilities. Elements Hydrogen through Neon*. Washington DC: NBS, 1966.
- [45] P. Finetti et al. “in preparation”.
- [46] C. Grazioli et al. “CITIUS: An infrared-extreme ultraviolet light source for fundamental and applied ultrafast science”. In: *Review of Scientific Instruments* 85.2, 023104 (2014). DOI: [http://dx.doi.org/10.1063/1.4864298](https://dx.doi.org/10.1063/1.4864298).
- [47] D. L. Windt. “IMD—Software for modeling the optical properties of multilayer films”. In: *Computers in Physics* 12.4 (1998), pp. 360–370. DOI: [10.1063/1.168689](https://doi.org/10.1063/1.168689).
- [48] B.L. Henke, E.M. Gullikson, and J.C. Davis. “X-Ray Interactions: Photoabsorption, Scattering, Transmission, and Reflection at $E = 50\text{--}30,000$ eV, $Z = 1\text{--}92$ ”. In: *Atomic Data and Nuclear Data Tables* 54.2 (1993), pp. 181–342. ISSN: 0092-640X. DOI: [10.1006/adnd.1993.1013](https://doi.org/10.1006/adnd.1993.1013).
- [49] F. Schäfers and M. Krumrey. *REFLEC: A Program to Calculate VUV/X-ray Optical Elements and Synchrotron Radiation Beamlines*. BESSY. 1996.
- [50] E. D. Palik. *Handbook of Optical Constants of Solids, Vol. 1, 2, 3*. Ed. by New York Academic Press. 1997.
- [51] G. De Ninno et al. “Chirped Seeded Free-Electron Lasers: Self-Standing Light Sources for Two-Color Pump-Probe Experiments”. In: *Phys. Rev. Lett.* 110 (6 2013), p. 064801. DOI: [10.1103/PhysRevLett.110.064801](https://doi.org/10.1103/PhysRevLett.110.064801).
- [52] E. Ferrari et al. “Single Shot Polarization Characterization of XUV FEL Pulses from Crossed Polarized Undulators”. In: *Scientific Reports* 5 (Aug. 2015), 13531 EP. DOI: [10.1038/srep13531](https://doi.org/10.1038/srep13531).
- [53] K. J. Kim. “Polarization characteristics of synchrotron radiation sources and a new two undulator system”. In: *Nuclear Instruments and Methods In Physics Research* 222.1-2 (1984), pp. 11–13. DOI: [10.1016/0167-5087\(84\)90497-6](https://doi.org/10.1016/0167-5087(84)90497-6).

- [54] Y. Li et al. “Study of controllable polarization sase fel by a crossed-planar undulator”. In: *EPAC 2008 - Contributions to the Proceedings*. 2008, pp. 2282–2284.
- [55] E. A. Schneidmiller and M. V. Yurkov. “Obtaining high degree of circular polarization at x-ray free electron lasers via a reverse undulator taper”. In: *Physical Review Special Topics - Accelerators and Beams* 16.11 (2013). DOI: [10.1103/PhysRevSTAB.16.110702](https://doi.org/10.1103/PhysRevSTAB.16.110702).
- [56] J. Bahrtdt et al. “Circularly polarized synchrotron radiation from the crossed undulator at BESSY”. In: *Review of Scientific Instruments* 63.1 (1992), pp. 339–342. DOI: [10.1063/1.1142750](https://doi.org/10.1063/1.1142750).
- [57] F. U. Hillebrecht et al. “Photoelectron diffraction in magnetic linear dichroism”. In: *Physical Review Letters* 75.15 (1995), pp. 2883–2886. DOI: [10.1103/PhysRevLett.75.2883](https://doi.org/10.1103/PhysRevLett.75.2883).
- [58] Y. K. Wu et al. “High-Gain Lasing and Polarization Switch with a Distributed Optical-Klystron Free-Electron Laser”. In: *Phys. Rev. Lett.* 96 (22 2006), p. 224801. DOI: [10.1103/PhysRevLett.96.224801](https://doi.org/10.1103/PhysRevLett.96.224801).
- [59] H. Deng et al. “Polarization switching demonstration using crossed-planar undulators in a seeded free-electron laser”. In: *Phys. Rev. ST Accel. Beams* 17 (2 2014), p. 020704. DOI: [10.1103/PhysRevSTAB.17.020704](https://doi.org/10.1103/PhysRevSTAB.17.020704).
- [60] E. Saldin, E. Schneidmiller, and M.V. Yurkov. *The Physics of Free Electron Lasers*. Springer Science, 2000.
- [61] <http://emanim.szialab.org/emanim.htm>.
- [62] Y. Ding and Z. Huang. “Statistical analysis of crossed undulator for polarization control in a self-amplified spontaneous emission free electron laser”. In: *Physical Review Special Topics - Accelerators and Beams* 11.3 (2008). DOI: [10.1103/PhysRevSTAB.11.030702](https://doi.org/10.1103/PhysRevSTAB.11.030702).
- [63] G. Geloni, V. Kocharyan, and E. Saldin. “Improvement of the crossed undulator design for effective circular polarization”. In: *FEL 2011 - 33rd International Free Electron Laser Conference*. 2011, pp. 61–64.
- [64] T. Tanaka and H. Kitamura. “Improvement of Crossed Undulator for Higher Degree of Polarization”. In: *AIP Conference Proceedings* 705.1 (2004), pp. 231–234. DOI: [10.1063/1.1757776](https://doi.org/10.1063/1.1757776).
- [65] L. Giannessi. Private Communication.
- [66] C. Spezzani et al. “Coherent Light with Tunable Polarization from Single-Pass Free-Electron Lasers”. In: *Phys. Rev. Lett.* 107 (8 2011), p. 084801. DOI: [10.1103/PhysRevLett.107.084801](https://doi.org/10.1103/PhysRevLett.107.084801).

Chapter 6

Coherence Control

The experiments enabled by ultrashort XUV/X-rays FELs, e.g. coherent control of quantum phenomena [1–3], nonlinear optics, etc., require the knowledge, and possibly the control, of the spectro-temporal content of individual pulses. While spatial coherence is also a property of FELs based on SASE [4], the capability of generating temporally coherent pulses is a distinctive feature of seeded FELs. Indeed, this is a natural consequence of the principle on which a seeded FEL relies: before emitting radiation, electrons interact with a coherent source, the seed, and, under given conditions, the latter transmits its coherence properties to the FEL light.

Seeded FELs have therefore the potential to produce spatially and temporally fully coherent pulses [5]. However, the ability to generate fully coherent pulses and shape their spectro-temporal content with high stability on a shot-to-shot basis is extremely challenging, due to the difficulties in precisely controlling the light generation process [6]. In addition to amplification, several factors contribute to the evolution of the electric field during the FEL process. A linear frequency chirp $d\omega/dt$ in the seed affects the emission process, causing a broadening of the spectral envelope [7]. Furthermore, before interacting with the seed, electrons are accelerated and can acquire a time-dependent energy profile. A curvature $d^2\gamma(t)/dt^2$ in the electron energy $\gamma(t)$ produces the same effect as a linear frequency chirp in the seed [8–10] and causes an additional linear frequency offset during amplification due to varying $d\gamma(t)/dt$ along the electron beam [11]. The interplay between these effects determines the FEL temporal phase, which has an impact on the spectral content of the radiated light [12].

In the following, we demonstrate the use of interferometry in the frequency domain to investigate the properties of the seeded FEL pulses. Moreover, we provide the first direct evidence of the temporal coherence of a seeded FEL working in the extreme ultraviolet spectral range and show the way to control the light generation process to produce Fourier-limited pulses. My personal contribution to the topics described in this Chapter has been manning and optimising the machine, as well as collecting data. I also found some optimisation knobs that greatly simplified the measurements, in particular concerning the electron/seed laser alignment in such configurations.

6.1 Phase-Locked FEL pulses

In a coherent control experiment, light pulses are used to guide the real-time evolution of a quantum system. This requires the coherence and the control of the pulses' electric-field

carrier waves. In the following we demonstrate the generation of two time-delayed phase-locked XUV pulses from a seeded FEL. The pulses are produced by two seed replicas locked in phase. The adopted approach also provides a method to investigate the longitudinal coherence of a seeded FEL. As we will see in Chapter 7 another approach to obtain phase-locked FEL pulses relies on the control of the phase of the electron beam with respect to the radiation in different undulator sections.

6.1.1 Experimental setup

The experiment was performed on FEL-1 and exploits the capability of the seed laser to trigger and drive the FEL process and generate coherent and controllable XUV pulses.

Fig. 6.1 shows the experimental setup for the generation of two time-delayed phase-locked pulses implemented at FERMI. The twin seed pulses are produced from a single pulse of the third harmonic of a Ti:Sa laser and temporally split into two pulses after transmission through a birefringent plate. The thickness of the birefringent plate and the group velocity difference for the two plate's orthogonal axes, rotated at 45° with respect to the laser polarization, determine the time delay τ between the two seed pulses. The polarization of both pulses is then adjusted to be parallel to the modulator one using adequate optical components. This ensures optimum seed-electron coupling in the modulator.

The relative phase between the carrier waves of the twin seed pulses $\Delta\phi_{seed}$ is controlled by fine tuning the incidence angle on the plate using a motorized rotation stage with minimum phase step of about $\lambda_{seed}/30$. The two seeds interact with the relativistic electron beam inside the modulator and give rise to a periodic energy modulation at the seed wavelength, which is confined to the position of the two seed pulses within the electron beam (see Fig. 6.1).

The electron beam used for the experiment had an energy of 1014 MeV, a flat ~ 550 A current profile and a duration of about 1 ps. The LPS was characterised by an almost constant energy chirp of the electron beam. The single-shot spectra are recorded by the online spectrometer.

6.1.2 Interferogram creation and measurements

Two mutually coherent pulses delayed in time produce a spectral interference pattern [13]. This configuration can be regarded as the temporal equivalent of the Young's double slit interferometer where the time-delayed pulses play the role of the spatially separated slits, and the spectrometer is the equivalent of the far-field screen. The interference arises in the frequency domain instead of the spatial one.

The resulting interferogram is characterized by the presence of interference fringes, the fringe spacing is inversely proportional to the time delay, and the interferogram envelope is a superposition of the spectral envelopes of the two individual pulses. The fringe distribution within the interferogram contains information on the spectral phase difference of the two interfering pulses. The maximum contrast, defined as the ratio between the difference of the maximum and minimum intensity of the spectrogram over the sum of the same quantities, is maximum when the two interfering pulses are identical, with a regular spacing between the fringes. If the two interfering pulses do not have the same amplitude (identical configuration) the fringes' contrast is smeared out and/or one can observe changes in the uniformity of the fringe pattern.

In the experiment, we were interested in the control of the fringe position inside the interferogram envelope. This can be achieved by controlling the carrier-envelope phase difference $\Delta\phi_{FEL}$ between the two FEL pulses.

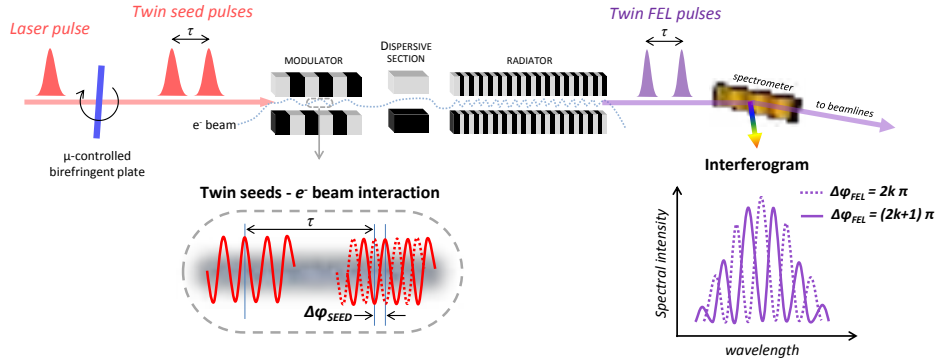


Figure 6.1: HGHG FEL in the two phase-locked pulses configuration. Two time-delayed seed pulses are created by transmission of a single laser pulse through a birefringent plate. The plate is motorized to precisely control the relative phase $\Delta\phi_{seed}$ between the two carrier waves of the twin seeds, which interact with the relativistic electron beam in the modulator. The time-delayed twin FEL pulses are spectrally overlapped and give rise to a spectral interference pattern acquired by an online spectrometer. The relative phase $\Delta\phi_{FEL}$ can be deduced from the distribution of the fringes in the interferogram. As an example, two cases are sketched. For the experiment reported here, $\tau = 280$ fs and the estimated duration of the individual FEL pulse is about 70 - 80 fs.

In the ideal case, for a homogeneous and symmetric interferogram, the relative phase $\Delta\phi_{FEL}$ between the two interfering pulses can be extracted from the position of the fringes as sketched in Fig. 6.1.

As the FEL emission in a seeded scheme is initiated by the coherent structure imprinted on the electrons by the seed laser itself, we expect that the two FEL pulses obtained using the above scheme will be mutually coherent and that their relative carrier-envelope phase can be precisely controlled. The relative phase between the two FEL pulses is related to the one between the two seeds according to

$$\Delta\phi_{FEL} = n \times \Delta\phi_{seed} + C, \quad (6.1)$$

where n is the harmonic number. C is a factor that includes the phase contribution due to the electron beam time-dependent energy profile and a phase difference possibly developed during pulses amplification in the radiator.

6.1.3 Interferogram analysis

Fig. 6.2(a) shows the evolution of the spectral fringes as a function of the rotation angle of the birefringent plate. The minimum rotation step size is $\lambda_{seed}/28.33$, corresponding to $\lambda_{FEL}/5.67$. Fig. 6.2(b) and (c) highlights the fringe displacement for each step. The ability to control the fringe displacement confirms that the phase relationship existing between the twin seed pulses is coherently transferred onto the two FEL pulses. This is a direct consequence of the principle on which a seeded FEL working in the harmonic generation configuration relies.

The analysis of a sequence of shot-to-shot interferograms keeping the twin seed phasing fixed contains complementary information on the stability of the phase locking. A collection of 2000 single-shot interferograms is shown Fig. 6.3(a). The shot-to-shot regularity of the interferogram indicates that the relative amplitude and phase profile of the pulses are conserved. The statistics on the shot-to-shot stability of the central fringe is shown in the

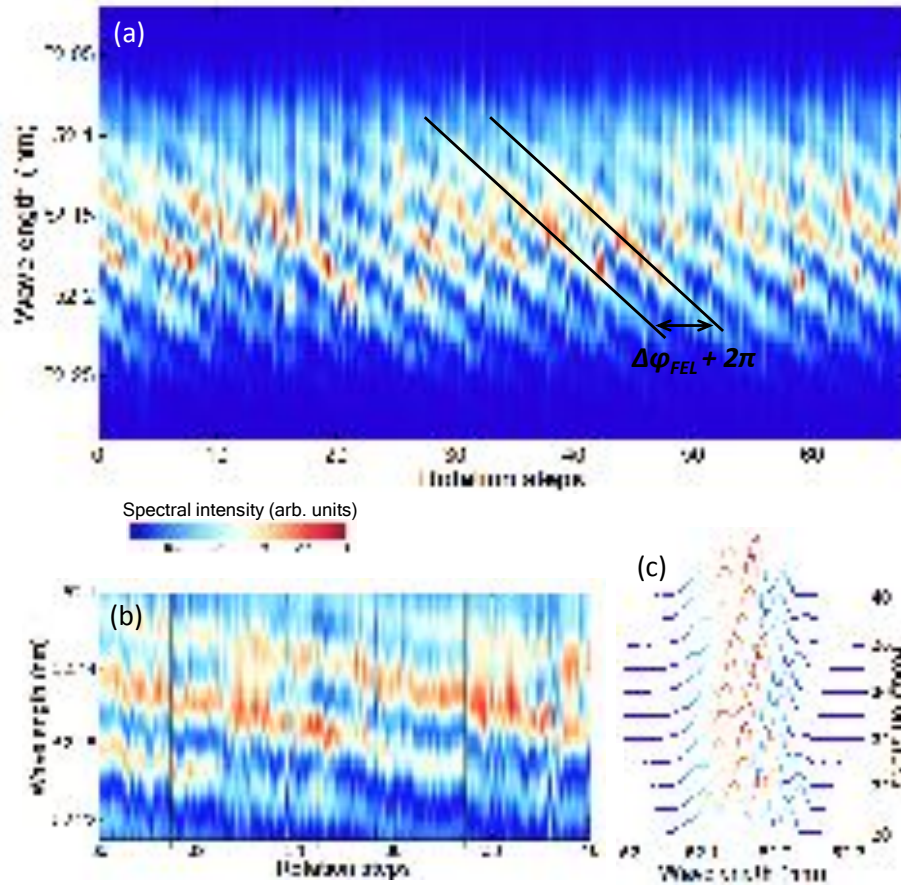


Figure 6.2: Interferogram from two phase-locked FEL pulses. (a) Evolution of the spectral interference fringes as a function of the rotation angle of the birefringent plate (see Fig. 6.1). (b) Zoom of the central part. At each rotation step, 20 consecutive single-shot spectra are acquired. (c) Single-shot profiles extracted from (b), one for each rotation step.

histogram of Fig. 6.3(c). The fringe (RMS) location stability is $\sim FS/12$, FS being the fringe spacing ($= 0.0372$ nm). This implies that the phase stability in between the two FEL pulses is about $\pi/6$ rads, corresponds to temporal fluctuations lower than 15 attoseconds between the carrier waves of two consecutive FEL pulses. The measured fringe instabilities are related to different effects, the main ones were identified to be the shot-to-shot variation of the electron beam properties and the timing jitter between the electron beam and the seed lasers. An example of such dependence is reported in Fig. 6.3(d), where the central interferogram wavelength and the arrival time of the electron beam (see Appendix A) show a significant correlation.

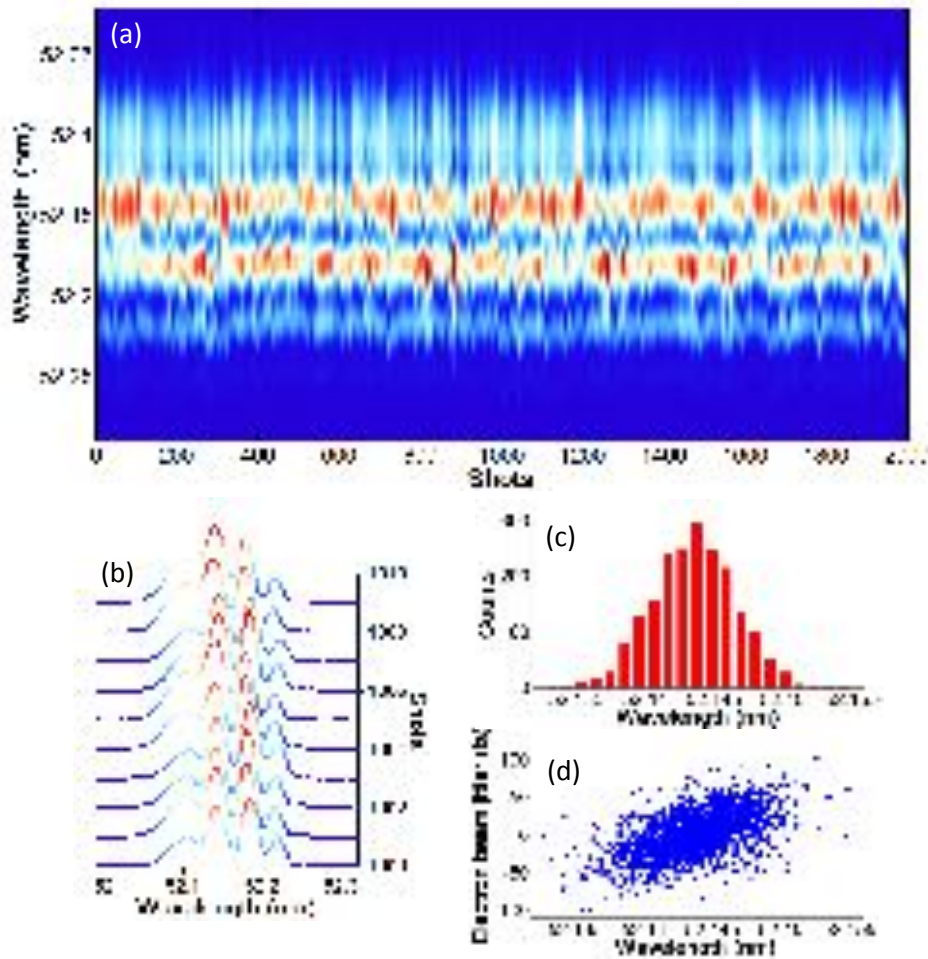


Figure 6.3: Analysis of the fringe stability. (a) Sequence of spectra acquired for a fixed angle of the birefringent plate. (b) Ten single-shot interferogram profiles extracted from (a). (c) Histogram showing the distribution of the position of a central fringe on the spectrometer. (d) Correlation between the fringe position and the time jitter of the electron beam.

Changes in the longitudinal electron beam properties experienced by the two time-delayed seed pulses can lead to the emission of non-identical FEL pulses and/or to variations in their relative phase with respect to the one introduced by the twin seeds. The

described interferometric method therefore can represent a valuable tool for monitoring the FEL stability and performance.

6.1.4 Summary

In conclusion, using an interferometric setup, we demonstrated phase-locking between two pulses from a seeded FEL and studied the control and the stability of their relative temporal properties. It turns out that the physical process on which an FEL relies preserves the mutual coherence driven by the two seed laser pulses. Finally, we identified the non-ideal electron beam as the main source of the remaining phase instability. In the general context of laser-driven light sources, we proved once again the capability to control and manipulate the light emitted by a seeded FEL [6, 14]. The setup is easy to implement. By extending the FEL output from two to a train of multiple phase-locked pulses, a frequency comb like spectrum could be generated [15, 16]. Moreover, the individual control of each pulse, specifically its spectral phase, can allow a vast range of coherent control applications at short wavelengths, such as quantum state holography [17]. The generation of phase-locked pulses could also be naturally extended to the XUV photon energies generated by FEL-2.

6.2 SPIDER reconstruction of FEL pulses

Single-shot characterization and control of the spectral and temporal features of FEL pulses are fundamental prerequisites for experiments aiming at taking full advantage of the laser-like properties of a seeded FEL. Such a characterization is a challenging task, mainly due to the strong material absorption of the light in the XUV-soft-X-rays wavelength range.

Only few effective techniques have been proposed to measure the duration of a femtosecond short-wavelength SASE pulse [18, 19]. In the following we demonstrate the possibility to reconstruct, both in the temporal and spectral domains, the envelopes and phases of a pulse generated by a seeded FEL using the spectral phase interferometry for direct electric-field reconstruction (SPIDER) method [20–24].

6.2.1 The SPIDER algorithm

SPIDER uses spectral shearing interferometry [25, 26] to retrieve the spectral phase of the incident pulse [22]. The spectral interferogram is generated by the interference in between two replicas of the pulse one wants to investigate. The replicas need to be identical one to another except for a shift in frequency with respect to each other [20].

Writing the electric field of the pulse one wants to characterize, in the frequency domain, as $E(\omega) = |E(\omega)| \exp(i\phi(\omega))$, the SPIDER signal reads

$$S(\omega) = |E(\omega)|^2 + |E(\omega + \Omega)|^2 + 2|E(\omega)||E(\omega + \Omega)| \cos(\phi(\omega) - \phi(\omega + \Omega) + \omega\tau), \quad (6.2)$$

where Ω is the spectral shear and τ is the temporal distance between the two pulses. The analysis of the interference pattern allows retrieval of the spectral phase $\phi(\omega)$ of the pulse, for a set of discrete frequencies separated by Ω [22], through an inversion routine [21]. The quantity $|E(\omega)|$ can be directly obtained from $S(\omega)$ or measured independently. A schematic description of the SPIDER algorithm is shown in Fig. 6.4.

The reconstruction procedure for recovering the spectral phase information from the interferogram is based on the Fourier transform of the sampled data, which is composed of three peaks, separated in time [21, 28]: a single “DC” peak due to the constant term in Eq. (6.2) near $t = 0$ and two “AC” sidebands due to the cosine term, located at $t = \pm\tau$.

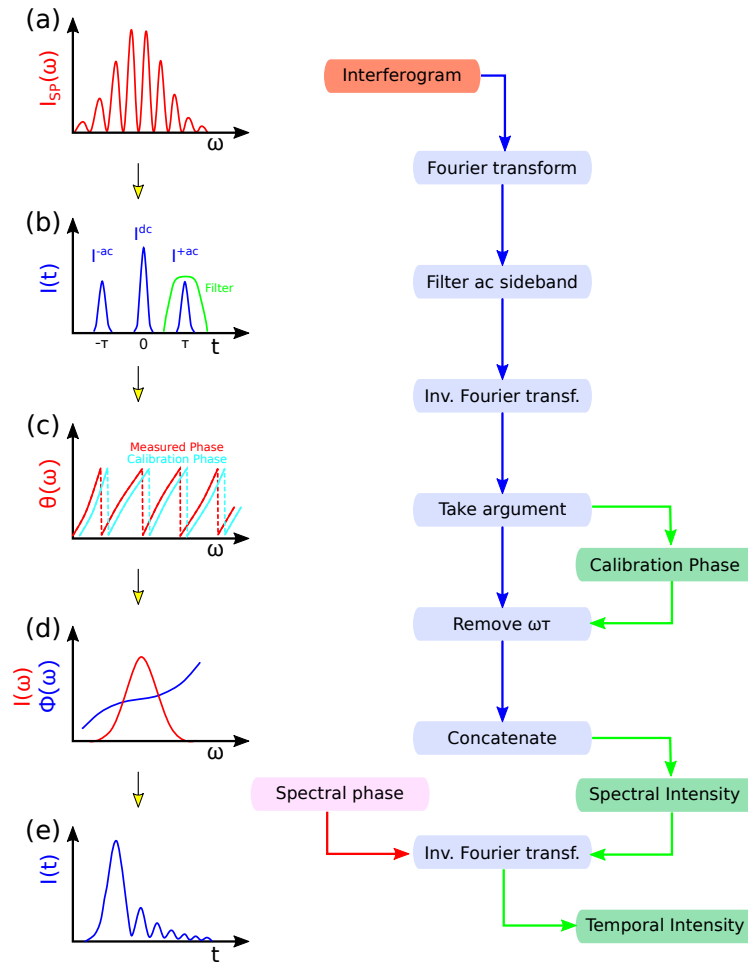


Figure 6.4: Schematic representation of the SPIDER reconstruction algorithm. After the interferogram is recorded (a) the Fourier transform of the signal is performed (b), which is composed of three peaks. By proper filtering one of the two “AC” sidebands and the “DC” peak and successive Inverse Fourier transform (c), it is possible to recover the argument of the cosine (Eq. (6.2)). Through a concatenation of this phase difference data, the spectral phase can be recovered (d). The temporal profile can be finally recovered by carrying out a Fourier transform of $E(\omega)$ (e). Image reproduced from [27].

The phase information is contained in the sideband peaks only and each of them contains all of the information [22]. By proper filtering the DC peak and one of the sidebands, and successive inverse Fourier transform, one can recover exactly the argument of the cosine term in Eq. (6.2). The phase term linear in the pulse separation ($\omega\tau$) can be removed by subtracting a calibration trace. The remaining phase data corresponds to the phase difference between the two frequencies in the pulse pair separated by the spectral shear. Through a concatenation of this phase difference data, the spectral phase can be recovered [29].

The temporal profile $|E(t)|$ and temporal phase $\phi(t)$ can be finally recovered by carrying out a Fourier transform of $E(\omega)$.

6.2.2 Generation of the interferogram

As mentioned, the electron-beam energy is generally characterized by a time-dependent profile. If two seed replicas separated by a time interval τ overlap with a quadratic zone of the $\gamma(t)$ curve, two FEL pulses, separated by the same temporal distance of the two seeds, are generated. The FEL pulses are also shifted in frequency by a shear Ω depending on the derivative of the quadratic curvature of the beam energy profile. If the electron beam properties are sufficiently homogeneous, the generated FEL pulses have equal intensities and temporal phases, satisfying the condition for the application of the SPIDER algorithm.

For the experiments reported in the following the electron beam energy was ~ 1 GeV, the energy spread ~ 150 keV, the slice emittance ~ 1 mm mrad and the peak current ~ 600 A on a flat profile of ~ 1 ps. In these conditions, the core of the electron beam, corresponding to the highlighted region in Fig. 6.5(a), is characterized by a dominant quadratic curvature of about 6.5 MeV/ps^{-2} in the beam energy profile $\gamma(t)$.

The seed replicas to generate the twin FEL pulses were obtained by splitting the pulse of the third harmonic of a Ti:Sa laser by means of adjustable polarization rotation and a birefringent plate, similar to the one described in the previous experiment. As the seeded FEL pulse properties critically depend on the seed laser properties, we manipulated the seed temporal duration and chirp using an adequate calcium fluoride lamina and/or an optical compressor based on transmission gratings. The seed wavelength was 261 nm and the replica separation $\tau = 230$ fs. The FEL was operated at $n = 5$ (i.e., 52.2 nm). At the end of the radiator, this results in the generation of two FEL pulses separated in time by τ and shifted by a frequency Ω , which is directly proportional to the amount of electron-energy quadratic chirp.

The twin FEL pulses yield a spectral interferogram, cfr. Fig. 6.5(c) on which the SPIDER algorithm relies that was recorded using on the on-line PADReS photon spectrometer [30]. As shown in Fig. 6.5(b), the interferograms evolve as a function of the relative delay between the seed replicas and the electron beam. Vertical cuts of the map provide single-shot interferograms, see Fig. 6.5(c). As expected, the central wavelength of the interferograms generated by the electrons in the quadratic region displays a linear shift. The good contrast of the interference fringes is a clear indication of the similarity of the interfering pulses. The measured shift between spectra separated by the temporal distance τ corresponds to the spectral shear Ω . For the experiments the maximum possible value of τ is determined by the extension of the highlighted region in Fig. 6.5, where the electron-beam energy profile is characterized by a dominant homogeneous quadratic dependence. The shear Ω is then determined by the amount of such a quadratic chirp. Outside this region, higher-order non-linear terms become non-negligible. This makes it impossible to generate (almost) identical FEL pulses and, therefore, apply the SPIDER reconstruction. In our working conditions, $\Omega = 1.7 \times 10^{13}$, which corresponds to $\Delta\lambda = 2\pi\Omega/\lambda^2 \simeq 0.025$ nm ($\lambda = 52.2$ nm).

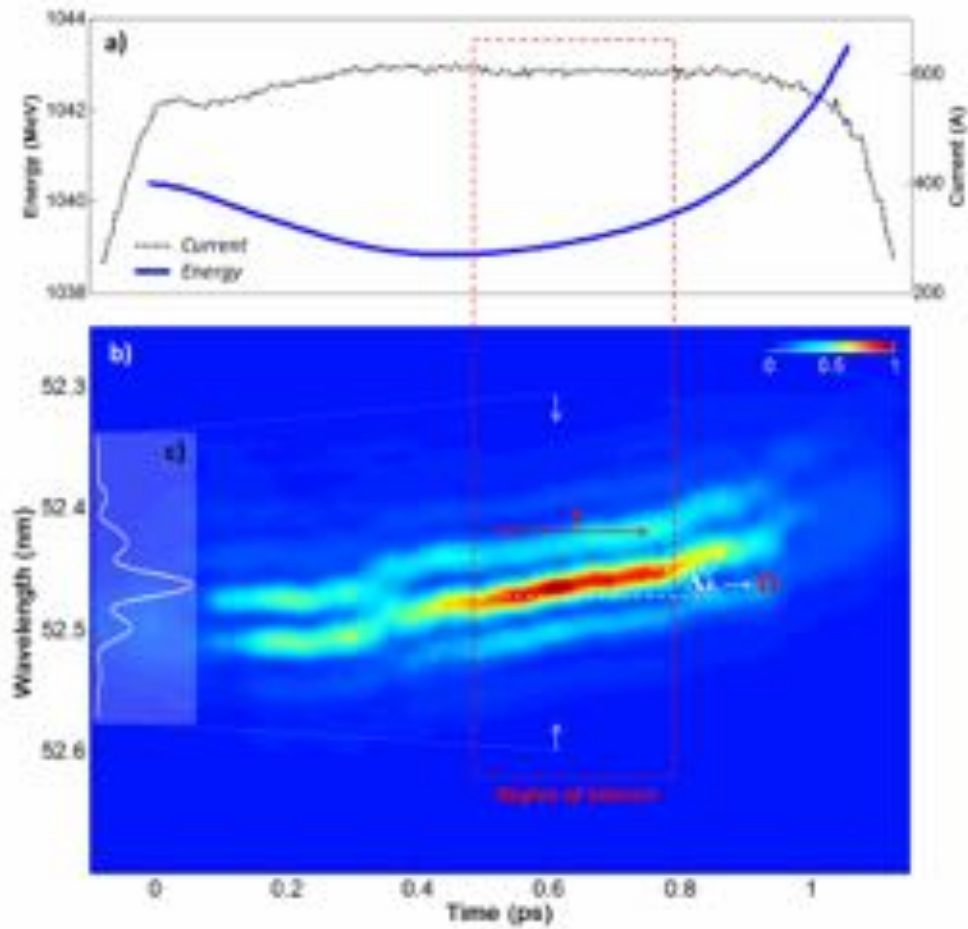


Figure 6.5: Generation of the FEL interferogram. (a) Energy and current time-dependent profiles of the FERMI electron beam (the bunch head comes at smaller times). In the highlighted region, the energy profile is characterized by a dominant and constant quadratic term. (b) FEL interferograms as a function of the temporal position of the leading seed pulse with respect to the electron beam. The region of interest corresponds to the overlap between the seed replicas and the electron-beam quadratic region. Also shown is the definition of the parameters τ and Ω . For the reported experiment, $\Omega = 1.7 \times 10^{13}$ Hz. (c) Vertical cut of the map, providing a single-shot interferogram. Image reproduced from [5].

6.2.3 Analysis of the interferogram

The interferograms in the region of interest highlighted in Fig. 6.5(b) were used to carry out the SPIDER analysis of the FEL pulse.

Figure 6.6 shows the result of the reconstruction in the spectral (Fig. 6.6(a)) and temporal (Fig. 6.6(b)) domains for an interferogram located in the middle of the region of interest. The temporal phase profile has a positive curvature which corresponding to a dominant positive linear frequency chirp on the pulse. This is consistent with the parameters of the machine, as both the electron beam energy and the seed pulses were characterized by a positive chirp. The obtained spectral bandwidth and pulse duration are, respectively, 6.3×10^{-2} nm and 71 fs (FWHM). The value of the bandwidth is very close (within a few per cent) to the one obtained by directly measuring the spectrum of a single FEL pulse, generated by one of the seed replicas. According to the existing theory [10], the FEL pulse duration, Δt_{FEL} , is expected to scale approximately as $\Delta t_{seed} \times n^{-1/3}$, where Δt_{seed} is the duration of the seed pulse. Using the parameters of the experiment the expected FEL pulse duration is 73.7 fs (FWHM), in good agreement with the reconstructed value. Notice that the time-bandwidth product, supposing a Gaussian profile of the pulse, is a factor 1.1 above the Fourier limit.

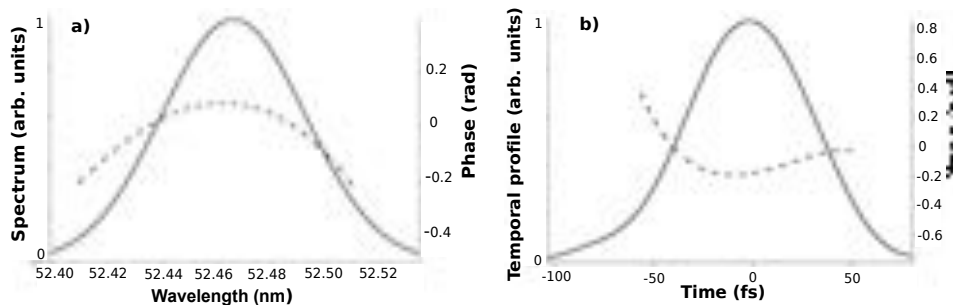


Figure 6.6: Spectro-temporal reconstruction of an FEL pulse. (a) Reconstruction of the spectral envelope and phase from an interferogram acquired in the middle of the region of interest shown in Fig. 6.5(b). (b) Reconstruction of the temporal envelope and phase. Due to the constraints in the choice of the working conditions, the tails of the temporal phase may be affected by spurious high-frequency terms. For this reason, the phase plots are truncated before the possible appearance of the artificial distortion (see also Fig. 6.7). Image reproduced from [5].

6.2.4 Reproducibility of the spectro-temporal reconstruction

The reproducibility of the presented method is demonstrated by comparing the reconstructions obtained for different positions in the region of interest and for different FEL shots, as reported in Fig. 6.7(a,b). Here lines with the same colour represent the reconstructions obtained from three consecutive interferograms at different seed laser-electron beam delays. One can see that the reconstructions are very similar between each other and the observed fluctuations in bandwidth and pulse duration are smaller than 10%, confirming also the stability of the machine.

We also repeated the experiment using two seed replicas with a negative linear frequency chirp and a duration of 180 fs (FWHM). The results, shown in Fig. 6.7(c,d), demonstrate a change in concavity of both spectral and temporal phases with respect to the previous case. This result shows that the chirp on the seed laser dominates the electron beam (energy) one.

The calculated time-bandwidth product results to be a factor 1.2 above the Fourier limit in this case, as the spectral bandwidth is 4.8×10^{-2} nm and the FEL pulse duration is 99 fs.

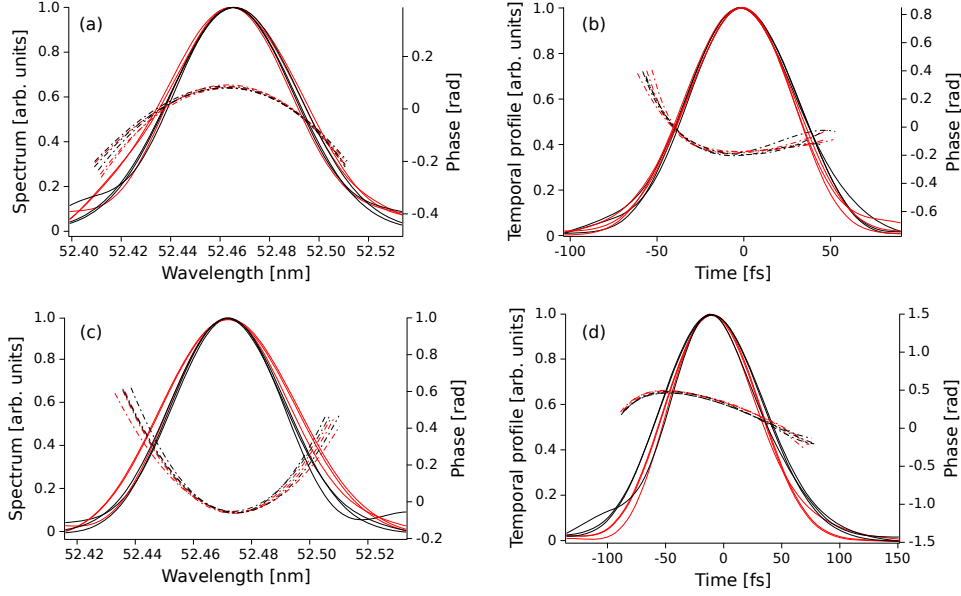


Figure 6.7: Statistical analysis of spectro-temporal reconstructions. *a,b*, Positive linear frequency chirp on the seed replicas (quadratic temporal phase: about 1 fs^{-5}): Reconstructions obtained from three consecutive FEL shots (lines of the same color) at fixed delay and for two different delays (represented by black and red colors) separated by 65 fs within the region of interest shown in Fig. 6.6(b). Continuous line: spectral and temporal envelopes; dotted lines: spectral and temporal phases. *c,d*, Negative linear frequency chirp on the seed replicas (quadratic temporal phase: about -4.5 fs^{-5}): Reconstructions obtained from three consecutive FEL shots (lines of the same color) at fixed delay and for two different delays (represented by black and red colors) within the region of interest shown in Fig. 6.6(b). Continuous line: spectral and temporal envelopes; dotted lines: spectral and temporal phases. For the sake of visualization, spectra were centered at the same wavelength. Image reproduced from [5].

6.2.5 Summary

The method we have implemented allows to carry out single-shot spectro-temporal characterizations of femtosecond XUV pulses produced by a seeded FEL. Our measurements also constitute the first direct evidence of the temporal coherence of a seeded FEL pulse in the XUV wavelength range. The comparison between the results reported in Fig. 6.7 for the two different seed conditions paves a way to fully control the FEL spectral and temporal properties by properly adjusting the seed laser chirp. This opens the way to the generation of flat-phase Fourier-limited femtosecond pulses in the XUV region using a seeded FEL, as we will see in the remaining part of this Chapter. The results are in agreement with previously developed theory. The described approach is independent of the wavelength of the radiation and can therefore be implemented on present and future facilities in order to monitor and shape the properties of a seeded FEL pulse.

6.3 Spectro-temporal shaping of seeded FEL pulses

By taking inspiration from the results reported in the previous section, we carried out a series of experiments aimed at demonstrating the possibility of fully controlling the spectro-temporal content of FEL XUV pulses by properly tuning the seed laser operating parameters. The results constitute the first experimental evidence of Fourier limited pulses from an FEL in the XUV spectral range. The possibility of tailoring the spectro-temporal content of intense short-wavelength pulses represents the first step towards efficient nonlinear optics in the XUV to x-ray spectral region and will enable precise manipulation of core-electron excitation using, e.g., coherent quantum control.

6.3.1 How to control the FEL pulse shape

As we have seen in Chapter 2, the FEL output at the n^{th} harmonic is driven by the electron bunching factor b_n , that can be written as [7, 10, 31]

$$b_n(t) = e^{-n^2 B^2/2} J_n(-nBA(t)) \exp(in(\phi_s(t) + \phi_e(t))), \quad (6.3)$$

where B is the dispersive section strength [10], J_n is the n^{th} order Bessel function, and $A(t)$ is the time-dependent energy modulation (normalized to the electron energy spread σ_γ), which is proportional to the envelope $a_0(t)$ of the seed laser electric field

$$a(t) = a_0(t) \sin(\omega_0 t + \phi_s(t)), \quad (6.4)$$

ω_0 being the central frequency. The exponent in the last factor, where $\phi_e(t) = (B/\sigma_\gamma)E(t)$, accounts for the slowly varying phase of the seed, i.e. $\phi_s(t)$, and for a possible time-dependent energy profile of the electron beam. As the microbunched beam is injected into the radiator it starts emitting coherent light. Initially the electron beam is rigid and the FEL electric field is directly proportional to the bunching factor in Eq. (6.3). Before saturation occurs [32–34], the shape of the field envelope is preserved despite amplification in the radiator. However, a small additional phase $\phi_a(t)$ due to the amplification process is introduced [8, 9, 12], so that the total FEL phase becomes

$$\phi_{FEL}(t) = n[\phi_s(t) + \phi_e(t)] + \phi_a(t). \quad (6.5)$$

The above equations provide the basis for FEL pulse shaping through the manipulation of the seed envelope $a_0(t)$ and phase $\phi_s(t)$.

Both the electron beam time-dependent energy profile and the phase developed during amplification affect the pulse properties [8–10, 12]. However, these effects can be fully compensated for by properly tuning the temporal phase of the seed laser. For the cases considered here, it suffices to expand each of the individual phase contributions $\phi_s(t)$, $\phi_e(t)$, and $\phi_a(t)$ into a power series in time up to the second order. While a linear-term coefficient $d\phi(t)/dt$ results in an absolute frequency (wavelength) shift [11], a quadratic-term coefficient $d^2\phi(t)/dt^2$ gives rise to a linear frequency chirp in the pulse [7]. A suitable seed laser chirp can then be used to counter the combined effects due to the electron beam quadratic energy curvature and the chirp developed during amplification.

Figure 6.8 highlights how the spectro-temporal content of FEL light can be shaped by tuning the operating parameters. First, Fig. 6.8(a), the bunching envelope, generated here by a Gaussian seed, can be modified by changing the strength B of the dispersive section. With increasing B , the bunching develops modulations as a function of time (Eq. (6.3)) due to the process of electron overbunching and rebunching [35, 36], leading to a pulsed structure. As emphasized above, the FEL pulse temporal shape directly corresponds to the

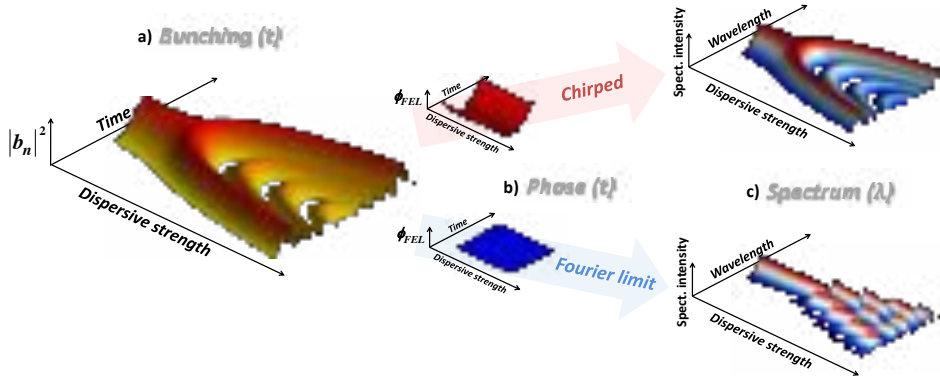


Figure 6.8: FEL pulse shaping through manipulations of the electron bunching envelope and FEL phase. (a) Theoretical bunching envelope ($|b_n(t)|^2$, see Eq. (6.3)), as a function of the dimensionless dispersive strength B . Just before the bifurcation B is optimized for maximum bunching, resulting in a single peak. Increasing B leads to peak splitting due to electron overbunching in the central part. The envelope develops a multipeak structure as a result of electron rebunching when B is increased even further. (c) The spectral map (FEL spectrum as a function of B) strongly depends on the FEL phase (b). For a significantly chirped FEL pulse there is a direct correspondence between the temporal and spectral domains (top). On the other hand, the spectral map of a Fourier limited pulse (with a flat phase) develops distinctive features with increasing B due to interference between the individual peaks in the multipeak bunching structure (bottom). For the sake of visualization, the bunching and spectral maps are normalized in amplitude for each value of B . Image reproduced from [6].

bunching envelope. Second, manipulating the FEL temporal phase using a chirped seed, Fig. 6.8(b), leads to a drastic modification of the FEL spectral content; see Fig. 6.8(c). While the spectral map (spectrum versus B) of a significantly chirped FEL pulse directly corresponds to its temporal map [37, 38], a Fourier limited pulse with a flat temporal phase shows a distinctively different spectral signature.

6.3.2 Experimental results

We verified the above predictions and demonstrated the possibility of controlling the spectro-temporal content of the FEL pulses with dedicated experiments. As described before, we can manipulate the seed laser chirp either by introducing a proper lamina and/or by using a grating-based optical compressor.

Figure 6.9(a) shows the measured spectral map if a strong positive chirped seed laser ($5.9 \times 10^{-5} \text{ rad/fs}^2$) is used to seed the FEL, that will exhibit a corresponding positive frequency chirp.

The parameters were chosen to be close to the ones of the simulation reported in the top part of Fig. 6.8(c). One can see that the FEL spectrum develops intensity modulations as B is increased, which directly correspond to the intensity modulations in the temporal domain. Excellent agreement between experiment and theory (inset) demonstrates that, despite amplification in the radiator, the FEL pulse envelope is preserved, justifying the use of Eqs. (6.3) and (6.5) to describe the spectro-temporal content of FEL light.

The next experiment, Fig. 6.9(b), was performed with a moderate positive chirp on the seed laser ($6.7 \times 10^{-5} \text{ rad/fs}^2$). Because the total FEL chirp is not high enough to satisfy the condition for the spectro-temporal equivalence [38], the central part of the spectral map

is significantly modified with appearance of intensity islands. Again, a remarkably good correspondence is obtained between experiment and theory.

Based on the two spectral signatures in Figs. 6.9(a) and 6.9(b), the next set of experiments was carried out by putting a negative chirp rate on the seed ($-2.0 \times 10^{-5} \text{rad/fs}^2$). A strong modification of the spectral content versus B with respect to the previous two cases is seen in Fig. 6.9(c), confirming the extremely high sensitivity of the spectral maps to the FEL phase. Experimental data once again fit well with calculations reported in the inset of the same figure.

Remarkably, the spectral signature corresponds to that of a Fourier limited pulse with a flat temporal phase, cfr. Fig. 6.8(c), bottom. The negative chirp rate on the seed compensates the positive chirp in the electron beam energy which was in the experiment $\sim 12 \text{ MeV/ps}^2$, measured at the end of the LINAC, and the chirp developed during the amplification stage. More precisely, because the phase contribution from the electron beam $\phi_e(t)$ is a function of B , the FEL chirp rate varies linearly from about -1 to $9 \times 10^{-5} \text{rad/fs}^2$ in the range of dispersive strengths used in Fig. 6.9(c), going through zero at $B \sim 0.14$, where full chirp compensation is achieved.

6.3.3 Summary

The experimental spectral maps in Fig. 6.9 and their striking agreement with theory, Eqs. (6.3) and (6.5), imply that we are able to fully manipulate the FEL output pulse by finely tuning the seed laser envelope and phase. The dispersive section can be used as an additional tuning knob, e.g. an FEL pulse train with a fixed phase relationship can be obtained by simply increasing the strength of the dispersive section. Our results demonstrate that, by adjusting the seed laser phase, a controllable amount of linear frequency chirp can be transferred to the FEL pulse, which can enable, e.g., chirped pulse amplification [39] on an FEL.

A careful tuning allows generation of Fourier limited pulses with a flat temporal phase. Such pulses are typically used as references in the field of coherent quantum control. Our results therefore enable full spectro-temporal shaping of intense ultrashort pulses in the XUV to soft-x-ray region using methods similar to the ones developed in the visible spectral region [40]. In combination with the possibility of engineering the FEL transverse radiation profile using HGHG [14], this sets the stage for entirely new experiments with full control of pulsed light at short wavelengths.

References

- [1] T. E. Glover et al. “Controlling X-rays with light”. In: *Nat Phys* 6.1 (Jan. 2010), pp. 69–74. DOI: [10.1038/nphys1430](https://doi.org/10.1038/nphys1430).
- [2] D. Avisar and D. J. Tannor. “Complete Reconstruction of the Wave Function of a Reacting Molecule by Four-Wave Mixing Spectroscopy”. In: *Phys. Rev. Lett.* 106 (17 2011), p. 170405. DOI: [10.1103/PhysRevLett.106.170405](https://doi.org/10.1103/PhysRevLett.106.170405).
- [3] K. C. Prince et al. “Coherent control with a short-wavelength free-electron laser”. In: *Nat Photon* 10.3 (Mar. 2016), pp. 176–179.
- [4] C. Pellegrini. “The history of X-ray free-electron lasers”. English. In: *The European Physical Journal H* 37.5 (2012), pp. 659–708. ISSN: 2102-6459. DOI: [10.1140/epjh/e2012-20064-5](https://doi.org/10.1140/epjh/e2012-20064-5).

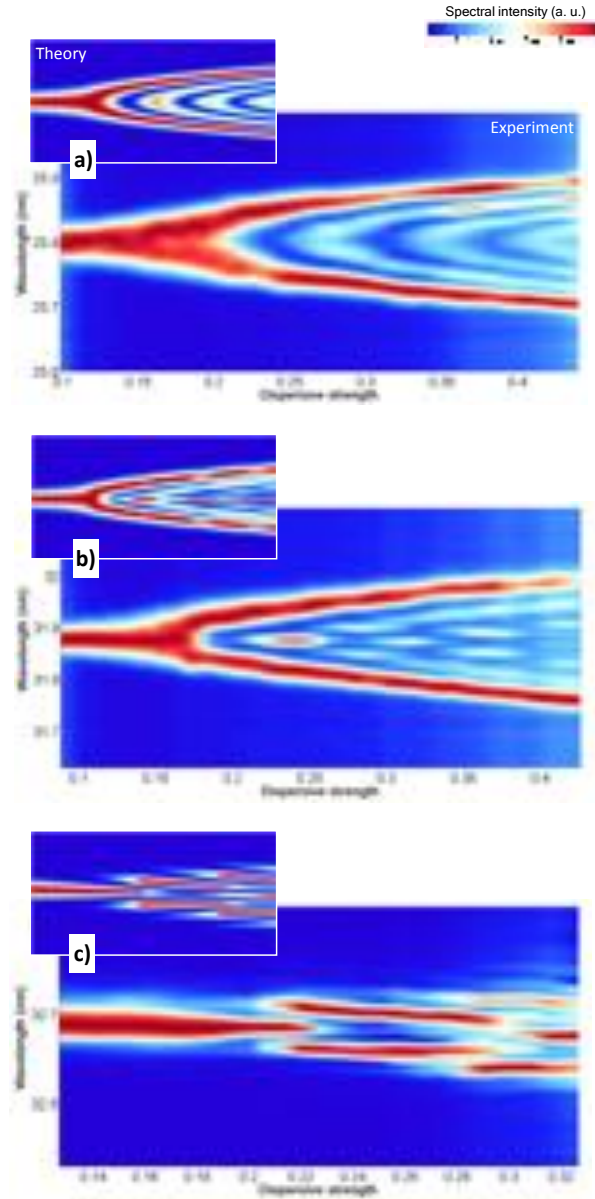


Figure 6.9: FEL pulse spectra as a function of the dimensionless dispersive strength for three different conditions of the linear frequency chirp on the seed laser. (a) Significant positive chirp, (b) moderate positive chirp, and (c) slight negative chirp for chirp compensated FEL pulses. Insets are theoretical spectral maps reproduced using Eqs. (6.3) and (6.5) in the spectral domain. The wavelength shift (spectral map tilting) in (c) is due to the contribution of a linear-term coefficient $d\phi(t)/dt$ from the electron beam energy profile. The experiment in (a) was done at $n = 10$ using all six radiator sections, while for (b) and (c) $n = 8$ and the number radiator sections was 4 and 5, respectively. In all cases, the e-beam energy, energy spread, current, bunch charge, and emittance were ~ 1.3 GeV, ~ 150 keV, ~ 600 A, ~ 500 pC, and ~ 1 mm mrad, respectively. For (a) and (b), the e-beam (positive) quadratic energy curvature was ~ 5 MeV/ps², while for (c) the value was ~ 12 MeV/ps². The data corresponding to each value of B are normalized in amplitude to their maximum value. Image reproduced from [6].

- [5] G. De Ninno et al. “Single-shot spectro-temporal characterization of XUV pulses from a seeded free-electron laser”. In: *Nat Commun* 6 (Aug. 2015). DOI: [10.1038/ncomms9075](https://doi.org/10.1038/ncomms9075).
- [6] D. Gauthier et al. “Spectrotemporal Shaping of Seeded Free-Electron Laser Pulses”. In: *Phys. Rev. Lett.* 115 (11 2015), p. 114801. DOI: [10.1103/PhysRevLett.115.114801](https://doi.org/10.1103/PhysRevLett.115.114801).
- [7] D. Ratner et al. “Laser phase errors in seeded free electron lasers”. In: *Phys. Rev. ST Accel. Beams* 15 (3 2012), p. 030702. DOI: [10.1103/PhysRevSTAB.15.030702](https://doi.org/10.1103/PhysRevSTAB.15.030702).
- [8] A. A. Lutman et al. “Impact of an initial energy chirp and an initial energy curvature on a seeded free electron laser: free electron laser properties”. In: *Journal of Physics A: Mathematical and Theoretical* 42.8 (2009), p. 085405.
- [9] A. Marinelli et al. “Comparative study of nonideal beam effects in high gain harmonic generation and self-seeded free electron lasers”. In: *Phys. Rev. ST Accel. Beams* 13 (7 2010), p. 070701. DOI: [10.1103/PhysRevSTAB.13.070701](https://doi.org/10.1103/PhysRevSTAB.13.070701).
- [10] G. V. Stupakov. *Effect of finite pulse length and laser frequency chirp on HHG and EEHG seeding*. Tech. rep. 14639. SLAC Internal Report 94, 2011.
- [11] T. Shaftan and L.-H. Yu. “High-gain harmonic generation free-electron laser with variable wavelength”. In: *Phys. Rev. E* 71 (4 2005), p. 046501. DOI: [10.1103/PhysRevE.71.046501](https://doi.org/10.1103/PhysRevE.71.046501).
- [12] J. Wu et al. “Interplay of the chirps and chirped pulse compression in a high-gain seeded free-electron laser”. In: *J. Opt. Soc. Am. B* 24.3 (2007), pp. 484–495. DOI: [10.1364/JOSAB.24.000484](https://doi.org/10.1364/JOSAB.24.000484).
- [13] J. Goodman. *Introduction to Fourier Optics*. Greenwood Village, CO: Robert & Company Publishers, 2005.
- [14] P. R. Ribič, D. Gauthier, and G. De Ninno. “Generation of Coherent Extreme-Ultraviolet Radiation Carrying Orbital Angular Momentum”. In: *Phys. Rev. Lett.* 112 (20 2014), p. 203602. DOI: [10.1103/PhysRevLett.112.203602](https://doi.org/10.1103/PhysRevLett.112.203602).
- [15] S.T. Cundiff and Y. Jun. “Colloquium: Femtosecond optical frequency combs”. In: *Reviews of Modern Physics* 75.325 (2003).
- [16] S. A. et al. Diddams. “An Optical Clock Based on a Single Trapped 199Hg+ Ion”. In: *Science* 293.825 (2001).
- [17] C. Leitch et al. “Quantum State Holography”. In: *Phys. Rev. Lett.* 80 (7 1998), pp. 1418–1421. DOI: [10.1103/PhysRevLett.80.1418](https://doi.org/10.1103/PhysRevLett.80.1418).
- [18] I. Grguras et al. “Ultrafast X-ray pulse characterization at free-electron lasers”. In: *Nat Photon* 6.12 (Dec. 2012), pp. 852–857. DOI: [10.1038/nphoton.2012.276](https://doi.org/10.1038/nphoton.2012.276).
- [19] C. Behrens et al. “Few-femtosecond time-resolved measurements of X-ray free-electron lasers”. In: *Nat Commun* 5 (Apr. 2014). DOI: [10.1038/ncomms4762](https://doi.org/10.1038/ncomms4762).
- [20] C. Iaconis and I. A. Walmsley. “Spectral phase interferometry for direct electric-field reconstruction of ultrashort optical pulses”. In: *Opt. Lett.* 23.10 (1998), pp. 792–794. DOI: [10.1364/OL.23.000792](https://doi.org/10.1364/OL.23.000792).
- [21] M.E. Anderson et al. “The effects of noise on ultrashort-optical-pulse measurement using SPIDER”. English. In: *Applied Physics B* 70.1 (2000), S85–S93. ISSN: 0946-2171. DOI: [10.1007/s003400000316](https://doi.org/10.1007/s003400000316).
- [22] T. Shuman et al. “Real-time SPIDER: ultrashort pulse characterization at 20 Hz”. In: *Opt. Express* 5.6 (1999), pp. 134–143. DOI: [10.1364/OE.5.000134](https://doi.org/10.1364/OE.5.000134).

-
- [23] Z. et al. Wu. “Spectral phase modulation and chirped pulse amplification in high gain harmonic generation”. In: *Proceedings of the 2004 FEL Conference*. 2004, pp. 285–288.
- [24] Y. Mairesse et al. “High Harmonic XUV Spectral Phase Interferometry for Direct Electric-Field Reconstruction”. In: *Phys. Rev. Lett.* 94 (17 2005), p. 173903. DOI: [10.1103/PhysRevLett.94.173903](https://doi.org/10.1103/PhysRevLett.94.173903).
- [25] V. A. Zubov and T. I. Kuznetsova. “Analysis of Temporal Characteristics of Optical Pulses by Means of an Acousto-Optical Cell”. In: *Laser Phys.* 2 (1992), pp. 73–76.
- [26] V. Wong and I. A. Walmsley. “Analysis of ultrashort pulse-shape measurement using linear interferometers”. In: *Opt. Lett.* 19.4 (1994), pp. 287–289. DOI: [10.1364/OL.19.000287](https://doi.org/10.1364/OL.19.000287).
- [27] https://en.wikipedia.org/wiki/Spectral_phase_interferometry_for_direct_electric-field_reconstruction.
- [28] M. Takeda, H. Ina, and S. Kobayashi. “Fourier-transform method of fringe-pattern analysis for computer-based topography and interferometry”. In: *J. Opt. Soc. Am.* 72.1 (1982), pp. 156–160. DOI: [10.1364/JOSA.72.000156](https://doi.org/10.1364/JOSA.72.000156).
- [29] C. Iaconis and I.A. Walmsley. “Self-referencing spectral interferometry for measuring ultrashort optical pulses”. In: *Quantum Electronics, IEEE Journal of* 35.4 (1999), pp. 501–509. ISSN: 0018-9197. DOI: [10.1109/3.753654](https://doi.org/10.1109/3.753654).
- [30] C. et al. Svetina. In: *Proc. SPIE 8139, Advances in X-Ray/EUV Optics and Components VI*. 81390J. 2011.
- [31] L. H. Yu. “Generation of intense UV radiation by subharmonically seeded single pass free electron lasers”. In: *Phys. Rev. A* 44.5178 (1991).
- [32] R. Bonifacio C. Pellegrini L. M. Narducci. “Collective instabilities and high-gain regime in a free electron laser”. In: *Opt. Comm.* 50.373 (1984).
- [33] E.L. Saldin, E.A. Schneidmiller, and M.V. Yurkov. “Coherence properties of the radiation from X-ray free electron laser”. In: *Opt. Commun.* 281 (2008), pp. 1179–1188.
- [34] G. Dattoli et al. “Longitudinal dynamics of high gain free electron laser amplifiers”. In: *Phys. Rev. ST Accel. Beams* 16 (3 2013), p. 030704. DOI: [10.1103/PhysRevSTAB.16.030704](https://doi.org/10.1103/PhysRevSTAB.16.030704).
- [35] M. Labat et al. “Pulse Splitting in Short Wavelength Seeded Free Electron Lasers”. In: *Phys. Rev. Lett.* 103 (26 2009), p. 264801. DOI: [10.1103/PhysRevLett.103.264801](https://doi.org/10.1103/PhysRevLett.103.264801).
- [36] D. Xiang et al. “Femtosecond Visualization of Laser-Induced Optical Relativistic Electron Microbunches”. In: *Phys. Rev. Lett.* 113 (18 2014), p. 184802. DOI: [10.1103/PhysRevLett.113.184802](https://doi.org/10.1103/PhysRevLett.113.184802).
- [37] G. De Ninno et al. “Chirped Seeded Free-Electron Lasers: Self-Standing Light Sources for Two-Color Pump-Probe Experiments”. In: *Phys. Rev. Lett.* 110 (6 2013), p. 064801. DOI: [10.1103/PhysRevLett.110.064801](https://doi.org/10.1103/PhysRevLett.110.064801).
- [38] D. Gauthier, B. Mahieu, and G. De Ninno. “Direct spectrotemporal characterization of femtosecond extreme-ultraviolet pulses”. In: *Phys. Rev. A* 88 (3 2013), p. 033849. DOI: [10.1103/PhysRevA.88.033849](https://doi.org/10.1103/PhysRevA.88.033849).
- [39] D. Strickland and G. Mourou. “Compression of amplified chirped optical pulses”. In: *Optics Communications* 56.3 (1985), pp. 219–221. ISSN: 0030-4018. DOI: [10.1016/0030-4018\(85\)90120-8](https://doi.org/10.1016/0030-4018(85)90120-8).

- [40] A. M. Weiner. “Ultrafast optical pulse shaping: A tutorial review”. In: *Optics Communications* 284.15 (2011). Special Issue on Optical Pulse Shaping, Arbitrary Waveform Generation, and Pulse Characterization, pp. 3669–3692. ISSN: 0030-4018. DOI: [10.1016/j.optcom.2011.03.084](https://doi.org/10.1016/j.optcom.2011.03.084).

Chapter 7

Two Color FEL

The advent of FEL sources delivering two synchronized pulses of different wavelengths has made available a whole range of novel pump-probe experiments [1].

The ability to create two synchronized FEL pulses of differing colours has enormous potential for femtosecond time-resolved studies [2, 3] as it opens up unique opportunities for studying the dynamic response in atomic, molecular and solid state systems by selectively tuning electron resonances in atoms. As a consequence it has engendered major research [4–7] and development [8–14] efforts at all FEL facilities worldwide, with the ambition of attaining wide ranging colour tunability and timing control.

Various two-colour configurations have been proposed, both for seeded [2, 8, 9, 12] and SASE [10–12] FEL sources. Initial configurations delivered two short FEL pulses with a controlled temporal separation in the range of a few hundred fs and a small photon wavelength separation ($\sim 1\%$). In the case of SASE, differing photon wavelengths are obtained by dividing the radiator in two slightly detuned sections [10]. In the case of external seeding, the FEL wavelength separation is controlled by acting on the seed laser wavelength and by taking advantage of a residual controllable energy chirp on the electron beam [2, 9]. For self-seeding schemes [15, 16], it has been demonstrated [12] that two seeded FEL pulses can be generated using two distinct Bragg diffraction lines in the self-seeding crystal recombined within the taper-tuned undulators. The possibility of producing two colours with a wider spectral separation (up to 30%) has been demonstrated recently at the SACLA hard X-ray SASE source by using the capabilities of a variable gap undulator [13].

Over the last decade, time-resolved studies made frequent use of short X-ray pulses as a probe that is coupled to an optical laser pump. Femto-slicing at synchrotrons [17–23], high harmonic generation in gases [24–27] and FEL sources [28–33] deliver XUV and X-ray pulses with sub-100 fs duration that have been used for studying the ultrafast dynamics of magnetic [17–28, 30, 32] and structural [21, 29–31] order in optical-laser pump/X-ray probe experiments.

A whole new class of pump-probe experiments that require both pump and probe to be element selective is created by combining the full coherence of seeded FELs with a broad and independent tunability of the two colours.

Tuning the wavelength to an atomic resonance provides the probe with element selectivity, which is of considerable interest especially for magnetic studies. Among the numerous exciting opportunities are studies of exotic properties of matter driven into non-equilibrium transient states by ultrabright X-ray pulses [34–37]. These studies are relevant to inertial fusion [38], planetary interior physics [39] and, more generally, to radiation-matter interactions [40].

Exploring the dynamics of matter driven to extreme non-equilibrium states by an intense ultrashort X-ray pulse is becoming reality, thanks to the advent of FEL technology that allows development of different schemes for probing the sample response at variable time delay with a second pulse [2].

In this Chapter we will describe in details how three different configurations has been successfully implemented at FERMI FEL-1 to obtain multiple-colour FEL pulses. Each configuration has being used in different proof-of-principle experiment in condensed matter and gas phase, demonstrating the possibility to use the machine in these exotic setups that were not anticipated during the design phase.

7.1 Two seed pulses, single radiator harmonic

In this section we report the successful generation of two FEL pulses starting from two external laser seed pulses in the HGHG configuration. The emitted FEL pulses have precise and controllable time delay, wavelength and intensity ratio. The highly coherent FEL pulse pairs are used in a proof-of-principle FEL pump/FEL probe experiment in the XUV wavelength range to examine the dynamics of a thin-metal layer structure.

7.1.1 Generation of twin FEL pulse

The process leading to the generation of ultrafast XUV/X-ray light pulses in a HGHG FEL, as we have seen in Chapter 3, begins with the interaction of an external optical laser, the seed, with the electron beam. If the seed radiation spectrum is contained inside the FEL gain bandwidth, the electron beam longitudinal phase space is sufficiently uniform (in current and energy) and the amplification process occurring in the radiator does not enter into the deep saturation regime, the output radiation properties in terms of spectrum, duration and arrival time are tightly correlated with those of the input seed laser pulse. As proposed in [41], a straightforward method for the generation of multiple pulses from an HGHG FEL consists of seeding the electron bunch with multiple laser pulses. In the specific configuration presented in the following, we use two UV seed pulses at slightly different central wavelengths, $\lambda_{seed,1}$ and $\lambda_{seed,2}$, both independently tunable in the 260-262 nm range, characterized by a temporal duration of 180 fs FWHM, with adjustable time separation and intensity ratio. As schematically shown in Fig. 7.1(a), these pulses are focused in the modulator and interact with the electron bunch. In the experiment the electron beam length was 750 fs, the energy was 1.2 GeV and the beam had a flat ~ 500 -600 A current profile.

As in a conventional HGHG scheme, the electron beam is first energy-modulated as it interacts with the two seed pulses in the modulator. Successive passage through a chromatic dispersion section leads to the formation of two density-modulated regions in which the seed properties are encoded into the electrons. Finally in the radiator, tuned at the n^{th} harmonic of the average of the two seed ($n = 7$ in our case), these two regions emit two temporally and spectrally independent FEL pulses at $\lambda_1 = \lambda_{seed,1}/n$ and $\lambda_2 = \lambda_{seed,2}/n$. The relative delay between the two FEL pulses can be controlled by adjusting the delay between the input seed pulses. As we have seen in Chapter 5, the FERMI radiators have variable polarization thus the output radiation can have any of the permitted output polarization states.

To produce the two seed pulse we introduced the pulse splitting already at the fundamental wavelength (784 nm) of the Ti:Sa regenerative amplifier. The infrared pulses were divided into two parallel, independent channels for third harmonic generation (THG), both equipped with a remotely controlled polarizer to tune the laser power to be used for the

seeding process, a delay stage to manipulate the relative path length and a shutter to block each seed arm independently. The central wavelength of both pulses can be independently tuned in the 260-262 nm range by rotation of the generating crystal. The output ultraviolet pulse durations and separation were measured by a cross-correlator using as a reference a fraction of the pulses from the Ti:Sa oscillator that seed the amplifier section of the seed laser. Different cross-correlation traces recorded during the experiment indicate the absence of any measurable timing jitter or drifts between the two generated ultraviolet pulses.

Using only the first pulse at λ_1 , responsible of seeding the “pump” FEL pulse, a fine scan of the relative seed/electron beam timing (Fig. 7.1(c)) was performed in order to find an optimum position in the leading edge of the electron bunch. This ensures that a sufficiently wide, unused portion of electrons towards the tail could accommodate the second ultraviolet pulse (probe). When both seed pulses were injected into the HGHG FEL, clean, twin peak output spectra were observed if the temporal delay between the two pulses was set in the proper range. The pump-probe delay adopted to perform the experiment reported below was between about 300 and 700 fs, limited on the upper side by the electron bunch length and on the lower one by the seed pulse duration. For shorter delays, interference effects lead to spectral modulation. Fig. 7.1(b) shows a typical spectrometer image of the twin FEL pulses generated with a time delay of 500 fs. One can see that the spectrum of the twin FEL pulses is extremely clean and stable.

The performance of the twin-pulse-seeding scheme in terms of spectral purity and intensity stability compared to single-seed FEL emission is displayed in Fig. 7.2. The results are obtained recording a number of consecutive spectra on both the online spectrometer (Fig. 7.2(a)) and the total FEL intensity with a gas monitor detector (Fig. 7.2(b)). The switching between single and double colour FEL emissions is obtained by blocking one of the seed laser arms, without the need to change the electron beam nor the undulator parameters.

By fitting the two-colour FEL spectra as a sum of two independent Gaussian curves, we estimate a negligible difference between the single and double FEL emissions, confirming the robustness of the pulse generation scheme. Statistical analysis of the spectra in Fig. 7.2(a) shows that the (RMS) bandwidth is about 25×10^{-3} nm ($\sim 0.05\%$ of the central wavelength). As one can see from Fig. 7.2(c) the shot-to-shot peak position (RMS) jitter is about 3×10^{-3} nm ($\sim 0.005\%$ of the central wavelength). The absolute single-wavelength intensities of the two FEL lines, obtained evaluating the area of the spectrum, are comparable to those of single FEL emission, see Fig. 7.2(b). The measured (RMS) shot-to-shot stability is about 15%, as reported in Fig. 7.2(d). In the described scheme, the intensity ratio between the pump and probe pulses can be tuned easily by changing the relative intensity of seed laser pulses or by changing the radiator tuning to favor the growth of one of the pulses over the other.

7.1.2 Proof-of-principle pump and probe experiment

The FEL pulses generated as described above has been used in a proof-of-principle pump-probe experiment, aimed at investigating the temporal evolution of the diffraction pattern generated by a titanium grating, for different intensities of the pump signal. A grating sample was chosen in order to achieve spatial separation of the diffraction patterns generated by the two FEL pulses, in order to distinguish the signal generated by the probe. The wavelength and intensity of each pulse were measured by the gas monitor and the online spectrometer (Fig. 7.1(a)). The maximum pulse intensity for the pump pulse was $30 \mu\text{J}$, corresponding to a fluence F of about 18.5 J/cm^2 on the sample, and was attenuated using a gas cell and/or Al solid-state filters. The diffraction measurements were carried out at the DiProI end station [42] using a $195 \pm 30 \mu\text{m}^2$ spot. As shown in Fig. 7.1(d), the pulses hit the

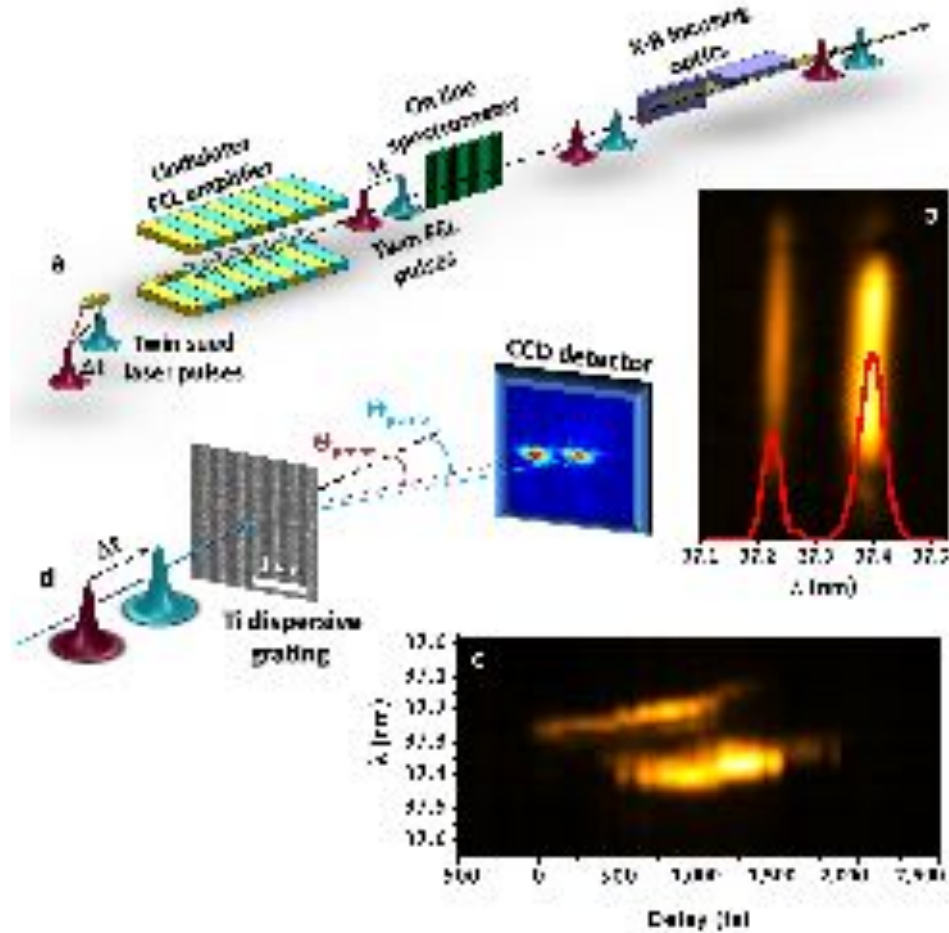


Figure 7.1: Generation and characterization of the twin-seeded FEL pulses and experimental set-up. (a) Two distinct ultraviolet laser pulses interact, with an adjustable delay, with a single electron bunch. Inside the FEL radiator, the two seeded regions emit XUV radiation at different wavelengths. The wavelength and temporal separation of generated twin FEL pulses are determined by the parameters of the seed laser pulses. The spectral purity, pulse intensities and widths of the pulses is monitored by an online spectrometer. (b) Typical spectrum of the twin-FEL pulses. (c) Sequence of FEL spectra obtained during a temporal scan of the seed laser pulse pair with respect to the electron bunch. The zero time is defined as the instant when the first laser pulse interacts with the electron bunch. Increasing the arrival time delay of the laser pulses with respect to the electron bunch, the emission of the second FEL pulse is evident after ~ 500 fs. (d) Layout of the detection system: the twin FEL pulses with different wavelengths, focused by K-B optics (shown in (a)), impinge on the Ti grating (80-nm thick and 165-nm wide Ti strips with 400-nm pitch fabricated on a 20-nm thick Si_3N_4 window) and are diffracted along the horizontal plane. The seventh order diffraction pattern is detected by a CCD camera placed off-axis with respect to the direct beam. Image reproduced from [2].

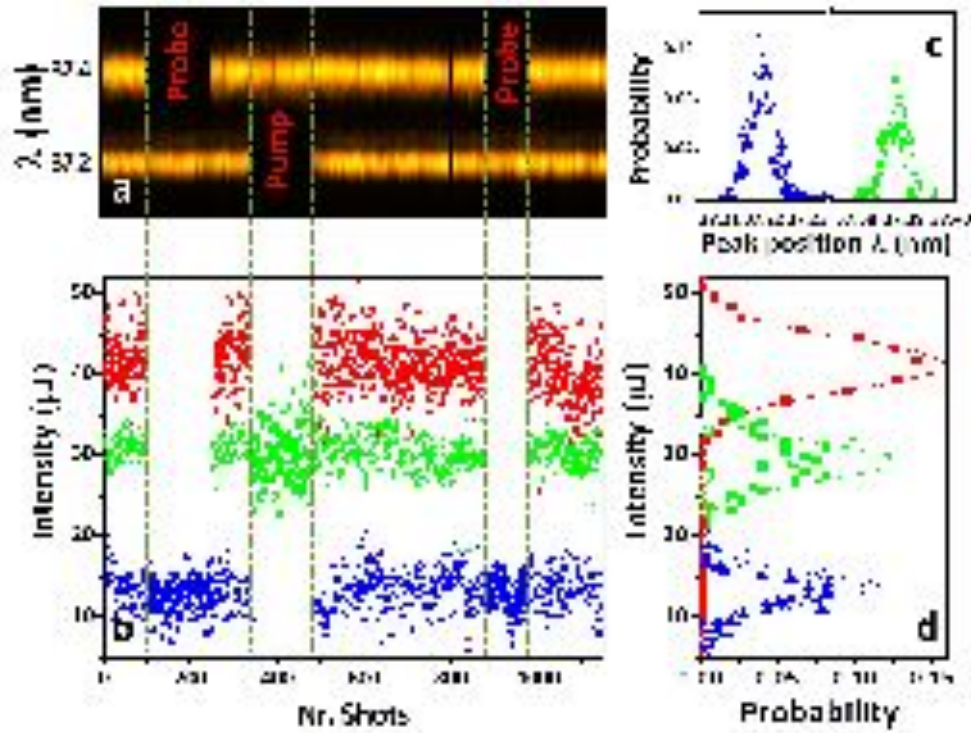


Figure 7.2: Spectral and intensity stability of twin-seeded FEL radiation. Sequence of 1150 consecutive single-shot FEL emission spectra (a) and corresponding intensities (b). Green dash lines highlight the selective block of one of the seed laser arms (pump or probe) in order to suppress one of the FEL pulses. The filled markers identify the FEL emission configuration: double FEL emission using twin laser seed pulses (red circles, total signal), single FEL emission probe signal only (blue triangles) and single FEL emission pump signal only (green squares). The open markers are the absolute intensities of a single pulse (green for pump and blue for probe) for two-colour emission, obtained from the corresponding peak area in the spectra. The probability distributions for the peak wavelength jitter and emission intensity are shown (respectively) in (c) and (d). The colours correspond to the configurations considered in panel (b). Image reproduced from [2].

sample at normal incidence and diffract along directions defined by the transmission grating angles $\theta_{1,2} = \sin^{-1}(N_d \cdot \lambda_{1,2}/b)$, where $\lambda_{1,2}$ are the FEL wavelengths, N_d is the diffraction order of the grating, characterized by a pitch b .

The two-colour pulses were tuned to wavelengths above the Ti $M_{2/3}$ edge, at $\lambda \sim 38$ nm. By tuning to an atomic resonance we become more sensitive in terms of photon deflection angle and absorption, as the monotonic wavelength dependence of both dispersive (δ) and absorptive (β) terms of the complex refractive index $n = 1 - \delta + i\beta$ undergoes sharp changes through the atomic resonances [43]. Consequently the diffraction peak intensities and positions are highly sensitive to the Ti ionization state at the arrival time of the probe pulse. Performing sets of measurements with different samples and varying the fluence, we determined that the “radiation damage” threshold is around 150 mJ/cm^2 .

Figure 7.3(a-c) show the obtained results in the low- F regime ($F < 150 \text{ mJ/cm}^2$) when the pump radiation induces minor changes in the Ti electronic structure. In this “unperturbed” regime the diffraction patterns have the expected peak position and, more relevantly, the two-colour (pump-probe) pattern is a sum of the pump (Fig. 7.3(a)) and the probe (Fig. 7.3(b)) peaks. This is evidenced by the deconvolution of the pump-probe line profile shown on Fig. 7.3(g) in its two radiation components profile (that is, pump Fig. 7.3(e) and probe Fig. 7.3(f)) weighted by their relative pulse intensity measured using the online spectrometer (Fig. 7.3(i-k)).

Figure 7.3(d) shows the single-shot, pump-probe pattern for the high- F regime, which results in a diffraction pattern where the contribution of the probe peak appears strongly attenuated (see also Fig. 7.3(h)). Since the adopted pulse durations and the delay (~ 500 fs) are shorter than the time scales of hydrodynamic expansion of the Ti (1-10 ps) [44, 45], the two pulses probe practically the same grating geometry. Indeed, we estimated that the expansion of the Ti grating line profile for the experimental conditions is smaller than 2.5 nm. Consequently, the distinct difference in the Fig. 7.3(c,d) patterns indicates that the intense pump pulse induces dramatic changes in the Ti electronic structure. In accord with previous studies [46, 47], the high degree of ionization created by the pump shifts the absorption resonances to shorter wavelengths. For wavelengths tuned to the material absorption resonance such shift will induce abrupt changes in the complex index of refraction n , resulting in a decrease of the diffracted peak intensity and width of the probe pulse.

The observed trend can be qualitatively understood in terms of the deposited energy during the pump pulse. In the low- F regime only less than 1% of Ti atoms are ionized by the pump pulse, with negligible effect on the optical properties of the material. Conversely, at high- F , almost all Ti atoms are ionized within a few 10s of fs. The generated primary photoelectrons then thermalize creating high ionization states through secondary electron emission and Auger decay. These events occur at time scales shorter than 100 fs [47, 48] and, as a result, the absorption edge is shifted towards shorter wavelengths [46, 49] and hence the same holds for the curves corresponding to δ and β . Figure 7.4 shows the calculated diffraction line-shape for the low- F (black line) and high- F (red line) regimes. In the latter case, for the probe pulse, we assumed a rigid shift towards a shorter wavelength using the tabulated wavelength dependence of δ and β [43], while no wavelength shift was considered for the pump.

Fig. 7.4(a) shows that the experimental result cannot be reproduced for a small absorption edge shift of 0.5 nm (that is, when the probe wavelength remains within the absorption edge windows) ~ 500 fs after the pump excitation. A fair agreement with experiments requires assuming an absorption edge shift of 2.3 nm (Fig. 7.4(b)): in this case the probe signal (green dash dot line) is quenched.

The trend is similar to the observed photo-induced transparency of Al [35] obtained by high-fluence FEL pulses and to the quenching of the X-ray resonant magnetic scattering sig-

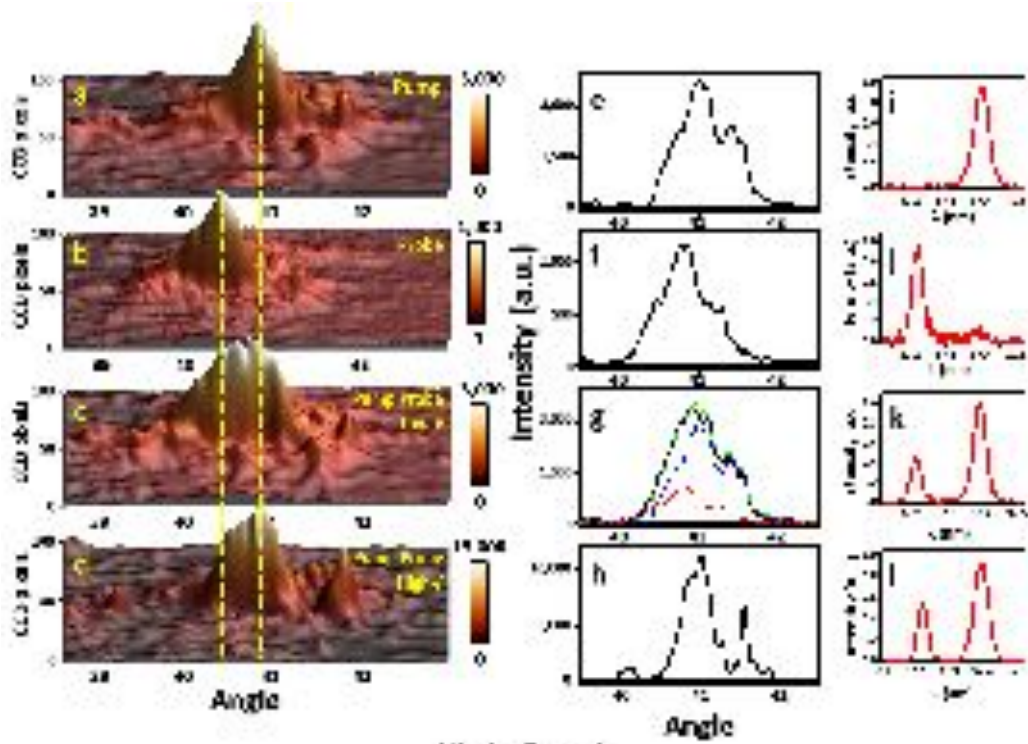


Figure 7.3: Diffraction as a function of the FEL intensity. Diffraction patterns obtained using $\lambda_1 = 37.39 \pm 0.03$ nm (pump) and $\lambda_2 = 37.22 \pm 0.03$ nm (probe) pulses with a pump-probe delay of 500 fs. (a) Single-colour low-F pump (~ 32 mJ/cm² per pulse). (b) Single-colour low-F probe (~ 9 mJ/cm² per pulse). (c) Two-colour low-F pump and probe (pump ~ 31 mJ/cm² per pulse, probe ~ 11 mJ/cm² per pulse). (d) Two-colour high-F single-shot pump and probe (pump ~ 2.5 J/cm², probe ~ 1.0 J/cm²). The low-F patterns in (a-c) are obtained integrating over 150 shots. Yellow dash lines indicate the positions of diffraction peaks for the pump and probe pulses of the low-F unperturbed state. The panels (e,f) show the diffraction line-shape along the dispersive direction of the Ti grating. In (g) the diffraction line profile of the pump-probe pattern (black line) is compared with the sum (dashed green line) of the pump (dashed blue line) and probe (dashed red line) profiles, weighted to the corresponding pulse intensity. In (h) the diffraction line-shape along the dispersive direction of the Ti grating is reported for the pump-probe case, when the pump had a high-F. The featured line-shape and the differences in the profiles of the pump and probe pulses are due to structural imperfections of the grating. The corresponding spectra of the incident beam are shown in the panels (i-l). Image reproduced from [2].

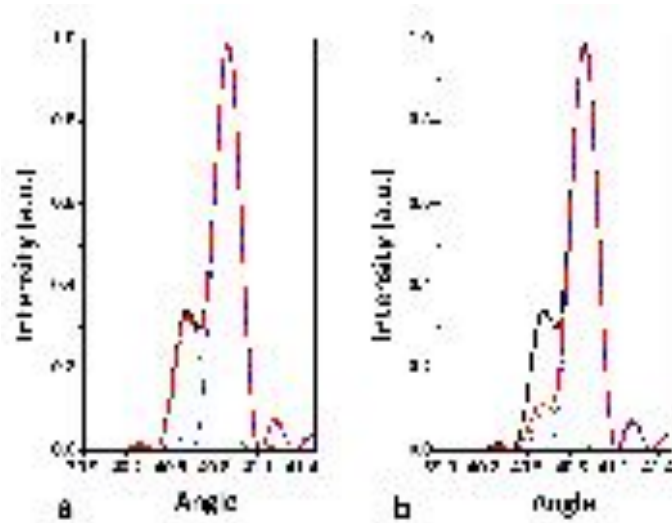


Figure 7.4: Simulated diffraction line-shape. Calculated diffraction line-shape for the Ti grating illuminated by the two twin FEL pulses at 37.2 and 37.4 nm. Black lines are obtained by assuming no wavelength shift of the optical constant (that is, low-F regime). Red lines panels (a,b) show the modification of the diffraction line-shape induced by 0.5 and 2.3 nm shift towards shorter wavelength of both δ and β for the probe pulse. Blue and green dash-dot lines correspond to the diffracted signal from the pump and the probe, respectively. In the simulation, the same experimental ratio of 3:1 between the intensity of the pump and the probe was assumed. Image reproduced from [2].

nal on Co/Pt multilayer systems using very intense FEL pulses [49]. However, the approach reported here has the remarkable potential advantage of providing time resolution in the sub-ps domain, allowing to follow the FEL-induced changes in material electronic structure and non-thermal ion motions.

7.1.3 Summary

We experimentally demonstrated the possibility to generate and use two distinct XUV FEL pulses with finely controllable wavelength and relative time delay by using a twin-pulse, external laser seeding of the HGHG-based FEL source. The FEL twin pulses used here had a relative time delay between 300 and 700 fs and central wavelengths of 37.2 and 37.4 nm, tuned to the Ti $M_{2,3}$ absorption edge. We exploited this newly developed tool to perform the first all-FEL-based, two-colour pump-probe experiment with specially designed Ti grating. For fluences $> 2 \text{ J/cm}^2$ the obtained pump-probe diffraction patterns indicate the occurrence of a photo-induced transparency. This evidences the high degree of Ti ionization created by the intense pump pulse, which results in a sensible shift of the Ti absorption edge to wavelengths shorter than the probe one.

This technique can easily be extended to generate pump-probe pulses with similar wavelength separation in the whole FEL-1 wavelength range. The minimum interpulse delay can be decreased to about 150 fs for the existing seed laser system. Shorter pulse delays comparable with the FEL pulse duration can be obtained by adopting another scheme that seeds with a single, frequency-chirped pulse and where deterministic spectro-temporal pulse-splitting occurs in the deep saturation regime of the FEL [50, 51], as discussed in Chapter 6. The current upper limit of delay between the two pulses can also be extended to above 1

ps by optimizing the FERMI photoinjector and linac in order to produce longer electron bunches with temporally flat output energy distributions. In the particular case reported here, the wavelength separation was limited to about 0.2 nm by the tuning bandwidth of the seed laser THG spectrum.

This limitation, as we will report in the following, can easily be overcome by using the optical parametric amplifier as a source of one of the pulses which could then be tuned to any desired wavelength of the present seed ultraviolet tuning range (that is, 228-262 nm). The other pulse could still be generated by the THG channel at 261 nm.

From a wider perspective, the concepts reported here for generating multiple and multi-colour coherent photon pulses with fully controllable parameters will open up the way to extend the most advanced, table-top ultrafast methods into the XUV/X-ray domain, thus potentially adding nanometre spatial resolution and atomic selectivity to these powerful experimental tools. This will advance our knowledge to the fundamental domains of materials science, paving the road to future nonlinear X-ray technologies that cannot even be foreseen today.

7.2 Two seed pulses, FEL radiator tuned at different harmonics for wide wavelength tunability

In the following we describe a major step forward using a new configuration of FEL-1 to deliver two FEL pulses with different wavelengths, each tunable independently over a broad (30%) spectral range and with adjustable time delay. The FEL scheme makes use of two seed laser beams of different wavelengths and of split radiator sections to generate two XUV pulses from distinct portions of the same electron bunch. The tunability range of this two-colour scheme meets the requirements of double-resonant FEL pump/FEL probe time-resolved studies. The performance of the configuration is demonstrated in a proof-of-principle magnetic scattering experiment in Fe-Ni compounds, by tuning the FEL wavelengths to the Fe and Ni 3p resonances.

Developing FEL sources that can produce two pulses with independently selectable wavelengths for the pump and the probe and with a well-defined time separation obviously widens the potential of FEL radiation for studying the dynamics of a process and makes it possible to associate the pump energy to a specific electronic excitation of a given element. One field that will surely profit from this new tool is magnetization dynamics in 3d-transition-metal and rare-earth based oxides and compounds [19, 20, 23, 52–56]: the presence of highly localized 3d and 4f orbitals and of mediated exchange interactions suggests that associating the pump energy to a specific electronic excitation will influence the magnetization dynamics profoundly, compared to using a non-resonant pump.

In the proof-of-principle time resolved scattering experiment on Fe-Ni compounds described in the following, we use the two-seed configuration to generate, from the same electron bunch, two FEL pulses with up to 30% spectral separation, see Fig. 7.5(a). The pump FEL pulse is used to excite the Fe 3p \rightarrow 3d transition resonantly, while the second FEL pulse, tuned to the Ni 3p \rightarrow 3d resonance, probes the ultrafast Ni magnetization dynamics (Fig. 7.5(b)). The experiment successfully reveals the potential of the aforementioned configuration for investigating structural, electronic and magnetization dynamics in the fields of condensed matter as well as atomic and molecular physics.

7.2.1 Scheme implementation

To implement the configuration the LINAC was operated at 1.3 GeV electron beam energy and 700 pC nominal charge, with moderate compression in order to produce an almost flat 500 A current electron bunch. The chosen settings provided a relatively long (~ 1 ps) electron bunch, satisfying the conditions for an effective twin-seeding with temporal separation of up to ~ 900 fs.

Two FEL pulses with a controlled delay can be produced by seeding the same electron bunch with two seed pulses [2]. Since in the HGHG seeding process the final FEL wavelength is determined mainly by λ_{seed} and it must be close to one of its harmonics, a way for delivering two-colour FEL pulses with very different wavelengths ($>10\%$ separation) relies on seeding the electron beam with two laser pulses and on sustaining the amplification process at both wavelengths independently (Fig. 1a). In order to achieve this, some constraints have to be dealt with. Both seed wavelengths $\lambda_{seed,1}$ (for the probe) and $\lambda_{seed,2}$ (for the pump) have to modulate the electron energy in the interaction region efficiently so their separation must be within the modulator working bandwidth. The dispersive section then converts the energy modulation into an electron density modulation that carries the harmonic components of both $\lambda_{seed,1}$ and $\lambda_{seed,2}$. The electron beam is now ready to emit one of these harmonics, selected by the resonance condition of the radiator (undulator gap). A large separation between the two colours can be obtained by dividing the radiator into two sub-sections (Rad_1 and Rad_2 in Fig. 7.5(a)), one resonant at $\lambda_{FEL,1} = \lambda_{seed,1}/m$ and the other at $\lambda_{FEL,2} = \lambda_{seed,2}/n$, with m and n integers. Since the radiator bandwidths are markedly narrower than the modulator one, we can emit efficiently the pump (or the probe) beam from one radiator sub-section only, while suppressing its amplification in the other, selectively. Finally, constraints on the temporal separation Δt between the two FEL pulses are set by interference between the laser seeds (lower limit) and by the electron bunch duration (upper limit). In the example reported below, we spanned delays ranging from 300 to 800 fs.

The Fe-3p resonant-pump and Ni-3p resonant-probe test experiment (Fig. 7.5) used two FEL pulses tuned to $\lambda_{FEL,2} = 23.2$ nm and $\lambda_{FEL,1} = 18.7$ nm, corresponding to the 11th harmonic of $\lambda_{seed,2} = 255$ nm and to the 14th harmonic of $\lambda_{seed,1} = 261.5$ nm, respectively.

In contrast to the configuration described in the previous section, in this experiment the seed laser was provided by two UV pulses, one at 255 nm generated by an optical parametric amplifier (OPA) and the other at 261.5 nm generated by a third harmonic generation (THG) setup. This approach made the twin-seeding possible at two different UV wavelengths, one of them tunable via the OPA. The intensities of the two pulses could be varied independently through remotely controlled waveplates. The time delay between the two seed pulses was measured using an optical cross-correlator, where each UV pulse was cross-correlated with an IR pulse derived from the ultrafast oscillator that seeds the Ti:Sa amplifier. A remotely controlled delay stage on the THG path was used to set the time delay between the two seed pulses, before recombining them through a 50% beam-splitter. Both seed pulses originate from the same source (laser oscillator and regenerative amplifier) and their relative time delay is very stable [57]. It has been verified that once set, the relative time delay between the two UV pulses (hence between the two FEL pulses) remains stable within less than ± 5 fs over a time span of two hours. This includes both short-term timing jitter and slow timing drifts. The adjustment and long-term stabilization of the spatial coincidence and collinearity of the two seed beams inside the FEL undulator, which are essential for obtaining the coincidence of the two FEL pulses on the sample, were obtained by using a dedicated feedback loop based on independent steering optics for each beam.

The radiator was divided into two sub-sections, Rad_1 and Rad_2, set to resonate with harmonic 14 of $\lambda_{seed,1}$ and harmonic 11 of $\lambda_{seed,2}$, respectively. The $\lambda_{seed,2} = 255$ nm OPA

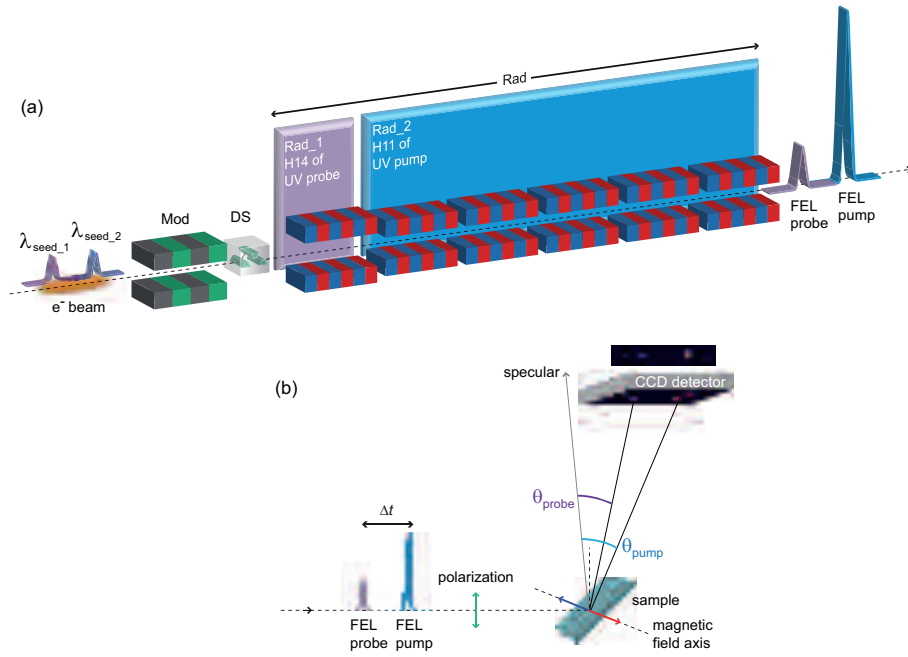


Figure 7.5: Schematic set-up for a two-colour double resonance FEL experiment. (a) Two-colour seeded FEL source configuration: the modulator (Mod), dispersive (DS) and radiator (Rad) sections of the FEL source are outlined. In the modulator section, two optical laser pulses of wavelength $\lambda_{seed,1}$ and $\lambda_{seed,2}$ delayed by Δt interact with the same electron bunch, imposing an energy modulation that is converted into density modulation in the DS. The first radiator sub-section Rad_1 is tuned to the 14th harmonic of $\lambda_{seed,1}$ and the second sub-section Rad_2 is tuned to the 11th harmonic of $\lambda_{seed,2}$, generating the FEL probe and pump pulses, respectively. (b) Magnetic scattering experiment: the two linear p-polarized FEL pulses reach the magnetic grating sample and diffract at different angles according to their wavelengths. The diffracted intensities are recorded by a two dimensional detector (CCD camera). The wavelength separation between pump and probe is detected as a spatial separation at the CCD, while their time separation Δt is defined by the delay between the two seed pulses.

seed produces a localized bunching at all the harmonics including the 11th that matches the resonance in Rad_2, generating 23.2 nm coherent emission which is amplified along the radiator. However, the beam has also bunching at the 18.2 nm 14th harmonic close to the resonant wavelength of Rad_1 (18.7 nm), which may produce unwanted emission. Similarly, the $\lambda_{seed,1} = 261.5$ nm THG seed induces a bunching at 18.7 nm (14th harmonic), which generates the FEL probe pulse in Rad_1, but also at 23.8 nm (11th harmonic) which may excite emission from Rad_2 tuned at 23.3 nm. In both cases, though, the separation between the undesired bunching wavelength and the radiator resonant wavelength is $>2\%$, i.e. larger than the $\sim 0.7\%$ gain bandwidth measured for the radiators [58]. It is the narrow bandwidth of the radiators compared to the modulator that makes it possible to produce time-delayed single frequency pump and probe FEL pulses from the same electron bunch.

We tested different distributions of the six undulator modules over the Rad_1 and Rad_2 radiator sub-sections. We obtained different power distributions between pump and probe by going from one module in Rad_1 and five in Rad_2 to three modules in each sub-section. All configurations provided satisfactory stable conditions for producing two-colour FEL pulses. Since in our test experiment the pump is required to be more energetic than the probe, five of the six available radiator modules were tuned to produce 23.2 nm pulses (Rad_2 in Fig. 7.5(a)), while the remaining module (Rad_1) was tuned to the probe wavelength. It was important, in this configuration, that Rad_1 was the first of the undulator modules, in order to prevent the smearing of the electron density modulation along the radiator section to degrade its performance. We verified also that one can switch readily the FEL pump and probe wavelengths, by reversing the time delay between OPA and THG generated seed pulses and inverting the gap settings of the Rad_1 and Rad_2 radiator sub-sections.

Fig. 7.6(a) shows the spectral distribution of the two UV seed laser pulses and Fig. 7.6(b) shows the FEL pulse energy as a function of the modulator gap, when using only the UV-probe or only the UV-pump seeds. The two curves of Fig. 7.6(b), which are normalized to the same amplitude, illustrate at each wavelength the extreme sensitivity of the FEL intensity to the modulator setting.

A modulator gap of 19.94 mm optimizes the FEL pump emission when seeding at $\lambda_{seed,2}$, while a gap of 19.60 mm is best when seeding at $\lambda_{seed,1}$ to produce the FEL probe pulse. The gap can be used as an adjustable parameter for the fine control of the relative efficiency in the generation of the pump and probe FEL pulses, thanks to the $\sim 3\%$ resonance bandwidth of the modulator. In our case, a good compromise was found at a gap of 19.75 mm, which made it possible to generate both $\lambda_{FEL,1} = 18.7$ nm and $\lambda_{FEL,2} = 23.2$ nm pulses, albeit with a reduced intensity. For the Fe-Ni experiment, the FERMI FEL source was characterized by pulse energies of up to ~ 10 μ J at the pump wavelength and ~ 1 μ J at the probe wavelength using these parameters. The corresponding fluence F at the sample surface was sufficient to reach, in our experiment, the damage threshold and single shot detection conditions for the pump and the probe pulses, respectively.

7.2.2 Resonant-pump/resonant-probe magnetic scattering experiment

We tested the two-colour twin-seeded FEL source by studying the resonant-pump/resonant-probe magnetization dynamics in Fe-Ni samples, using the IRMA reflectometer [59] installed at the DiProI beamline.

The samples were a 20 nm thick permalloy ($\text{Ni}_{0.81}\text{Fe}_{0.19}$ alloy) film deposited on a Si grating and a 12.5 nm thick NiFe_2O_4 layer epitaxially grown on $\text{MgAl}_2\text{O}_4(001)$. Both samples were structured as line gratings with a period of ~ 600 nm. They worked as dispersive elements, separating different wavelengths at the level of the CCD detector [24, 25]. All

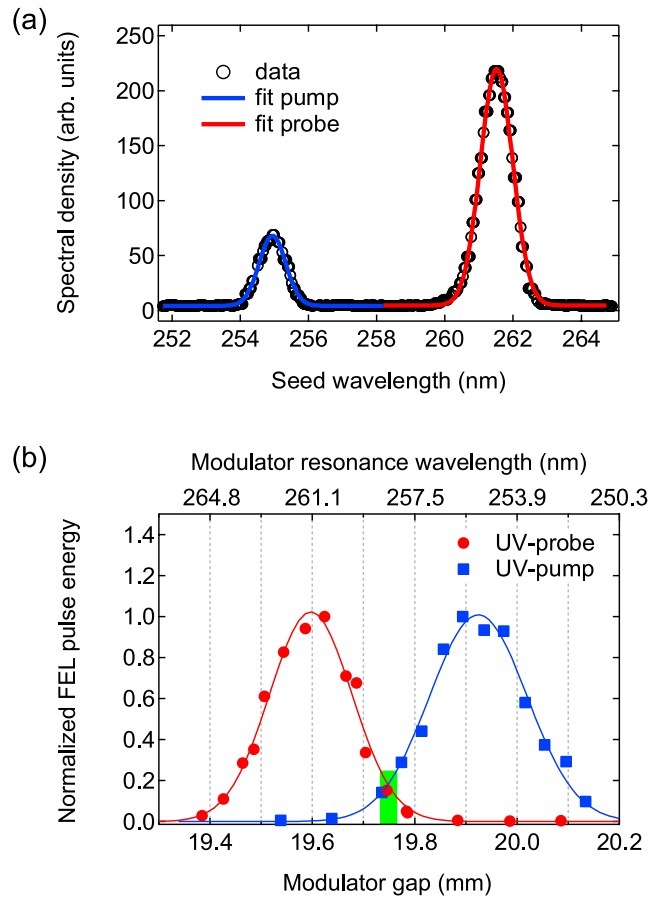


Figure 7.6: Seed pulses and modulator setting. (a) Spectral properties of the UV laser twin-seed source. Lines are Gaussian fits to the $\lambda_{seed,1} = 261.5$ nm (red) and $\lambda_{seed,2} = 255$ nm (blue) probe and pump contributions, respectively. (b) Modulator gap dependence of the FEL output for the two seed laser wavelengths. Red circles and blue squares refer to seeding at 261.5 and 255 nm, respectively. Each point is the average of 100 consecutive FEL shots. Lines represent Gaussian fits to the intensity distributions. The curves are normalized to the same average maximum, showing that tuning the modulator gap to 19.75 mm (green bar) makes it possible to seed with two colours simultaneously, preserving a fraction of the maximum pulse energy.

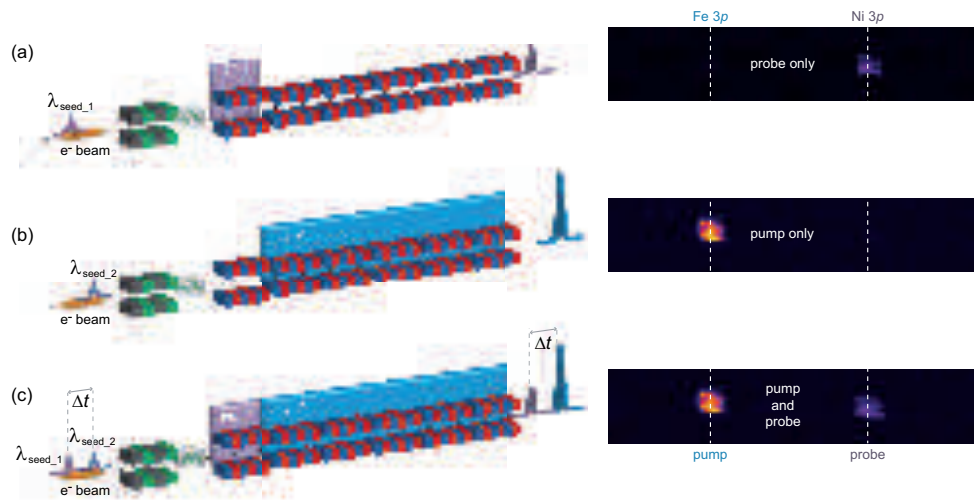


Figure 7.7: FEL source configuration and scattering data recording. Diffracted intensity from the 20 nm thick permalloy grating sample at 46.3° incidence. Data are collected under different seeding conditions (schematics on the left) using a position sensitive CCD detector (images on the right); the 1025×202 pixels images correspond to $13.84 \times 2.73 \text{mm}^2$ and cover $\sim 1.48^\circ$ in scattering angle. (a) The $\lambda_{\text{seed},1} = 261.5$ nm laser pulse is sent through the modulator, turning on the Ni-3p resonant FEL emission at $\lambda_{\text{FEL},1} = 18.7$ nm in Rad_1 (14th harmonic) and no emission from Rad_2. (b) The $\lambda_{\text{seed},2} = 255$ nm laser pulse generates the Fe-3p resonant FEL emission at $\lambda_{\text{FEL},2} = 23.2$ nm in the radiator section Rad_2 (11th harmonic) and no emission from Rad_1. (c) Both seed laser pulses, delayed by Δt , interact with the electron bunch, generating Fe-3p resonant pump and Ni-3p resonant probe FEL pulses, also delayed by Δt .

Bragg peaks generated by the grating samples at different wavelengths fell within the angular acceptance of the detector and could be collected simultaneously (see Fig. 7.7). The FEL polarization was set to linear vertical in order to optimize the sensitivity to the sample magnetization in transverse geometry, i.e. with the external magnetic field applied normal to the scattering plane and parallel to the lines of the grating sample (see Fig. 7.5(b)). Using a horseshoe electromagnet an initial 80 mT pulse field, parallel to the sample surface and normal to the scattering plane was applied. The scattered intensity was collected in an applied field of 20 mT, guaranteeing the sample magnetic saturation. The scattering signal was measured at 46.5 deg incidence, near the Brewster condition, in order to reduce the non-magnetic contributions and maximise the magnetic contrast [24, 25, 60–62].

The pump fluence at the sample was evaluated by correcting the pump energy measured at the source for the transport-line transmission, focal spot size ($\sim 80 \times 80 \mu\text{m}^2$) and angle of incidence. The maximum fluence at the sample was ~ 40 and $\sim 3 \text{ mJ/cm}^2$ for the pump and the probe, respectively.

In the following, the magnetic signal is defined as an asymmetry ratio, i.e. as the difference between scattered intensities measured for opposite signs of the applied field divided by their sum, as shown in Fig. 7.8.

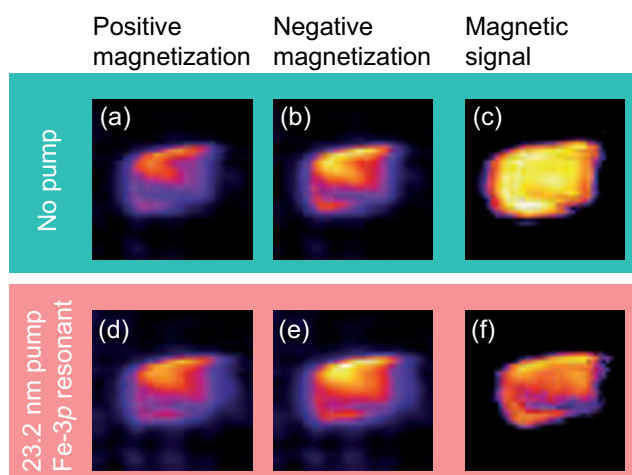


Figure 7.8: Magnetic signal in the scattering data. Diffracted intensity at the Ni-3p resonant probe wavelength with no pump (a-c) and following a Fe-3p resonant pump pulse (d-f). The pump fluence is $F = 8 \text{ mJ/cm}^2$, the delay Δt is 450 fs. (a, d) and (b, e) diagrams refer to a positive and negative saturating magnetic field, respectively. The magnetic signal, expressed as the asymmetry ratio, is shown in (c, f). Each picture is 128×128 pixels, corresponding to $1.73 \times 1.73 \text{ mm}^2$.

At each given delay Δt , the Ni magnetic signal was measured as a function of the pump fluence F . The pump wavelength was tuned either to the Fe-3p resonance ($\lambda_{FEL,2} = 23.2 \text{ nm}$) or off-resonance ($\lambda_{FEL,2} = 25.5 \text{ nm}$), the latter being obtained simply by tuning the radiator sub-section Rad.2 to the 10th harmonic of the $\lambda_{seed,2}$ seed laser wavelength, instead of the 11th. It is worth underlining that according to calculations based on tabulated optical constants [43] the fraction of pump energy absorbed by the sample at 23.2 nm and at 25.5 nm differs by less than 2% for both permalloy and ferrite films. First, we explored the ultrafast Ni demagnetization while varying the delay Δt between the FEL probe and pump by adjusting the delay between the corresponding seed laser pulses. An example of delay dependence spanning the 300-800 fs range is shown in Fig. 7.9 where the Ni magnetic signal

is reported after a Fe-3p resonant pump pulse with fluence $F = 10 \text{ mJ/cm}^2$ (dots and squares refer to Ni-ferrite and permalloy samples, respectively).

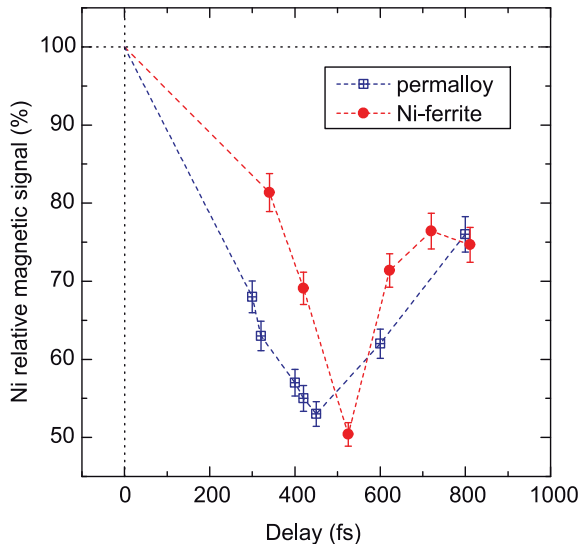


Figure 7.9: Time dependent magnetic signal. Ni demagnetization in the permalloy (blue squares) and the Ni-ferrite (red circles) samples at several delays Δt between probe and pump pulses ($F = 10 \text{ mJ/cm}^2$). Vertical error bars represent the (RMS) spread in the results of 50 measurements. The maximum fluctuation in the pump-probe delay over the measurement duration ($\pm 5 \text{ fs}$) is smaller than the point width. Lines are a guide to the eye.

The asymmetry ratio in the Bragg peak intensity is calculated over a limited detector area of $\sim 100 \times 100 \mu\text{m}^2$ to ensure homogeneous pump fluence and the Ni magnetic signal is normalized to its static value measured with no pump. The main advantage of this two-colour scheme over the one presented before is the ability to tune both $\lambda_{FEL,1}$ and $\lambda_{FEL,2}$ to selected values over a broad range. It is also important to stress that this scheme makes the switching between on and off-resonance pumping fast and easy. As mentioned before, this can be achieved simply by changing the gap of the Rad.2 radiator sub-section in order to select a different harmonic of the $\lambda_{seed,2}$ wavelength.

An example of on/off-resonance pumping is given in Fig. 7.10. It shows the Ni magnetic signal (normalized to its static value) measured at a fixed time delay of $\sim 400 \text{ fs}$ for a FEL pump wavelength tuned to the Fe-3p resonance ($\lambda_{FEL,2} = 23.2 \text{ nm}$, red circles) or off-resonance ($\lambda_{FEL,2} = 25.5 \text{ nm}$, blue squares) as a function of the pump fluence F . The permalloy results (Fig. 7.10(a)) do not reveal a measurable effect of the pump wavelength: both curves show the same F -dependence of the Ni magnetic signal, which attains a $\sim 50\%$ reduction at $\sim 10 \text{ mJ/cm}^2$. On the contrary, pumping at the two on/off-resonance wavelengths results in an apparent difference in Ni demagnetization behaviour when F exceeds $\sim 5 \text{ mJ/cm}^2$ in the case of Ni-ferrite (Fig. 7.10(b)). The observed differences between ferrite and permalloy behaviour, see Fig. 7.9 and 7.10, can be ascribed to the direct hybridization of delocalized Fe and Ni 3d-orbitals in ferromagnetic permalloy vs. indirect exchange (via oxygen) of more localized 3d orbitals in ferrimagnetic NiFe_2O_4 . These early results are intriguing and more studies are under consideration to shed light on the observed pump wavelength dependence.

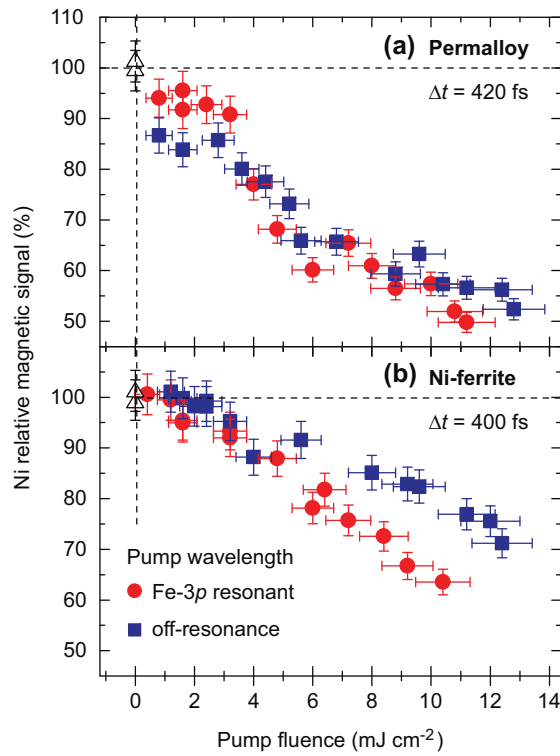


Figure 7.10: Resonant vs. non-resonant pumping. Pump fluence dependence of the Ni demagnetization in permalloy (a) and Ni-ferrite (b) at ~ 400 fs delay, comparing the results for Fe-3p resonant ($\lambda_{FEL,2} = 23.2$ nm, red circles) and non-resonant ($\lambda_{FEL,2} = 25.5$ nm, blue squares) FEL pump pulses. The Ni magnetic signal is reported as the asymmetry ratio in the Bragg peak intensity, normalized to the value measured with no pump (triangles). Horizontal error bars account for pump energy measurement accuracy and source intensity fluctuations.

7.2.3 Summary

We have developed and tested a new FEL setup capable of delivering two-colour time-delayed pulses with independent wavelength tunability over a wide spectral range (18.7 - 25.5 nm). Combined with the seeded scheme of the source, this provides improved conditions for two-colour FEL experiments that require tuning both the pump and the probe to selected atomic resonances. The potential of this two-colour scheme has been demonstrated by a scattering experiment that probes the magnetization dynamics in systems containing two magnetic elements, Fe and Ni. Undoubtedly, it can find original applications in many other fields of condensed matter, atomic and molecular physics.

From a technical point of view the solution that we propose is based on seeding the same electron bunch with two independent laser pulses and on splitting the FEL radiator in two subsections. On the one hand, this solution offers the possibility of selectively tuning the two FEL colours over a very wide range. It may go well beyond the 30% bandwidth demonstrated here, by amplifying different harmonics of the seed wavelengths in each radiator sub-section. On the other hand, using two laser seeds that modulate the same electron bunch and two radiators imposes some constraints on the relationship between the $\lambda_{FEL,1}$ and $\lambda_{FEL,2}$ wavelengths, both in terms of FEL intensity and of possible gaps in the range of wavelengths that can be spanned.

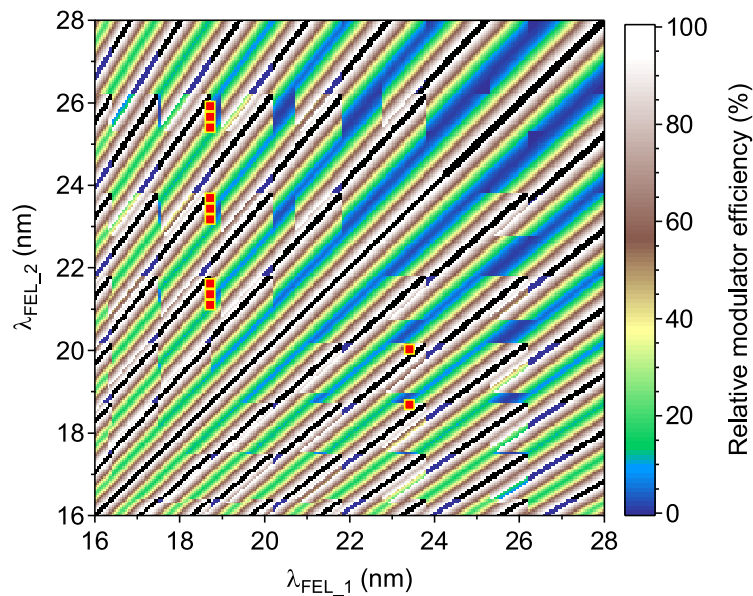


Figure 7.11: Calculated source efficiency over the 16-28 nm range. The colour code represents the relative modulator efficiency at $\lambda_{FEL,1}$ and $\lambda_{FEL,2}$ when the modulator gap is set to resonate with their average value. The calculation uses radiator harmonics from 9 to 16 and λ_{seed} values between 228 and 262 nm. Black dots correspond to $(\lambda_{FEL,1}, \lambda_{FEL,2})$ couples whose λ_{seed} values are within the radiator bandwidth and cannot be produced using the proposed source scheme. Red circles identify the couples of wavelengths explored during the test experiment.

Fig. 7.11 summarizes the calculated source performance when $\lambda_{FEL,1}$ and $\lambda_{FEL,2}$ span the 16-28 nm range, showing that marked intensity variations are present. The colour code represents the relative modulator efficiency for each couple of wavelengths, calculated assuming that the modulator resonance is set to the average value of $\lambda_{FEL,1}$ and $\lambda_{FEL,2}$.

Both seed wavelengths are allowed to span the 228 - 262 nm range covered by the OPA and radiator harmonics from 9 to 16 are considered. The finite modulator bandwidth defines the maximum intensity that can be obtained for each $(\lambda_{FEL,1}, \lambda_{FEL,2})$ combination, hence the efficiency of the two-colour process. The radiator bandwidth imposes limitations on the independent tunability of $\lambda_{FEL,1}$ and $\lambda_{FEL,2}$: black dots forming diagonal lines in Fig. 7.11 mark couples of wavelengths whose corresponding λ_{seed} values are close enough to be amplified in both radiator sub-sections. In this case four FEL pulses, and not two, would be generated and the proposed two-colour scheme does not work properly. Fig. 7.11 shows calculations over the 16-28 nm range that broadly covers the wavelengths used in our test experiment and the black circles localize on the figure the pairs of FEL wavelengths that were actually explored for the Fe-Ni double resonant pump-probe measurements.

In principle, a much wider range of λ_{FEL} values extending up to 90 nm can be covered by using the full set of harmonics available at FERMI.

The accessible delay range between the pump and the probe is limited by the generation of the two FEL pulses from the same electron bunch of finite temporal length. In our experiment, we spanned the 300 - 800 fs range and an extension to 200 - 1000 fs can be envisaged. This remains a strong constraint on the class of dynamic phenomena that can be addressed. Concerning ultra-fast demagnetization, in particular, many systems of interest feature response times of the order of 200 fs [22, 27, 63], at the limit of the accessible range. Further developments can be envisaged for improving the source characteristics, such as the twin-bunch mode recently demonstrated in SASE configuration [11]. The implementation of a similar scheme at FERMI would provide a more efficient bunching at the two wavelengths, a more efficient coupling in the radiator sections and, in fine, a significant increase in the energy per pulse, which could attain tens of μJ for both the pump and the probe. Moreover, using two independent bunches would provide additional flexibility for tuning the two λ_{seed} wavelengths and would soften the constraints on the temporal separation between pump and probe pulses. Another significant improvement, already planned at FERMI, implies a second OPA for tuning both λ_{seed} wavelengths independently, as shown in the calculations of Fig. 7.11. The desired resonant condition for both the pump and the probe FEL pulses could be finely matched. Finally, it is worth remembering that the FERMI radiator section is composed of APPLE-II type undulators [64] delivering radiation of selectable polarization, either circular (right/left) or linear (vertical/horizontal). Therefore our two-colour source offers the possibility of choosing the polarization state of each pulse independently, which may be especially important in atomic and molecular physics studies.

The two-colour XUV source that we have developed at FERMI already has potential for many interesting and original studies in magnetization dynamics and beyond. For instance, it can cover the 3p resonances of any couple of elements among Mn, Fe, Co and Ni, making a wide class of relevant magnetic materials accessible to resonant FEL pump/resonant FEL probe experiments. More generally, it enables the excitation of a particular energy and polarization selected resonance on a well-defined atomic site in a complex system and makes it possible to study its dynamics with the second FEL pulse, by choosing for the probe another electronic subshell or another atomic site. This new source will provide unprecedented opportunities for probing in a highly selective way the dynamics of complex relaxation processes, such as Auger cascades or sequential multiple ionization, and of charge transfer processes in large molecules and clusters.

7.3 One seed pulse, two harmonics locked in phase

While many experiments, previously possible at long wavelengths only, such as multiphoton ionization [65], pumping an atomic laser [66], and four-wave mixing spectroscopy [67] have successfully taken advantage of the unique characteristics of the light emitted by XUV FELs, an important optical technique, coherent control [68–70], has not yet been demonstrated on FELs, because it requires a degree of longitudinal coherence not available in SASE-based sources [71–74].

Coherent control using lasers involves steering a quantum system along two or more pathways to the same final state, and manipulating the phase and wavelength of light to favour this state. The technique represents a major achievement in the quest to understand and control the quantum world.

To achieve coherent control with lasers two light pulses with commensurate wavelengths and almost overlapping arrival times are needed, with full control of the relative phase. In order to implement the scheme we used two FEL harmonics produced by the same electron beam, seeded by a single laser pulse and we properly tuned the radiator in order to have emission at two different FEL harmonics with proper wavelength relation.

In the experiment reported in the following we demonstrated and exploit the longitudinal coherence of two-colour XUV light from FERMI by adopting a radically different approach to tuning the phase with respect to the conventional one implied in laser sources. Instead of generating the light and manipulating the phase subsequently, two FEL pulses with variable phase difference are directly generated. The phase difference is controlled by changing the strength of the magnetic phase shifters between the radiator sections tuned at the two wavelengths. This approach to obtain phase-locked FEL pulses is different from the one described in Chapter 6 as it allows for an arbitrary large separation in the wavelength of the two pulses, that only need to satisfy the harmonic relation.



Figure 7.12: Scheme used in the present study. Red waves indicate schematically the first-harmonic radiation, and blue waves the second-harmonic radiation.

7.3.1 Scheme implementation

Between each pair of undulators of FEL-1, a phase shifter lengthens the path of the electrons by nm-scale increments, thus allowing tuning of the relative phase between the bunched electron beam and the co-propagating photon beam. This is the key to our approach, as n undulators are set to the first harmonic, $6 - n$ are set to the second harmonic and the phase shifters between the two groups are used to adjust the phase difference between the harmonics. In the experiment reported in the following five undulators were set to the first harmonic and the last to the second harmonic, in order to obtain the intensity ratio required. A schematic representation of the setup used during the experiment is reported in Fig. 7.12.

Fig. 7.13(a) shows theoretical simulations of the temporal intensity profiles and relative phase of first and second-harmonic pulses for the wavelengths used in the test experiment described below (~ 63.0 and ~ 31.5 nm). The two pulses show good temporal overlap with calculated pulse durations of ~ 120 and ~ 100 fs while the phase has a mean variation of 0.07 rad at 31.5 nm.

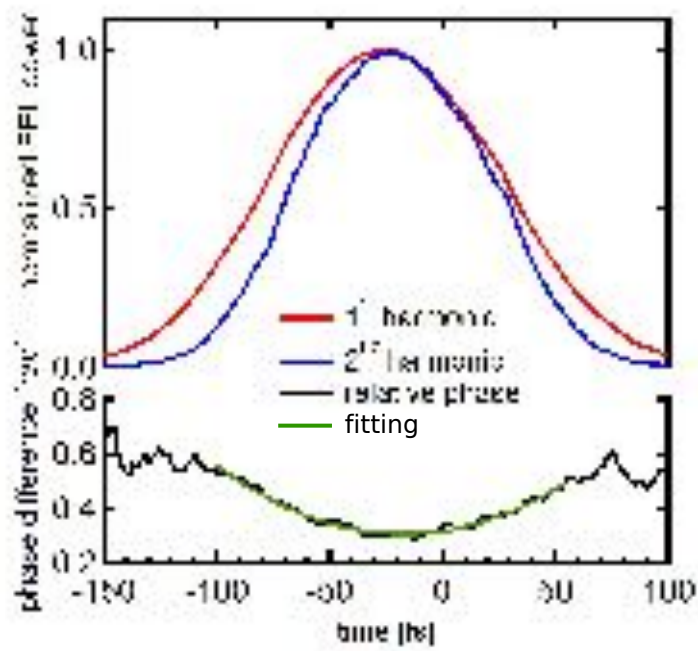


Figure 7.13: Simulated intensities of the first and second harmonics (red and blue curves) as a function of time, and their phase difference (black curve), with a quadratic fit (green curve). Simulations performed by E. Allaria and L. Giannessi.

One of the concerns for this scheme is to have two distinct FEL pulses produced in each of the two undulator sections. To ensure that the condition is met, we measured the intensity of the second harmonic radiation, i.e. at the wavelength of the last undulator, as a function of the phase shifter between the two groups. The corresponding data is reported in Fig. 7.14 for both the intensity monitor signal and the integrated spectrum of the last undulator. The recorded intensity shows a flat dependency on the phase shifter setting, demonstrating that the second harmonic signal that could still be produced in the first five undulators (tuned at the fundamental) does not interfere with the emission of the second undulator group.

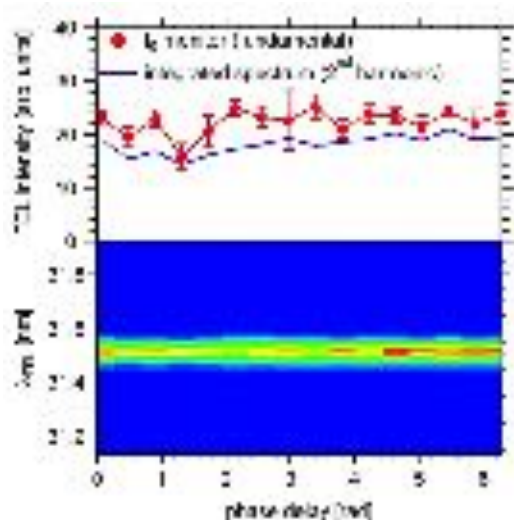


Figure 7.14: Upper panel: intensity of the first harmonic (I_0 monitor, red), monitored by the gas absorption intensity monitor of PADReS, and intensity of the second harmonic, determined from the spectrometer (blue curve). Error bars indicate the (RMS) variation for each measured point. Lower panel: false colour scale spectrum averaged over 21 shots is shown on the vertical axis, against phase delay (the zero is arbitrary).

7.3.2 Test experiment

The aim for the test experiment was to demonstrate the possibility of implementing the coherent control technique to FEL pulses. To do so, we investigated the Velocity Map Imaging (VMI) signal of Ne atoms and looked for asymmetries. The VMI spectrometer works by projecting the sphere of the photoelectrons ionized by the FEL pulses on a plane surface. By proper inversion of the image one is able to recover the angular distribution of the electrons and detect the asymmetry induced for different values of the phase between the two FEL pulses.

For the test experiment, the $2s^22p^5(^2P_{3/2}^0)4s$ resonance of Ne at 62.97 nm (hereafter “4s resonance”) was selected and the first five undulators were tuned accordingly. The sixth undulator was set to radiate at the second harmonic, 31.49 nm, while the phase shifter between the fifth and sixth undulators controlled the relative phase. The wavelengths were optimized in order to have the maximum VMI signal.

Fig. 7.16(a) reports the possible excitation channels for the Ne electrons. $2p$ electrons can be emitted by two quantum paths. Either a single photon excitation, with frequency 2ω , induces the emission of an electron as an s or d -wave, or a double two photon excitation,

each with frequency ω , as a p or f -wave. The second-harmonic field of the FEL ionizes the gas through a first-order process, whereas the first-harmonic field ionizes the gas through a second-order process. The intensities of the two FEL pulses were adjusted in order to have similar ionization rates. Choosing the $4s$ resonance enhances the cross-section for the two-photon process and selects an outgoing p -wave, without a significant f -wave contribution. Due to the non-linear nature of the process [75] and different parity of the outgoing electronic wave packets generated by the two wavelengths, symmetry breaking occurs in the photoelectron angular distribution with respect to the plane perpendicular to the electric vector of the light [76]. The asymmetry depends strongly on the relative phase of the two fields.

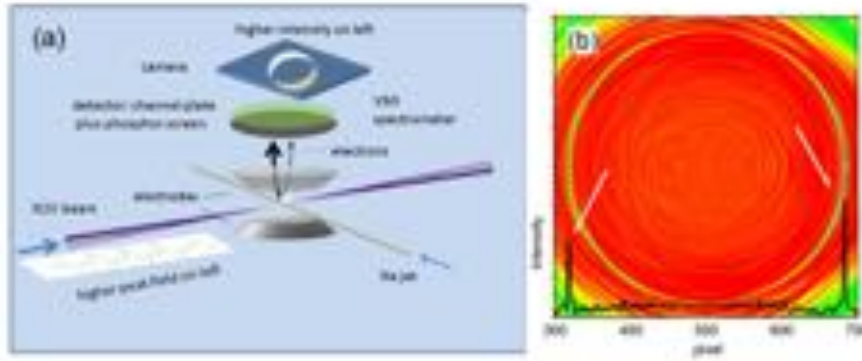


Figure 7.15: (a) Schematic setup. The bichromatic light beam with fixed phase relation crosses the atomic jet of Ne and ionizes the atoms. The Velocity Map Imaging (VMI) spectrometer measures the angular distribution of ejected electrons. The intensity is higher on the left or right, depending on the phase difference. (b) Typical inverted VMI image, 6000 shots. The strong, sharp ring is due to Ne $2p$ electrons, emitted by first and second harmonic light. A line profile across the centre of the image is shown (black line) at the bottom, demonstrating the left-right asymmetry (white arrows).

The measurement setup used for the experiment is schematically shown in Fig. 7.15(a), while an example of a Velocity Map Imaging (VMI) spectrometer image is reported in Fig. 7.15(b). The two colour phase-locked FEL pulses cross an atomic jet of Ne and ionizes the atoms. The VMI spectrometer measures the angular distribution of ejected electrons. The observed intensity on the spectrometer image is higher on the left or right, depending on the phase difference in between the two FEL pulses.

The “left-right” asymmetry was quantified by the parameter A_{LR} ,

$$A_{LR} = \frac{I_L - I_R}{I_L + I_R}, \quad (7.1)$$

where I_L and I_R are the integrated intensities on the left and right of the image.

Figure 7.16(b) shows the asymmetry parameter A_{LR} as a function of the phase shift $\Delta\phi$. Clear oscillations are present with a periodicity of 2π . The phase shift can be converted into temporal delay Δt according to

$$\Delta t = \frac{\Delta\phi}{2\omega}. \quad (7.2)$$

The measured oscillations therefore correspond to a period of 105 attoseconds at the second

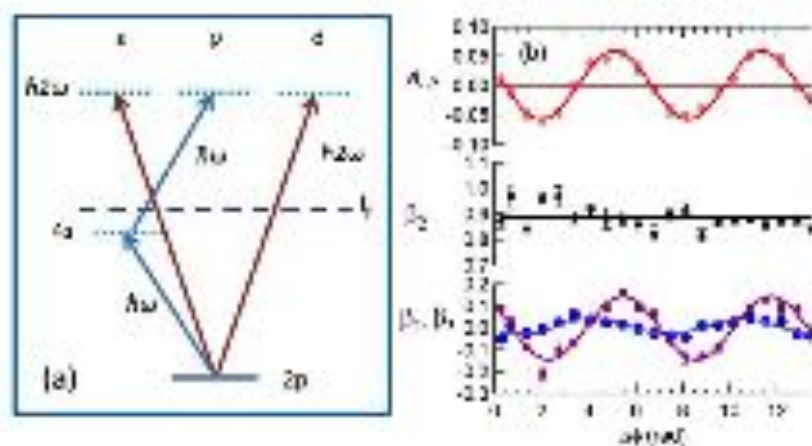


Figure 7.16: (a) Scheme of the present experiment. A photoelectron may be ejected as a p -wave by a two-photon process, or as an $(s + d)$ -wave by a one-photon process. (b) Asymmetry parameter A_{LR} as a function of $\Delta\phi$ (red curve), and β_1 (blue), β_3 (magenta) and β_2 (black) parameters as a function of phase. Markers: experimental data; lines: sinusoidal fits for β_1 and β_3 , linear fit for β_2 .

harmonic. The measurement steps were approximately 10 as, but other scans were performed with steps of 900 zeptoseconds.

To understand the asymmetry in detail, the angular distribution was fitted with Legendre polynomials [77], each characterized by a β parameter. The even ($\beta_m m = 2, 4, \text{etc.}$) and odd ($\beta_m m = 1, 3, \text{etc.}$) parameters describe the symmetric and antisymmetric parts of the distribution, respectively.

Fig. 7.16(b) reports the results for β_1 and β_3 parameters, obtained via a fitting procedure. The obtained results are consistent with the calculated errors, while β_2 shows a larger deviation, possibly indicating systematic errors. Comparing the data qualitatively to the calculated spectra of a simpler system, atomic hydrogen [78], one can see that the key characteristics are reproduced. β_2 is in fact constant while β_1 and β_3 oscillate with a phase lag consistent with lowest-order perturbation theory.

For infinite pulses and the transitions of Fig. 7.16(a), the lag is derived as $\arg\left(\frac{2\sqrt{2}}{5} - \frac{D_s}{D_d}\right)$, where $\frac{D_s}{D_d}$ is the ratio of the complex first-order ionization amplitudes into the s and d channels (red arrows in Fig. 7.16(a)). Frozen-core Hartree-Fock calculations of D_s and D_d , using a simple model based on the perturbation theory and neglecting non-resonant two-photon transitions, predict a lag of approximately 0.55 rad for Neon. The discrepancy indicates a breakdown of this theory under our experimental conditions.

7.3.3 Summary

The present result demonstrates the possibility of producing two commensurate phase-locked FEL pulses. Attosecond-level phase control has been achieved. This result opens the way to completely new experiments in the XUV and soft X-ray spectral regions, characterized by a complete control of the wavelength, polarization, phase and intensity. The lower wavelength limit of the facility provides access to core levels of different atoms, and thus chemical specificity in coherent control experiments, a feature otherwise impossible for experiments

that involve optical lasers. The mentioned time resolution may allow the study of ultrafast dynamic phenomena, such as Wigner delays in photoemission.

References

- [1] E. Ferrari et al. “Accepted in Nat. Comm.” In: ().
- [2] E. Allaria et al. “Two-colour pump–probe experiments with a twin-pulse-seed extreme ultraviolet free-electron laser”. In: *Nat Commun* 4 (Sept. 2013). DOI: [10.1038/ncomms3476](https://doi.org/10.1038/ncomms3476).
- [3] F. Bencivenga et al. “Multi-colour pulses from seeded free-electron-lasers: towards the development of non-linear core-level coherent spectroscopies”. In: *Faraday Discuss.* 171 (0 2014), pp. 487–503. DOI: [10.1039/C4FD00100A](https://doi.org/10.1039/C4FD00100A).
- [4] F. Ciocci et al. “Two Color Free-Electron Laser and Frequency Beating”. In: *Phys. Rev. Lett.* 111 (26 2013), p. 264801. DOI: [10.1103/PhysRevLett.111.264801](https://doi.org/10.1103/PhysRevLett.111.264801).
- [5] G. Marcus, G. Penn, and A. A. Zholents. “Free-Electron Laser Design for Four-Wave Mixing Experiments with Soft-X-Ray Pulses”. In: *Phys. Rev. Lett.* 113 (2 2014), p. 024801. DOI: [10.1103/PhysRevLett.113.024801](https://doi.org/10.1103/PhysRevLett.113.024801).
- [6] L. T. Campbell, B. W. J. McNeil, and S. Reiche. “Two-colour free electron laser with wide frequency separation using a single monoenergetic electron beam”. In: *New Journal of Physics* 16.10 (2014), p. 103019.
- [7] E. Chiadroni et al. “Two Color {FEL} Driven by a Comb-like Electron Beam Distribution”. In: *Physics Procedia* 52 (2014), pp. 27–35. ISSN: 1875-3892. DOI: [10.1016/j.phpro.2014.06.006](https://doi.org/10.1016/j.phpro.2014.06.006).
- [8] G. De Ninno et al. “Chirped Seeded Free-Electron Lasers: Self-Standing Light Sources for Two-Color Pump-Probe Experiments”. In: *Phys. Rev. Lett.* 110 (6 2013), p. 064801. DOI: [10.1103/PhysRevLett.110.064801](https://doi.org/10.1103/PhysRevLett.110.064801).
- [9] B. Mahieu et al. “Two-colour generation in a chirped seeded free-electron laser: a close look”. In: *Opt. Express* 21.19 (2013), pp. 22728–22741. DOI: [10.1364/OE.21.022728](https://doi.org/10.1364/OE.21.022728).
- [10] A. A. Lutman et al. “Experimental Demonstration of Femtosecond Two-Color X-Ray Free-Electron Lasers”. In: *Phys. Rev. Lett.* 110 (13 2013), p. 134801. DOI: [10.1103/PhysRevLett.110.134801](https://doi.org/10.1103/PhysRevLett.110.134801).
- [11] A. Marinelli et al. “Multicolor Operation and Spectral Control in a Gain-Modulated X-Ray Free-Electron Laser”. In: *Phys. Rev. Lett.* 111 (13 2013), p. 134801. DOI: [10.1103/PhysRevLett.111.134801](https://doi.org/10.1103/PhysRevLett.111.134801).
- [12] A. A. Lutman et al. “Demonstration of Single-Crystal Self-Seeded Two-Color X-Ray Free-Electron Lasers”. In: *Phys. Rev. Lett.* 113 (25 2014), p. 254801. DOI: [10.1103/PhysRevLett.113.254801](https://doi.org/10.1103/PhysRevLett.113.254801).
- [13] T. Hara et al. “Two-colour hard X-ray free-electron laser with wide tunability”. In: *Nat Commun* 4 (Dec. 2013). DOI: [10.1038/ncomms3919](https://doi.org/10.1038/ncomms3919).
- [14] A. Marinelli et al. “High-intensity double-pulse X-ray free-electron laser”. In: *Nat Commun* 6 (Mar. 2015). DOI: [10.1038/ncomms7369](https://doi.org/10.1038/ncomms7369).
- [15] et al J. Amann. “Demonstration of self-seeding in a hard X-ray free-electron laser”. In: *Nature Photonics* 6 (2012). ISSN: 0168-9002. DOI: [10.1038/nphoton.2012.180](https://doi.org/10.1038/nphoton.2012.180).
- [16] D. Ratner et al. “Experimental Demonstration of a Soft X-Ray Self-Seeded Free-Electron Laser”. In: *Phys. Rev. Lett.* 114 (5 2015), p. 054801. DOI: [10.1103/PhysRevLett.114.054801](https://doi.org/10.1103/PhysRevLett.114.054801).

-
- [17] C. Stamm et al. “Femtosecond modification of electron localization and transfer of angular momentum in nickel”. In: *Nat Mater* 6.10 (Oct. 2007), pp. 740–743. DOI: [10.1038/nmat1985](https://doi.org/10.1038/nmat1985).
- [18] C. Boeglin et al. “Distinguishing the ultrafast dynamics of spin and orbital moments in solids”. In: *Nature* 465.7297 (May 2010), pp. 458–461. DOI: [10.1038/nature09070](https://doi.org/10.1038/nature09070).
- [19] I. Radu et al. “Transient ferromagnetic-like state mediating ultrafast reversal of anti-ferromagnetically coupled spins”. In: *Nature* 472.7342 (Apr. 2011), pp. 205–208. DOI: [10.1038/nature09901](https://doi.org/10.1038/nature09901).
- [20] M. Wietstruk et al. “Hot-Electron-Driven Enhancement of Spin-Lattice Coupling in Gd and Tb 4f Ferromagnets Observed by Femtosecond X-Ray Magnetic Circular Dichroism”. In: *Phys. Rev. Lett.* 106 (12 2011), p. 127401. DOI: [10.1103/PhysRevLett.106.127401](https://doi.org/10.1103/PhysRevLett.106.127401).
- [21] S. O. Mariager et al. “Structural and Magnetic Dynamics of a Laser Induced Phase Transition in FeRh”. In: *Phys. Rev. Lett.* 108 (8 2012), p. 087201. DOI: [10.1103/PhysRevLett.108.087201](https://doi.org/10.1103/PhysRevLett.108.087201).
- [22] A. Eschenlohr et al. “Ultrafast spin transport as key to femtosecond demagnetization”. In: *Nat Mater* 12.4 (Apr. 2013), pp. 332–336. DOI: [10.1038/nmat3546](https://doi.org/10.1038/nmat3546).
- [23] N. Bergeard et al. “Ultrafast angular momentum transfer in multisublattice ferrimagnets”. In: *Nat Commun* 5 (Mar. 2014). DOI: [10.1038/ncomms4466](https://doi.org/10.1038/ncomms4466).
- [24] C. La-O-Vorakiat et al. “Ultrafast Demagnetization Dynamics at the *M* Edges of Magnetic Elements Observed Using a Tabletop High-Harmonic Soft X-Ray Source”. In: *Phys. Rev. Lett.* 103 (25 2009), p. 257402. DOI: [10.1103/PhysRevLett.103.257402](https://doi.org/10.1103/PhysRevLett.103.257402).
- [25] C. La-O-Vorakiat et al. “Ultrafast Demagnetization Measurements Using Extreme Ultraviolet Light: Comparison of Electronic and Magnetic Contributions”. In: *Phys. Rev. X* 2 (1 2012), p. 011005. DOI: [10.1103/PhysRevX.2.011005](https://doi.org/10.1103/PhysRevX.2.011005).
- [26] S. Mathias et al. “Probing the timescale of the exchange interaction in a ferromagnetic alloy”. In: *Proceedings of the National Academy of Sciences* 109.13 (2012), pp. 4792–4797. DOI: [10.1073/pnas.1201371109](https://doi.org/10.1073/pnas.1201371109). eprint: <http://www.pnas.org/content/109/13/4792.full.pdf>.
- [27] S. Günther et al. “Testing spin-flip scattering as a possible mechanism of ultrafast demagnetization in ordered magnetic alloys”. In: *Phys. Rev. B* 90 (18 2014), p. 180407. DOI: [10.1103/PhysRevB.90.180407](https://doi.org/10.1103/PhysRevB.90.180407).
- [28] B. Pfau et al. “Ultrafast optical demagnetization manipulates nanoscale spin structure in domain walls”. In: *Nat Commun* 3 (Oct. 2012), p. 1100. DOI: [10.1038/ncomms2108](https://doi.org/10.1038/ncomms2108).
- [29] W. Zhang et al. “Tracking excited-state charge and spin dynamics in iron coordination complexes”. In: *Nature* 509.7500 (May 2014), pp. 345–348. DOI: [10.1038/nature13252](https://doi.org/10.1038/nature13252).
- [30] P. Beaud et al. “A time-dependent order parameter for ultrafast photoinduced phase transitions”. In: *Nat Mater* 13.10 (Oct. 2014), pp. 923–927. DOI: [10.1038/nmat4046](https://doi.org/10.1038/nmat4046).
- [31] J. N. Clark et al. “Imaging transient melting of a nanocrystal using an X-ray laser”. In: *Proceedings of the National Academy of Sciences* 112.24 (2015), pp. 7444–7448. DOI: [10.1073/pnas.1417678112](https://doi.org/10.1073/pnas.1417678112). eprint: <http://www.pnas.org/content/112/24/7444.full.pdf>.
- [32] M. Forst et al. “Spatially resolved ultrafast magnetic dynamics initiated at a complex oxide heterointerface”. In: *Nat Mater* 14.9 (Sept. 2015), pp. 883–888. DOI: [10.1038/nmat4341](https://doi.org/10.1038/nmat4341).

- [33] Ph. Wernet et al. “Orbital-specific mapping of the ligand exchange dynamics of Fe(CO)₅ in solution”. In: *Nature* 520.7545 (Apr. 2015), pp. 78–81. DOI: [10.1038/nature14296](https://doi.org/10.1038/nature14296).
- [34] A. L. Kritcher et al. “Ultrafast X-ray Thomson Scattering of Shock-Compressed Matter”. In: *Science* 322.5898 (2008), pp. 69–71. DOI: [10.1126/science.1161466](https://doi.org/10.1126/science.1161466). eprint: <http://www.sciencemag.org/content/322/5898/69.full.pdf>.
- [35] B. et al. Nagler. “Turning solid aluminium transparent by intense soft X-ray photoionization”. In: *Nat Phys* 5.9 (Sept. 2009), pp. 693–696. DOI: [10.1038/nphys1341](https://doi.org/10.1038/nphys1341).
- [36] S. M. Vinko et al. “Creation and diagnosis of a solid-density plasma with an X-ray free-electron laser”. In: *Nature* 482.7383 (Feb. 2012), pp. 59–62. DOI: [10.1038/nature10746](https://doi.org/10.1038/nature10746).
- [37] J.P. Marangos. “Introduction to the new science with X-ray free electron lasers”. In: *Contemporary Physics* 52.6 (2011), pp. 551–569. DOI: [10.1080/00107514.2011.607290](https://doi.org/10.1080/00107514.2011.607290). eprint: <http://dx.doi.org/10.1080/00107514.2011.607290>.
- [38] John Lindl. “Development of the indirect drive approach to inertial confinement fusion and the target physics basis for ignition and gain”. In: *Physics of Plasmas* 2.11 (1995), pp. 3933–4024. DOI: [10.1063/1.871025](https://doi.org/10.1063/1.871025).
- [39] J. J. Fortney et al. “Frontiers of the physics of dense plasmas and planetary interiors: Experiments, theory, and applications”. In: *Physics of Plasmas* 16.4 (2009). DOI: [10.1063/1.3101818](https://doi.org/10.1063/1.3101818).
- [40] E.G. Gamaly. “The physics of ultra-short laser interaction with solids at non-relativistic intensities”. In: *Physics Reports* 508.4-5 (2011), pp. 91–243. ISSN: 0370-1573. DOI: [10.1016/j.physrep.2011.07.002](https://doi.org/10.1016/j.physrep.2011.07.002).
- [41] H. P. Freund and P. G. O’Shea. “Two-Color Operation in High-Gain Free-Electron Lasers”. In: *Phys. Rev. Lett.* 84 (13 2000), pp. 2861–2864. DOI: [10.1103/PhysRevLett.84.2861](https://doi.org/10.1103/PhysRevLett.84.2861).
- [42] F. Capotondi et al. “Invited Article: Coherent imaging using seeded free-electron laser pulses with variable polarization: First results and research opportunities”. In: *Review of Scientific Instruments* 84.5 (2013). DOI: [10.1063/1.4807157](https://doi.org/10.1063/1.4807157).
- [43] B.L. Henke, E.M. Gullikson, and J.C. Davis. “X-Ray Interactions: Photoabsorption, Scattering, Transmission, and Reflection at E = 50-30,000 eV, Z = 1-92”. In: *Atomic Data and Nuclear Data Tables* 54.2 (1993), pp. 181–342. ISSN: 0092-640X. DOI: [10.1006/adnd.1993.1013](https://doi.org/10.1006/adnd.1993.1013).
- [44] H. N. Chapman et al. “Femtosecond time-delay X-ray holography”. In: *Nature* 448.7154 (Aug. 2007), pp. 676–679. DOI: [10.1038/nature06049](https://doi.org/10.1038/nature06049).
- [45] S. P. Hau-Riege et al. “Sacrificial Tamper Slows Down Sample Explosion in FLASH Diffraction Experiments”. In: *Phys. Rev. Lett.* 104 (6 2010), p. 064801. DOI: [10.1103/PhysRevLett.104.064801](https://doi.org/10.1103/PhysRevLett.104.064801).
- [46] S.-K. Son, H. N. Chapman, and R. Santra. “Multiwavelength Anomalous Diffraction at High X-Ray Intensity”. In: *Phys. Rev. Lett.* 107 (21 2011), p. 218102. DOI: [10.1103/PhysRevLett.107.218102](https://doi.org/10.1103/PhysRevLett.107.218102).
- [47] B. Ziaja and N. Medvedev. “Modelling ultrafast transitions within laser-irradiated solids”. In: *High Energy Density Physics* 8.1 (2012), pp. 18–29. ISSN: 1574-1818. DOI: [10.1016/j.hedp.2011.11.004](https://doi.org/10.1016/j.hedp.2011.11.004).
- [48] N. Medvedev, H. O. Jeschke, and B. Ziaja. “Nonthermal phase transitions in semiconductors induced by a femtosecond extreme ultraviolet laser pulse”. In: *New Journal of Physics* 15.1 (2013), p. 015016.

-
- [49] L. Müller et al. “Breakdown of the X-Ray Resonant Magnetic Scattering Signal during Intense Pulses of Extreme Ultraviolet Free-Electron-Laser Radiation”. In: *Phys. Rev. Lett.* 110 (23 2013), p. 234801. DOI: [10.1103/PhysRevLett.110.234801](https://doi.org/10.1103/PhysRevLett.110.234801).
- [50] M. Labat et al. “Pulse Splitting in Short Wavelength Seeded Free Electron Lasers”. In: *Phys. Rev. Lett.* 103 (26 2009), p. 264801. DOI: [10.1103/PhysRevLett.103.264801](https://doi.org/10.1103/PhysRevLett.103.264801).
- [51] G. De Ninno et al. “Chirped Seeded Free-Electron Lasers: Self-Standing Light Sources for Two-Color Pump-Probe Experiments”. In: *Phys. Rev. Lett.* 110 (6 2013), p. 064801. DOI: [10.1103/PhysRevLett.110.064801](https://doi.org/10.1103/PhysRevLett.110.064801).
- [52] T. A. Ostler et al. “Ultrafast heating as a sufficient stimulus for magnetization reversal in a ferrimagnet”. In: *Nat Commun* 3 (Feb. 2012), p. 666. DOI: [10.1038/ncomms1666](https://doi.org/10.1038/ncomms1666).
- [53] C. E. Graves et al. “Nanoscale spin reversal by non-local angular momentum transfer following ultrafast laser excitation in ferrimagnetic GdFeCo”. In: *Nat Mater* 12.4 (Apr. 2013), pp. 293–298. DOI: [10.1038/nmat3597](https://doi.org/10.1038/nmat3597).
- [54] M. Finazzi et al. “Laser-Induced Magnetic Nanostructures with Tunable Topological Properties”. In: *Phys. Rev. Lett.* 110 (17 2013), p. 177205. DOI: [10.1103/PhysRevLett.110.177205](https://doi.org/10.1103/PhysRevLett.110.177205).
- [55] S. Mangin et al. “Engineered materials for all-optical helicity-dependent magnetic switching”. In: *Nat Mater* 13.3 (Mar. 2014), pp. 286–292. DOI: [10.1038/nmat3864](https://doi.org/10.1038/nmat3864).
- [56] L. Le Guyader et al. “Nanoscale sub-100 picosecond all-optical magnetization switching in GdFeCo microstructures”. In: *Nat Commun* 6 (Jan. 2015). DOI: [10.1038/ncomms6839](https://doi.org/10.1038/ncomms6839).
- [57] M. B. Danailov et al. “Towards jitter-free pump-probe measurements at seeded free electron laser facilities”. In: *Opt. Express* 22.11 (2014), pp. 12869–12879. DOI: [10.1364/OE.22.012869](https://doi.org/10.1364/OE.22.012869).
- [58] E. Allaria et al. “FEL-1 current status and recent achievements”. FERMI Machine Advisory Committee. 2014.
- [59] M. Sacchi et al. “Ultrahigh-vacuum soft x-ray reflectometer”. In: *Review of Scientific Instruments* 74.5 (2003), pp. 2791–2795. DOI: [10.1063/1.1568552](https://doi.org/10.1063/1.1568552).
- [60] C. Spezzani et al. “Magnetization and Microstructure Dynamics in Fe/MnAs/GaAs(001): Fe Magnetization Reversal by a Femtosecond Laser Pulse”. In: *Phys. Rev. Lett.* 113 (24 2014), p. 247202. DOI: [10.1103/PhysRevLett.113.247202](https://doi.org/10.1103/PhysRevLett.113.247202).
- [61] M. Sacchi et al. “Magnetic dichroism in reflectivity and photoemission using linearly polarized light: $3p$ core level of Ni(110)”. In: *Phys. Rev. B* 58 (7 1998), pp. 3750–3754. DOI: [10.1103/PhysRevB.58.3750](https://doi.org/10.1103/PhysRevB.58.3750).
- [62] M. Hecker et al. “Soft X-ray magnetic reflection spectroscopy at the $3p$ absorption edges of thin Fe films”. In: *Journal of Electron Spectroscopy and Related Phenomena* 144–147 (2005), pp. 881–884. DOI: [10.1016/j.elspec.2005.01.151](https://doi.org/10.1016/j.elspec.2005.01.151).
- [63] B. Vodungbo et al. “Laser-induced ultrafast demagnetization in the presence of a nanoscale magnetic domain network”. In: *Nat Commun* 3 (Aug. 2012), p. 999. DOI: [10.1038/ncomms2007](https://doi.org/10.1038/ncomms2007).
- [64] S. Sasaki. “Analyses for a planar variably-polarizing undulator”. In: *Nuclear Instruments and Methods in Physics Research Section A: Accelerators, Spectrometers, Detectors and Associated Equipment* 347.1-3 (Aug. 1994), pp. 83–86. DOI: [10.1016/0168-9002\(94\)91859-7](https://doi.org/10.1016/0168-9002(94)91859-7).

- [65] L. Young et al. “Femtosecond electronic response of atoms to ultra-intense X-rays”. In: *Nature* 466.7302 (July 2010), pp. 56–61. DOI: [10.1038/nature09177](https://doi.org/10.1038/nature09177).
- [66] N. Rohringer et al. “Atomic inner-shell X-ray laser at 1.46 nanometres pumped by an X-ray free-electron laser”. In: *Nature* 481.7382 (Jan. 2012), pp. 488–491. DOI: [10.1038/nature10721](https://doi.org/10.1038/nature10721).
- [67] F. Bencivenga et al. “Four-wave mixing experiments with extreme ultraviolet transient gratings”. In: *Nature* 520.7546 (Apr. 2015), pp. 205–208. DOI: [10.1038/nature14341](https://doi.org/10.1038/nature14341).
- [68] P. Brumer and M. Shapiro. “Control of unimolecular reactions using coherent light”. In: *Chemical Physics Letters* 126.6 (1986), pp. 541–546. ISSN: 0009-2614. DOI: [10.1016/S0009-2614\(86\)80171-3](https://doi.org/10.1016/S0009-2614(86)80171-3).
- [69] C. Brif, R. Chakrabarti, and H. Rabitz. “Control of quantum phenomena: past, present and future”. In: *New Journal of Physics* 12.7 (2010), p. 075008.
- [70] F. Ehlötzky. “Atomic phenomena in bichromatic laser fields”. In: *Physics Reports* 345.4 (2001), pp. 175–264. ISSN: 0370-1573. DOI: [10.1016/S0370-1573\(00\)00100-9](https://doi.org/10.1016/S0370-1573(00)00100-9).
- [71] A. Singer et al. “Hanbury Brown–Twiss Interferometry at a Free-Electron Laser”. In: *Phys. Rev. Lett.* 111 (3 2013), p. 034802. DOI: [10.1103/PhysRevLett.111.034802](https://doi.org/10.1103/PhysRevLett.111.034802).
- [72] F. Lehmkuhler et al. “Single Shot Coherence Properties of the Free-Electron Laser SACLA in the Hard X-ray Regime”. In: *Scientific Reports* 4 (2014), p. 5234. DOI: [10.1038/srep05234](https://doi.org/10.1038/srep05234).
- [73] M. D. Alaimo et al. “Mapping the transverse coherence of the self amplified spontaneous emission of a free-electron laser with the heterodyne speckle method”. In: *Opt. Express* 22.24 (2014), pp. 30013–30023. DOI: [10.1364/OE.22.030013](https://doi.org/10.1364/OE.22.030013).
- [74] R. Bachelard et al. “Wavefront Analysis of Nonlinear Self-Amplified Spontaneous-Emission Free-Electron Laser Harmonics in the Single-Shot Regime”. In: *Phys. Rev. Lett.* 106 (23 2011), p. 234801. DOI: [10.1103/PhysRevLett.106.234801](https://doi.org/10.1103/PhysRevLett.106.234801).
- [75] I. Franco and P. Brumer. “Minimum requirements for laser-induced symmetry breaking in quantum and classical mechanics”. In: *Journal of Physics B: Atomic, Molecular and Optical Physics* 41.7 (2008), p. 074003.
- [76] Z.-M. Wang and D. S. Elliott. “Determination of the Phase Difference between Even and Odd Continuum Wave Functions in Atoms through Quantum Interference Measurements”. In: *Phys. Rev. Lett.* 87 (17 2001), p. 173001. DOI: [10.1103/PhysRevLett.87.173001](https://doi.org/10.1103/PhysRevLett.87.173001).
- [77] G. A. Garcia, L. Nahon, and I. Powis. “Two-dimensional charged particle image inversion using a polar basis function expansion”. In: *Review of Scientific Instruments* 75.11 (2004), pp. 4989–4996. DOI: [10.1063/1.1807578](https://doi.org/10.1063/1.1807578).
- [78] A. N. Grum-Grzhimailo et al. “Interfering one-photon and two-photon ionization by femtosecond VUV pulses in the region of an intermediate resonance”. In: *Phys. Rev. A* 91 (6 2015), p. 063418. DOI: [10.1103/PhysRevA.91.063418](https://doi.org/10.1103/PhysRevA.91.063418).

Appendices

Appendix A

Diagnostics

A.1 Electron beam diagnostics

In order to measure the electron beam properties an adequate diagnostics system is required. The beam properties one is usually interested in can be grouped with respect to the beam propagation direction. Properties on planes orthogonal to the propagation direction are usually referred as “transverse” while properties on planes parallel to the propagation direction are also called “longitudinal”. A further classification can be implemented depending on whether the beam can or cannot propagate further from the measurement location conserving the same properties. In the first case it is customary to refer to “non-destructive” diagnostics, opposed to the “destructive” ones. The non-destructive measurements are particularly useful to stabilize the machine as they can be performed on line on shot-by-shot basis and therefore be used as a signal for dedicated feedback loops. The destructive measurements are instead mainly used to check the beam properties in the optimization phases.

A.2 The transverse diagnostics

The transverse properties that are of interest for a LINAC-based facility are the beam position and sizes. The beam centroid position can be measured in a non-destructive using dedicated beam position monitors (BPM). The beam horizontal and vertical centroid position is determined by comparing the signals coming from four antennas installed on the beam pipe in a quadrant configuration.

The electron beam trajectory along the LINAC is monitored by 31 stripline BPM [1] with 20 μm (RMS) resolution, and can be modified by changing 24 couples of steering magnets (correctors) both in horizontal and vertical plane. Along both undulator chains the position accuracy required for FEL operations required the usage of cavity BPMs [2] with 5 μm (RMS) resolution.

The beam size can be measured, in a destructive configuration, by means of one of the 16 fluorescent multi-screens that can be inserted into the path of the electrons. The multi-screen stations are equipped with Optical Transition Radiation (OTR) [3] and Yttrium Aluminium Garnet (YAG) targets [4]. The signal generated by the target is acquired using a CCD camera. The resolution of the screen/CCD setup has been estimated to be $\sim 40 \mu\text{m}$ in the case of the YAG target and $\sim 20 \mu\text{m}$ for the OTR. The multi-screens are mainly used for emittance and Twiss functions’ reconstruction using the quadrupole scan technique [5]. The measurement is critical for matching the beam optics with the designed one [6].

A.2.1 The wire-scanner

Recently a PSI developed prototype wire-scanner setup has been installed at the LINAC end and can be used for non-destructive beam profile measurements [7]. The working principle in this case relies on the beam loss measurement as a thin wire is made interact with the electron beam.

The device is constituted of an in-vacuum scanning hardware and scintillator-fibers for out-vacuum detection of the beam-losses [8]. The wire-fork can be inserted 45-deg with respect to vertical axis by means of a UHV linear-feed-through motorized by a stepper-motor and equipped with an encoder. Two pairs of Tungsten wires are stretched on the fork frame to scan the beam profile along the horizontal and vertical directions. The two pairs of wires have a diameter of 5 and 13 μm , respectively, to ensure a geometrical resolution in the range 1.3-3.3 μm (RMS). When the wire intercepts the electron beam, a shower of high energy primary scattered electrons and secondary particles is forward emitted at a small angle in proportion to the fraction of the beam charge that is intercepted by the wire. Scanning the wire at constant speed and detecting the beam losses allows the single projection of the beam profile to be reconstructed. The wire losses have been measured with three Saint Gobain Scintillator fibers (1 mm diameter): two were placed in the LINAC tunnel, before the beam stopper, respectively 2.48 m and 5.52 m downstream the device, while the third one was installed in the undulator hall, at about 8.40 m from the device. A fourth loss monitor, a Cerenkov fiber, has been placed in the LINAC tunnel, at about 4.5 m from the wire-scanner. The second fiber is placed at distance that maximize the beam losses signal and it is taken as the reference for the measurement.

In Fig. A.1 an example of the horizontal beam profile acquired measuring the four radiation monitors is reported when the 5 μm wire was scanned at 0.1 mm/s, together with the measured horizontal beam size versus the wire scan speed, looking at the second fiber signal. The results indicate a beam size smaller than the resolution of the screen systems, so for a reliable beam size measurement the wire-scanner is required in the case of FERMI.

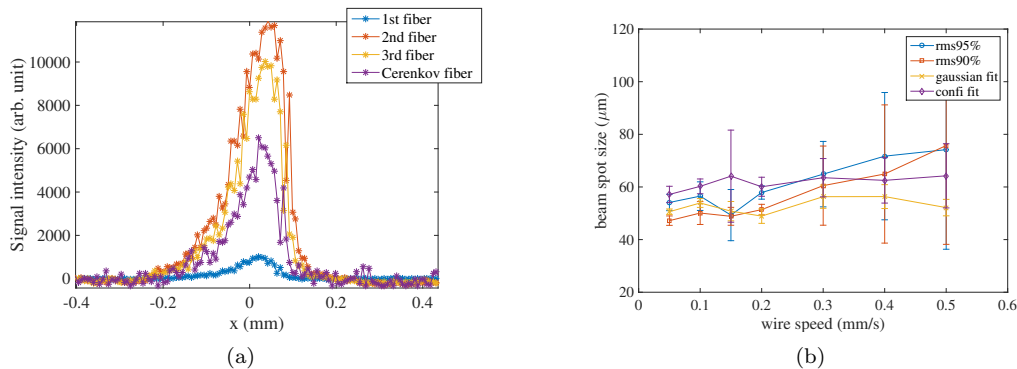


Figure A.1: Measurements of beam size with the wire-scanner located at the LINAC end. Right: Horizontal beam profile as acquired by the four monitors for the vertical 5 μm wire scanning at 0.1mm/s. Left: Horizontal beam size (σ_x) versus the wire speed obtained by processing the second fiber signal using different data processing.

A.3 Timing system

FERMI is the first FEL fully synchronized by means of optical fibers [9]. This is required in order to have a stable phase reference to the timing system for all the distributed clients that require it, over the whole length of the facility. The timing system synchronizes, with femtosecond accuracy, the different LINAC components together with the different laser systems present along the machine and the longitudinal diagnostics.

The requirements for a seeding facility are tighter than the ones of a SASE facility due to the seeding process itself [6]. In fact the superposition in between the electron beam and the seed laser must be kept as stable as possible in order to really take advantage of the improvements in the radiation quality induced by the HGHG process. Typical bunch lengths for the electron beam are several hundreds of fs FWHM and 100 to 200 fs for the seed laser. However the properties of the beam in terms, e.g., of energy, current and emittance change along the bunch (energy chirp). The effective region of the electron beam for the FEL generation is therefore reduced to less than 500 fs. Only recently the capability to have a longer flat electron beam have been demonstrated [10], but it is still not in normal use.

The term timing system indicates all the systems needed to generate and to distribute, over stabilized media, the phase reference signal. The phase reference signal is the clock signal used to synchronize all the accelerator systems needing femtosecond stability, e.g. the RF plants, the laser systems and the longitudinal diagnostics. The frequency of the phase reference has been selected to be equal to 2998.01 MHz, corresponding to the same frequency of the RF plants that power the accelerating sections of the LINAC. The synchronization must be kept stable for long time periods and large distances.

A.4 The longitudinal diagnostics

Longitudinal diagnostics are instruments developed to perform measurements in the longitudinal axis of the reference system, i.e. in the direction of the electron motion.

In the case of an FEL in general, and of FERMI in particular, the beam properties one is interested in are both the whole beam ones (emittance, energy, sizes, etc.), as well as the ones of small longitudinal “slices” of the beam itself. This is because the FEL process happens, in a seeded FEL, only in the part of the electron beam which interacts with the seed laser itself, that is usually <200 fs long. Typical longitudinal measurements performed during FERMI operations are slice beam energy, energy spread and energy chirp, current distribution, bunch length, arrival time jitter, etc.

At FERMI, several innovative non-destructive longitudinal diagnostics have been engineered and successfully installed on the machine and will be presented in the following.

A.4.1 The relative Bunch Length Monitor (BLM)

Both the absolute and the relative bunch length measurements are key parameters to the FERMI operation. A relative Bunch Length Monitor (BLM) system has been designed measuring such quantity on a shot-to-shot basis [11]. It is based on the measurement of the coherent radiation power generated by the electron beam as it travels through designed regions of a bunch compressor chicane. If one considers the coherent edge radiation generated as the beam travels through the last dipole of the chicane, a pyro-detector is needed. If instead one relies on the coherent diffraction radiation generated in a ceramic gap the measurement can be done using a set of diodes sensitive to wavelengths in the mm range.

The two possibilities were both implemented as their sensitivity depends on the different possible operating conditions for the machine.

The diagnostic based on the first source covers a range in bunch duration from 0.15-1 ps, while the second process can be used in the range 1-5 ps. In the case of FERMI a replica of the diagnostic is present at each bunch compressor chicane. A series of mirrors are installed in the LINAC tunnel in order to collect and collimate the radiation up to the detectors. The signal produced is used to stabilize the electron bunch length using a feedback system [12].

A.4.2 The Bunch Arrival Monitor (BAM)

The Bunch Arrival Monitor (BAM) developed for FERMI is based on the original idea of the DESY advanced diagnostics group [13]. The arrival time of each electron bunch is measured with respect to a reference signal provided by the timing system. The electrical pulse response is generated by the electron bunch itself and acquired through a pick-up mounted on the beam-pipe. When the electron bunch arrival time varies also the temporal overlap between the electrical signal from the pickup and the optical timing pulse changes. This changes the amplitude of the signal seen by the sampling pulse. In this way the pick-up signal can be used to modulate the amplitude of one of the pulses of the optical reference and this amplitude variation can be measured using a commercial 12 GHz Mach-Zehnder type electro-optical modulator (MZM). Several BAM stations have been installed along the beam path at FERMI, namely two along the LINAC, just after each of the two bunch compressor chicanes (BC01 and BC02) and one before each of the two FEL beamlines FEL-1 and FEL-2, see Fig. 3.1.

To operate the BAM a coarse and fine timing alignment of the electron bunch signal and the reference timing pulse are required, as well as a calibration [9]. This can be done using a calibrated optical delay line that changes the delay in between the two signals. In this way, by sweeping the sampling pulse over the pickup response, one can obtain the calibration factor that converts the amplitude of the modulation into arrival time variation, in fs.

While the system is auto-calibrated, nevertheless a cross calibration check has been performed in order to validate the response of the diagnostics, using a different approach. To do so we correlated the BAM signal at the first bunch compressor (BC01) with the ones of a time-calibrated BPM located at the center of the chicane on a shot-to-shot basis, while also artificially inducing a sinusoidal change in the time of flight of the electron beam through the chicane itself. As the electron beam is ultra-relativistic its arrival time is mainly influenced by a change in the trajectory inside the chicane itself.

In Fig. A.2 the results of the cross-calibration measurements are reported, as a function of the shot number (Fig. A.2(a)). In Fig. A.2(b) the analysis of the correlation between the two devices is presented. The correlation coefficient of the measurement is larger than 99% which confirms that the self-calibration process of the BAM is adequate.

After confirmation of the BAM calibration, we tried to estimate an upper limit for the resolution of the arrival time measurement. To do that we analyzed the shot-to-shot correlations in between the BC01 and FEL-1 BAM stations. In Fig.A.3 we report the correlation over 1000 shots. The width of the distribution is mainly due to the resolution of the instruments, that we assure are contributing equally to the broadening of the distribution. If we can also neglect the possible contributions to the jitter in the arrival time due to other LINAC elements in between the two devices, mainly accelerating cavities, we can estimate an upper estimation of the resolution of the BAMs arrival time measurement lower than 8 fs. The mentioned assumptions are reasonable as the correlation coefficient we measured is always $> 95\%$. BAMs represent the reference arrival time diagnostic for FERMI and are routinely used to investigate time jitter sources. Typical values for the arrival time jitter

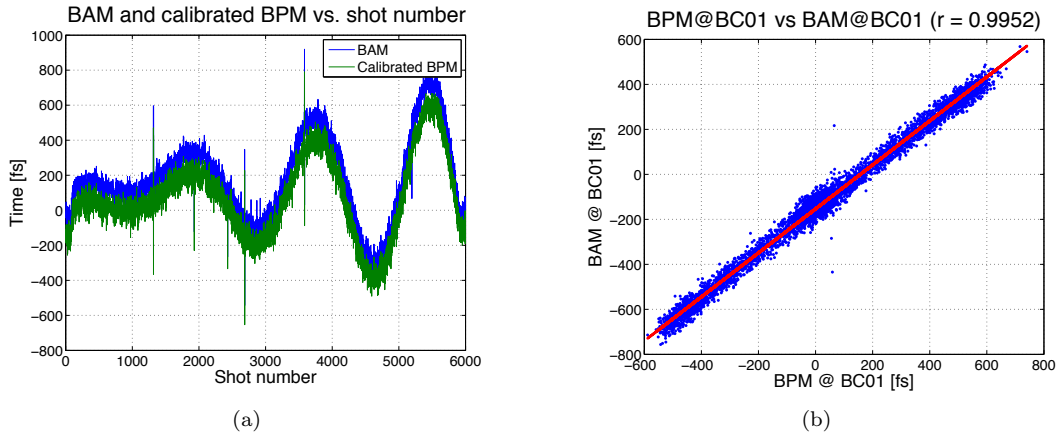


Figure A.2: BAM calibration using the BPM in the BC01 chicane. The time-of-flight through the chicane has been artificially altered, inducing a sinusoidal perturbation with increasing amplitude. Left: BAM and BPM arrival time variation (in fs) as a function of the shot number. Right: Correlation between the two devices. The correlation coefficient is larger than 99%.

are ~ 60 fs (RMS) after the BC01 chicane and ~ 70 fs (RMS) at the beginning of the FEL-1 line.

A.4.3 Electro-optical sampling (EOS)

At the beginning of each of the FEL lines (cfr. Fig.3.1) an electro-optical sampling (EOS) station [14], based on the spatial encoding scheme [15] is installed. The working principle of the system is based on the measurement of the change in the polarization properties of a laser passing through an electro-optical (EO) crystal. The crystal, usually ZnTe or GaP, is located in the vicinity of the electron beam and its transmission properties are influenced by the electric field generated by the beam itself. As the EO crystal is placed with a tilt with respect to the electron beam path, the temporal profile of the electron beam is mapped in space and can be accessed with the EOS technique. An optical delay line is used to calibrate the system. The EOS is capable of providing both time jitter and longitudinal profile measurements in a non-destructive way.

In Fig.A.4 we report the results of the time jitter measurements taken at the EOS station together with a comparison with the nearby BAM station, together with the shot-to-shot correlation in between the two devices. The arrival time was artificially modulated as described above. The upgrade in the locking electronics for the EOS laser [16] were effective in reducing the measurement noise that was initially affecting the system [17]. The correlation coefficient for the two diagnostics results to be larger than 99%, showing a really satisfactory agreement.

The spatial encoding scheme used for the FERMI EOS allows also to measure the longitudinal charge distribution profile in the electron beam. An example of 30 consecutive EO signals are reported in Fig. A.5 for a 700 pC beam charge. The measured profile is in agreement with the one measured using the RF deflecting cavity at the LINAC end. The advantage in using the EOS is that the measure can be done on line while the FEL emission is undergoing. The profiles can also be used to estimate a time arrival jitter of ~ 40 fs (RMS)

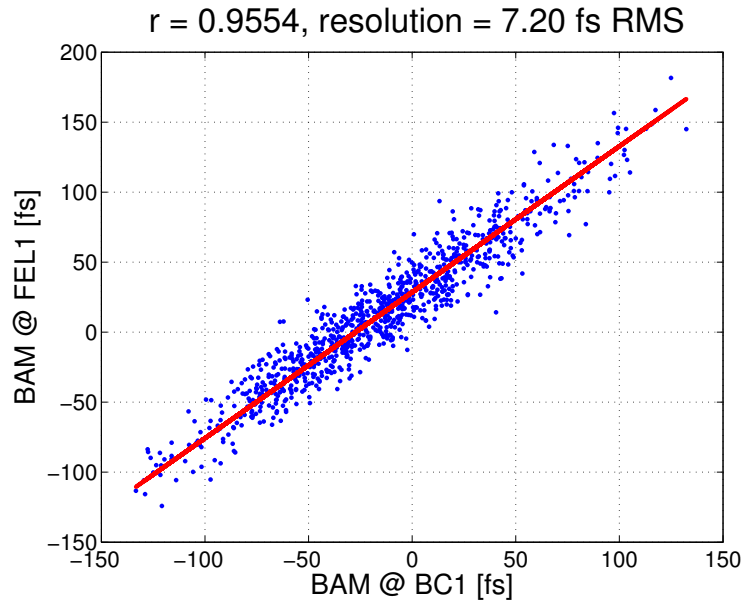


Figure A.3: Estimation of the BAM resolution. By splitting in quadrature the width of the the shot-to-shot correlations between the BC01 BAM and the FEL-1 BAM we are able to estimate an upper limit of the resolution which is less than 8 fs (RMS). Possible arrival time variations due to jitters in the accelerating cavities in between the two BAMs stations have been neglected. We also assumed identical performance of the two stations.

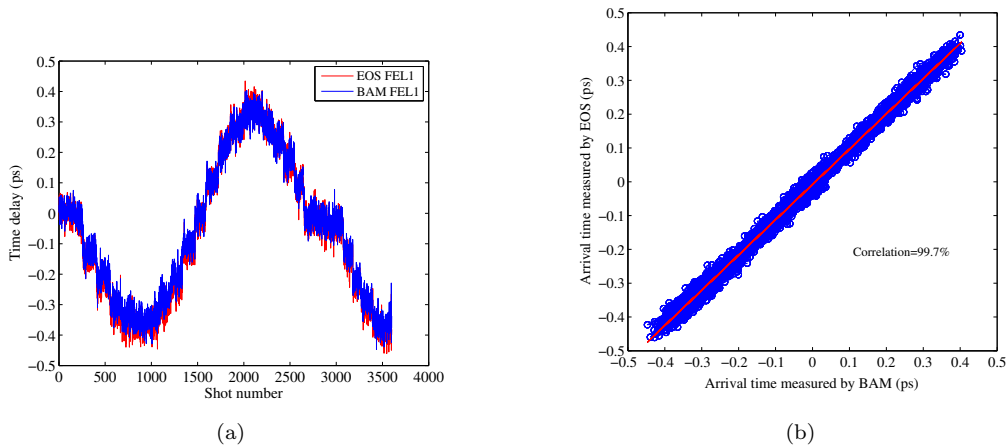


Figure A.4: Measurement of arrival time jitter at the EOS station and comparison with the nearby BAM station. Left: EOS and BAM arrival time jitter measurements as a function of the shot number. Right: Correlation in the shot-to-shot measurement between the two devices. The correlation coefficient has been found to be larger than 99%.

of the electron beam.

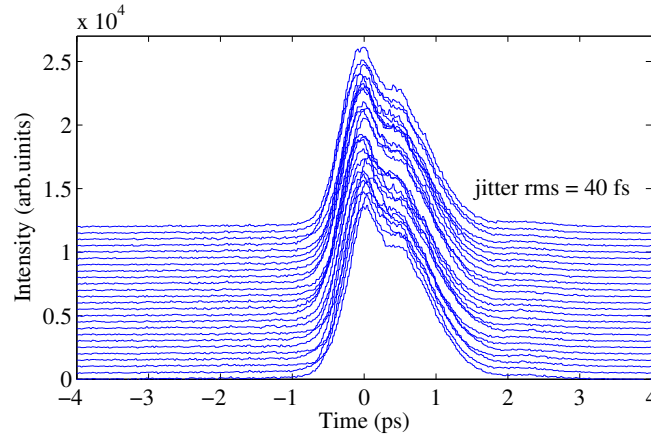


Figure A.5: EO signal of 30 consecutive shots obtained using the EOS system. The arrival time jitter can be estimated to be ~ 40 fs (RMS).

A.5 RF deflectors

FERMI is equipped with three RF-deflecting cavities [18, 19]. One is located after the first bunch compressor [20] and two at the LINAC end [21], indicated by red boxes in Fig. 3.1.

The working principle of the RF deflector is to provide a null deflecting voltage to the bunch centroid and stretches the electrons linearly from the head to the tail of the bunch, when its RF phase is properly set. In this way electrons transverse displacement are correlated with their longitudinal position along the bunch. Coupling the RF deflector with a diagnostic fluorescent screen can be used to characterize the bunch current profile and the time-sliced parameters, as the slice emittance.

As already presented in the BAM section, we were able to check the calibration of the arrival time variations by artificially change the time-of-flight in the BC01 chicane. This approach can be also followed to check the RF-deflector calibration. In Fig.A.6 we report the results of the calibration process, for both the BAM and the deflected beam profile at the linac end, as a function of the shot number. The agreement between the two measurements is satisfactory (correlation coefficient $\sim 95\%$) despite some differences, mainly due to slow drifts in the klystron powering the cavity. Furthermore we can estimate the resolution of the RF-deflector measurements, which in the FERMI case at the LINAC end is of the order of 50 fs (RMS).

A.6 Longitudinal phase space characterization

A detailed knowledge of the longitudinal phase space of the electron bunch, i.e. the electron energy distribution as a function of the electron temporal position along the bunch, is of paramount importance to successfully commissioning and operate an FEL. At this purpose the beam stretched via the RF deflector can be sent into an energy spectrometer that chromatically disperses electrons in the other transverse plane. In the case of FERMI the deflection is happening in the vertical direction as the bending magnet spectrometers are

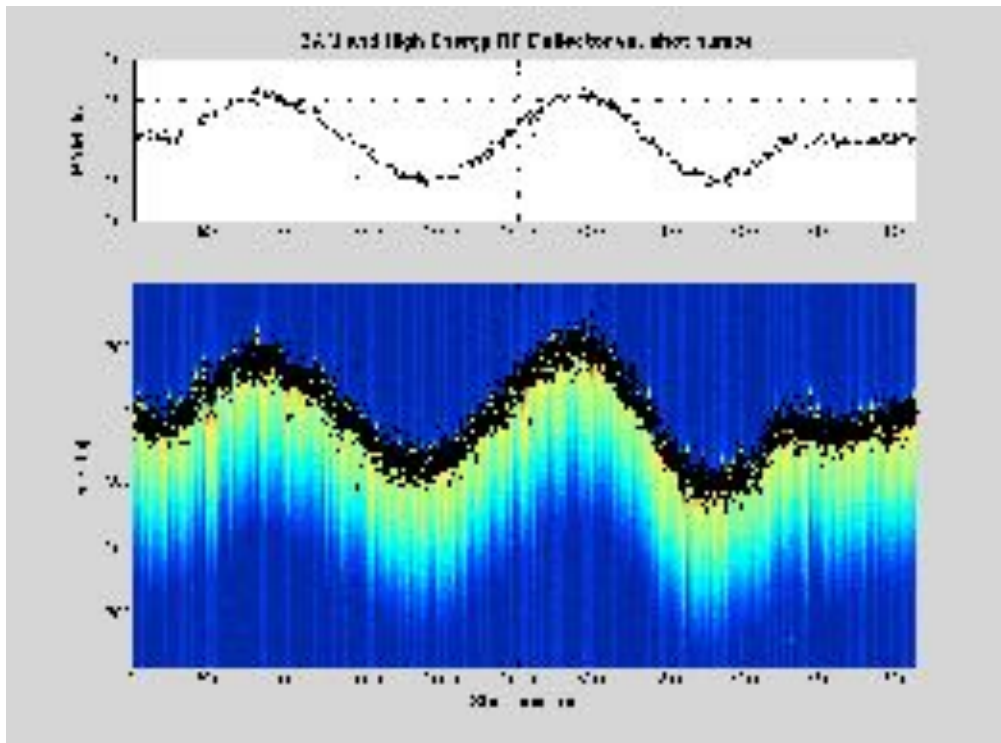


Figure A.6: Measurement of the arrival time variation at the LINAC end, while a sinusoidal perturbation was induced in the BC01 chicane. Both the BAM measurement (top) and the deflected beam profile (bottom) are reported, as a function of the shot number. For the profile, the beam head position is also highlighted for an easier comparison with the BAM results. The agreement between the two measurements is satisfactory and the estimated resolution for the RF-deflector is ~ 50 fs (RMS).

in the horizontal direction. The bunch longitudinal phase space can then be visualized on a fluorescent screen system (YAG crystal + CCD camera) placed downstream, as shown Fig. A.7(a). Temporal slicing of the data in the acquired image, i.e. selecting small vertical portions of the longitudinal phase space, provides the current profile (red line in Fig. A.7(b)) and the uncorrelated energy spread (blue line in Fig. A.7(b)) along the bunch. Unfortunately, this measurement is destructive and is not available during the FEL operations. The use of a deflecting cavity after the undulator would be required for a non-invasive and online characterization of the electron beam phase space and FEL induced effects on the electron beam [22].

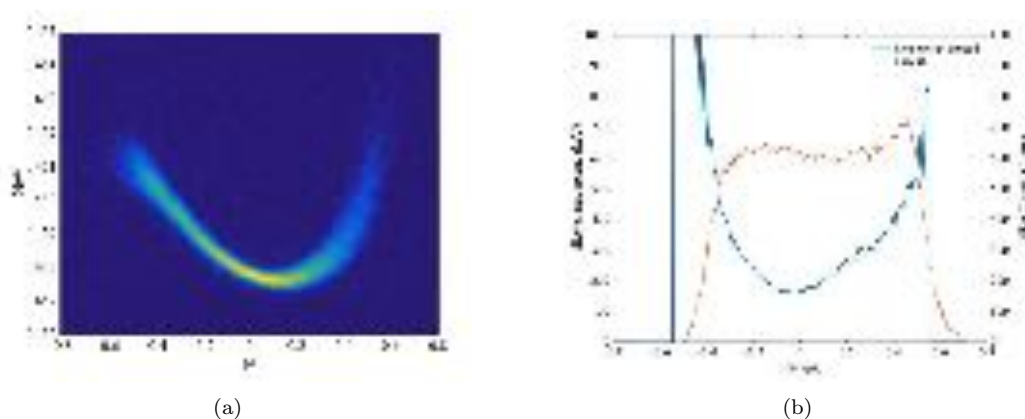


Figure A.7: Longitudinal phase space measurement and reconstruction at the LINAC end, for an electron bunch with 700 pC charge. Left: imaged LPS on a YAG screen in the energy spectrometer. Right: Time-sliced current (red line) and energy spread (blue line) along the bunch obtained by analyzing the image.

A.7 The hole

In a seeded FEL the interaction between the electron beam and the seed laser modify locally the energy distribution of the electron beam [23]. By taking advantage of the correlation between time and energy in the case of a quasi-linearly chirped electron beam and the fact that the FERMI seed laser pulse is much shorter than the electron beam duration, longitudinal measurements of the e-beam pulse length, local energy chirp and current are possible. After a proper calibration that allows to convert the horizontal coordinate of the MBD images into fs, it is possible to retrieve the relative position between the e-beam and the seed laser in fs and measure the jitter between the two.

Experimental results, reported in Fig.A.8, clearly show the presence of an hole in the electron beam spectrum when the seed laser is present. By measuring the evolution of the hole in the MBD spectra we can measure the changes in the relative timing between the electron beam and the seed laser for each shot: an example of a series of 200 seeded shots is reported in Fig.A.9. With this method we are able to measure a jitter of about 70 fs (RMS) between the laser and the electron beam.

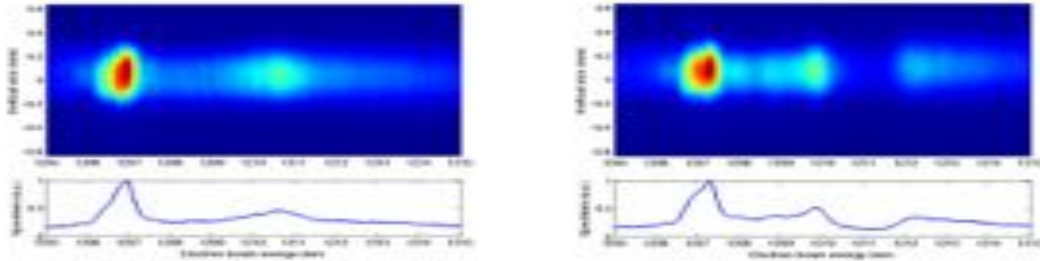


Figure A.8: The electron beam energy spectrum in MBD. Left: unseeded case. Right: seeded case. In specific configurations of the LINAC, the electron beam measured at the end of the accelerator shows strong linear time-energy correlation. Experimental results clearly show an hole in the electron beam spectrum as a result of the seeding process. Image reproduced from [23].

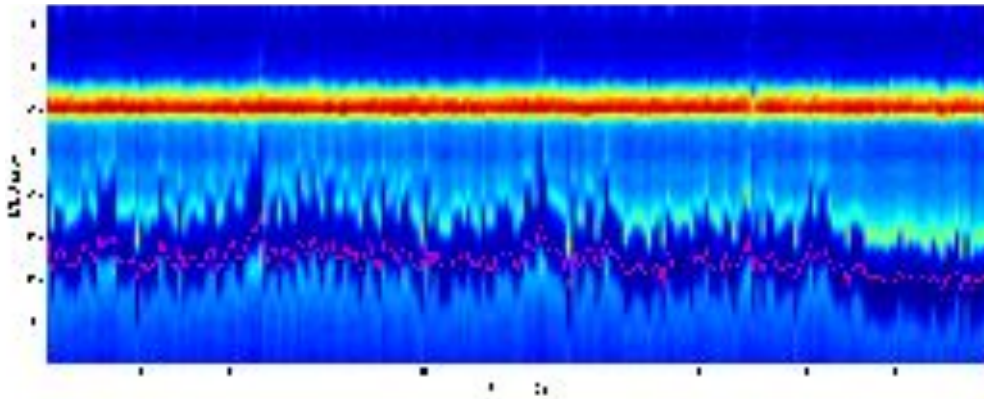


Figure A.9: Sequence of 200 seeded electron beam spectra measured in MBD. While the peak is fixed in energy, the position of the seed induced hole is moving. After a proper calibration, it is possible to retrieve the relative position between the e-beam and the seed in fs and measure the timing jitter between the two, which turns out to be ~ 70 fs (RMS). By measuring the evolution of the hole we can also evaluate the changes in the relative timing between the electron and seed laser for each shot. Image reproduced from [23].

A.8 Conclusions and prospective

We presented the longitudinal diagnostics and typical measurements performed at FERMI. The instruments are routinely used during FEL commissioning and user experiment and constitute one of the key components that contribute to FERMI reliability. The diagnostics and feedback systems are capable of keeping the time jitter of the electron beam well under control, with typical values at the undulator line of around 70 fs (RMS). Continuous improvements are undergoing, in order to increase the measurement capabilities and to further improve the reliability. A major update for machine operations will be the inclusion of the different longitudinal feedbacks into a single tool. Long term upgrades include the possibility of moving one high energy RF-deflector from the LINAC end to the undulator chain end, to include the BAMs output in timing feedback loops, to improve the EOS system for on-line longitudinal beam profile measurements during FEL operations and finally to take advantage of the hole effect as FEL emission diagnostic.

References

- [1] *Libera Single-Pass detector*. Instrumentation Technologies.
- [2] M. Dal Forno et al. “The Cavity Beam Position Monitor (BPM)”. In: *CAS 2011: Cern Accelerator School*. 2011.
- [3] V.L. Ginzburg and V.N. Tsytovich. *Transition radiation and Transition Scattering*. Adam Hilger, Bristol, UK, 1990.
- [4] W. Graves, P.G. O’Shea, and E.D. Johnson. In: *Proc. of PAC 1997*. Vancouver, Canada, 1997, p. 1993.
- [5] J. Rossbach and P. Schmüser. “Basic course on accelerator optics”. In: *Proc. of general accelerator physics school of CERN 1992*. Vol. 1. CERN, Geneva. 1994, p. 17.
- [6] C. J. et al. Bocchetta. *FERMI@Elettra FEL Conceptual Design Report*. Sincrotrone Trieste, 2007.
- [7] G. Penco et al. “Beam Optics Measurements at FERMI by Using Wire-Scanner”. In: *FEL 2015: Proceedings of the 37th International Free-Electron Laser Conference*. 2015.
- [8] G.L. Orlandi et al. “Design and Test of Wire-Scanners for SwissFEL”. In: *FEL 2014: Proceedings of the 36th International Free-Electron Laser Conference*. Basel, Switzerland, 2014.
- [9] M. Ferianis et al. “The Copper Free FERMI Timing System: Implementation and Results”. In: *Proc. Beam Instrumentation Workshop*. 2010, pp. 398–402.
- [10] G. Penco et al. “Experimental Demonstration of Electron Longitudinal-Phase-Space Linearization by Shaping the Photoinjector Laser Pulse”. In: *Phys. Rev. Lett.* 112 (4 2014), p. 044801. DOI: [10.1103/PhysRevLett.112.044801](https://doi.org/10.1103/PhysRevLett.112.044801).
- [11] M. Veronese et al. “Absolute Bunch Length Measurement Using Coherent Diffraction Radiation”. In: *Phys. Rev. Lett.* 110 (7 2013), p. 074802. DOI: [10.1103/PhysRevLett.110.074802](https://doi.org/10.1103/PhysRevLett.110.074802).
- [12] M. Lonza G. Gaio. “Automatic FEL Optimization at FERMI”. In: *ICALEPCS2015: Proceedings of the 15th International Conference on Accelerator and Large Experimental Control Systems*. 2015.
- [13] F. Loehl. “Optical Synchronization of a Free Electron Laser with femto-second precision”. PhD thesis. Hamburg, (Germany): Hamburg University, 2009.

- [14] M. Veronese et al. “First Operation of the Electro Optical Sampling Diagnostics of the FERMI@Elettra FEL”. In: *IBIC2012: Proceedings of the 2012 International Beam Instrumentation Conference*. 2012, TUPA43.
- [15] A. L. Cavalieri et al. “Clocking Femtosecond X Rays”. In: *Phys. Rev. Lett.* 94 (11 2005), p. 114801. DOI: [10.1103/PhysRevLett.94.114801](https://doi.org/10.1103/PhysRevLett.94.114801).
- [16] M. Veronese et al. “New Results of FERMI FEL1 EOS Diagnostics with Full Optical Synchronization”. In: *IBIC2014: Proceedings of the 2014 International Beam Instrumentation Conference*. 2014.
- [17] E. Ferrari et al. “Longitudinal Phase Space Characterization at FERMI@Elettra”. In: *IBIC2013: Proceedings of the 2013 International Beam Instrumentation Conference*. 2013.
- [18] M. Petronio. “Research and Applications of Radio-Frequency Deflecting Cavities”. PhD thesis. University of Trieste, 2009.
- [19] M. Röhrs. “Investigation of the Phase Space Distribution of Electron Bunches at the FLASH LINAC Using a Transverse Deflecting Structure”. PhD thesis. Hamburg, (Germany): Hamburg University, 2008.
- [20] P. Craievich et al. “A Low-Energy RF Deflector for the FERMI@Elettra Project”. In: *Proceedings of the 2010 Free-Electron Laser Conference*. Malmo, Sweden, 2010.
- [21] P. Craievich et al. “Implementation of Radio-Frequency Deflecting Devices for Comprehensive High-Energy Electron Beam Diagnosis”. In: *Nuclear Science IEEE Transactions* 62.120705 (1 2015).
- [22] C. Behrens et al. “Few-femtosecond time-resolved measurements of X-ray free-electron lasers”. In: *Nat Commun* 5 (Apr. 2014). DOI: [10.1038/ncomms4762](https://doi.org/10.1038/ncomms4762).
- [23] E. Allaria et al. “Energy slicing analysis for time-resolved measurement of electron-beam properties”. In: *Phys. Rev. ST Accel. Beams* 17 (1 2014), p. 010704. DOI: [10.1103/PhysRevSTAB.17.010704](https://doi.org/10.1103/PhysRevSTAB.17.010704).

Appendix B

Data Acquisition and Analysis

The acquisition and analysis of the machine data is a critical task to be carried on and is critical for the success of every experiment. In the following we will present the implementation of a MATLAB-based acquisition program that, exploiting the real time capabilities of the TANGO control system, is routinely used at FERMI for acquiring various machine parameters and electron beam properties together with most FEL signals on a shot-by-shot basis. Analysis of the saved data files is performed with a second code that can retrieve correlations and can be used to study dependence of FEL properties on machine parameters.

B.1 Real time capabilities at FERMI

The control system of FERMI uses the Tango [1] toolkit to provide an effective integration of technical systems and the software controlling them. A distributed real-time framework is integrated into the control system and provides the capability to measure the seed laser, electron and FEL output photon properties on a pulse-to-pulse basis [2]. With this framework, a unique “bunch number” time-stamp is distributed to all of the low level computers. Most of the measurement system detectors (e.g., electron and photon diagnostics) and actuators (e.g., power supplies) are synchronized with the bunch trigger and can have the bunch number associated to their measurements. Using the Tango bindings, the FERMI control system allows interfacing the accelerator instrumentation to Matlab. This capability has been used to develop various scripting procedures and GUIs to permit user interaction with the machine and has been extensively used for the commissioning of both FEL-1 [3] and FEL-2 [4].

B.2 The acquisition program

In this section we describe the MATLAB code implemented at FERMI for real time acquisition of relevant machine and FEL output signals. A brief description of the main features and components of the code will be presented. Acquisitions are first setup from the RT MATLAB graphical user interface (GUI), see Fig. B.1, that allows the user to define the type of acquisition and select some of the device signals to be acquired. Before the main acquisition begins, a one shot record of the most important machine parameters (e.g., undulator gap settings, dipole and quadrupole magnet currents, lasers intensities, ...) is acquired to provide a snapshot of the machine and FEL configuration. This information is stored and saved in the final archival data file. The predefined list of the acquired devices in principle

saves all the relevant information that will allow reconstruction of the LINAC and FEL state during the data analysis phase. When needed, the list of saved signals can be changed on a case-by-case basis via a user-defined configuration file.

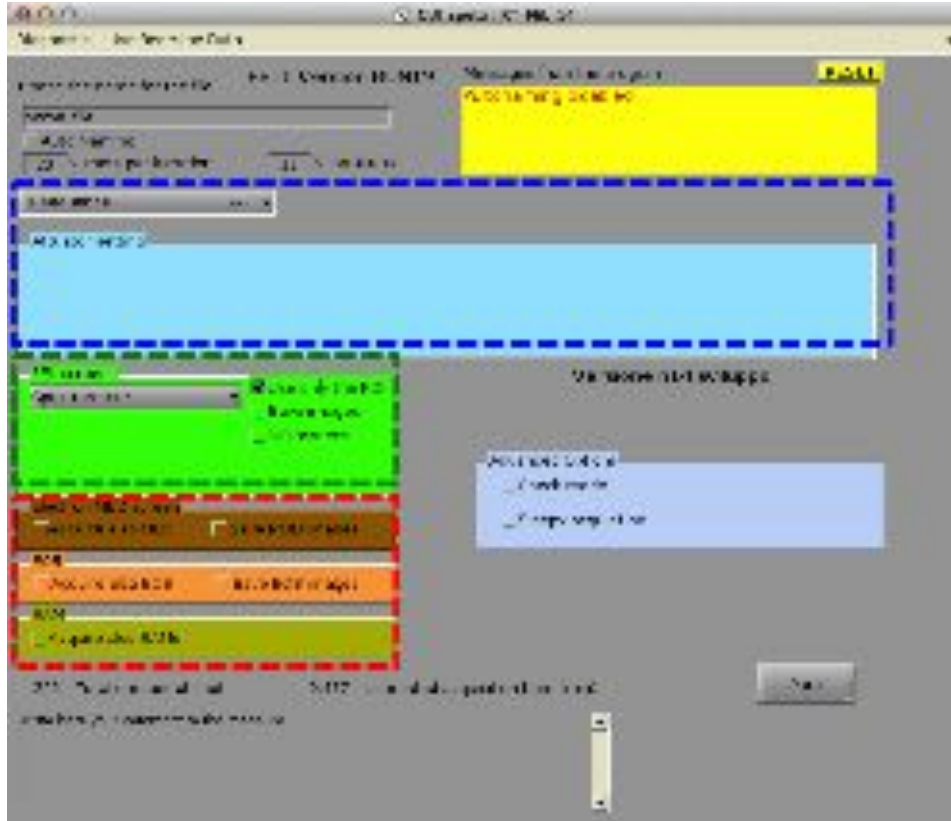


Figure B.1: Graphical user interface for RT acquisition of FERMI machine instruments.

B.2.1 Types of acquisition

The region highlighted in blue in Fig. B.1 is used to select the type of acquisition. At present three possible acquisition types are available: “RT sequence”, “actuator scan” and “script scan”. The RT sequence is the standard acquisition of the specified list of the machine devices, without any LINAC or FEL parameter being purposefully changed (i.e., “scanned”). The type of sequence is normally used to collect large quantities of data for statistical studies (e.g. correlations). The user can decide the length of the acquisition by deciding the number of shots acquired. The actuator scan allows the user to actively change a particular machine parameter (e.g., the seed laser power or a dispersion section magnet strength) in order to map the response of the FEL. The parameter is selected from a predefined list as shown in Fig. B.2.

Further options for defining the parameters of the scan (number of shots per individual scan parameter value acquired, the total range and number of parameters values scanned, accuracy, ...) are also available to the user (see Fig. B.3). At present standard actuator scans involve a linear change of actuator value.

acquired in synchronization with all the other diagnostics for those case they are needed and are made available (see the red highlighted region in Fig. 1). This includes the bunch arrival monitors (BAMs), electro-optical sampling (EOS) station and the main electron beam dump. After the acquisition is started, both messages about the scan progress are reported on the dedicated space in the GUI and selected data are shown within a dedicated figure. After acquisition is concluded, a logbook-ready image is displayed together with a summary of the acquisition, showing a small subset of the acquired data. An example is reported in Fig. B.4 where the FEL intensity and the FEL spectra are plotted as a function of the actuator used during the acquisition (in this case the seed laser delay). The plot also reports the name of the file that is saved at the end of the acquisition.

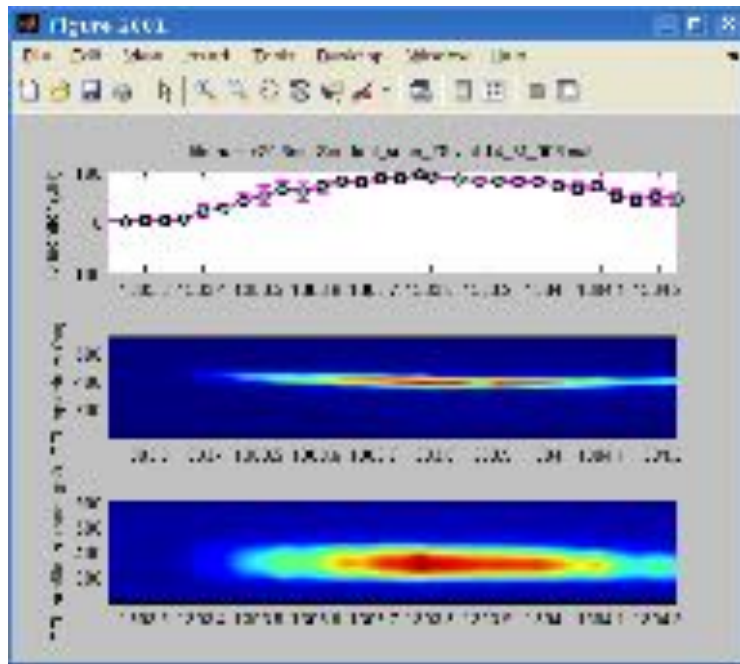


Figure B.4: Example of logbook-ready image produced by the program at the end of a scan.

The data file is saved in a MATLAB format, which allows a reasonably good compression, and contains all the acquired data as well as additional information such as the version of the code used, an optional user-defined comment to the acquisitions that can be inserted from the dedicated panel in the GUI, and the time of the acquisition.

A database entry is also written after each successive acquisition with the settings used and a summary of the machine configuration and parameters such as intensity and so on. This is extremely useful during data analysis and reduction.

B.3 The analysis program

After the data is taken and stored, a separate MATLAB-based program is available to analyze the information. An image of the graphical user interface is reported in Fig. B.5.

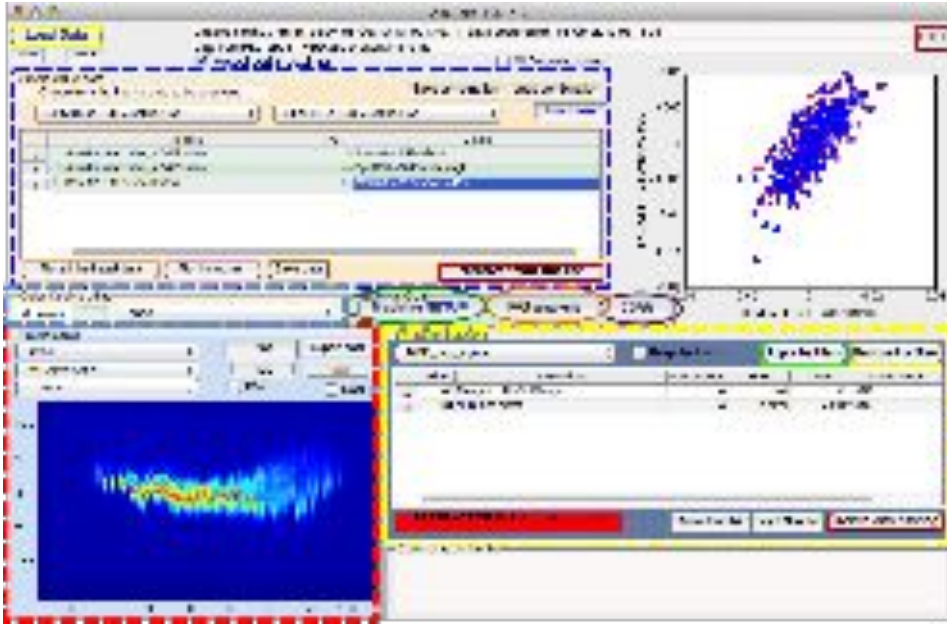


Figure B.5: Graphical user interface for the data analysis program.

B.3.1 Data selection

After a file is loaded, all the acquired “single value” devices present in file are recognized and listed in the two tab-listed region highlighted in blue in Fig. B.5. The two tab-lists allow the user to select an x-y combination whose preview is then shown in the side image. When the chosen x-y pair is considered acceptable, the user can add it to a table below. The data listed in the table is then considered for the final plotting, statistics computation and data exporting according to the user interests. Vector-like quantities (e.g., spectra profiles) are listed in a separate tab (the red highlighted region in Fig. B.5) and are visualized as false colours images. The vertical axis corresponds to 1D vector coordinate of each single profile while the horizontal direction corresponds to the different acquired bunches. A preview plot can also be done either by ordering bunches with time or according to the settings of a third device. This option is very useful for identifying correlation between the FEL spectra and other machine parameters as shown in Fig. B.6.

B.3.2 Data filtering

Filter tools are available to improve the effective S/N ratios and to weed out bad shots. The user can define filter parameters by mean of the dedicated panel (yellow highlighted region in Fig. B.5). The tab-list allows the user to select any of the acquired “single value” data and use it for filtering bad shots. In the particular case shown in Fig. B.5 the charge at the beginning of the LINAC and the position at the last e-beam screen are considered. The acceptance filter can be set by specifying extremes or by defining number of (RMS) sigmas. The program indicates to the user the amount of data that are rejected both in total and from each individual filter. Once the user has defined a filter configuration, it can be applied resulting in only the good shots will be used for all further analysis and plots. In in the graphs generated by the code, a label is inserted to emphasize the use of the filter and the

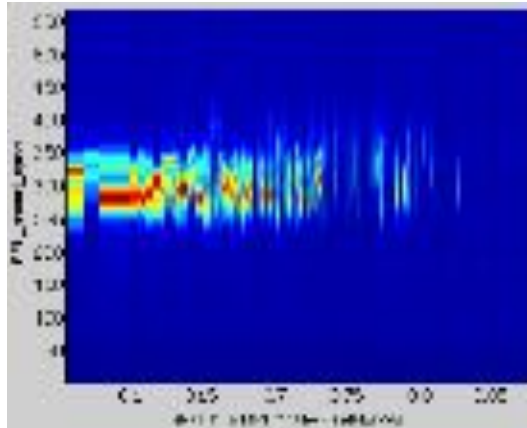


Figure B.6: FEL spectral profiles ordered as a function of the transverse electron beam position in a dispersive region.

percentage of used data (Figs. B.7, B.8, B.10).

B.3.3 Data analysis and plot

The data selected and listed in the table can be visualized in separate MATLAB figures. Various plots are generated depending on the type of acquisition and the user particular interests. In case of an “actuator scan” acquisition, if the actuator is selected for horizontal axis independent variable, an average and error bar are also calculated and plotted (Fig. B.7).

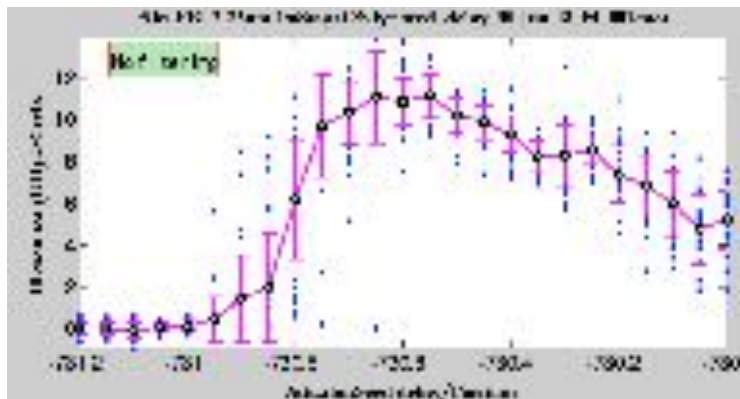


Figure B.7: Plot generated for a scan acquisition.

Because the acquired data are synchronized by bunch number, they can be used to visualize correlations between different parameters. This can be done by plotting as an example, the FEL intensity as a function of electron beam parameters. It can also be exploited to show the correlation in FEL-2 between the first stage emission and the second stage emission (Fig. B.8).

A visualization of the correlation between three separate machine parameters is also possible by using the dedicated “color coding” panel (the light blue highlighted region in Fig. B.5). An example is shown in Fig. B.9.

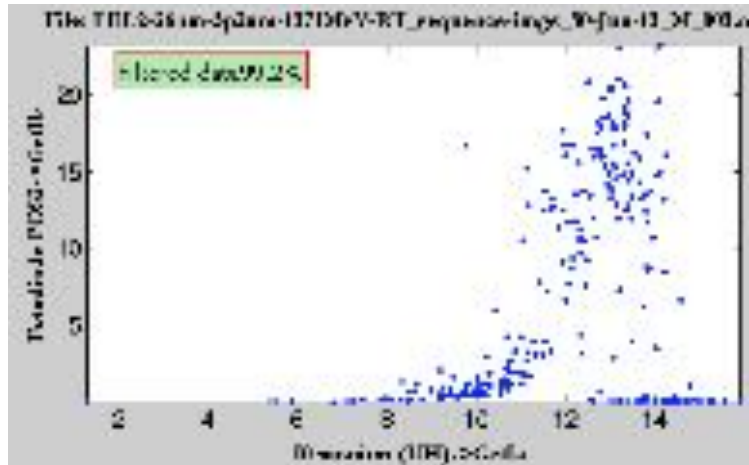


Figure B.8: Intensity of second stage vs the first stage emission from FEL-2 operated at 5nm.

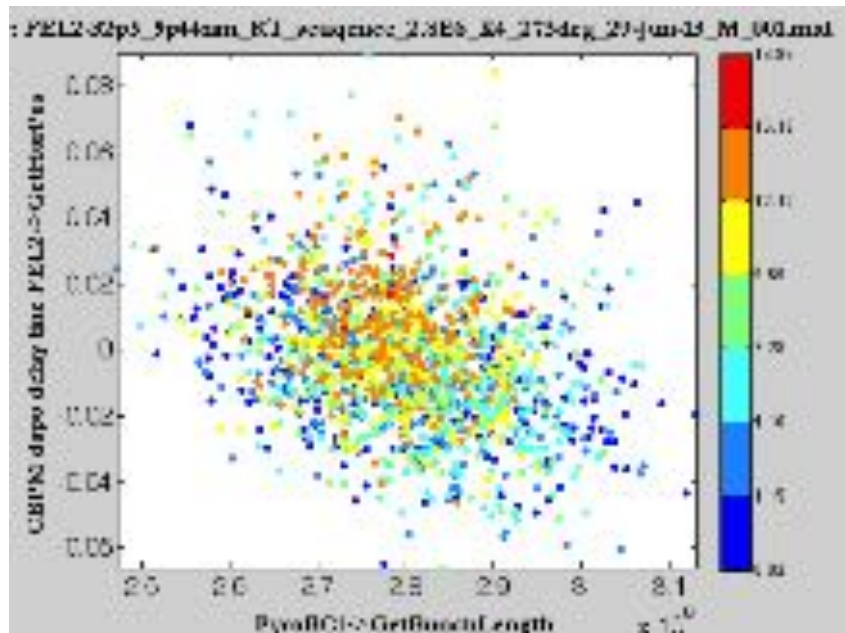


Figure B.9: FEL intensity in color code as a function of the beam compression and position signals.

A statistical analysis of the selected data is also possible and the distribution of the variable values can be plotted together with the calculated average and standard deviation values (Fig. B.10).

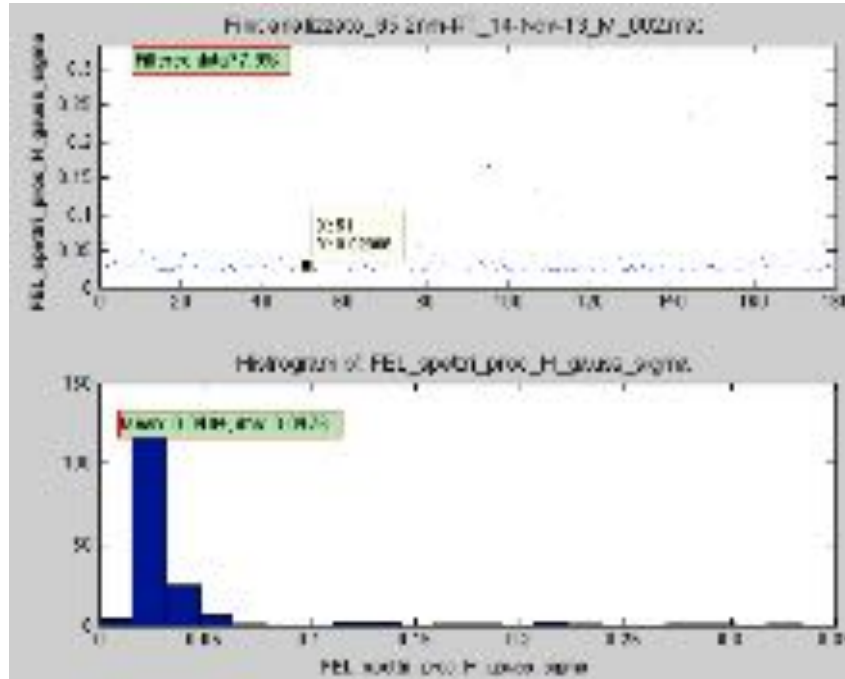


Figure B.10: Histogram distribution of the data selected.

The plotting of the profiles (1D vectors) is handled by the Profile Viewer utility (red highlighted region in Fig. B.5). A typical image showing the analyzed FEL spectrum as a function of on scanned parameter (dispersive section) together with the trend of the FEL intensity is shown in Fig. B.11.

If needed the data selected and listed in the table can be exported in ASCII format for further analysis or processing with external programs.

B.3.4 Visual correlator

Looking for hidden correlations in large sets of data can be a time consuming operation. Also, in normal operating conditions some correlations should be always present, ideally always with the same correlation coefficient. In order to have an overall indication of the correlations present in the machine, we developed a visual correlator tool (purple circle in Fig. B.5), which displays, in false color representation, all the correlation coefficients of the acquired data. An example of image obtained in this way is reported in Fig. B.12. Each row and column corresponds to the data of all the different devices that are acquired on a shot-to-shot basis during the acquisition. As one can expect the image is symmetric with respect to the top-left bottom-right diagonal. Each element along the diagonal itself corresponds to the autocorrelation, so it is equal to 1. A data-tip can be used to display a summary of the devices that are correlated by each point. Using the scroller on the right one can also filter out the correlation coefficients below a certain value.

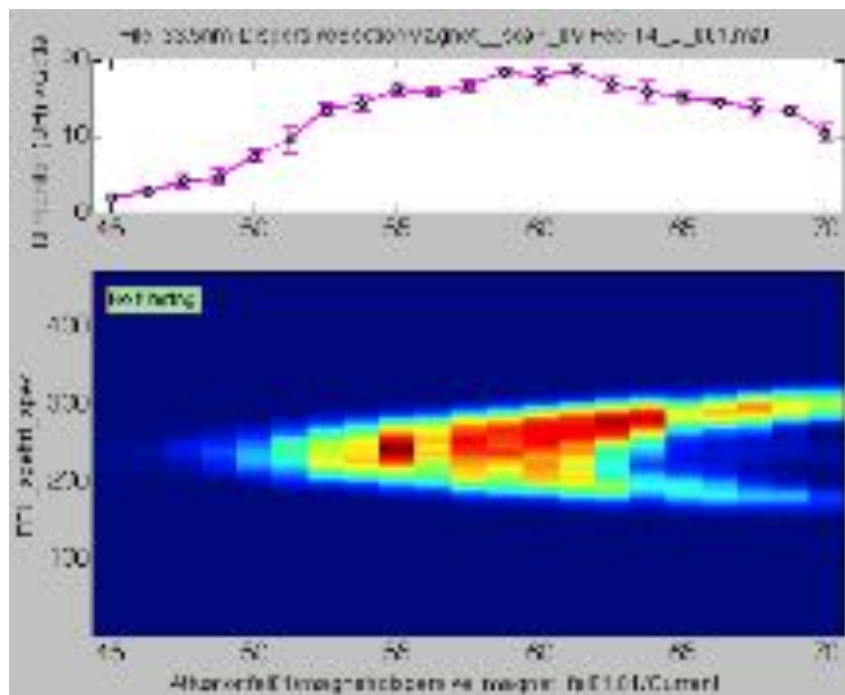


Figure B.11: Plot generated for a scan acquisition when a profile is selected, e.g., the FEL spectrum.



Figure B.12: False color representation of the correlation coefficient in between the acquired data.

B.3.5 Image analysis

For those data files where diagnostic screen data were taken with images or profiles, an external program can be used by means of the dedicated button (orange circle in Fig. B.5) to determine various quantities such as the centroid and (RMS) size in the two transverse planes. For files with profiles, e.g. FEL spectra, Gaussian fit to the output are used to determine bandwidth and central wavelength. These quantities can then be added to the list of “single value” data and correlated against individual machine signals in the case of RT sequences or against the scan parameter in actuator scans. In Fig. B.13 the GUI for the profile and image analysis dedicated program is shown.

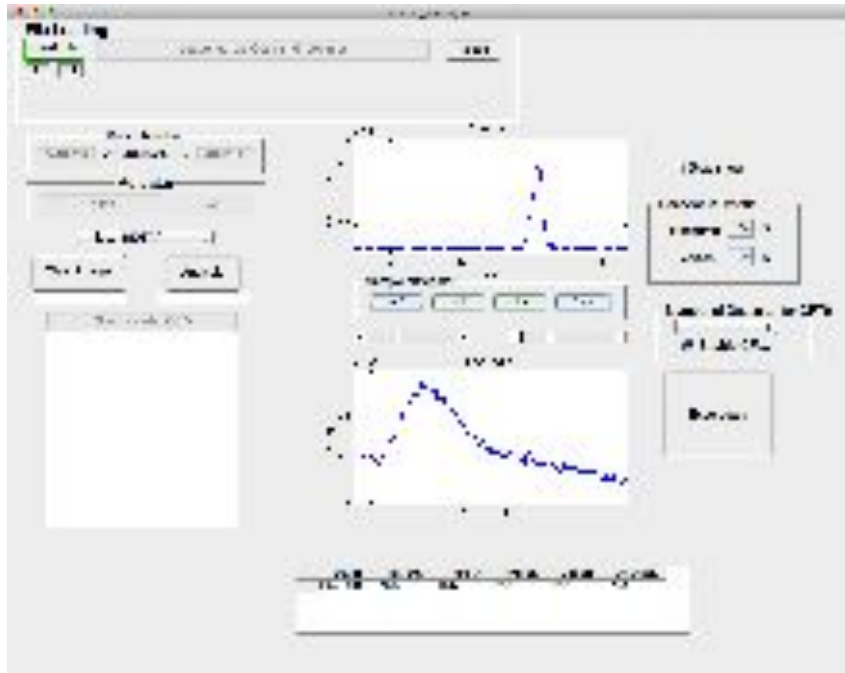


Figure B.13: Graphical user interface for the dedicated image analysis program.

B.3.6 Machine setup

The machine configuration snapshot produced by the acquisition program at the moment of the acquisition can be easily visualized by using a dedicated tool that is launched from the main GUI (green circle in Fig. B.5). The tool automatically recognizes the devices and produces a user-friendly table with their names and corresponding values divided by machine sectors as shown in Fig. B.14.

B.4 Conclusion

Over the past two years we have steadily improved the acquisition and analysis programs. Currently, more than half of all FERMI commissioning data is taken with them. Moreover, many scientific users on FERMI are also using the acquisition program (or specially modified

Parameter	Value	Unit	Default	Min	Max	Step
undulator_1	0.000000	m	0.000000	-0.000000	0.000000	0.000000
undulator_2	0.000000	m	0.000000	-0.000000	0.000000	0.000000
undulator_3	0.000000	m	0.000000	-0.000000	0.000000	0.000000
undulator_4	0.000000	m	0.000000	-0.000000	0.000000	0.000000
undulator_5	0.000000	m	0.000000	-0.000000	0.000000	0.000000
undulator_6	0.000000	m	0.000000	-0.000000	0.000000	0.000000
undulator_7	0.000000	m	0.000000	-0.000000	0.000000	0.000000
undulator_8	0.000000	m	0.000000	-0.000000	0.000000	0.000000
undulator_9	0.000000	m	0.000000	-0.000000	0.000000	0.000000
undulator_10	0.000000	m	0.000000	-0.000000	0.000000	0.000000

Figure B.14: Tool to visualize the machine snapshot showing the setting for the FEL undulators at the moment of the acquisition.

versions) for their studies. Since the acquired data is archived and is more-or-less self-describing in terms of contents, as the analysis program is improved, we are able to extract additional information from older data runs.

References

- [1] TANGO Controls: <http://www.tango-controls.org>.
- [2] M. Lonza et al. “Status Report of the FERMI@Elettra Control System”. In: *Proceedings of ICALEPCS2011*. 2011.
- [3] E. Allaria et al. “Highly coherent and stable pulses from the FERMI seeded free-electron laser in the extreme ultraviolet”. In: *Nature Photonics* 6.10 (2012), pp. 699–704. DOI: [10.1038/nphoton.2012.233](https://doi.org/10.1038/nphoton.2012.233).
- [4] E. Allaria et al. “Two-stage seeded soft-X-ray free-electron laser”. In: *Nature Photonics* 7.11 (2013), pp. 913–918. DOI: [10.1038/nphoton.2013.277](https://doi.org/10.1038/nphoton.2013.277).

Acknowledgments

I would like to thank all the peoples I had the opportunity and the privilege to work with during my PhD. I would like to thank my supervisor prof. Giovanni De Ninno for his guidance, support and all the patience he always has, with this Thesis in particular. I also thank prof. Alfonso Franciosi who supervised the Thesis and supported my PhD, together with Michele Svandrlik and Alessandro Fabris. I also thank prof. Paolo Camerini. The Manuscript was significantly improved thanks to the comments and corrections of the Referees dr. Sven Reiche and dr. David Garzella.

It has been a pleasure and an honour to be part of the FERMI commissioning team. Luca Giannessi has been an inspiration and a guidance for the work presented in this Thesis. I like to thank Enrico Allaria for the continuous support, patience and help in these years, as well as for having proofread parts of the initial Manuscript. A similar thank you goes to William M. Fawley for his uncommon patience and wisdom.

This Thesis would have been impossible without the work of all the teams collaborating to FERMI, which I thank a lot. I hope you can forgive me all for bothering you, even at ungodly hours.

In a completely random order I would like to say thank you to all the colleagues I had the opportunity to collaborate with: Giuseppe Penco, Bruno Diviacco, Simone Di Mitri, Mauro Trovò, Eleonore Roussel, David Gauthier, Carlo Spezzani, Maurizio Sacchi, Marco Veronese, Fabio Rossi, Mario Ferianis, Lars Fröhlich, Zhirong Huang, Jens Viefhaus, Simone Spampinati, Davide Castronovo, Miltcho Danailov, Alexander Demidovich, Paolo Sigalotti, Paolo Cinquegrana, Marco Zangrando, Lorenzo Raimondi, Nicola Mahne, Michele Manfreda, Carlo Callegari, Flavio Capotondi, Emiliano Principi, Claudio Serpico, Federico Gelmetti, Massimo Milloch, Giulio Gaio and all the machine operators.

I hope you had as nice times with me as I had with you all.

I will always remember the first time I heard about Free-Electron Lasers, and yes, I am referring to you dr. Riccardo Comin and to your suggestion, you are the best and it's your fault. A special thank you to Giulio, Alma and their TNT pub where many discussions took place. A mention for N. Burbaki and his invaluable lessons is also due. Prof. De Stefano and his bat-problems are always in my heart. This Thesis would have been impossible without the Sincro RUN team and its talented members. Thanks to coach Pencon, to Lupen and Ivan as well as to Pietro. Concerning the running, Cristian, you are really the one to blame for having me introduced to it. Thank you for that and for the support a good friend can offer.

A special thank you to my family who gave me the possibility to study and to do what I really like, despite all the difficulties. A kiss to Angela, thank you for always being there with me.